EVALUATION OF OXIDE CATHODES FABRICATED VIA FLAME ASSISTED VAPOUR DEPOSITION TECHNIQUE

by

Sumittra CHAROJROCHKUL

Thesis submitted for the
Degree of Doctor of Philosophy of the University of London
and the
Diploma of Imperial College

Department of Materials
Imperial College of Science, Technology and Medicine
Prince Consort Road
South Kensington
London SW7 2BP



BIBL
LONDON
UNIV.

September 1998

"For my parents and family who support me always."

ABSTRACT

Flame Assisted Vapour Deposition technique (FAVD) has been used to fabricate thick cathode films for high temperature Solid Oxide Fuel Cells (SOFC) operating at 700°C-850°C. The materials selection is based on the electrical conductivity, chemical and thermal compatibilities of the systems.

The effects of the processing parameters on the deposited films have been investigated such as the effects of deposition temperature, the flow rate of the precursor solution, the distance between the spray nozzle and the substrate, and the concentration and ratio of fuel in the precursor solution. The processing parameters were modelled using a software package based on finite volume method. The modelling results support the experimental observations.

The cathode material deposited in the investigation of FAVD technique was a porous strontium doped lanthanum manganese oxide ($La_{1-X}Sr_XMnO_3$ or LSM) film on an 8mol% yttria stabilised zirconia (YSZ) electrolyte substrate. The cathode/electrolyte system has been modified using a thin, dense interlayer between an electrolyte and a cathode as follows:

gadolinium doped cerium oxide (CGO), and
yttrium doped cerium oxide (YDC).

These cathode/electrolyte systems with interlayer were characterised using various techniques such as a Scanning Electron Microscopy, an AC-Impedance Spectroscopy, a DC 4-point measurement (van der Pauw) and an X-Ray Diffractrometry. Some systems were examined after annealing for 100 hours and 600 hours at 900°C in air to study the variation of an area specific resistivity (ASR) of the cathode with time. An overall result has shown an improvement in using an interlayer between the electrolyte and the cathode. This can enhance the use of a strontium doped lanthanum cobalt oxide ($(La_{0.8}Sr_{0.2}CoO_3$ or LSC) which has a higher electrical conductivity than the conventional LSM with YSZ electrolyte.

ACKNOWLEDGEMENTS

Throughout the years of hard working, the followings have contributed for my success in many different ways. I would like to express my gratitude towards all of them.

I would like to thank my supervisor, Dr. K.L. Choy, for moulding me into a competent researcher. I have learnt a lot from her in terms of both research and ordinary life. My work would never have been completed without Prof. B.C.H. Steele, who guided me through all the difficulties with suggestions and comments that gave me inspiration. His advice never failed to increase my motivation.

Thanks to Mr. R. Rudkin for the discussion about electrical measurements and SOFCs in general which are very useful. Instant literature can also be found from him. Mr R. Sweeney is always very helpful when I have any problems with XRD. Mr. A. Willis, and Mr. N. Salpadoru are helpful in both technical aid and advice. Thanks to Dr. D. Waller, Dr. J. Lane, Mrs. P. Carry, Dr. N. Coleman, Mr. A. Berenov, and Dr. J. Bae for the useful advice and help. Also, I would like to thank Dr. N. Kiratzis who was helping with the FAVD apparatus in the first year. The unforgetable person is Dr. R. Lothian who was very helpful with my modelling work, a big thank you here.

Dr. F. Lowrie was a very nice office-mate in addition of her useful advice, both technical and life in my early years.

Thanks these two friends who were unfortunate enough to proofread my thesis; Mr. S. Haque and Miss E. Akser. No one can live without friends and they have made my life here colourful and helped each other with any problems ; Mr. J.D. Vyas, Dr. W. Bai, Miss L.M. Lee, Miss H.J. Ahn, Miss. C. Meenakarn, Miss K. Maneeratana and the special person, Miss P. Saewong.

The last person I would like to acknowledge is Dr. C. Fisher who helped me with the thesis proofreading. Thanks for the encouragements when I need them the most during the writing up period.

My study in U.K. would not be possible without the scholarship from the Government of Thailand.

TABLE OF CONTENTS

ABSTRACT 3

ACKNOWLEDGEMENTS 4

TABLE OF CONTENTS 5

LIST OF TABLES 10

LIST OF FIGURES 13

LIST OF ABBREVIATIONS 20

CHAPTER 1 : PREFACE 21

CHAPTER 2 : LITERATURE REVIEW 24

2.1 BACKGROUND TO FUEL CELLS 24

2.1.1 CLASSIFICATION OF FUEL CELLS 24

2.1.2 FUEL CELL EFFICIENCY 29

2.2 SOLID OXIDE FUEL CELLS 32

2.2.1 COMPONENTS OF A SOLID OXIDE FUEL CELL 33

2.2.2 SOLID OXIDE FUEL CELL DESIGNS 36

2.3 ELECTROLYTES 41

2.3.1 ZrO_2 BASED ELECTROLYTES 41

2.3.2 CeO_2 BASED ELECTROLYTES 42

2.4 CATHODES 45

2.4.1 REACTIONS AT THE CATHODE 45

2.4.2 MICROSTRUCTURAL REQUIREMENTS 49

2.4.3 LANTHANUM MANGANITE ($LaMnO_3$) 52

2.4.4 Sr-DOPED LANTHANUM MANGANITE ($La_{(1-X)}Sr_XMnO_3$) 55

2.4.5 LANTHANUM COBALTITE ($LaCoO_3$, LCO) 62

2.4.6 OTHER OXIDES 63

2.4.7 OVERVIEW OF CATHODE MATERIALS 64

2.5 FABRICATION OF SOFC COMPONENTS 66
2.5.1 SINTERING ROUTE 66
2.5.2 VAPOUR PHASE ROUTE 68

2.6 SUMMARY 73

CHAPTER 3 : EXPERIMENTAL PROCEDURES 74

3.1 PREPARATION OF SUBSTRATES 74

3.2 PREPARATION OF PRECURSORS 74

3.3 FLAME ASSISTED VAPOUR DEPOSITION (FAVD) 76

3.4 CHARACTERISATION TECHNIQUES 82
3.4.1 STRUCTURAL CHARACTERISATION 82
3.4.2 ELECTRICAL PROPERTIES 83

CHAPTER 4: EFFECT OF PROCESS PARAMETERS IN THE DEPOSITION OF $La_{1-X}Sr_XMnO_3$ 88

4.1 RATIO OF ETHANOL/WATER IN THE PRECURSOR SOLUTION 90
4.1.1 CRYSTAL STRUCTURE 97

4.2 FLOW RATE OF PRECURSOR SOLUTION 99
4.2.1 $La_{0.61}Sr_{0.18}MnO_3$ 99
4.2.2 CRYSTAL STRUCTURE 101
4.2.3 $(La_{0.82}Sr_{0.18})_{0.9}MnO_3$ 102
4.2.4 CRYSTAL STRUCTURE 106

4.3 PRESSURE OF THE COMPRESSED AIR 107
4.3.1 CRYSTAL STRUCTURE 110

4.4 DISTANCE BETWEEN THE SPRAY NOZZLE AND THE SUBSTRATE 111
4.4.1 $La_{0.61}Sr_{0.18}MnO_3$ 112
4.4.2 CRYSTAL STRUCTURE 115
4.4.3 LSM 116

4.5 CONCENTRATION OF THE PRECURSOR SOLUTION 119
4.5.1 CRYSTAL STRUCTURE 129

4.6 STOICHIOMETRY STUDY OF LSM 130

4.7 CHEMICAL REACTIONS 132

4.8 TEMPERATURE DISTRIBUTION 135

4.9 SUMMARY 139

CHAPTER 5 : ELECTRICAL PROPERTIES OF $La_{1-X}Sr_XMnO_3$ 142

5.1 ELECTRICAL CONDUCTIVITY 142

5.1.1 $La_{0.82}Sr_{0.18}MnO_3$ 142

5.1.2 $(La_{0.82}Sr_{0.18})_{0.9}MnO_3$ 146

5.1.3 IMPROVED LSM 148

5.2 ELECTROCHEMICAL PROPERTY OF LSM 152

5.3 SUMMARY 160

CHAPTER 6 : IMPROVED CATHODE 161

6.1 CGO INTERLAYER ON YSZ 162

6.2 YDC INTERLAYER ON YSZ 171

6.3 EFFECT OF ANNEALING TIME 174

6.3.1 LATERAL ELECTICAL RESISTIVITY 175

6.3.2 AREA SPECIFIC RESISTIVITY 180

6.4 EFFECT OF OXYGEN PARTIAL PRESSURE 190

6.5 CALCULATED ELECTRODE ASR 193

6.6 SUMMARY 198

CHAPTER 7 : MODELLING 200

7.1 EXPERIMENTAL SETUP 200

7.2 OVERVIEW 202

7.3 BASIC EQUATIONS IN MODELLING 203

7.3.1 HEAT TRANSFER AND FLUID FLOW GOVERNING EQUATIONS IN THE GAS PHASE 203

7.3.2 SECONDARY PHASE EQUATIONS 206

7.3.3 MODELS FOR TURBULENT FLOW 208

7.3.4 CHEMICALLY REACTING FLOW MODELS 211

7.3.5 MODELS DESCRIBING THE SYSTEM CHEMISTRY 214

7.3.6 PDF MODELLING OF TURBULENCE-CHEMISTRY INTERACTION 214

7.4 PROPERTIES OF FLUIDS 216

7.4.1 DENSITY 216

7.4.2 SPECIFIC HEAT CAPACITY 216

7.4.3 TRANSPORT PROPERTIES 216

7.5 BOUNDARY CONDITIONS 217

7.5.1 SPECIFIED VELOCITY BOUNDARY CONDITIONS 217

7.5.2 OUTLET BOUNDARIES 218

7.5.3 SYMMETRY BOUNDARIES 218

7.5.4 WALL BOUNDARIES 218

7.6 PARAMETERS AND CONDITIONS 219

7.6.1 PDF MODEL 219

7.6.2 FLUENT 220

7.7 RESULTS 222

7.7.1 EFFECT OF MIXTURE FRACTIONS 222

7.7.2 EFFECT OF DROPLET SIZE 225

7.8 DISCUSSION 227

7.8.1 EFFECT OF MIXTURE FRACTION 227

7.8.2 EFFECT OF AMOUNT OF ALCOHOL 228

7.8.3 EFFECT OF DROPLET SIZE 230

7.9 SUMMARY 231

CHAPTER 8 : CONCLUSIONS AND FUTURE WORK 232

8.1 : CONCLUSIONS 232

8.2 : FUTURE WORK 235
8.2.1 FAVD METHOD 235
8.2.2 ELECTRICAL PROPERTIES 236

LIST OF PUBLICATIONS 237

CHAPTER 9 : REFERENCES 238

APPENDIX 249

LIST OF TABLES

Chapter 2

Table 2.1 Power capacity and applications of fuel cells [4].

Table 2.2 Ionic conductivities of various electrolytes

Table 2.3 Electrical conductivity of $La_{1-X}Sr_XMnO_3$.

Table 2.4 Electrical conductivity of cathode materials.

Table 2.5 Area Specific Resistivities (ASRs) of cathode materials on YSZ.

Table 2.6 Coefficients of thermal expansion of some cathode materials.

Table 2.7 Kinetic data of selected cathode materials.

Table 2.8 Advantages and disadvantages of some conventional processing techniques.

Table 2.9 Coefficient of Thermal Expansion of selected materials for SOFCs.

Chapter 4

Table 4.1 Fixed parameters in the effect of ethanol/water ratio depositions

Table 4.2 Deposition of $La_{0.82}Sr_{0.18}MnO_3$ at various ethanol/water ratios.

Table 4.3 Deposition of $La_{0.82}Sr_{0.18}MnO_3$ at various ethanol/water ratios at the flow rate of 10 ml/min.

Table 4.4 Phases identification of films deposited at various temperatures.

Table 4.5 Results of LSM0.61 films deposited at various flow rates.

Table 4.6 Results of LSM0.9 films deposited at various flow rates.

Table 4.7 Controlled parameters for the investigation of the pressure of the compressed air.

Table 4.8 Results of $La_{0\ 82}Sr_{0.18}MnO_3$ films deposited at various pressures.

Table 4.9 Controlled process parameters in the deposition of $La_{1-X}Sr_XMnO_3$ at various distances

Table 4.10 Results of LSM0.61 films deposited in the investigation of the effect of d.

Table 4.11 Results of LSM films deposited in the investigation of the effect of d.

Table 4.12 Descriptions and comments of LSM film in the investigation of precursor concentration.

Table 4.13 Impurity phases in different concentration of the precursor solution.

Table 4.14 Deposition temperatures and stoichiometry of La : Sr : Mn.

Table 4.15 Parameters used for the temperature distribution investigation.

Chapter 5

Table 5.1 Lateral electrical resistivities of $La_{0.82}Sr_{0.18}MnO_3$ from dc 4-point (Van der Pauw) technique at various precursor concentrations.

Table 5.2 Lateral electrical resistivities of $La_{0.82}Sr_{0.18}MnO_3$ from dc 4-point (Van der Pauw) technique at various air pressures.

Table 5.3 Lateral electrical resistivities of $(La_{0.82}Sr_{0.18})_{0.9}MnO_3$ from dc 4-point (Van der Pauw) technique.

Table 5.4 Deposition conditions of LSM0.61.

Table 5.5 Deposition conditions of LSM duplex structure.

Table 5.6 Lateral electrical resistivities of improved LSM.

Table 5.7 Deposition conditions and Area Specific Resistivity (ASR) of LSM.

Chapter 6

Table 6.1 Deposition parameters of CGO and LSC.

Table 6.2 Descriptions and comments of CGO/LSC films.

Table 6.3 Electrode ASRs and lateral electrical resistivities (ρ) of CGO/LSC films.

Table 6.4 Phases present and thickness of CGO/LSC interlayers.

Table 6.5 Deposition parameters of YDC interlayer.

Table 6.6 Lateral electrical resistivities and ASRs of YC/LM and YC/LC.

Table 6.7 Lateral electrical resistivities, ρ, (Ω/cm) of selected combinations of cathode/interlayer films.

Table 6.8 Activation energy of the reciprocal of ρ in eV, of selected combinations of cathode/interlayer films.

Table 6.9 Activation energies (eV) of the reciprocal of ASRs after several annealing periods.

Table 6.10 Calculated R_{chem} for $La_{0.8}Sr_{0.2}CoO_{3-\delta}$.

Table 6.11 Microstructural parameters for CG/LC10 and YC/LC.

Appendix

Table A1 Electrode ASRs and activation energy (E_A) of the reciprocal of ASR for sample LSC30 at several annealing periods.

Table A2 Electrode ASRs and activation energy (E_A) of the reciprocal of ASR for sample LSC12 at several annealing periods.

Table A3 Electrode ASRs and activation energy (E_A) of the reciprocal of ASR for sample CG/LC10 at several annealing periods.

Table A4 Electrode ASRs and activation energy (E_A) of the reciprocal of ASR for sample YC/LC at several annealing periods.

Table A5 Electrode ASRs and activation energy (E_A) of the reciprocal of ASR for sample YC/LM at several annealing periods.

Table A6 ASRs of sample LSC30 after annealing for 600 hours.

Table A7 ASRs of sample LSC12 after annealing for 100 hours.

LIST OF FIGURES

Chapter 2

Fig. 2.1 Efficiencies of fuel cells.

Fig. 2.2 Schematic diagram of a solid oxide fuel cell.

Fig. 2.3 Sealless tubular design.

Fig. 2.4 The segmented-cell-in-series design.

Fig. 2.5 The monolithic design (a) coflow and (b) crossflow configurations.

Fig. 2.6 (a) The bipolar plate design and (b) stacking of cells.

Fig. 2.7 The cubic fluorite crystal structure.

Fig. 2.8 Reaction steps of oxygen reduction at a triple phase boundary.

Fig. 2.9 Schematic diagram of cathode reactions at a TPB.

Fig. 2.10 Schematic diagram of cathode reactions at electrode/electrolyte interface.

Fig. 2.11 An ideal perovskite structure, $LaMnO_3$.

Fig. 2.12 Phase diagram of the La_2O_3-Mn_2O_3 system.

Fig. 2.13 Chemical potential diagram of the La-Zr-Mn-O system.

Fig. 2.14 $La_{1-X}Sr_XMnO_3$ nonstoichiometry versus oxygen partial pressure.

Fig. 2.15 Conductivity of LSM as a function of temperature and Sr content.

Fig. 2.16 Conductivity of $La_{0.8}Sr_{0.2}MnO_3$ as a function of oxygen partial pressure.

Fig. 2.17 (a) Reaction products formed at the LSM/YSZ interface as a function of strontium content and temperature and (b) Chemical potential diagram of the La-Sr-Mn-Zr-O system at 1300°C.

Chapter 3

Fig. 3.1 A schematic diagram of the Flame Assisted Vapour Deposition apparatus.

Fig. 3.2 The original FAVD apparatus.

Fig. 3.3 Sketches of the ceramic holder.

Fig. 3.4 A sketch of a deposition enclosure.

Fig. 3.5 FAVD apparatus with a quartz tube.

Fig. 3.6 A cross-section of a symmetrical cell.

Fig. 3.7 A schematic diagram of an AC impedance spectroscopy sample holder.

Fig. 3.8 (a) A typical AC-impedance spectrum and b) A series circuit referring to the semicircles in the spectrum.

Fig. 3.9 Combinations of the resistances from the 4-point contacts.

Chapter 4

Fig. 4.1 A sketch of various combustion zones in the FAVD method.

Fig. 4.2 Surface morphology and cross-sectioned films deposited at various ratios of ethanol to water ; (a) 80/20, (b) 75/25, (c) 70/30, and (d) 60/40.

Fig. 4.3 A sketch of the relationship between the combustion zone and the deposition process.

Fig. 4.4 Surface morphology and cross-section of films deposited at various ratios of ethanol to water ; (a) 80/20, (b) 75/25, (c) 70/30, and (d) 50/50. The flow rate of the precursor solution was 10 ml/min.

Fig. 4.5 XRD patterns of LSM films deposited at (a) 680°C-710°C, (b) 650°C-690°C, (c) 480°C-530°C, and (d) 300°C-350°C.

Fig. 4.6 Surface morphology and cross-sectioned of LSM0.61 films deposited at a) 5.5 ml/min, b) 10 ml/min, and c) 17 ml/min.

Fig. 4.7 XRD patterns of LSM films deposited in section 4.2.1 at flow rate (a) 5.5 ml/min, (b) 10 ml/min, and (c) 17 ml/min.

Fig. 4.8 Surface morphology and cross-sectioned LSM0.9 films deposited using 80/20 ethanol/water ratio at (a) 10, (b) 12 ml/min, and (c) 15 ml/min, and 70/30 ethanol/water ratio at (d) 10, (e) 12 , and (f) 15 ml/min.

Fig. 4.9 A typical XRD pattern of LSM film deposited in section 4.2.3.

Fig. 4.10 Surface morphology and cross-sectioned of $La_{0.82}Sr_{0.18}MnO_3$ films deposited at (a) 15 psi, (b) 22 psi, and (c) 26 psi.

Fig. 4.11 A sketch of deposition processes at various compressed air pressures.

Fig. 4.12 XRD patterns of LSM films deposited at (a) 17 psi, (b) 22 psi, (c) 26 psi, and (d) 26 psi after annealing.

Fig. 4.13 Surface morphology and cross-sectioned LSM0.61 films deposited at distance (a) 8 cm, (b) 12 cm, and (c) 16 cm between the spray nozzle and the substrate.

Fig. 4.14 A sketch of the deposition process at various distances in the combustion zone.

Fig. 4.15 XRD patterns of films deposited at distance (a) 16 cm and (b) 8 cm between the spray nozzle and the substrate.

Fig. 4.16 Surface morphology and cross-sectioned LSM films deposited at distance (a) 10 cm, and (b) 12 cm and the flow rate 12 ml/min. (c) and (d) are at distance 10 cm and 12 cm at the flow rate 10 ml/min.

Fig. 4.17 Surface morphology and cross-sectioned LSM deposited from 0.1 Molar precursor solution at ethanol/water ratio (a) 80/20, (b) 75/25, (c) 70/30, and (d) 60/40.

Fig. 4.18 Surface morphology and cross-sectioned LSM deposited from 0.075 Molar precursor solution at ethanol/water ratio (a) 80/20, (b) 75/25, and (c) 70/30.

Fig. 4.19 Surface morphology and cross-sectioned LSM deposited from 0.05 Molar precursor solution at ethanol/water ratio (a) 80/20, (b) 75/25, (c) 70/30, and (d) 60/40.

Fig. 4.20 Surface morphology and cross-sectioned LSM deposited from 0.025 Molar precursor solution at ethanol/water ratio (a) 80/20, (b) 75/25, (c) 70/30, and (d) 65/35.

Fig. 4.21 Surface morphology and cross-sectioned LSM deposited from 0.01 Molar precursor solution at ethanol/water ratio (a) 80/20, (b) 70/30, and (c) 60/40.

Fig. 4.22 A sketch of particle agglomerations when the concentration of the precursor is (a) low, (b) moderate, and (c) high.

Fig. 4.23 XRD patterns of LSM powder from (a) 70% and (b) 80% ethanol/water.

Fig. 4.24 A sketch of a temperature distribution of FAVD technique for the 80 % ethanol precursor solution

Fig. 4.25 A sketch of a temperature distribution of FAVD technique for the 70 % ethanol precursor solution

Fig. 4.26 (a) surface morphology and (b) cross-section of FAVD film showing the change from individual particles to connected particles.

Chapter 5

Fig. 5.1 Conductivity of LSM films deposited at various precursor concentrations.

Fig. 5.2 Conductivity of LSM films deposited at various air pressures.

Fig. 5.3 Conductivity of LSM films deposited at various flow rate and ethanol/water ratios.

Fig. 5.4 An improved LSM with composition, LSM0.61, (a) surface morphology and (b) cross-section.

Fig. 5.5 An improved LSM with microstructure, LSM-du, (a) surface morphology and (b) cross-section.

Fig. 5.6 Conductivity vs 1/Temperature of LSM

Fig. 5.7 Microstructures of (a) LSMX, (b) LSMY, and (c) LSMZ.

Fig. 5.8 XRD patterns of (a) LSMY, (b) LSM-du, and (c) LSM0.61

Fig. 5.9 AC-impedance responses of (a) LSMY and (b) LSM-du at various temperatures.

Chapter 6

Fig. 6.1 Surface morphology and cross-sections of (a) CG/LC10, (b) CG/LC30, (c) CG/LC97, (d) CG/LC11, (e) CG/LC14, and (f) CG/LC17.

Fig. 6.2 AC-impedance responses of (a) CG/LC10, (b) CG/LC11.

Fig. 6.3 (a) Surface morphology and (b) cross sections of YC/LM. (c) and (d) are as above for YC/LC.

Fig. 6.4 AC-impedance responses of (a) YC/LM and (b) YC/LC.

Fig. 6.5 Surface morphology and cross-section of (a) LSC30, (b) LSC12, (c) CG/LC10, (d) YC/LC, and (e) YC/LM.

Fig. 6.6 Surface morphology and cross-section of (a) LSC30, (b) LSC12, (c) CG/LC10, (d) YC/LC and (e) YC/LM after annealing (see overleaf).

Fig. 6.7 Plots of electrode ASRs after certain annealing periods at (a) 800°C and (b) 900°C for LSC30, LSC12, CG/LC10, YC/LC, and YC/LM.

Fig 6.8 AC-impedance responses of sample LSC30 after annealing for (a) 10 hours, (b) 100 hours, and (c) 600 hours.

Fig 6.9 AC-impedance responses of sample LSC12 (a) as deposited and (b) after annealing for 100 hours.

Fig 6.10 AC-impedance responses of sample CG/LC10 (a) as deposited and (b) after annealing for 94 hours.

Fig 6.11 AC-impedance responses of sample YC/LC (a) as deposited and (b) after annealing for 100 hours.

Fig 6.12 AC-impedance responses of sample YC/LM (a) as deposited and (b) after annealing for 100 hours.

Fig. 6.13 Plots of gb ASRs after certain annealing periods at 400°C for (a) LSC30, (b) LSC12, (c) CG/LC10, (d) YC/LC, and (e) YC/LM.

Fig. 6.14 Plots of bulk ASRs after certain annealing periods at 400°C for (a) LSC30, (b) LSC12, (c) CG/LC10, (d) YC/LC, and (e) YC/LM.

Fig. 6.15 Plots of (a) electrode ASRs, (b) gb ASRs, and (c) bulk ASRs of LSC30 at various oxygen partial pressures.

Fig. 6.16 Plots of (a) electrode ASRs, (b) gb ASRs, and (c) bulk ASRs of at various oxygen partial pressures.

Fig. 6.17 Surface Exchange Coefficient (k) of CG/LC10 and YC/LC with annealing time.

Fig. 6.18 Self-Diffusion Coefficient of Oxygen (D*) of CG/LC10 and YC/LC with annealing time.

Fig. 6.19 Combination of k and D* of CG/LC10 and YC/LC with annealing time.

Chapter 7

Fig. 7.1 A grid of the model setup.

Fig. 7.2 Boundary conditions of the model used in this Chapter.

Fig. 7.3 Temperature distribution contours at different mixture fractions for 70% alcohol solution.

Fig. 7.4 Maximum Temperature versus Mixture Fraction for the 70% alcohol.

Fig. 7.5 The Maximum Temperature for Various Percentages of Alcohol and Mixture Fractions.

Fig. 7.6 The flow velocity vectors of a mixture fraction 0.2 for 70% alcohol solution.

Fig. 7.7 Mass fraction of chemical species present for 50%, 70%, and 80% alcohol mixtures.

Fig. 7.8 Temperature distribution contours of various droplets size (a) 10, (b) 50, (c) 100, (d) 10-50, (e) 10-100, and (f) 50-100 microns when the mixture fraction was fixed at 0.2.

Appendix

Fig. A1 AC-impedance responses of (a) CG/LC30, (b) CG/LC97, (c) CG/LC14, and (d) CG/LC17.

Fig. A2 AC-impedance responses of sample LSC30 after annealing for (a) 20 hours and (b) 36 hours.

Fig. A3 AC-impedance responses of sample LSC12 after annealing for (a) 10 hours, (b) 20 hours, and (c) 36 hours.

Fig. A4 AC-impedance responses of sample CG/LC10 after annealing for (a) 4 hours, (b) 14 hours, and (c) 30 hours.

Fig. A5 AC-impedance responses of sample YC/LC after annealing for (a) 10 hours, (b) 20 hours, and (c) 36 hours.

Fig. A6 AC-impedance responses of sample YC/LM after annealing for (a) 10 hours, (b) 20 hours, and (c) 36 hours.

Fig. A7 AC-impedance responses before annealing and after 100 hours annealing in the range of low temperature for (a) LSC30, (b) LSC12, (c) CG/LC10 (94 hours), (d) YC/LC, and (e) YC/LM (see overleaf).

Fig. A7 AC-impedance responses before annealing and after 100 hours annealing in the range of low temperature (e) YC/LM.

Fig. A8 AC-impedance responses of sample LSC30 in oxygen partial pressure (a) 0.10 atm and (b) 0.05 atm.

Fig. A9 AC-impedance responses of sample LSC12 in oxygen partial pressure (a) 0.10 atm and (b) 0.05 atm.

Fig A10 XRD patterns of sample LSC30 after annealing for (a) 10 hours, (b) 36 hours, (c) 100 hours, and (d) 600 hours.

Fig A11 XRD patterns of sample LSC12 (a) as deposited, after annealing for (b) 10 hours, (c) 36 hours, and (d) 100 hours.

Fig A12 XRD patterns of sample CG/LC10 (a) as deposited, after annealing for (b) 4 hours, (c) 30 hours, and (d) 94 hours.

Fig A13 XRD patterns of sample YC/LC (a) as deposited, after annealing for (b) 10 hours, (c) 36 hours, and (d) 100 hours.

Fig A14 XRD patterns of sample YC/LM (a) as deposited, after annealing for (b) 10 hours, (c) 20 hours, (d) 36 hours, and (e) 100 hours.

Fig. A15 Temperature distribution contours of at different mixture fractions for 50% alcohol solution.

Fig. A16 Temperature distribution contours of at different mixture fractions for 80% alcohol solutions.

Fig. A17 Mass fraction of oxygen gas present for (a) 50%, (b) 70%, and (c) 80% alcohol solutions.

Fig. A18 Mass fraction of water present for (a) 50%, (b) 70%, and (c) 80% alcohol solutions.

Fig. A19 Mass fraction of carbon monoxide present for (a) 50%, (b) 70%, and (c) 80% alcohol solutions.

Fig. A20 Mass fraction of carbon dioxide for (a) 50%, (b) 70%, and (c) 80% alcohol solutions.

LIST OF ABBREVIATIONS

AFC	=	Alkaline Fuel Cell
ASR	=	Area Specific Resistivity
CGO	=	Cerium-gadolinium oxide
LSC	=	Lanthanum strontium cobalt oxide
LSM	=	Lanthanum strontium manganese oxide
MCFC	=	Molten Carbonate Fuel Cell
PAFC	=	Phosphoric Acid Fuel Cell
PMFC	=	Polymer Membrane Fuel Cell
SEM	=	Scanning Electron Microscopy
SOFC	=	Solid Oxide Fuel Cell
XRD	=	X-Ray Diffraction
YDC	=	Cerium-yttrium oxide
YSZ	=	Zirconium-yttrium oxide (8 mol%)

Chapter 1 : PREFACE

There are many types of power generation systems which convert different states of energy into electricity. Conventional systems of power generation are hydro power, nuclear power, tidal power, wind power, and power from fossil fuel including oil, natural gas etc. The efficiency of each system is fairly low, in both the theoretical evaluations of the system itself, and the limitation in energy conversion. Fossil fuel has its own problem of a renewal period of millions' years. Most of them cause pollution which then affects the environment. There has been great concern over this problem for many years. For example, acid rain causes damage to forests, monuments and buildings. Wastes from the sites are generally harmful and detrimental to ecological systems. There have been increasing difficulties with nuclear power such as the radioactive leakage and radioactive wastes. Although these power generators can produce low-cost electricity, the scale of production must be large enough to cover the enormous fixed capital cost. Therefore it is not economical to produce on a small scale. There have been many attempts to develop more suitable energy conversion systems by either using solar energy operated in a solar cell or an electrochemical reaction in a fuel cell.

A fuel cell is very similar to a vehicle's battery in terms of energy conversion theory. The energy conversion is based on the electrochemical reactions of chemicals in the cell which are fuel and oxidant liquid or gas. Because of its finite length of operation, a fuel cell becomes more interesting as it is operative as long as the fuel and oxidant are constantly supplied to the system.

Fuel cells in general have many advantages over conventional power generators. Its conversion efficiency is not subjected to the Carnot-cycle limitations associated with heat engines [1 , 2]. The potential for co-generation is also high enough to be applicable. In addition, it causes a much lower amount of pollution. The modular construction can minimise the siting restrictions [2]. Among many types of fuel cells, the solid oxide fuel cell (SOFC) performs with the highest overall efficiency using fossil fuels along with the molten carbonate fuel cell (MCFC) although, the SOFC is more flexible as it is suitable for small units as well as large

scale plants. Nevertheless, some difficulties arise from the fabrication of the cell components, materials selection and high operating temperature associated with SOFC which have to be overcome before this technology becomes commercially viable.

A novel method of Flame Assisted Vapour Deposition (FAVD) has been used to deposit a porous cathode film for SOFCs in our research. This method has a similar principle to conventional CVD in which a film is deposited from the vapour phase. It is a cost effective method which yields a film of reasonable quality both in terms of microstructure and electrical properties. The effect of processing parameters on the microstructure and properties of deposited films has been investigated for the deposition of $La_{1-X}Sr_XMnO_3$ films. Furthermore, some processing parameters have been computationally modelled using the software package FLUENT. The results obtained from this model have been used to support the experimental results.

The cathode material used in this research is $La_{1-X}Sr_XMnO_3$ (LSM) and 8mol% Y_2O_3 stabilised ZrO_2 (YSZ) is used as an electrolyte. Both of them are generally used in the production of SOFC prototypes. The improvement in performance of the LSM cathode has been obtained by modifying either the microstructure or modifying the composition.

LSM is not the best electronic conductor at SOFC operating temperatures (700°C – 850°C) as other materials such as $La_{1-X}Sr_XCoO_3$ (LSC) which exhibits higher conductivities by at least one order of magnitude. However, LSC is not chemically and thermo-mechanically compatible with YSZ. To solve this problem, an interlayer between these two components can be introduced. The materials of interest as an interlayer are Gd_2O_3 doped CeO_2 (CGO) and Y_2O_3 doped CeO_2. These two selections have higher ionic conductivities than YSZ and the coefficients of thermal expansion are in between LSC and YSZ.

In this thesis, the FAVD method has been used for the deposition of all films. In Chapter 2, the background literature concerning all the work done have been summarised. The deposition method and characterisation techniques are described in

Chapter 3. The effect of processing parameters has been studied in the deposition of LSM in Chapter 4 while the electrical conductivities and improvements of LSM have been reported in Chapter 5. The observations and electrical conductivities of cathodes with an interlayer have shown an interesting performance which is described in Chapter 6. In Chapter 7, some processing parameters of FAVD method have been modelled. The results obtained suggest the same trend as those from experiments. The conclusions and future work are in Chapter 8 while all the references in this thesis are listed in Chapter 9. Some detailed figures and data from Chapter 6 and 7 are included in the appendix.

Chapter 2 : LITERATURE REVIEW

Fuel cells in general have many advantages over conventional power generators, such as their conversion efficiency not being subject to the Carnot-cycle limitations associated with heat engines [1,2]. The potential for cogeneration is also high enough to be practical. In addition, they cause much less pollution. Their modular construction has minimal siting restrictions. Nevertheless, there are still some difficulties with fabrication of fuel cell components, materials selection, and the high operating temperatures employed.

2.1 BACKGROUND TO FUEL CELLS

A typical fuel cell consists of three main parts, which are:

CATHODE | ELECTROLYTE | ANODE.

The main principle of such a cell is that the fuel is oxidised at the anode and oxygen is reduced at the cathode, therefore there are electrons circulating via the external circuit. The type of fuel cell is classified by its electrolyte, type of charge carrier and its operating conditions, as will be explained later. In general, five types of fuel cell can be classified according to the type of electrolyte [1]. Their operating temperatures vary from 60°C up to 1000°C, depending on the type of electrolyte and the reactions involved.

2.1.1 CLASSIFICATION OF FUEL CELLS

(i)The Alkaline Fuel Cell (AFC)

This type of fuel cell was developed for the Apollo Lunar Module in the 1960's. This fuel cell uses an alkaline liquid as the electrolyte. Normally, liquid potassium hydroxide is used with only pure oxygen and pure hydrogen gases as the oxidant gas and fuel gas, respectively. The hydroxide ion is the charge carrier in this

cell. The electrolyte is sensitive to contaminants and is degraded by even a small amount of carbon dioxide to form potassium carbonate [1]. The operating temperature range is between 60°C to 120°C.

(ii) The Phosphoric Acid Fuel Cell (PAFC)

This type of fuel cell uses phosphoric acid as the electrolyte. This system can tolerate carbon dioxide and a small concentration of carbon monoxide, and uses the same gases as the AFC. The operating temperature is slightly higher, about 200°C. The hydronium ion is the charge carrier in this case. The corrosiveness of the acid electrolyte is a major problem for PAFCs.

(iii) The Polymer Membrane Fuel Cell (PMFC)

PMFC uses hydrogen gas and oxygen gas as in the AFC and PAFC, but with a solid polymer electrolyte. This system is less corrosive than the acid type because the only liquid in this system is pure water. However, using pure hydrogen supply is expensive and has a low energy density when stored. PMFCs are also expensive because fabrication of the polymer membrane itself is costly. This type of fuel cell is operated at very low temperature, not greater than 100°C. Therefore, it is of great interest for the development of low temperature fuel cells for transport/electric vehicle applications.

(iv) The Molten Carbonate Fuel Cell (MCFC)

It uses a molten salt as the electrolyte and thus the corrosion of components is a serious problem. This system is more flexible as it operates with air, and carbon dioxide and hydrocarbons can be supplied to the anode as fuel. Generally, carbonate salts are used as the electrolyte hence the conducting species is the carbonate ion. The operating temperature is 650°C, which increases the severity of corrosion. Although the cost of materials is high, this system is relatively cheap when used for large-scale plants.

(v) The Solid Oxide Fuel Cell (SOFC)

This SOFC uses air as the oxidant gas with methane or methanol as the fuel. The electrolyte is a ceramic oxide. Two types of charge carriers have been used: oxygen ions (O^{2-}) and protons (H^{+}). Carbon monoxide gas can be used as fuel in oxygen ion conductor fuel cells but not in other types [2]. The type of electrolyte used also determines on which side of the cell water is produced. Water is produced on the oxidant side in proton conductor fuel cells, and on the fuel side in oxygen ion conductor fuel cells. Proton conduction has been reported for hydrogen production from steam electrolysis [3]. Only oxygen ion conductors are being considered for use in SOFCs in this thesis.

Typically, oxygen ion conductors require high temperatures, 500°C-900°C, to operate. Although the fabrication of components and the cost of materials for SOFCs are more expensive than other types of power generation, other advantages make them attractive, such as availability of fuel and materials, cost of fuel, and their total conversion efficiency. Fig. 2.1 compares the efficiencies of each type of fuel cell, showing that SOFCs have conversion efficiencies of up to 60%, the highest of all fuel cells.

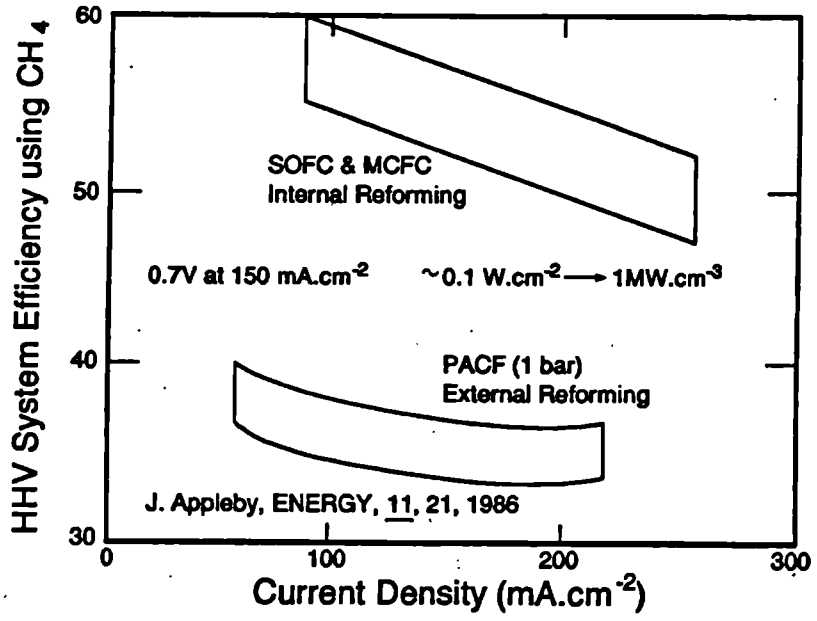


Fig. 2.1 : Efficiencies of fuel cells [225].

The type, power capacity and application of fuel cells which have been commissioned are summarised in Table 2.1 below.

Table 2.1: Power capacity and applications of fuel cells [4].

Type	Capacity	Application
AFC	1.5 kW	Apollo Programme
	12 kW	Space Shuttle Orbiter
PAFC	11 MW	Power Plant
PMFC	1 kW	Gemini Programme
	200 kW	Transport bus in Canada
MCFC	2 MW	Power Plant
SOFC	100 kW	Power Plant

Fig. 2.1 clearly shows that the efficiencies of the high temperature fuel cells, MCFCs and SOFCs, are much higher than those operated at low temperatures. The main reason is that the high operating temperature allows internal reforming of the fuel. Hydrogen gas as a fuel is expensive and difficult to handle, therefore a hydrocarbon fuel is used. Hydrocarbon fuels have to be reformed to hydrogen at high temperature at around 600°C-700°C. High temperature fuel cells are able to combine the reforming process together with the fuel cell operation, so that the overall efficiency is enhanced to well over 50 %. The total efficiencies of the low operating temperature fuel cells can never be greater than 35 - 40 %.

An MCFC system is cost effective only if operated as a large-scale plant, whereas an SOFC system is more flexible that it can be used for a large-scale plant as well as residential units and transport vehicles.

Westinghouse has developed a solid oxide fuel cell with a tubular cell design which has been operated as a power unit of 100 kW capacity. The demonstration unit has begun the operation in the Netherlands since March, 1998 [5]. Siemens has produced a fuel cell stack based on a bipolar plate design that uses hydrogen and oxygen to give a maximum power of 1.8 kW at a current density of 0.8 A/cm^2. A

stack of fuel cell for a bi-polar plate design consists of number of single cell (cathode/electrolyte/anode), connected in series with an interconnect in between each cell. Reports are available concerning a 100 kW power plant [5] and the application of SOFCs in electric vehicles [6]. The 100 kW plant is a combined heat and power (CHP) unit that supplies electrical power and hot water with a maximum operating efficiency of 47 % and uses natural gas as the fuel [5]. For electric vehicles, the SOFC cell can attain an output of 10 kW, which is enough to power passenger cars. It uses naphtha as fuel and is operated at 850°C-880°C. This car actually uses a combined (or 'hybrid') system of SOFCs and secondary batteries. The hybrid system provides an improvement in energy efficiency over the internal combustion engine.

Fuels most commonly used nowadays are reformed hydrocarbons or alcohols such as methane and methanol [4]. Methane and steam can be used directly in a solid oxide fuel cell operating at high temperature. Methanol is more suitable for use in applications such as electric vehicles.

2.1.2 FUEL CELL EFFICIENCY

The efficiency of a fuel cell depends on many factors; the thermodynamic efficiency, the voltage efficiency, the heating value efficiency, the current efficiency, the fuel processor efficiency and the power conditioner efficiency [7].

(i) Thermodynamic efficiency

Assuming that the electrochemical reaction goes to completion, the Gibbs free energy change, ΔG, is equivalent to the electrical energy. The maximum thermodynamic efficiency, therefore, is:

$$\varepsilon_T = \frac{\Delta G}{\Delta H} \qquad \text{-----} \quad (2.1)$$

where ΔG is the Gibbs free energy and ΔH is the enthalpy of the reaction.

(ii) Voltage efficiency

The voltage efficiency, ε_V, is the ratio of the operating cell voltage under load, E, to the open-circuit voltage, E_r, which is:

$$\varepsilon_V = \frac{E}{E_r} \qquad \text{-----} \quad (2.2)$$

The polarization or overpotential, η, may arise as a loss between the open-circuit voltage and the expected reversible voltage. There are three types of polarization: those due to charge transfer, diffusion, and ohmic losses. These losses are all cumulative.

(a) Charge transfer polarization (η_A)

The charge transfer polarization is the potential required to overcome the activation energy of the electrochemical reactions. It is the potential necessary to reduce the energy barrier so that the electrode reaction can proceed at a desirable rate. This polarization is related to the adsorption of reactant onto the surface of the electrode,

electron transfer, desorption of product and any steps in the reaction. At the high operating temperatures in SOFCs, the charge transfer polarization is low as the reaction rate is normally high.

(b) Diffusion polarization (η_D)

This loss is influenced by the mass transport effect of gases and/or species involved in the reactions within the electrode. Mass transport is a function of temperature, pressure, concentration and the physical properties of the system. The reactant gases diffuse through the pores in an electrode, therefore, the structure of the electrode is important.

(c) Ohmic polarization ($\eta\Omega$)

This is the overall resistance to conduction of ions through the electrolyte, electrons through the electrodes and the current collectors, and across the interfaces between cell components. It includes both ionic and electronic resistances.

(iii) Current efficiency

This is the efficiency in converting the reactants to the reaction products which is defined as the ratio of the actual current produced, j, to the current available from the complete electrochemical conversion of the fuel, j_F.

$$\varepsilon_J = \frac{j}{j_F} \qquad \text{-----} \quad (2.3)$$

This current efficiency is commonly known as "fuel utilization".

(iv) Heating value efficiency

In the case of a fuel containing some impurities or combustibles, energy is required to convert all the chemical energy involved into heat energy. This is defined as the amount of heat energy available to generate electricity from the fuel species per amount of heat energy required to convert all combustible species in the fuel gases.

(v) System efficiency

This is the efficiency in all the systems involved in a fuel cell including the fuel processor, power conditioner, and by-product heat utilization. The by-product heat is used to generate additional electricity in a gas turbine or steam turbine, and to supply hot water and steam. The efficiency is then increased by putting this by-product heat to use.

(vi) Overview of fuel cell efficiency

The overall efficiency of an SOFC stack can be improved by combining it with other types of power generators. For high temperature SOFCs which are operated at a temperature greater than 850°C, Westinghouse has developed a project that combines an SOFC with a gas turbine. The exhaust gases from the SOFC at high temperature can be used in the gas turbine. Hence, efficiencies of up to 70 % can be reached.

For low temperature SOFCs (operating temperature in the range 600°C-700°C), a Combined Heat and Power (CHP) system is more favourable. In other words, CHP or co-generation utilises the used gases at high temperature for heating purposes such as boiling hot water. The target of this low temperature SOFC is use in a small unit building or for transport. As the operating temperature is low, a stainless steel bipolar plate can be used as the interconnect material instead of a doped $LaCrO_3$.

2.2 SOLID OXIDE FUEL CELLS

The reactions taking place in a fuel cell are mainly electrochemical reactions of an oxidant gas (air or O_2) being reduced at the cathode and fuel gases (H_2 and CO) being oxidised at the anode. Therefore, oxygen ions are generated at the cathode and accepted at the anode. The accumulated electrons are transported via the external circuit to maintain charge balance.

The reaction at cathode is:

$$\tfrac{1}{2}O_2 + 2e^- \rightarrow O^- \qquad \text{-----} \quad 2.1$$

and at anode, the reaction is:

$$H_2 + O^= \rightarrow H_2O + 2e^- \qquad \text{-----} \quad 2.2$$

The overall reaction is:

$$H_2 + \tfrac{1}{2}O_2 \rightarrow H_2O \qquad \text{-----} \quad 2.3$$

A schematic of a single cell and the various reactions involved is shown in Fig. 2.2.

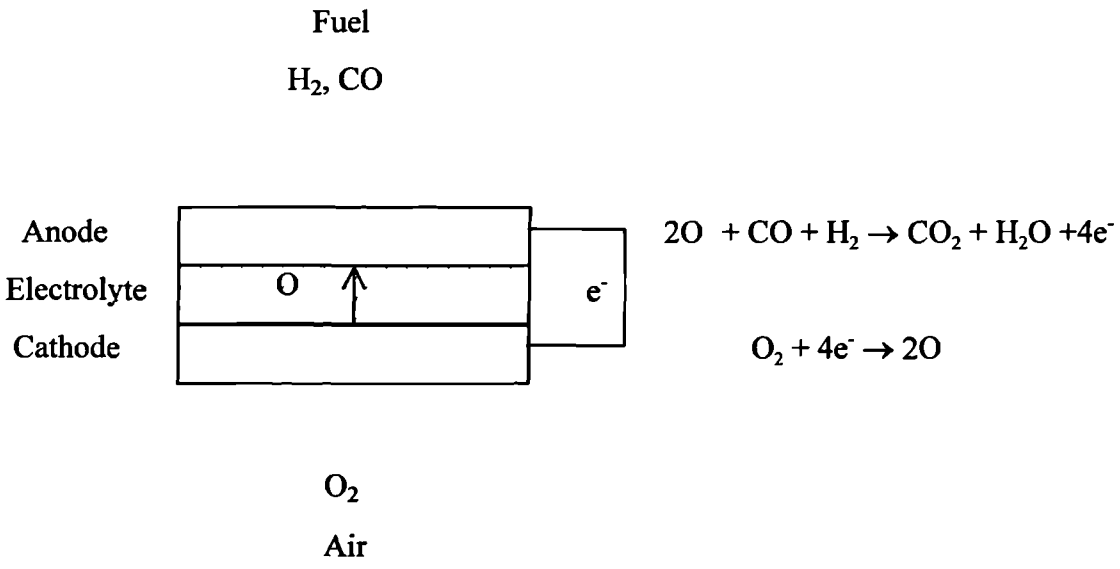


Fig. 2.2 : Schematic diagram of a solid oxide fuel cell.

At the interface between the anode and the electrolyte, oxygen ions react with hydrogen gas to form water and provide electrons as in reaction 2.2.

2.2.1 COMPONENTS OF A SOLID OXIDE FUEL CELL

There are four main components in a fuel cell : an electrolyte, an anode, a cathode and an interconnect. Each component must be compatible with the others in terms of chemistry, morphology, phase and dimensions which will be explained for individual components in more detail below [2]. Another important property is the compatibility of their coefficients of thermal expansion at high temperatures. All components must have similar coefficient values to prevent cracking during fabrication and operation [2]. Further requirements that depend on the function of each component are described below.

The four main components of a fuel cell are described briefly, followed by detailed descriptions of electrolytes and cathodes in a later session since the aim of this research is to investigate and develop a cathode material for an SOFC. In a later chapter, an interlayer consisting of an electrolyte in combination with a cathode is described with improved electrochemical properties of the cathode/electrolyte interface.

2.2.1.1 Electrolyte Materials

The principal properties of electrolytes are high ionic conductivity, phase stability from room temperature to ~1100°C, chemical compatibility with electrodes and interconnect materials in both oxygen and fuel gas atmospheres, and gas tightness. Consequently, the microstructure of an electrolyte must be fully dense. The mechanical property mostly desired is high fracture toughness [8].

Yttria stabilised zirconia (YSZ) is the most commonly used electrolyte for application in a solid oxide fuel cell. However, other oxides are of interest such as doped ceria (CeO_2), doped bismuth oxide (Bi_2O_3), lanthanum gallate ($LaGaO_3$), and other conducting oxides [7]. Doped bismuth oxide is a very good ionic conductor; however, it is severely degraded under reducing atmosphere. Lanthanum gallate has higher ionic conductivity than doped ceria and doped zirconia at SOFC operating temperature [9]. It is also stable in a reducing atmosphere down to an oxygen partial

pressure of 10^{-20} atm. The coefficient of thermal expansion matches that of $La_{0.84}Sr_{0.16}MnO_3$ [10]. Electrolyte materials such as YSZ and doped ceria are discussed in more detail in the next section.

2.2.1.2 Electrode materials

The principal properties necessary for the electrodes are good electrocatalytic behaviour, compatibility with the connected ceramic electrolyte, high electrical conductivity and low cost [11]. In addition, high catalytic activity is required for oxygen reduction at the cathode and for fuel oxidation at the anode [8]. Electrode materials must be sufficiently porous to provide large reactive surface area and be able to be formed into films with good adherence to the electrolyte [8].

(i) Anodes

These must be chemically stable under the reducing conditions in the fuel-containing atmosphere [8]. This property limits the material used to selected metals (eg. nickel and cobalt) and stable oxides. Nickel is commonly used because of its low cost. There are some problems for application at high temperatures, such as the thermal expansion coefficient mismatch (compared with the YSZ electrolyte) and the porous structure. Nickel has a much higher coefficient of thermal expansion than YSZ. This problem is overcome by dispersing YSZ into the nickel metal to form a Ni-YSZ cermet. The YSZ added brings down the thermal expansion coefficient value of pure nickel close to that of the YSZ electrolyte while maintaining a porous structure at high temperatures. Ni-ZrO_2 cermet has been used since the 1960's but was later replaced by CeO_2 based materials for intermediate temperature SOFCs [11]. Mixed-conducting oxides based on Y_2O_3-ZrO_2-TiO_2 solid solutions have been investigated [12].

(ii) Cathodes

Cathodes are required to be stable under oxidising atmospheres. Only noble metals (Pt, Au and Ag) and electronically conducting metal oxides can be considered [8]. The noble metals are not practically suitable owing to their high cost. In addition, these metals tend to vapourise during long term operation.

Doped lanthanum manganite ($La_{1-X}Sr_XMnO_3$) and doped lanthanum cobaltite ($LaCoO_3$) are typically considered for this application. At an operating temperature of 700°C and with CeO_2 based electrolytes, $La_{0.6}Sr_{0.4}Fe_{0.8}Co_{0.2}O_3$ is an effective cathode material [11].

2.2.1.3 Interconnect materials

Interconnects are used to combine single cells into a multi-cell stack by connecting the anode of one cell to the cathode of the next cell [8]. The properties required are high electronic conductivity but negligible ionic conductivity. Moreover, the material should have high mechanical strength, physical and electrochemical gas tightness and good adherence to the electrode materials. This material must be stable over a wide range of oxygen partial pressures. Perovskite type ceramics based on $LaCrO_3$ are the most suitable materials because of their refractoriness [2,8,11], in addition to meeting the other requirements for the interconnection component. This perovskite material is stable in the atmospheres experienced by an interconnect in an SOFC at 1000°C.

Recently, Siemens have attempted to use a flat metal separator plate for the interconnect [13]. The metal alloy used was Cr-5Fe-$1Y_2O_3$ at an operating temperature of 750°C-950°C. This alloy has a higher electronic conductivity than $LaCrO_3$. Both materials have coefficients of thermal expansion compatible with that of YSZ. For intermediate temperature fuel cells (500°C-750°C), ferritic stainless steel is a good candidate for an interconnect material. The coefficient of thermal expansion matches that of gadolinia-doped ceria.

2.2.2 SOLID OXIDE FUEL CELL DESIGNS

There are many designs of solid oxide fuel cell which each offers various advantages and disadvantages. The two most common designs are the tubular form and the flat plate form. The tubular design can be further divided into two slightly different design concepts. These are :

- Sealless Tubular
- Segmented Cell in Series.

The flat plate form is based on stacking of cells in layers of flat plates, offers improved performance and higher power density relative to the tubular design. Flat plate type designs can be divided into two broad groups:

- Monolithic
- Bipolar Plate.

All designs are based on the same concept of optimising electrochemical reaction per unit volume. The designs and performances of each of them are summarised below.

2.2.2.1 Sealless Tubular Design

This design was developed by Westinghouse in 1984 [14]. It is the most advanced among several SOFC configuration concepts. It needs a closed-one-end Air Electrode Support (AES) tube in which layers of electrolyte, fuel electrode (anode) and interconnect have been coated. Air flows inside the tube while the fuel flows outside as in Fig. 2.3. Each cell is then connected electrically together in series and parallel to form a unit of power generation [2].

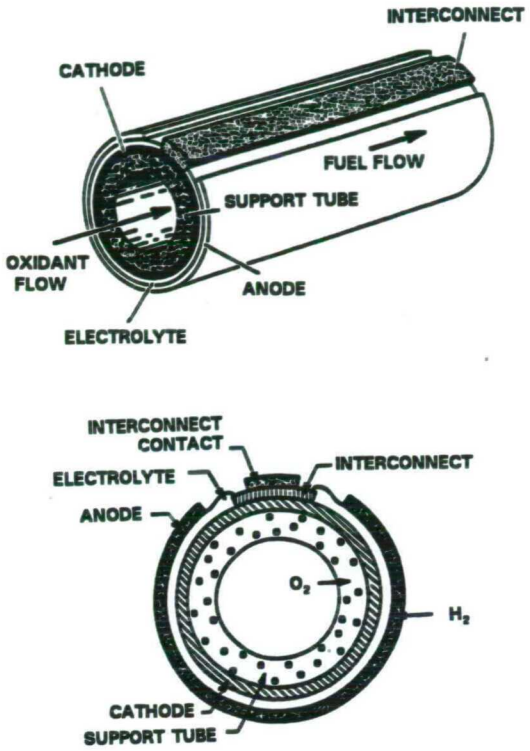


Fig. 2.3: Sealless tubular design [15]

With this sealless design, the problems of forming gas tight seals between ceramic components at high temperature have been overcome as one tube consists of one cell. Thermal expansion mismatch between components can be compensated for within each cell. This reduces the likelihood of cracking.

2.2.2.2 Segmented-Cell-in-Series Design

This cell has either a bell-and-spigot configuration or a rounded cell configuration as shown in Fig. 2.4. Fuel flows inside the tube while the oxidant air flows on the outside of the tube. The bell-and-spigot type still needs a porous support, on which is deposited an anode layer, followed by the electrolyte and the cathode. The rounded cell type has the same layer configuration but with a self-supported electrolyte. The interconnect joins the cathode and the electrolyte of one cell with the anode and electrolyte of another cell.

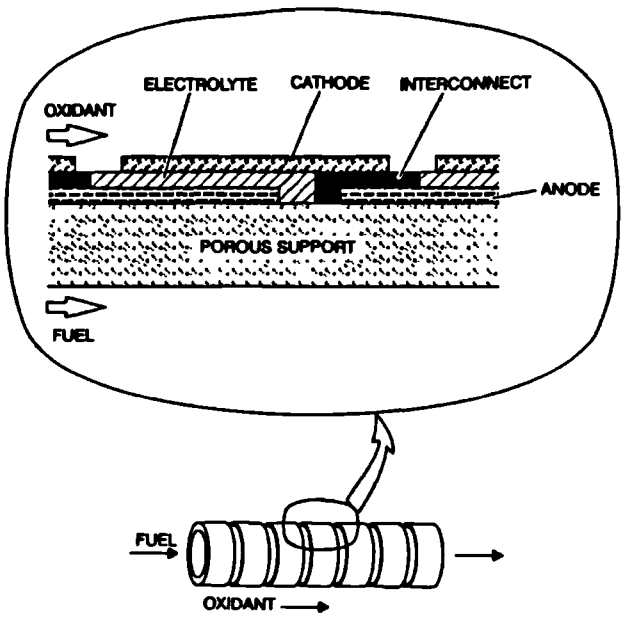


Fig. 2.4: The segmented-cell-in-series design [16].

Cells of this design are connected in series. This results in a higher stack efficiency than a single cell of the same size due to less power wastage from resistance losses because the first cell in series has a higher output voltage. Gas tight seals are needed as the fuel and oxidant must be separated. The thick support tube may hinder gas transport and therefore performance.

2.2.2.3 Monolithic Design

The geometry of the monolithic design offers an increase in the active surface-to-volume ratio of the fuel cell. The surface-to-volume ratio is increased by up to nearly six times compared to that of the parallel tube fuel cell [17]. There are two possible configurations with this design; the coflow and the crossflow configurations (Fig. 2.5).

The coflow configuration consists of a stack of anode/electrolyte/cathode units joined by interconnects. The flow of fuel and flow of oxidant are in the same direction and parallel. The crossflow configuration is a slightly different modification although it consists of the same stacks of anode/electrolyte/cathode and interconnect. The fuel and oxidant flow perpendicular to each other.

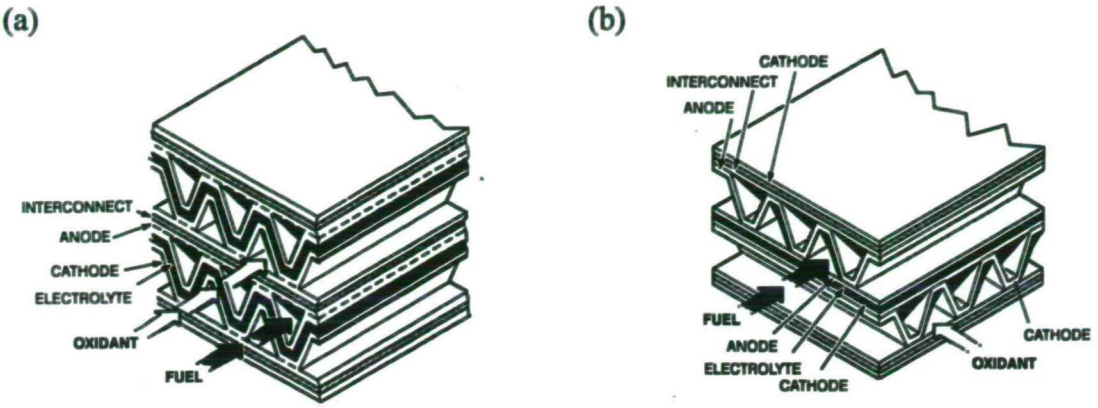


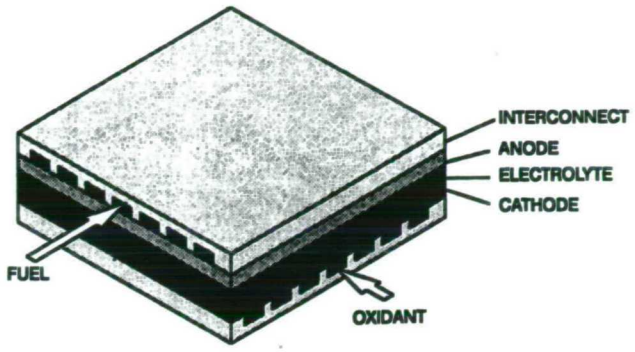
Fig. 2.5:The monolithic design (a) coflow and (b) crossflow configurations [2].

Since the cell size is small and the surface area is high, the power density is high. The difficulty in this design is its fabrication. Cracking is mainly due to thermal expansion coefficient mismatch. Studies showed that even a small difference in the coefficients of thermal expansion of different layers can result in large stresses and cause cracking parallel to the plane of the layers [18]. The performance of multi-cell stacks of this design is inferior to the performance of a single cell [19].

2.2.2.4 Bipolar Plate Design

In this design, the gases flow perpendicular to each other as in the crossflow configuration of the monolithic design. However, the cell consists of layers of anode/electrolyte/cathode and interconnect to form a thin flat plate while the interconnect contains channels for the gas to flow through (Fig. 2.6). The interconnect in this design connects the cathode of one cell to the anode of the next cell. This design permits a simple series connection between cells without the need for external cell interconnects as in the tubular design [4]. Most electrolytes used in this design are deposited as relatively thick layers so as to be self-supporting.

(a)



(b)

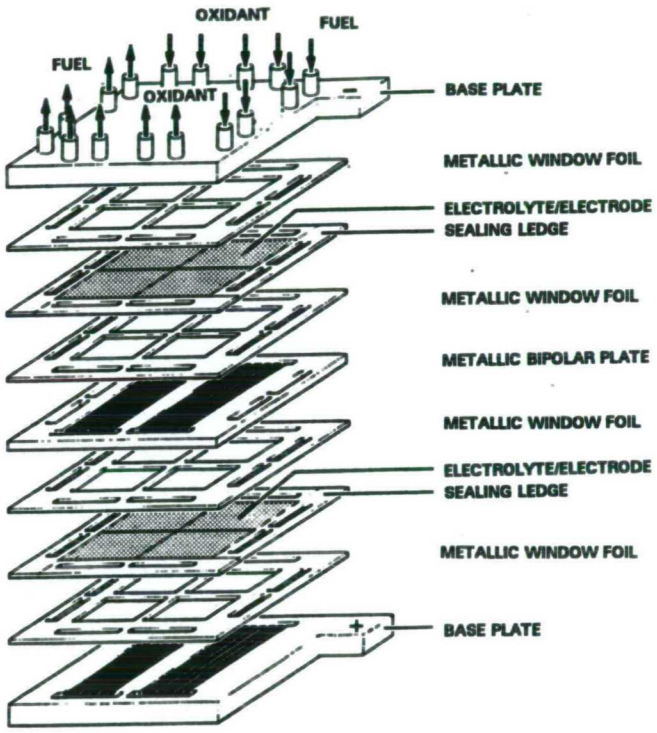


Fig. 2.6: (a) The bipolar plate design [2] and (b) stacking of cells [20].

The flat plate design results in better performance over the tubular design due to lower internal resistance losses. In terms of fabrication, this design is less complicated than others which require masking at high temperature and complex shapes. Flat plates of cathode/electrolyte/anode are separated by a bipolar plate which is fabricated separately and added to the cell during stacking. The cell sealing is proven to be difficult for this configuration whereas the sealless tubular design configuration can overcome this problem. Fabrication is a major problem of this design in terms of cost and difficulties in forming large-scale units. In addition, materials selection is also another problem.

2.3 ELECTROLYTES

The ionic conductors which are mostly considered for use as the electrolyte in SOFCs, are doped ZrO_2, and doped CeO_2. These materials are used at different operating temperatures.

2.3.1 ZrO_2 BASED ELECTROLYTES

SOFCs containing these electrolytes in association with special metallic or cermet interconnect bi-polar plate materials have been operated at 700-900°C [11]. ZrO_2 based electrolytes are used widely because they have an adequate level of oxygen ion conductivity as well as stability in both oxidising and reducing atmospheres [2].

Pure ZrO_2 undergoes phase transformations at high temperatures. The crystal structure transforms from monoclinic to tetragonal and tetragonal to cubic with increasing temperature. With the addition of certain oxides, the high temperature, high symmetry forms of ZrO_2 can be stabilised down to room temperature. For electrolyte applications, the cubic fluorite structure is preferred because this gives the highest ionic conductivity, but a relatively high concentration of dopant e.g. 8 mol % Y_2O_3 is required. The most common stabilising oxide used is Y_2O_3 and the resulting material is referred to as yttria-stabilised zirconia (YSZ). The crystal structure of YSZ is typically a cubic fluorite as shown in Fig. 2.7.

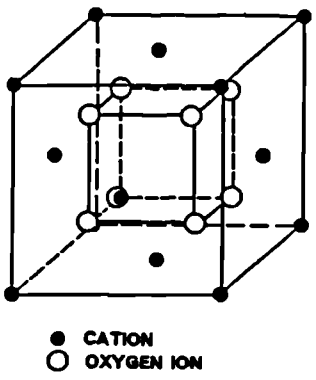


Fig. 2.7: The cubic fluorite crystal structure [7].

The trivalent cations (Y^{3+}) substitute for the tetravalent lattice cations (Zr^{4+}), creating oxygen vacancies. This reaction may be written using Kröger-Vink notation as :

$$Y_2O_3 \xrightarrow{ZrO_2} 2Y'_{Zr} + V_O^{\cdot\cdot} + 3O_O^{\times} \qquad \text{-----} \quad 2.4$$

An oxygen ion (O^{2-}) moves from the cathode side to the anode side via the oxygen vacancies in the oxide. Therefore, higher oxygen vacancy concentration promotes higher conductivity of the electrolyte.

Alternative dopants to Y_2O_3 include CaO, MgO, Sc_2O_3 and some rare-earth oxides [2]. Y_2O_3 is the preferred dopant for ZrO_2 electrolytes because of its availability, the adequate conductivity it provides and its reasonable cost. Sc_2O_3- and Yb_2O_3-doped zirconias show higher ionic conductivities than YSZ but are considerably more expensive. Another point to be considered is that the fracture strength of YSZ decreases with increasing temperature [11]. The tetragonal phase displays higher oxygen ion mobility than the cubic phase.

2.3.2 CeO_2 BASED ELECTROLYTES

These have been used in conjunction with ferritic stainless steel interconnect bi-polar plate materials for the operation of SOFCs between 450-700°C.

CeO_2-based electrolytes have even higher ionic conductivity than YSZ although the efficiency is reduced in the presence of fuel gas [8]. CeO_2 has the cubic fluorite structure from room temperature to its melting point, and therefore does not require stabilisation as does zirconia. However, as cerium is a tetravalent cation like zirconium, oxygen vacancies must be introduced by a similar process to that of doped zirconia, that is by substitution of divalent or trivalent cations, in order to exhibit rapid oxygen ion conductivity. The benefit of doped CeO_2 is that it can be optimally doped to 2-3 % oxygen vacancies.

The classic dopants are CaO and Y_2O_3. More recently, CeO_2 has been doped with rare-earth oxides such as Gd_2O_3 [11], La_2O_3 [21], Nd_2O_3 [21], Sm_2O_3 [21], Yb_2O_3 [21] and SrO [22] in order to improve its properties. A great deal of research has been done on $Ce_{1-X}Gd_XO_{2-X/2}$ (CGO) due to its high ionic conductivity [23,24,25,26]. Another dopant which shows higher ionic conductivity is samaria (Sm_2O_3). Most work on samaria-doped ceria has been carried out in Japan [27].

Mixing ZrO_2, Y_2O_3, CeO_2, and Al_2O_3 together resulted in ceramics with ionic conductivities inferior to that of YSZ at intermediate-to-high temperatures, but good conductivities at temperatures below 400°C [28]. Miliken et al [29] have reported that a mixed ionic-electronic conductor, $Ce_{0.8}Gd_{0.19}Pr_{0.01}O_2$, yields higher cell performance than a cell containing a CGO electrolyte.

Electrolyte films of ceria electrolytes have been fabricated using different processing techniques, such as spray pyrolysis [30], slurry coating [30], slip casting [30], RF ion plating [30], plasma spraying [30,31], and screen printing [32]. A more sophisticated technique, electrochemical vapour deposition, has been used to deposit $(Y_2O_3)_{0.11}(CeO_2)_{0.89}$ [33] and YSZ onto porous electrodes [34].

The ionic conductivities of various candidate electrolytes are summarised in Table 2.2.

Table 2.2: Ionic conductivities of various electrolytes

Electrolyte	Ionic conductivity (S/cm)	Reference
La_2O_3 (10mol%) - CeO_2	0.020	[35]
Y_2O_3 (20mol%) - CeO_2	0.055	[36,37]
Gd_2O_3 (20mol%) - CeO_2	0.083	[36]
Sm_2O_3 (20mol%) - CeO_2	0.117	[36]
CaO (10mol%) - CeO_2	0.035	[38]
SrO (10mol%) - CeO_2	0.050	[39]
Nd_2O_3 (15mol%) - ZrO_2	0.014	[40]
Y_2O_3 (8mol%) - ZrO_2	0.10	[40]
Sm_2O_3 (10mol%) - ZrO_2	0.058	[40]
Sc_2O_3 (10mol%) - ZrO_2	0.25	[40]
Yb_2O_3 (10mol%) - ZrO_2	0.11	[40]
$La_{0.8}Sr_{0.2}Ga_{0.8}Mg_{0.2}O_3$ [+]	0.10	[9]
$La_{0.8}Sr_{0.2}Ga_{0.8}Mg_{0.2}O_3$ [~]	0.31	[9]
Bi_2O_3 [+]	> 0.10	[2]

The ionic conductivities of ceria electrolytes were measured at 800°C and those of doped zirconia electrolytes were measured at 1000°C.

+ ionic conductivity at 700°C.

~ ionic conducvitity at 1000°C.

2.4 CATHODES

In this section, various matters pertaining to cathodes - the reactions involved, microstructural requirements, and candidate materials - are discussed.

Although $LaCoO_3$ (LCO) has a higher electrical conductivity than $LaMnO_3$ (LMO), LMO is stable over a wider range of oxygen partial pressures. In addition, LCO tends to react with YSZ at high temperatures and the thermal expansion coefficient is much greater than that of $LaMnO_3$ [2]. $LaMnO_3$ has a thermal expansion coefficient compatible with YSZ but reacts with zirconia at temperatures above 1200°C. Strontium is the common dopant for both oxides. Other oxides are discussed briefly at the end of this section.

2.4.1 REACTIONS AT THE CATHODE

The overall chemical reaction at the cathode is:

$$O_2 + 2V_O^{\cdot\cdot} + 4e^- = 2O_O^x \qquad \text{-----} \quad 2.5$$

In fact, various reactions occur simultaneously at the electrolyte/cathode interface and the triple phase boundary (TPB) where electrode, electrolyte, and gas phases meet. Several of these reactions have each been proposed as the rate controlling step for oxygen reduction [2]. The main reaction steps are:

1. Diffusion of gaseous oxygen in the pores of the electrode [41,42]

$$O_{2,bulk} = O_{2,pore}$$
$$O_{2,pore} = O_{2,TPB} \qquad \text{-----} \quad 2.6$$

2. Adsorption of oxygen on the electrode and the electrolyte [43,44]

$$O_{2,cathode} = O_{2\,ad,cathode}$$
$$O_{2,cathode} = O_{2\,ad,TPB} \qquad \text{-----} \quad 2.7$$

3. Dissociation of oxygen molecules into atoms [45,46]

$$O_{2ad,cathode} = 2O_{ad,cathode}$$
$$O_{2ad,TPB} = 2O_{ad,TPB} \quad \text{-----} \quad 2.8$$

4. Diffusion of oxygen along the electrode surface [45,47,48] and Diffusion of oxygen atoms through the electrode [49,50]

$$2O_{ad,cathode} = 2O_{ad,TPB} \quad \text{-----} \quad 2.9$$

6. Diffusion of electrons in the electrolyte [51,52]

$$e^-_{electrolyte/anode} = e^-_{electrolyte/cathode} \quad \text{-----} \quad 2.10$$

7. Diffusion of oxygen ions in the electrolyte [42,53,52,54]

$$O^{2-}_{TPB} = O^{2-}_{electrolyte/anode} \quad \text{-----} \quad 2.11$$

8. Oxygen reduction at the cathode surface [1,8]

$$\tfrac{1}{2}O_{2,pore} + V^{\cdot\cdot}_{O,cathode} + 2e^-_{cathode} \rightarrow O^{x}_{O,cathode} \quad \text{-----} \quad 2.12$$

9. Charge transfer [55,56]

$$O_{ad,TPB} + 2V^{\cdot\cdot}_{O,TPB} + 4e^-_{TPB} = 2O^{x}_{O,TPB} \quad \text{-----} \quad 2.13$$

Some of these steps are illustrated in Fig. 2.8.

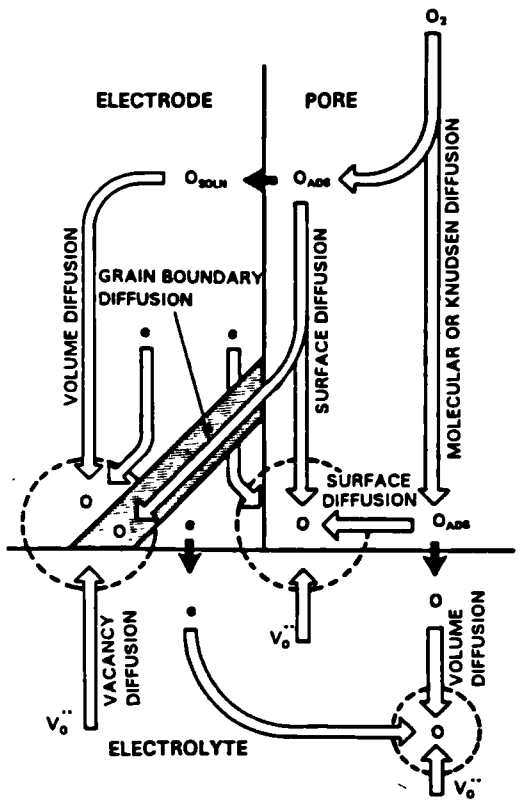


Fig. 2.8: Reaction steps of oxygen reduction at a triple phase boundary [57].

The rate-determining step for oxygen reduction depends on the cathode material, electrolyte, particle morphology, and temperature range. The behaviour of the porous cathode is dominated by interfacial oxygen surface exchange reactions and diffusive processes as the diffusion coefficient for ions in the solid is much smaller than that for the gas molecules in the pores [58]. Rate-determining steps can be suggested from AC impedance measurements.

The reactive area for oxygen gas is not limited to the TPB but can spread over the electrode surface. This is related to the defect chemistry of the cathode material. The concentration of oxygen adsorption sites is related to the concentration of defects in the electrode [2]. For materials with low oxygen diffusion coefficients, such as noble metals and lanthanum manganite, the reactions occur at or near the TPB (Fig. 2.9). The high amounts of TPBs result in low values of electrode resistance [59].

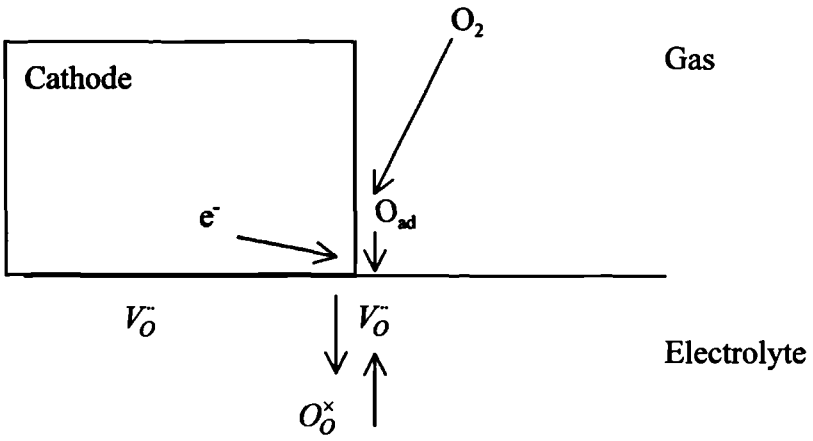


Fig. 2.9 : Schematic diagram of cathode reactions at a TPB.

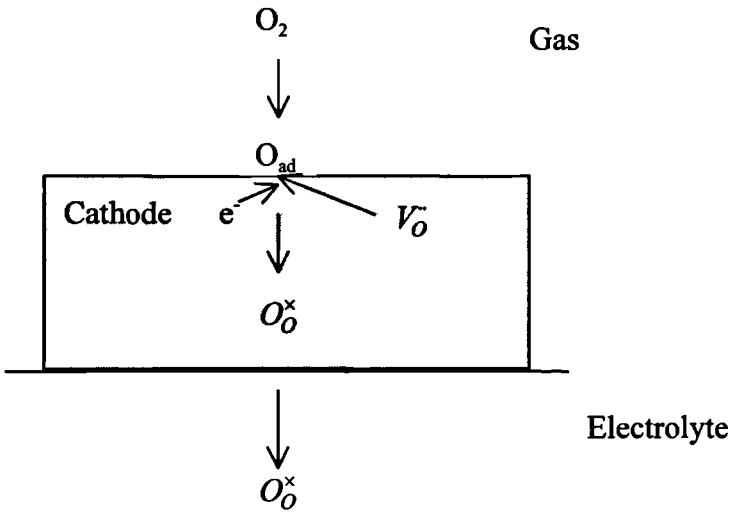


Fig. 2.10 : Schematic diagram of cathode reactions at electrode/electrolyte interface.

In contrast, in materials with high oxygen diffusion coefficients - the so-called Mixed Electronic-Ionic Conductors (MEICs), for example lanthanum cobaltite and indium oxide - reactions also occur along the electrode/electrolyte interface (Fig. 2.10). This enhances the reactions taking place at both the TPB and along the electrode/electrolyte interface which improves overall conductivity.

2.4.2 MICROSTRUCTURAL REQUIREMENTS

The main requirement of the cathode microstructure concerns the triple phase boundary. High TPB length reduces the electrode overpotential [60], whereas increased contact area gives larger electrode capacitance [61]. The TPB length can vary with the particle sizes; $2x10^2$ cm/cm^2 for 100 microns size particle diameter to $2x10^4$ cm/cm^2 for 1 micron size particle diameter [62]. The high TPB length is critical for an electronic conductor cathode which has poor ionic conductivity such as doped lanthanum manganite (LSM). A different model has been proposed for porous MEIC cathodes, such as doped lanthanum cobaltite. This is discussed later.

2.4.2.1 Electronic Conducting Cathode

The thickness of the cathode layer is chosen depending on the self-diffusion coefficient and the surface exchange coefficient as explained by Steele [63]. The optimum thickness can be calculated as follows.

The magnitude of the electrode resistive term (R_E) is determined by the rate-controlling step in equation 2.4. The rate-controlling step could be due to Faradaic charge-transfer, mass transport limitations or the chemical reaction kinetics. All the overpotential expressions are very similar therefore the electrode resistance can be expressed as (see Butler-Volmer equation for the low field approximation):

$$R_E = \frac{RT}{zFj_E} \qquad \text{-----} \quad (2.4)$$

where R_E = electrode resistance (Ωcm^2),

R = gas constant (8.314 $Jmol^{-1}K^{-1}$),

T = temperature (K),

z = charge of the ion,

F = Faradaic constant ($96.5x10^3$ $Cmol^{-1}$), and

j_E = characteristic molar flux (cm^2s^{-1})

The ionic resistance ,R_O (Ωcm^2) is replaced by L/σ, where L is the thickness of the oxide ceramic in cm, and σ is the specific ionic conductivity in S/cm.

$$R_O = \frac{L}{\sigma} \qquad \text{-----} \quad (2.5)$$

BIBL LONDON UNIV

When the bulk resistance equals the surface control resistance, equations (2.4) and (2.5) can be combined to give:

$$\frac{RT}{zFj_E} = \frac{L}{\sigma} \qquad \text{-----} \quad (2.6)$$

The characteristic electrode current density has been shown [64,65,66] to be

$$j_E = \frac{zFk}{V_m} \qquad \text{-----} \quad (2.7)$$

where V_m = the molar volume of oxygen in the oxide membrane (cm^3), and

k = the surface exchange coefficient of oxygen (cm/s).

By combining equations (2.6) and (2.7), we therefore obtain:

$$\sigma = \frac{(zF)^2 kL}{V_m RT} \qquad \text{-----} \quad (2.8)$$

From the Nernst-Einstein equation:

$$\sigma_i = \frac{D^*(zF)^2}{V_m RT} \qquad \text{-----} \quad (2.9)$$

where D* is the self diffusion coefficient (cm^2/s). All that remains is the substitution of (2.8) into (2.9) to give:

$$L_d = \frac{D^*}{k} \qquad \text{-----} \quad (2.10)$$

This length, L_d, is the length at which the oxygen flux changes from being controlled by the surface reactions to being controlled by bulk diffusion. For $La_{0.8}Sr_{0.2}MnO_3$, L_d was calculated to be 0.1 μm, which is the minimum length for bulk diffusion control to be dominant.

For a dense electrode, it is also possible to calculate an effective resistance by using the value of the oxygen ion conductivity in the mixed conducting oxide. For example, substituting (2.5) in (2.9) gives:

$$R_O = L_t \frac{V_m RT}{D^*(zF)^2} \qquad \text{-----} \quad (2.11)$$

where L_t is the thickness of a dense mixed conducting oxide cathode.

From the kinetic data provided in the overview later in this chapter, L_t for $La_{0.8}Sr_{0.2}MnO_3$ operated at 1000°C has been calculated to be approximately $1x10^{-4}$ μm [62]. This means significant oxygen flux can only be sustained in a very thin film. More details of the calculation of these parameters for TPBs in porous electrodes can be found in ref. [62].

2.4.2.2 Mixed Electronic-Ionic Conducting Cathodes

Adler et al [67] have developed a model for AC impedance response of an electrolyte with symmetrical porous mixed conducting cathodes. The processes contributing to the electrode polarisation resistance are assumed to be the diffusion of oxygen ions in the mixed conductor and the exchange of oxygen gas at the mixed conductor/gas interface. Following the assumption of the model, it can be shown that the Area Specific Resistivity (ASR) between the electrode and electrolyte interface is equal to a chemical resistance, R_{chem} which is defined as :

$$R_{chem} = \left(\frac{RT}{2F^2}\right)\sqrt{\frac{\tau}{(1-\varepsilon)c_v D_v a r_0(\alpha_f + \alpha_b)}} \qquad \text{-----} \quad (2.12)$$

where R = gas constant (8.314 J/molK),

T = temperature (K),

F = Faradaic constant,

τ = solid phase tortuosity,

ε = porosity,

c_v = oxygen vacancy concentration (mol/cm^3),

D_v = vacancy diffusion coefficient,

a = surface area (cm^{-1}),

r_0 = exchange neutral flux density,

α_f and α_b are transfer coefficients of the order of unity that depend on the specific mechanism of the exchange reaction.

The chemical resistance therefore depends on the microstructural parameters of the porous cathode, namely its surface area, porosity, and tortuosity.
When $r_0(\alpha_f + \alpha_b) = k$, and $c_v D_v = c_{mc} D^*$, equation (2.12) can be rewritten as:

$$R_{chem} = \left(\frac{RT}{2F^2}\right)\sqrt{\frac{\tau}{(1-\varepsilon)D^* a c_{mc} k}} \qquad \text{-----} \quad (2.13)$$

where c_{mc} = the concentration of oxygen sites in the cathode material as obtained from the lattice parameter,

k = surface exchange coefficient of oxygen (cm/s), and

D* = self-diffusion coefficient of oxygen (cm^2/s).

Equation (2.13) is more practical in use as the values of k and D* can be measured directly using Secondary Ion Mass Spectrometer (SIMS).

The values of the ASR, the oxygen diffusion coefficient and the surface exchange coefficient of selected cathode materials are summarised later in this chapter.

2.4.3 LANTHANUM MANGANITE ($LaMnO_3$)

2.4.3.1 Structure

$LaMnO_3$ is a perovskite-structured oxide. The crystal structure is slightly distorted from the ideal perovskite structure shown in Fig. 2.11, resulting in orthorhombic symmetry for the undoped material.

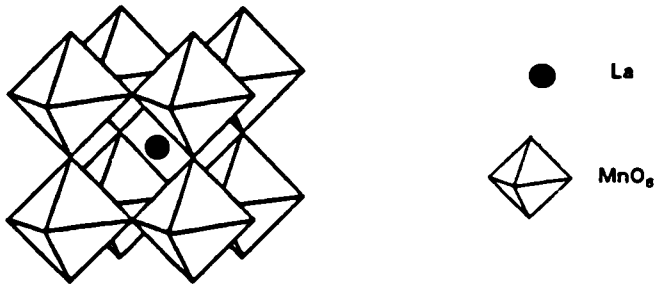


Fig. 2.11: An ideal perovskite structure, $LaMnO_3$ [2].

The phase diagram of the La_2O_3-Mn_2O_3 system presented in Fig. 2.12 clearly shows the existence of the perovskite phase around the composition of 50/50 mol% [68].

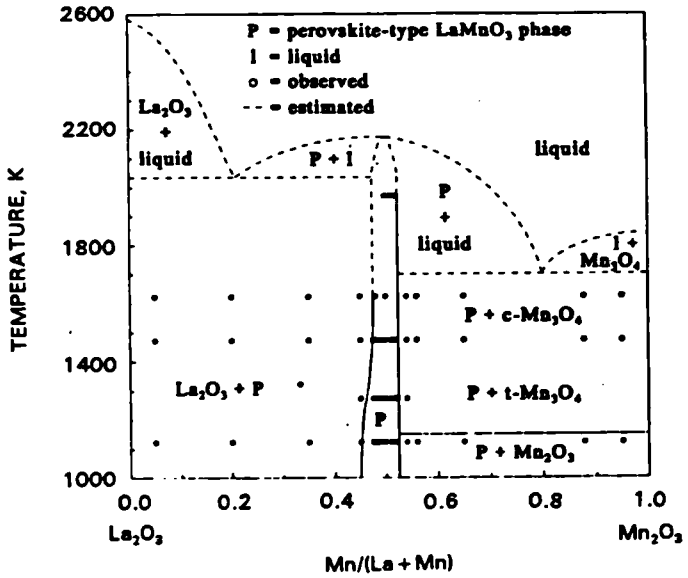


Fig. 2.12: Phase diagram of the La_2O_3-Mn_2O_3 system [68].

The melting point of $LaMnO_3$ is around 1880°C [68]. It is easy to introduce nonstoichiometry as Mn^{4+} is stable at high temperature. The crystal structure of $LaMnO_3$ undergoes a phase transformation from orthorhombic to rhombohedral symmetry at various temperatures according to various reports from 285°C [69] to 450°C [70].

2.4.3.2 Properties

Lanthanum manganite was found to have superior electrical conductivity when compared to other perovskite compounds at 700°C [69] i.e.:

$$\sigma(LaMnO_3) > \sigma(LaCrO_3) > \sigma(LaFeO_3)$$

The high electrical conductivity is due to the presence of Mn^{4+}, which introduces a large number of charge carriers (holes). These charge carriers move by a hopping mechanism with the holes localized at Mn^{4+} sites between jumps [69]. The nonstoichiometric form of LMO is $LaMnO_{3+\delta}$, which means the structure contains excess oxygen that δ is accommodated by cation vacancies. The ionic conductivity is then low because of the low concentration of $V_O^{\cdot\cdot}$.

2.4.3.3 Cathode Stability

Formation of La_2O_3 in $LaMnO_3$ perovskite is not desirable as this compound reacts with water to form a hygroscopic compound, $La(OH)_3$. This hydroxide can cause cracking and lead to disintegration of $LaMnO_3$ and $La_{1-x}Sr_xMnO_3$. A chemical potential diagram for the La-Zr-Mn-O system at 1300°C has been constructed, based on existing thermodynamic data, Fig. 2.13 [71]. When $La_2Zr_2O_7$ is formed, some of the Mn ions are oxidised. Dissolving of Mn ions into YSZ is always accompanied by reduction of the Mn ions [71]. Under reducing conditions, $La_{1-x}Sr_xMnO_3$ completely dissociated into La_2O_3, $SrMnO_3$, La_2MnO_4 and MnO

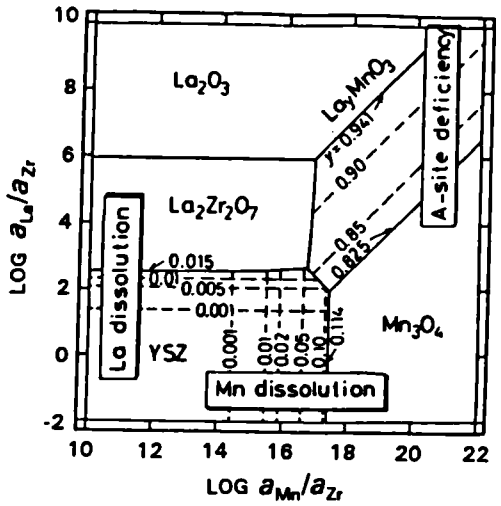


Fig. 2.13: Chemical potential diagram of the La-Zr-Mn-O system [71].

2.4.4 Sr-DOPED LANTHANUM MANGANITE ($La_{(1-X)}Sr_XMnO_3$)

2.4.4.1 Structure

(i) $La_{1-X}Sr_XMnO_3$ (LSM)

LSM has a rhombohedral structure at low Sr concentrations and at low temperature. At high x (x > 0.3) and high temperatures, the structure changes to a cubic perovskite [72,73,74]. Different preparation techniques, pressure, and atmosphere yield LSM of different crystal structures [75,76,73]. When the Sr content is increased, $Mn^{3+} \rightarrow Mn^{4+}$ which results in a less distorted cubic structure [73] because Mn^{4+} has a smaller ionic radius than Mn^{3+}. The degree of distortion decreases with increasing x [77].

(ii) Nonstoichiometric LSM

LSM is always found to be nonstoichiometric, $La_{1-X}Sr_XMnO_{3\pm\delta}$. The amount of excess oxygen decreases with increasing x [78]. Fig. 2.14 shows a plot of $La_{1-X}Sr_XMnO_{3\pm\delta}$ nonstoichiometry with oxygen partial pressure. At low O_2 pressures, an oxygen deficiency was found. A defect model based on the formation of association

pairs between divalent Mn ions and O^{2-} vacancies has been proposed to elucidate the nonstoichiometric behaviour of LSM as shown in reaction 2.14 .

$$2Mn_{Mn}^{\bullet} + O_O^x \Leftrightarrow 2Mn_{Mn}^x + V_O^{\bullet\bullet} + \tfrac{1}{2}O_2 \qquad \text{----- 2.14}$$

It is able to explain the oxygen pressure dependence of oxygen nonstoichiometry, electrical conductivity and chemical diffusion coefficient [79,80].

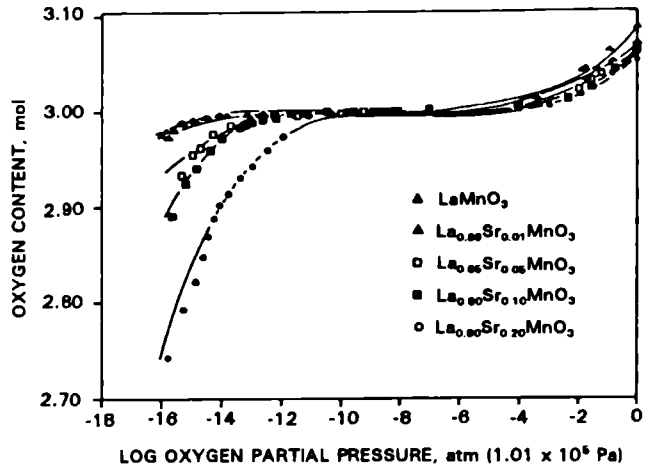


Fig. 2.14 : $La_{1-X}Sr_XMnO_{3\pm\delta}$ nonstoichiometry versus oxygen partial pressure [81].

The unit cell volume of lanthanum-deficient $La_{y-x}Sr_xMnO_3$, was found to be less than that of stoichiometric LSM [75]. An A-site deficient compound, $(La_{0.7}Sr_{0.3})_{0.94}MnO_3$ exhibited oxygen stoichiometry while other Sr contents led to oxygen deficiency at 750°C [82].

2.4.4.2 Reaction at TPBs

Dense LSM has been shown to have different cathodic reaction mechanisms to porous film [83]. The oxygen ionic conductivity using a dense electrode measured by the Hebb-Wagner polarization method was $5.9x10^{-8}$ S/cm at 800°C.

Impedance measurement of a Sr-doped $LaMnO_3$/YSZ cathode found three time constants indicating three possible rate-determining steps [84]. The three semicircles seen in the impedance spectrum of a $La_{0.85}Sr_{0.15}MnO_3$/YSZ system

corresponded to the charge transfer reaction of oxygen ions at high frequency, and the peroxide dissociation and diffusion at medium and low frequencies [85]. In addition, it was suggested that the oxygen reduction kinetics are limited by the dissociation of oxygen molecules and subsequent migration of adsorbed oxygen atoms at the TPB where the charge transfer occurs [86]. It has been proposed that the dissociation of oxygen molecules adsorbed on a strontium-doped $LaMnO_3$ cathode in contact with YSZ is the rate-determining step at 800°C [87]. The dopant content influences the electrode overpotential, especially at high current density [87] and it was shown that the rate-determining step involved dissociation of oxygen molecules. A certain level of oxygen vacancies is present which influences the exchange rate of oxygen at the surface [88]. The electrocatalytic activity can be increased by increasing the cathodic polarization where the cathode is partly reduced, thus increasing the oxygen vacancy concentration [84].

The fast process at the $La_{0.85}Sr_{0.15}Mn_{0.98}O_3$/YSZ interface was charge transfer while the slow processes were a coupling between charge transfer and mass transport which increased due to sintering [89]. The mass transfer was attributed to surface diffusion of reduced oxygen intermediates towards the TPB. An elementary model of LSM/LZO/YSZ was proposed according to the formation of $La_2Zr_2O_7$ at the interface [89].

An LSM cathode fabricated by electrochemical vapour deposition was found to have a very large interfacial area. The polarization was only 1mV at a current density of 3 A/cm^2 [90,91]. The interfacial resistance was less than 0.01 Ωcm^2 in air.

The cathodic polarization of a $La_{0.85}Sr_{0.15}\overset{Mn}{\underset{|}{}}O_3$ film prepared by screen printing increased when the effective electrode area decreased or when the amount of agglomerates was increased. These effects were due to using too low a sintering temperature (1000°C) and too thin a cathode layer (<25microns) [92]. The ohmic loss followed the same trend as the cathodic polarization but showed no effect for thick cathodes.

Oxide ions in bulk LSM were investigated using SIMS and found to diffuse via a vacancy diffusion mechanism [93]. The surface reaction rate constant was very low, 10^{-8}-10^{-7} cm/s, while the criterion set by Steele [3] was k >10^{-5}-10^{-4} cm/s. The bulk diffusion of oxide ions was negligible at around 10^{-14} cm^2/s [67].

2.4.4.3 Properties

(i) Electrical conductivity

A 4-point Van der Pauw method was used for electrical conductivity measurements of various LSM compositions at different temperature.

Table 2.3 : Electrical conductivity of $La_{1-X}Sr_XMnO_3$.

Composition	Temperature (°C)	Conductivity (S/cm)	Reference
$LaMnO_3$	950	90-100	75
$La_{0.9}Sr_{0.1}MnO_3$	1000	130	94
$La_{0.84}Sr_{0.16}MnO_3$	RT	25.6	74
	1000	133	74
$La_{0.8}Sr_{0.2}MnO_3$	1000	175	94
$La_{0\ 65}Sr_{0.35}MnO_3$	1000	200	72
$La_{0.6}Sr_{0.4}MnO_3$	700	100	95,96
$La_{0.55}Sr_{0.4}MnO_3$	950	250-300	75
$La_{0.5}Sr_{0.5}MnO_3$	700	360	97
	800	320	97
	900	300	97
	1000	290	98
$La_{0.45}Sr_{0.55}MnO_3$	960	250	99
$La_{0\ 45}Sr_{0\ 55}MnO_3$	1000	450	72

LSM shows a relatively small variation in electrical conductivity with a moderate change of Sr dopant at 1000°C. The electrical conductivity data reveal $La_{0.5}Sr_{0.5}MnO_3$ to be a metallic type conductor [97]. Yasuda [99] observed metallic type conduction at x = 0.5, semiconductor type at x = 0.8 and a metal-semiconductor transition at x = 0.6 over the temperature range 20°C-1000°C. Fig. 2.15 shows the electrical conductivity as functions of temperature and Sr content.

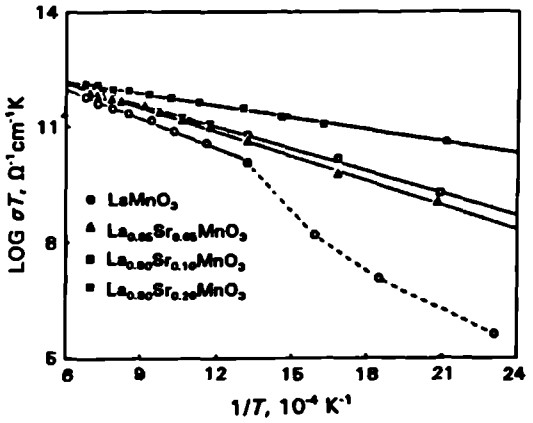


Fig. 2.15 : Conductivity of LSM as a function of temperature and Sr content [94].

(ii) Effect of oxygen partial pressure

Yasuda et al [79,80] claimed that $La_{0.8}Sr_{0.2}MnO_3$ has high electrical conductivity only at oxygen partial pressures higher than 10^{-8} atm. At an oxygen pressure lower than 10^{-8} atm, the electrical conductivity over the temperature range 850°C-1000°C was reasonably constant.

The amount of Mn^{4+} remained constant at low temperature but was measurable due to the holes generated from Sr doping at high temperature. It can be concluded that the number of desorbing oxygens equals half the number of dopant Sr atoms as shown in reaction 2.15.

$$2SrO \xrightarrow{LaMnO_3} 2Sr'_{La} + V_O^{\bullet\bullet} + 2O_O^x \qquad \text{----- 2.15}$$

Introduction of the dopant ion Sr^{2+} is equivalent to introducing $SrMnO_3$ into $LaMnO_3$ as indicated in the following defect reaction :

$$SrMnO_3(LaMnO_3) + Mn_{Mn}^{\bullet} \Leftrightarrow Sr_{La}' + 2Mn_{Mn}^{x} + 2O_O^{x} + V_O^{\bullet\bullet} + \frac{1}{2}O_2 \quad \text{-----} \quad 2.16$$

The mean valence or mean oxidation state of Mn was enhanced by Sr doping (+3.3 when x=0, +3.5 when x=0.5) [100]. An effect of the conductivity with oxygen partial pressure is shown in Fig. 2.16.

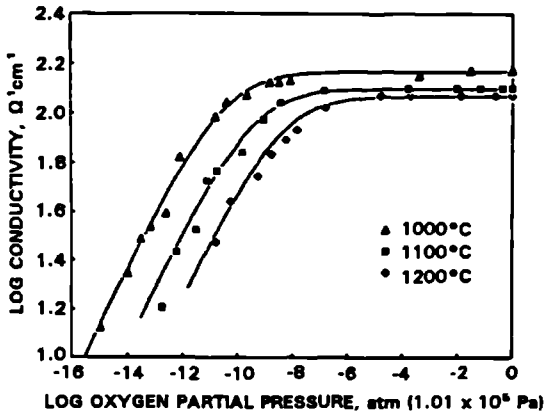


Fig. 2.16 : Conductivity of $La_{0.8}Sr_{0.2}MnO_3$ as a function of oxygen partial pressure [94].

2.4.4.4 Stability

After sintering at 1200°C for 12 hours, La_2O_3 was detected using XRD in LSM of composition $x \leq 0.5$ [77].

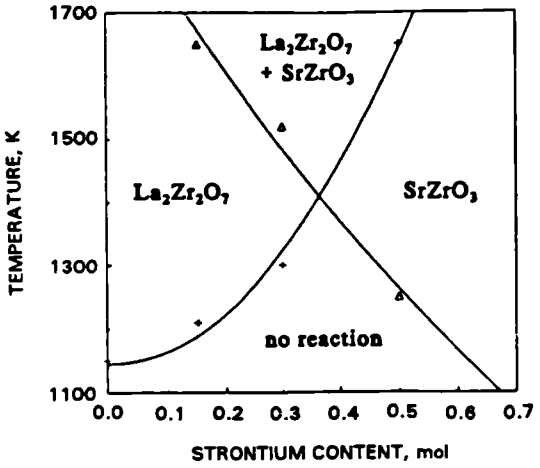
(i) LSM/YSZ interface

(a) $La_{1-x}Sr_xMnO_3$

When $La_{1-x}Sr_xMnO_3$ was in contact with YSZ at 1200°C for 2 hours, $La_2Zr_2O_7$ and $SrZrO_3$ were detected at x = 0.1 and 0.7, respectively. LSM can be in equilibrium with these two phases, or one of them depending on the strontium content and

temperature as in Fig. 2.17 (a). Phases can be plotted in a chemical potential diagram as functions of activities as shown in Fig. 2.17 (b).

(a)



(b)

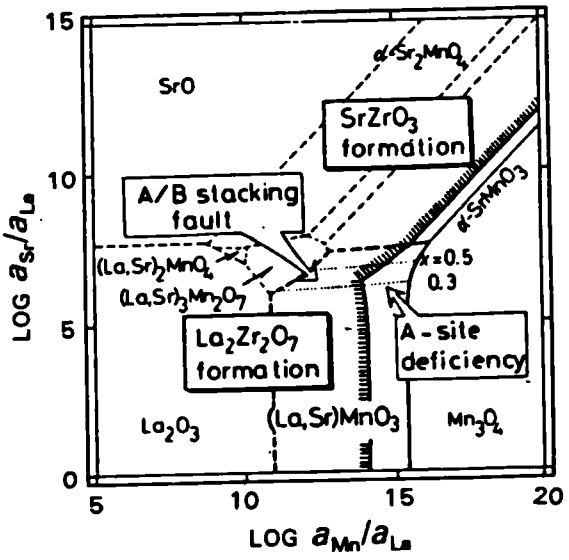


Fig. 2.17 : (a) Reaction products formed at the LSM/YSZ interface as a function of strontium content and temperature and (b) Chemical potential diagram of the La-Sr-Mn-Zr-O system at 1300℃ [101].

(b) La deficiency $La_{y-x}Sr_xMnO_3$

- Mn_3O_4 was detected at the TPB of $La_{0.6}Sr_{0.3}MnO_3$, $La_{0.6}Sr_{0.2}MnO_3$, $La_{0.7}Sr_{0.2}MnO_3$, $La_{0.7}Sr_{0.1}MnO_3$, and $La_{0.7}MnO_3$ after annealing at 1200°C in air for 20 hours [75]. However, Stochniol et al [102] claimed that no reaction products with YSZ were found for $La_{0.65}Sr_{0.3}MnO_3$/YSZ heated to 1670K for 200 hours.
- $La_2Zr_2O_7$ was found at $x \leq 0.3$ and $SrZrO_3$ was found at $x \geq 0.3$. Both products were found when $x = 0.3$ for the stoichiometric oxygen.
- La deficiency at $x \geq 0.5$ was found to prevent the formation of $La_2Zr_2O_7$ [103].
- An extended operation at 950°C can lead to the decomposition of $La_2Zr_2O_7$.

(ii) LSM/Interconnect Interface

No reaction or localization was observed for the $La_{0.8}Sr_{0.2}MnO_3/La_{0.8}Sr_{0.2}CrO_3$ interface at 1300°C for 20 hours [104]. The $(La_{0.75}Sr_{0.25})_{0.99}MnO_3/La_{0.75}Ca_{0.25}CrO_3$ system was found to be stable under SOFC operating conditions after trial runs of 300 hours [105]. No manganese oxide segregation was observed in LSM but $CaMnO_3$ was detected at the interconnect. This compound did not cause severe degradation as it is an electronic conductor.

A spinel of $Mn(Cr,Fe)_2O_4$ formed at the interface of $La_{0.84}Sr_{0.16}MnO_3$/Cr-5Fe-1Y_2O_3 at 950°C after 1000 hours [106]. This left the remaining area of rich in La and Sr, which are able to form further undesirable compounds such as La_2O_3 and $SrCrO_4$.

2.4.5 LANTHANUM COBALTITE ($LaCoO_3$, LCO)

LCO is a perovskite material as is LMO, but it has a rhombohedral crystal structure from room temperature to 1000°C [107,108]. At high temperature, LCO always shows an oxygen deficiency [109]. Compared with LMO, LCO is less stable in a reducing atmosphere. Doping LCO enhances the electrical conductivity, but also reduces the stability [110].

Sr and Ca are typical dopants for LCO. The electrical conductivity of $La_{1-x}Sr_xCoO_3$ (LSC) is superior to that of $La_{1-x}Ca_xCoO_3$ for the same dopant level.

LCO is not stable in contact with YSZ at high temperature, forming $La_2Zr_2O_7$ [111,112,113]. The Sr in LSC also reacts with YSZ to form $SrZrO_3$ [111,114,115]. These two phases are not desirable as they inhibit the reaction at the TPB. LCO-based oxides normally have much higher coefficients of thermal expansion than YSZ. The difference is significant enough to cause cracking due to thermal mismatch.

2.4.6 OTHER OXIDES

(i) In_2O_3-Based Materials

Indium oxide doped with tin (ITO) has a high electrical conductivity [116,117,118]. However, this material is expensive and not thermodynamically stable [7]. In addition, the coefficient of thermal expansion of ITO is very much lower than that of YSZ.

(ii) $GdCoO_3$-based materials

$GdCoO_3$ on its own has a fairly low electrical conductivity as compared with LSM. After doping with Sr, it shows a comparable conductivity to that of LSM, but a second phase of $SrZrO_3$ has been detected at temperatures above 850°C [119].

(iii) $Pr(Mn,Co)O_3$–based Materials

$Pr_{0.6}Mn_{0.4}O_3$ shows less reaction in contact with YSZ and has a low overpotential loss [96,120]. However, the electrical conductivities of $Pr_{0.8}Sr_{0.2}CoO_3$ and $Pr_{0.6}Mn_{0.4}O_3$ are lower than that of LSC.

(iv) $La_{0.6}Sr_{0.4}Co_{0.2}Fe_{0.8}O_3$ (LSCF)

This material has been proven to have a very high electrical conductivity at intermediate temperatures (600°C - 800°C) [121, 122]. Nevertheless, the CTE of this material is much higher than that of YSZ.

2.4.7 OVERVIEW OF CATHODE MATERIALS

Electrical conductivities, Area Specific Resistivities (ASRs), and CTEs of the materials described above are summarised in Table 2.4, 2.5, and 2.6, respectively.

Table 2.4: Electrical conductivity of cathode materials.

Material	Temperature (°C)	Electrical Conductivity (S/cm)	Reference
$La_{0.8}Sr_{0.2}MnO_3$	1000	175	94
$La_{0.6}Sr_{0.4}MnO_3$	700	100	95,96
$La_{0.3}Ca_{0.63}MnO_3$	850	200	123
$(La_{0.5}Ca_{0.5})_{0.9}MnO_3$	1000	160	124
$La_{1-x}Sr_xCoO_3$	1000	1000	119
$La_{0.9}Sr_{0.1}CoO_3$	700	1000	110,125
$La_{0.6}Sr_{0.4}CoO_3$	700	2000	126
$La_{0.6}Sr_{0.4}CoO_3$	700	500	125
$La_{0.6}Sr_{0.4}Co_{0.2}Fe_{0.8}O_3$	560	100	127
$La_{0.6}Sr_{0.4}Co_{0.98}Ni_{0.02}O_3$		1500	95
$Pr_{0.6}Mn_{0.4}O_3$	900	240	96,120
$Pr_{0.8}Sr_{0.2}Mn_{1-x}Co_xO_3$	700	1.63 for x=0	128

Table 2.5 : Area Specific Resistivities (ASRs) of cathode materials on YSZ.

Material	Temperature (°C)	ASR (Ωcm^2)	Reference
$La_{0.8}Sr_{0.2}MnO_3$	800	140	121
	900	30	121
$La_{0.6}Sr_{0.4}MnO_3$	800	11.2	129
	900	2.7	129
$La_{0.6}Sr_{0.4}CoO_3$	800	0.8	130
$La_{0.6}Sr_{0.4}Co_{0.2}Fe_{0.8}O_3$	650	0.8	127

Table 2.6 : Coefficients of thermal expansion of some cathode materials.

Material	CTE ($x10^{-6}$ K^{-1})	Reference
$La_{0.9}Sr_{0.1}MnO_3$	12.0	131
$La_{0.6}Sr_{0.4}MnO_3$	13.0	95, 96
$La_{0.5}Sr_{0.5}MnO_3$	13.2	98
$La_{0.9}Ca_{0.1}MnO_3$	10.1	132
$La_{0.5}Ca_{0.5}MnO_3$	11.4	132
$LaCoO_3$	23.7	125
$La_{0.9}Sr_{0.1}CoO_3$	20.1	110,125
$La_{0.8}Sr_{0.2}CoO_3$	17.4	125
$La_{0.6}Sr_{0.4}Co_{0.2}Fe_{0.8}O_3$	>16	127
$LaCo_{0.6}Ni_{0.4}O_3$	17	133
$Pr_{0.6}Mn_{0.4}O_3$	12	96, 120
$Pr_{0.8}Sr_{0.2}Mn_{1-x}Co_xO_3$	<12	128

The kinetic data of selected cathode materials including oxygen diffusion coefficients (D*), and surface exchange coefficients (k) at various temperatures are listed in Table 2.7.

Table 2.7 : Kinetic data of selected cathode materials [67].

Material	Temperature (°C)	D* (cm^2/s)	k (cm/s)
$La_{0.5}Sr_{0.5}MnO_3$	700	2×10^{-15}	1×10^{-8}
	800	8×10^{-14}	1×10^{-7}
$La_{0.8}Sr_{0.2}CoO_3$	700	1×10^{-8}	3×10^{-6}
	800	2×10^{-8}	5×10^{-6}
$La_{0.6}Sr_{0.4}Co_{0.2}Fe_{0.8}O_3$	854	7.4×10^{-8}	2.4×10^{-5}
	761	1.5×10^{-8}	3.6×10^{-6}
	663	1.5×10^{-9}	6.3×10^{-7}

2.5 FABRICATION OF SOFC COMPONENTS

As mentioned in the previous section, one of the major problems of SOFCs is the fabrication of cell components. Many techniques are being used to fabricate thin/thick film components for SOFCs. They are all different in terms of process principles, conditions and cost.

The two main techniques by which films are currently being fabricated successfully are based on the sintering route and the vapour phase route.

The thermal spraying method including plasma spraying involves spraying of the desired material in a molten or liquid form onto a substrate. Plasma spraying has been used extensively for the fabrication of YSZ films [30,134,135]. Generally, thermal spraying techniques are used to deposit films on a metallic substrate [136], since the thermal shock is too severe for deposition onto ceramic substrates.

2.5.1 SINTERING ROUTE

The majority of ceramic fabrication techniques follow the sintering route. The major difference between them is the method of preparing the green body before sintering. Some of the successful techniques used in the fabrication of YSZ electrolyte and electrode films for SOFCs are dip-coating [137], sol-gel [138], transfer printing [139], thermal spray sintering [140], screen printing [141], spray pyrolysis [30,134,135,142], slip casting [30,134,143], and slurry coating [138]. Tape casting and tape calendering [144] are the techniques being used widely in the commercial sector and several reports on the resulting mechanical properties have been published [145,146,147,148,149]. All the techniques mentioned above require an electrode to act as a substrate. Slip casting is also used to prepare electrode supports [135]. These processes can be followed by the formation of PEN laminate and co-sintering. However, co-sintering raises other issues such as the different sintering temperatures required for each component of the fuel cell. The microstructure then deviates from the ideal and this degrades the properties. Removal of binders from the green body can cause cracking of the films. Moreover,

during co-sintering diffusion between two interfaces such as between $La_XSr_{1-X}MnO_3$ and ZrO_2 [150] may occur. Cracking and delamination in the cell after sintering, owing to the thermal expansion mismatch between layers, is another problem that arises. Tailoring the powders of each component has been shown to be effective in reducing the thermal expansion coefficient mismatch during sintering [151,152].

2.5.1.1 Slurry Coating Method

The slurry coating method involves coating a water suspension of electrolyte, or *slurry*, on a substrate and drying it at room temperature. After drying, it is heated to high temperature (1400°C -1500°C) for an hour, and then the process of coating, drying and heating is repeated to reach the required thickness. The component is then sintered at the elevated temperature for 5 hours. This process produces a dense film.

2.5.1.2 Slip Casting Method

This is done by casting slurry in a mould. This process can be repeated many times to fabricate complex shapes. The green body so produced requires sintering, which is similar to the final process of slurry coating. Using this technique, a sintered body containing only a few small pores can be produced [134].

2.5.1.3 Spray Pyrolysis

This technique involves the spraying of solution onto a heated substrate of about 100°C - 200°C. The temperature is increased to ~600°C to decompose the solute and any remaining solvent. The process is repeated until the required thickness is achieved. The final step is sintering at ~1400°C -1500°C for 5 hours. Films obtained from this process typically show large cracks at the surface [134].

2.5.1.4 Tape Casting

This technique is a casting of slurry of the powders and organic binders onto a flat surface. The slurry is spread under a relatively slowly moving doctor blade to

control the thickness. After the casting process, the tape is dried to remove the solvent and then sintered. The sintering temperature for a dense YSZ electrolyte is ~1300°C - 1500°C [153,154]. For a porous LSM electrode, the sintering temperature is in the same range [155,156].

2.5.1.5 Tape Calendering

A thin continuous tape is produced by squeezing the polymer/ceramic mixture (electrolyte/electrode powder and organic binders) between two rolls. The required thickness can be obtained by varying the space between the two rolls. The film produced has high uniformity. Thin, dense electrolyte films in the range of 1 to 10 μm thick are fabricated using this technique [157]. The sintering process is similar to those mentioned above. For a porous LSM electrode, it is sintered at 1300°C - 1400°C [158,159,160]. However, the heating rate is critical as the fast evaporation of polymer binders may cause bubbles in the tape, leading to cracking [7].

2.5.2 VAPOUR PHASE ROUTE

The vapour phase is utilised by two main techniques for fabricating ceramic films. These are distinguished by the reaction during deposition, *viz* whether it is a physical or chemical reaction [161]. Ceramics prepared by a vapour phase route do not require sintering at high temperatures.

2.5.2.1 Physical Vapour Deposition Technique (PVD)

The physical vapour deposition technique (PVD) is based on evaporation, sputtering or ion plating. This process has to be carried out in a high vacuum. The substrate must be placed exactly in line with the target material as this is a line-of-sight process. There are many different heating methods such as resistance heating and RF (Radio Frequency) coupling (for evaporating), sputtering, and microwave heating. RF ion plating and RF sputtering follow this principle to deposit thin YSZ films (< 1 micron) on electrodes substrates [134,138,162]. Control of the

stoichiometry of multicomponent oxides using the PVD technique has proven to be difficult.

(i) RF Ion Plating Method

The material to be deposited, for example YSZ, is evaporated by an electron beam. The evaporated species are ionised in Ar plasma and accelerated by a dc bias which is connected to the substrate holder [134]. This is enhanced by Radio Frequency coupling. The temperature at the substrate is typically 400°C. The whole process is carried out *in vacuo*. YSZ films obtained by this deposition method contain pores or cracks, which are not suitable for a porous substrate. Consequently, this method is not appropriate for fuel cell component fabrication. The cost of this apparatus is expensive due to a vacuum chamber requirement.

(ii) RF Sputtering

This method is based on the ion bombardment of the material to be deposited. Ions and atoms of the material being bombarded are ejected from the solid and deposited on a substrate. This technique uses radio waves to achieve ion bombardment. As a vacuum chamber is required, the cost is high and the deposition time is slow [134].

2.5.2.2 Chemical Vapour Deposition Technique (CVD)

The Chemical Vapour Deposition technique (CVD) is performed in the vapour phase from either gaseous, liquid or solid precursors. A chemical reaction occurs on or in the vicinity of the heated substrate to form a coating [163]. As the process has to be carried out in a closed chamber to achieve high temperatures, the quality of the coating is good but costly. The reaction chamber can be at atmospheric pressure, low pressure or ultra high vacuum. Precursors used are generally expensive and toxic.

As far as the conventional CVD technique is concerned, the deposited film has a well controlled microstructure, uniformity and adhesion. A thickness of less

than 10 microns can be easily achieved. Another processing technique which requires lower cost is preferable, however, but still maintaining the same film quality. There are many modifications of this technique based on chemical vapour phase reactions.

(i) Electrochemical Vapour Deposition Technique (EVD)

EVD is used to produce dense YSZ electrolyte films on porous substrates at elevated temperature and reduced pressures [164,165]. This process relies on the conductivity of ionic and electronic species in the precursors. A pore closure reaction, in which metal halide reacts with water to form a metal oxide which fills up the pores, is controlled by CVD. The metal halide and water supplied are on either side of the porous substrate. An electrochemical reaction occurs after the pores are filled. Film growth from the closed pores occurs according to the Wagner oxidation process whereby oxygen ions from the reduction of water on one side travel to the other side and react with the metal halide to form an oxide [166]. The film from this technique has a dense structure and uniform thickness. This technique is used commercially in the production of sealless tubular SOFCs [167]. The cost of this EVD technique is very expensive, especially with regards to the cost of the apparatus.

(ii) Electrostatic Assisted Vapour Deposition (EAVD)

A more recent technique in the field of CVD is EAVD which has been shown to be able to successfully deposit both porous and dense films for SOFC application [168,169]. The general method is similar to the spray pyrolysis technique, except that the spray solution is charged beforehand. When the solution is sprayed it is emitted as fine droplets. As these droplets are charged, the deposition geometry can be controlled, by using the charging attraction.

(iii) Combustion CVD (CCVD)

Combustion CVD combines the basic principles of Metal Organic CVD and the flame spraying technique by which a liquid precursor solution is sprayed through

a flame. An oxide film is deposited on a substrate, which is held in the flame. The maximum thickness of the deposited film has been found to be 1.2 μm for the deposition of YSZ on stainless steel [170]. A similar technique can be used to produce thin films of YSZ [171]. So far, the thickness of films produced by this alternate method is too thin for application in SOFCs.

(iv) Flame Assisted Vapour Deposition (FAVD)

Flame Assisted Vapour Deposition uses a flame as the heat source instead of a furnace. It is a combination of spray pyrolysis and flame synthesis whereby an atomised solution is sprayed through a flame in an open atmosphere. Decomposition and combustion reactions occur, resulting in a stable film deposited on a heated substrate. The whole deposition process is performed at a relatively low temperature and at a high flow rate. There are some reports of this technique being used for coating of SiO_2 [172], $YBa_2Cu_3O_x$ [173,174], Al_2O_3 [175] and $PbTiO_3$-based oxides [175]. A YSZ coating on a single crystal of MgO has been deposited using this technique [176]. This technique is capable of depositing both dense and porous films, and hence it has been selected for deposition of SOFC electrolytes and cathodes.

Table 2.8 below gives a summary of the advantages and disadvantages of some techniques used in preparation of SOFCs components [134].

Table 2.8: Advantages and disadvantages of some conventional processing techniques.

Fabrication Technique	Thickness	Advantages	Disadvantages
Slurry coating	10 μm-	High utilisation of materials and not affected by surface roughness.	Slow process and cracks can form due to shrinkage during sintering.
Slip casting	150 μm-	High utilisation of materials and yields good pin hole free film. Simple to perform.	Low mechanical strength (self supported) and component size limited to small areas.
Spray pyrolysis	10 μm-	Unaffected by substrate roughness and needs low preparation temperature.	Low utilisation of materials and slow process. Difficult to deposit dense electrolyte and requires further heat treatment
RF ion plating	2 μm-	Suitable for ceramics and possibility of reactive ion plating.	Deviation of composition between source and deposited films. Line-of-sight process, expensive.
RF sputtering	2 μm-	Possibility of reactive sputtering.	Low deposition rate and deviation of composition between source and deposited films. Line-of-sight process, expensive.
CVD and EVD	thin and thick films	Dense films	Low deposition rate and expensive.
Plasma spraying	100 μm-	Suitable for ceramics with high melting point and for sequential fabrication of components. High deposition rate.	High heating and cooling rates leading to thermal shock. Not suitable for the fabrication of dense electrolyte.
EAVD	1 μm-	Suitable for dense and porous films	Specific configurations are necessary for particular types of coatings
FAVD	1 μm-20 μm	Suitable for porous films	Difficult to control processing parameters.

2.6 SUMMARY

From all the aspects mentioned in this chapter, various interesting points have been expanded and explored in this thesis based on the SOFC of bi-polar plate configuration. As the cost of fabrication is one of major problems involved in SOFCs, a novel method of FAVD has been used to deposit porous films of LSM cathode for the YSZ electrolyte, operating at 800°C-900°C. These choices of cathode and electrolyte have been made according to the availability and materials, data, and satisfactory properties as both of them are typically used for these applications. For the SOFC operating at intermediate temperatures (650°C-800°C), ceria-based electrolytes are a good candidate. Since LSC has a compatible CTE with doped ceria and has high electrical conductivity in this range of temperature, it is also selected as a cathode material. The coefficient of thermal expansion of selected materials are summarised in Table 2.9.

Table 2.9 : Coefficient of Thermal Expansion of selected materials for SOFCs.

Component	Material	CTE ($x10^{-6}$ K^{-1})	Reference
Cathode	$La_{0.79}Sr_{0.18}MnO_3$	12.4	123
	$La_{0.8}Sr_{0.2}CoO_3$	17.4	125
Electrolyte	YSZ (8mol%)	10.8	37
	$Ce_{0.8}Gd_{0.2}O_{1.9}$	13.2	177
Interconnect	$La_{0.8}Sr_{0.2}CrO_3$	11.1	178

Chapter 3 : EXPERIMENTAL PROCEDURES

3.1 PREPARATION OF SUBSTRATES

YSZ SUBSTRATES

8 mol% YSZ pellets were prepared by a conventional ceramic sintering process. The 8 mol % YSZ powder supplied by TOZOH (Japan) was pressed into green body pellet of size 13 mm. These pellets were then sintered at 1500°C for 2 hours with heating and cooling rates of 300°C/hour. The diameter of YSZ pellets after sintering was 10 mm and the density was greater than 97 %. The thicknesses of pellets were between 500 microns to 1 mm.

GADOLINIA DOPED CERIA SUBSTRATES

$Ce_{0.9}Gd_{0.1}O_{1.95}$ plates were prepared using a tape calendering method. The green body plate was sintered at 1500°C for 5 hours. The 99.9 % $Ce_{0.9}Gd_{0.1}O_{1.95}$ powder was supplied by Rhone-Poulenc (France). The size of plate after sintering was about 10 mm. x 10 mm. and 300 microns thick.

3.2 PREPARATION OF PRECURSORS

PRECURSOR FOR DEPOSITION OF LSM

Nitrate powders of 99.9% $La(NO_3)_3 \cdot xH_2O$, 99+% $Sr(NO_3)$, and 98% $Mn(NO_3)_2 \cdot 6H_2O$ supplied from Aldrich Chemicals were dissolved in deionised water at the ratio of La : Sr : Mn = 0.82 : 0.18 : 1, to make an aqueous solution. Ethanol 99.9% was then added to the solution to make the solution of desired concentration. The ratio of ethanol to water was varied from 50 : 50 to 80 : 20, and the concentration of the precursor was varied from 0.01 M to 0.10 M.

PRECURSOR FOR DEPOSITION OF LSC

The precursor preparation procedures are similar to that described above for the deposition of LSM, but 99% $Co(NO_3)_2 \cdot 6H_2O$ (Aldrich Chemicals) powder was used instead of 98 % $Mn(NO_3)_2 \cdot 6H_2O$. The ratio of La : Sr : Co = 0.8 : 0.2 : 1, and the ratio of ethanol to water was varied from 70 : 30 to 75 : 25, but the concentration of the precursor was fixed at 0.05 M as it was proven to be the optimum concentration of the solution from the deposition of LSM.

PRECURSOR FOR DEPOSITION OF LCO

The powders were mixed to make a precursor solution of La : Co ratio of 1:1. The concentration of the precursor was 0.05 M. The precursor preparation procedures are similar to that of LSM and LSC.

PRECURSOR FOR DEPOSITION OF CGO

Powders of 99 % $Ce(NO_3)_3 \cdot 6H_2O$, and 99.9 % $Gd(NO_3)_3 \cdot 6H_2O$ from Aldrich Chemicals were dissolved in deionised water at the ratio Ce : Gd = 0.8 : 0.2, and subsequently, ethanol was added to the mixture to make a precursor solution of 0.05 M.

PRECURSOR FOR DEPOSITION OF YDC

The precursor preparation procedure is similar to that of CGO but the powder of 99.9 % $Y(NO_3)_3 \cdot 6H_2O$ was used instead of Gd to mix with Ce powder at the ratio Ce : Y = 0.85 : 0.30. The concentration of the solution was fixed at 0.05 M.

3.3 FLAME ASSISTED VAPOUR DEPOSITION (FAVD)

A sketch of the FAVD apparatus is shown in Fig. 3.1. An appropriate substrate was cleaned in acetone prior to each deposition and heated up to ~200°C by means of a hot plate, then a natural gas flame (Bunsen burner) carried on the heating up close to the expected deposition temperature at around 600°C. A thermocouple was placed next to the substrate to monitor the temperature during the deposition which is called 'deposition temperature'. The precursor of the film to be deposited was drawn from the source using a peristaltic pump at a set flow rate, through the spray nozzle (atomiser). The precursor was then atomised across the flame to the substrate situated vertically below the spray nozzle. The distance between the spray nozzle and the flame, and between the flame and the substrate was fixed throughout the deposition process. The process of deposition and annealing were run simultaneously. The deposition was performed continuously for 30 seconds and the substrate was annealed for 30 seconds repeatedly. After completing the film deposition, the substrate was given a final annealing for 2-3 minutes at the same temperature to ensure there were no unreacted species or vapour remaining in the film. Finally, the substrate was cooled down at a rate of 300°C per hour to room temperature with the combination of the flame source and the hot plate.

The variable parameters in this FAVD are the ratio of ethanol/water and the concentration of the precursor solution, the flow rate of the precursor, the pressure of the compressed air, and the distance between the spray nozzle and the substrate. Effects of these parameters are studied in Chapter 4.

For the deposition of electrolyte/cathode interlayer, the deposition procedure is the same but the electrolyte film was deposited first and then followed by the deposition of the cathode layer. When a symmetrical cell of interlayer is required, the substrate was turned up-side-down after the deposition of each film. There are two combinations in the deposition of this symmetrical cell of interlayer, which will be explained further in Chapter 6.

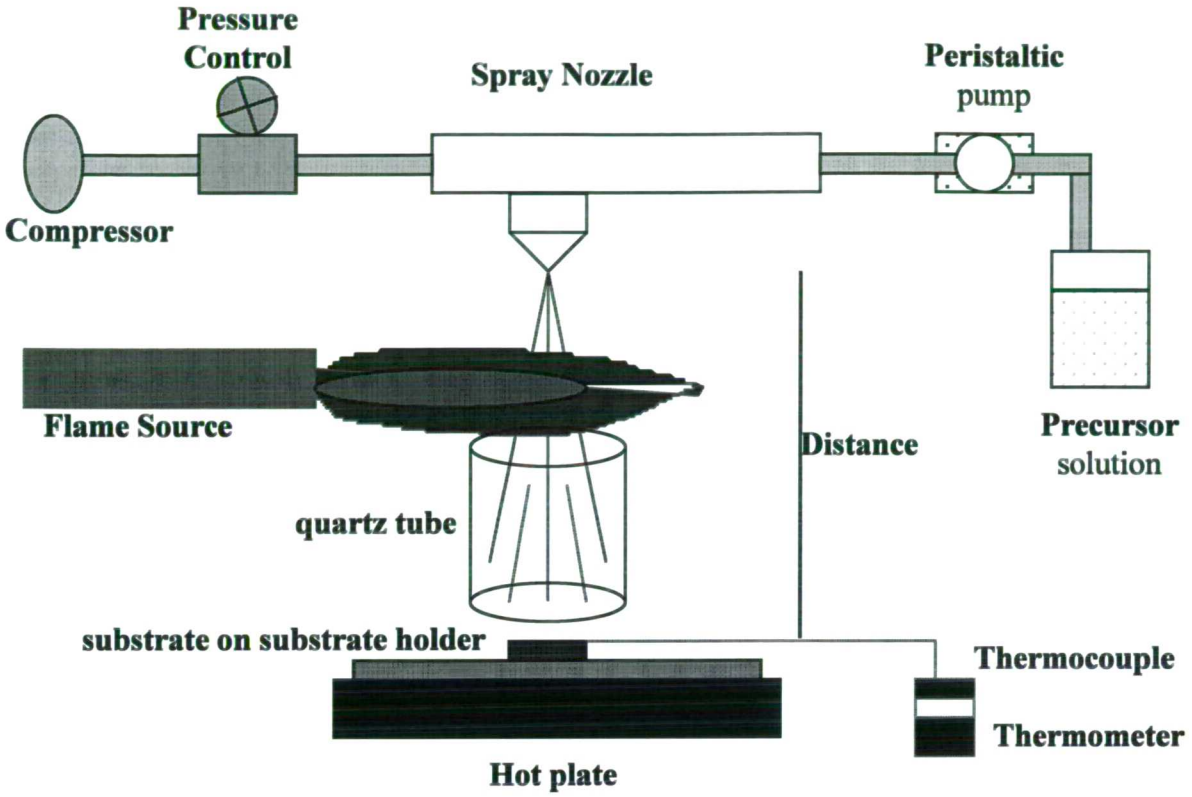


Fig. 3.1 : ***A schematic diagram of the Flame Assisted Vapour Deposition apparatus.***

This FAVD apparatus shown above has been modified from the original setup to yield a better control during deposition process and improve the coating reproducibility. Fig. 3.2 shows the original setup.

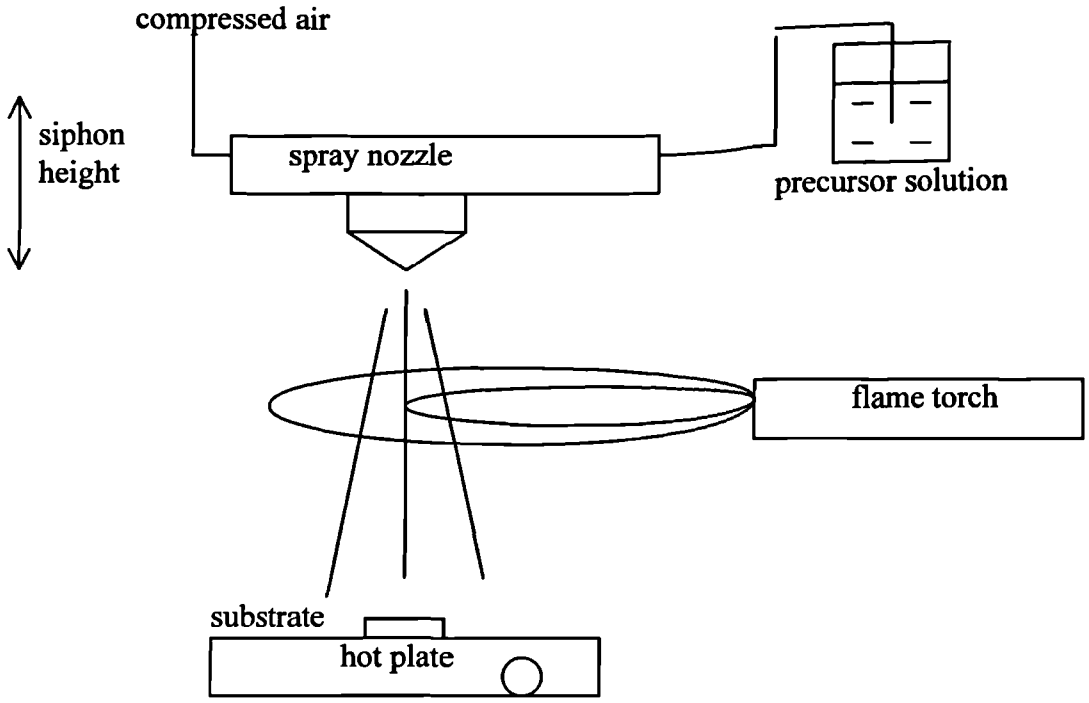


Fig. 3.2 : The original FAVD apparatus

The original setup uses the pressure from the siphon height and the compressed air to atomise the precursor solution through the spray nozzle. This had proven to be difficult to control, and inconvenient to operate. The modifications that were made are described below.

3.3.1. PERISTALTIC PUMP

A peristaltic pump has been used to generate a controlled flow rate of the precursor solution, which can be accurately measured. The flow rate is fixed throughout the deposition and not varied with the height of the solution. The flow of solution can be turned on and off immediately, which is important in the deposition and in emergency. However, the type of pump used has three rollers in generating the flow of liquid in a tube to flow in one direction, at the same time, gaps between the rotation of rollers cause pulsation in the flow. This pulsation affects the flow of the solution and therefore the deposition temperature. It has been minimised by introducing water reservoirs in the tube (connected tubes of different sizes). The

pulsation was reduced as the water in the reservoirs, flow to the nozzle during pulsing from the gap between rollers.

3.3.2 COMPRESSED AIR PRESSURE CONTROL (omnifit)

The compressed air supplied directly from a compressor had a pressure that was too high and the pressure at the spray nozzle was not known, when the pressure drop in the pipeline was taken into account. An air pressure control has been utilised to control the pressure within a desirable range (lower than 30 psi). The air pressure can then be switched on and off instantly.

3.3.3 SUBSTRATE HOLDER

The hot plate used has a metal surface in which the coefficient of thermal expansion is very different from the ceramic substrate. This caused cracking during deposition. In addition, the position of thermocouple next to the substrate was difficult to maintain at the same position in different deposition. Therefore, a ceramic holder was introduced to overcome these problems. The ceramic holder was fabricated from a commercial machinable ceramic (MACOR- trademark). With this ceramic holder, the problem due to thermal mismatch has been removed and the thermocouple has been properly positioned in all the depositions. The plan and cross-section of the holder are shown in Fig. 3.3.

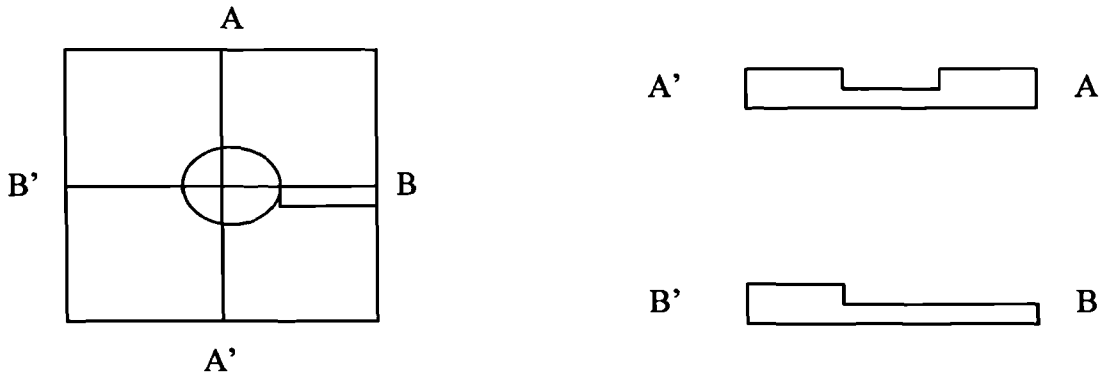


Fig. 3.3 : Sketches of the ceramic holder.

3.3.4 DEPOSITION ENCLOSURE

The deposition is carried out in an open air, in a fume cupboard. The turbulence in the fume cupboard, influences the flow of droplets, the chemical reactions and the deposition temperature. As the fume cupboard is needed for safety reason, an enclosure was introduced to prevent the turbulence effects and direct the flow in the desired direction. An aluminium enclosure was constructed to cover the apparatus but still allowed gases to be sucked through the fume hood. A sketch of this cage is shown in Fig. 3.4. With the use of this enclosure, the deposition could be controlled without any external effects from turbulence.

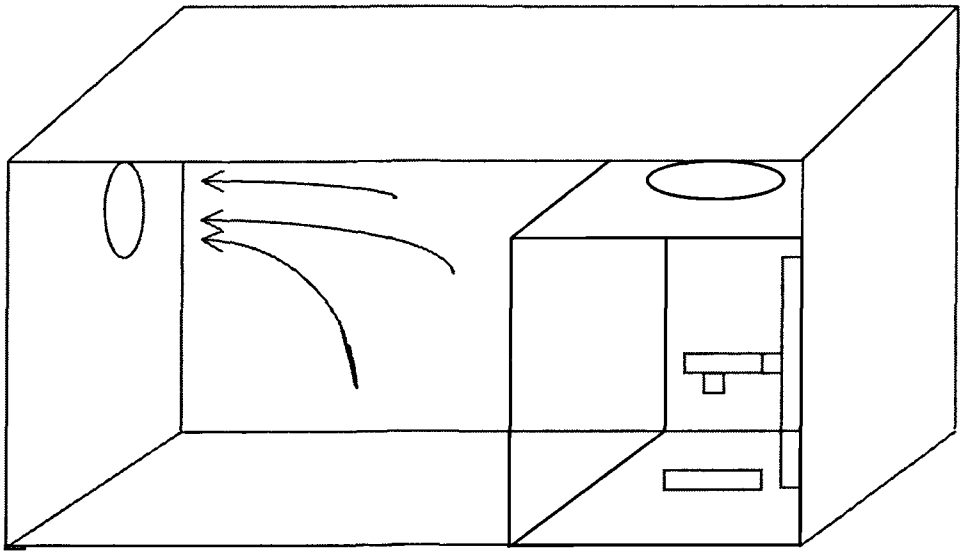


Fig. 3.4 : A sketch of a deposition enclosure.

3.3.5 A QUARTZ TUBE

With the aluminium enclosure, the deposition temperature was not disturbed by the turbulence in a fume cupboard. Nevertheless, the temperature fluctuation was controlled within a narrow range of ± 20 °C. A quartz tube of length 6 cm and 4 cm in diameter was introduced in between the flame tip and the substrate, to smoothen the temperature fluctuation. It has been proved to yield a better control over the temperature, to within an acceptable range of ± 15 °C to ± 10 °C. The temperature

fluctuates more if a quartz tube is too short. A setup with this quartz tube is shown in Fig. 3.5.

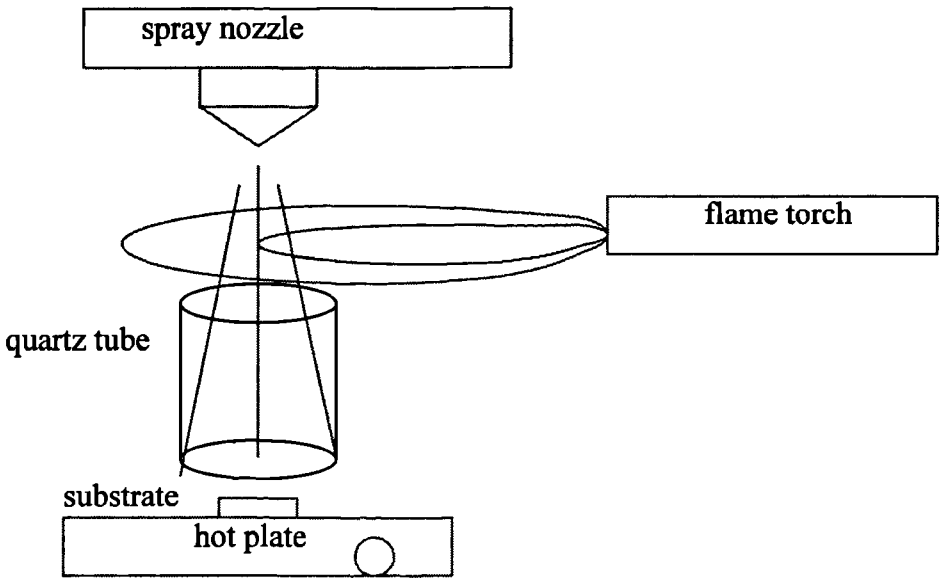


Fig. 3.5 : FAVD apparatus with a quartz tube.

3.4 CHARACTERISATION TECHNIQUES

3.4.1 STRUCTURAL CHARACTERISATION

3.4.1.1 MECHANICAL TEST

Qualitative scratch tests were performed on the coated substrates to evaluate the adhesion of the coating to the substrate. The surface of a deposited substrate was evaluated using adhesive tapes. If the film was powdery, powder can be removed easily and the film was categorised as powdery.

3.4.1.2 OPTICAL MICROSCOPY

The deposited films were observed under an optical microscope for a quick determination of a dense or porous structure. The presence of any cracks or powder on the coated surface could be detected easily.

3.4.1.3 SCANNING ELECTRON MICROSCOPY (SEM)

Surface morphology and fracture cross-sectioned of the deposited films were studied under SEM of model JOEL JSM-T220A using the secondary and back-scattered electron modes. The porosity, particle sizes and thickness of coated films were estimated. The SEM (JOEL JSM 35CF) equipped with Energy Dispersive Analysis X-ray (EDAX) was used to examine the elements present in the samples quantitatively. The basic principle is that characteristic x-rays are generated when incident electrons knock out an inner shell electron of one of the sample atoms. The atom then relaxes by an electron in another shell falling into the vacant state. The energy of this x-ray is the difference between the two energy levels which is characteristic of a particular element.

3.4.1.4 X-RAY DIFFRACTOMETRY

The crystal structure of the deposited films were analysed using x-ray diffraction method. A computer aided Philips PW1710 diffractometer was used at the operating current and voltage of 40 mA and 40 mV, respectively. The target used was copper which generated CuKα radiation of wavelength 1.54178 x 10^{-10} m incident on the sample surface. The number of orientations of the crystal grains for the incident x-

rays could be increased by spinning the sample stage. Samples were analysed over the angular range 10° to 90° 2θ. The diffraction patterns were collected and processed with the aid of Philips PC-APD software. These patterns were compared with the standard XRD data called the JCPDS data. Crystal structures were then identified in which the unit cell lattice parameters could be calculated from the d-spacings and the reflection planes for a particular system.

3.4.2 ELECTRICAL PROPERTIES

3.4.2.1 AC IMPEDANCE SPECTROSCOPY

AC impedance spectroscopy is a technique used to investigate the electrodic behaviour of cathode materials and the interface of electrolyte/electrode systems. AC impedance measurements were performed on symmetrical cells which consisted of porous electrodes that were deposited on both sides of the electrolyte pellet (Fig. 3.6). The thickness of the electrodes on both sides are approximately equal.

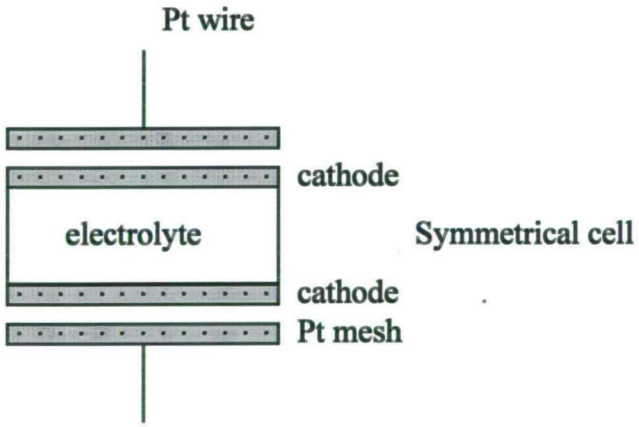


Fig. 3.6 : A cross-section of a symmetrical cell.

Fig. 3.7 shows the sketch of an AC impedance spectroscopy sample holder. A computer-controlled Solartron SI 1260 Impedance/Gain-Phase analyser was used to

measure the complex impedance of a symmetrical cell. The measurements were carried out as a function of temperature from 270°C - 770°C and a function of oxygen partial pressure. Platinum wires and mesh were used to provide an electrical contact to each side of the electrode. The frequency of the applied sinusoidal electrical perturbation was ranged from 0.01 Hz to 32 MHz. The amplitude of this applied signal was fixed at 50 mV peak to peak. The various processes that contribute to the behaviour of the electrochemical cell can be distinguished.

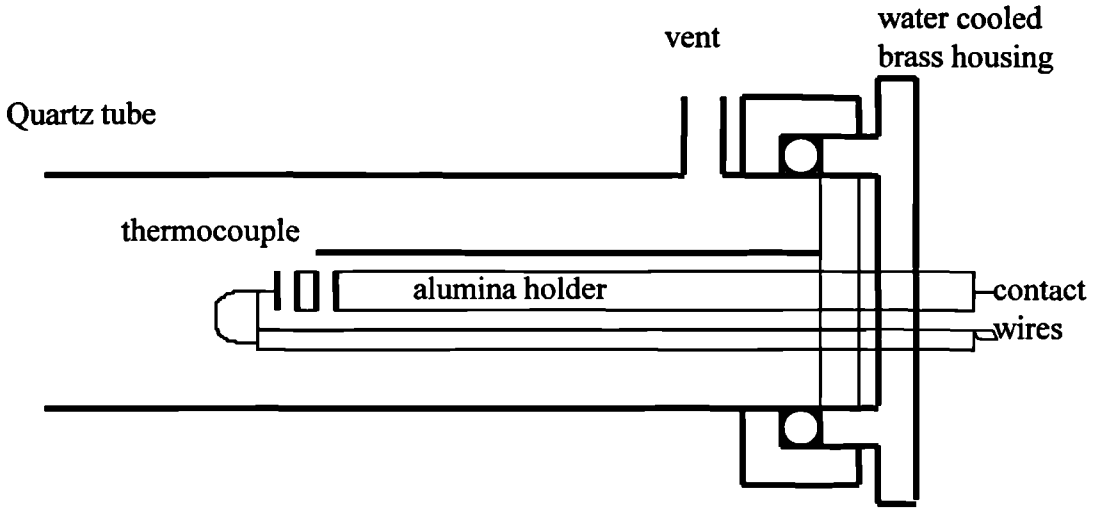
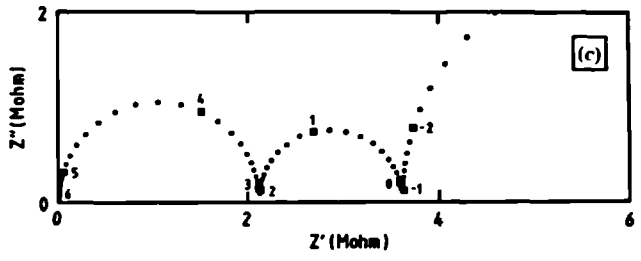


Fig. 3.7 : A schematic diagram of an AC impedance spectroscopy sample holder.

A typical AC-impedance spectrum consists of three semicircles referring to the electrolyte grain interior or bulk (R_{gi}), electrolyte grain boundary (R_{gb}), and the electrode (R_e) resistances. These can be interpreted as a parallel circuit of resistances and capacitance connected in series, Fig. 3.8.

(a)



(b)

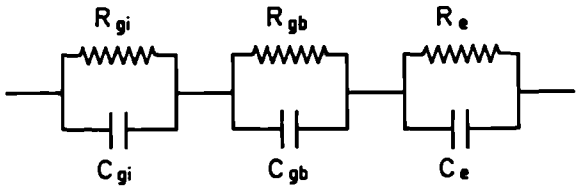


Fig. 3.8 : a) A typical AC-impedance spectrum [179] and b) A series circuit referring to the semicircles in the spectrum [180].

The intercepts at the real axis of a semicircle mark the resistance of that process. ASR is the resistance of the surface area between the electrolyte and the electrode. The log of conductivity (reciprocal of ASR) times temperature is then plotted versus the reciprocal of temperature, according to the Arrhenius type equation. The activation energy is obtained from the slope of this straight line.

$$\sigma_T = \frac{\sigma_0}{T} \exp^{\frac{-E_A}{RT}} \qquad \text{-----} \quad (3.1)$$

where σ_T = conductivity (reciprocal of ASR) ($\Omega^{-1}cm^{-2}$)

σ_0 = pre-exponential constant

E_A = activation energy (J/mol)

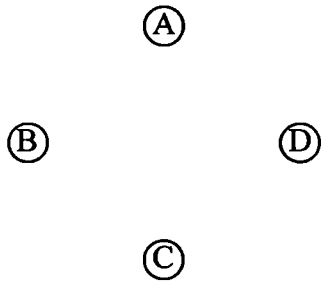
T = temperature (K)

R = gas constant (8.314 J/mol K)

3.4.2.2 DC 4-POINT (VAN der PAUW) TECHNIQUE

The electrical conductivity of a porous electrode film was measured using the four-point van der Pauw technique [181] as a function of temperature from room temperature to 700°C. The sample holder is similar to that of the AC impedance spectroscopy measurement but with four platinum beads in contact with the surface

of the electrode layer by means of a mechanical pressure. The sample situated in a furnace with an air atmosphere. A known current was applied across two adjacent platinum point contacts and the voltage generated across the other two points were measured using a multi-meter. This procedure was repeated with at least four combinations of adjacent platinum point contacts. These combinations are shown in Fig. 3.9.



$R_1 = V_{AB}/I_{CD}$

$R_2 = V_{BC}/I_{AD}$

$R_3 = V_{CD}/I_{AB}$

$R_4 = V_{DA}/I_{BC}$

$R_5 = V_{AC}/I_{BD}$

$R_6 = V_{BD}/I_{AC}$

Fig. 3.9 : Combinations of the resistances from the 4-point contacts.

From Ohm's Law :

$$R = \frac{V}{I} \qquad \text{-----} \quad (3.2)$$

where, R is the electrical resistance (Ω),

V is the electrical voltage (V), and

I is the electrical current (A),

therefore, the electrical resistivity, ρ, can be calculated from :

$$\rho = \frac{\pi t}{\ln 2}\left(\frac{R_1 + R_2 + R_3 + R_4}{4}\right) \qquad \text{-----} \quad (3.3)$$

where t is the thickness of the electrode layer, and R_i is the resistance of the i^{th} electrode combination.

The activation energy can be calculated from a straight line obtained from the Arrhenius type of plot between log (conductivity x temperature) versus the reciprocal of temperature, in the same manner as in equation 3.1.

Chapter 4: EFFECT OF PROCESS PARAMETERS IN THE DEPOSITION OF $La_{1-X}Sr_XMnO_3$

In this chapter, various parameters involved in the deposition of LSM using the FAVD technique, were investigated and discussed. There are the ratio of ethanol/water, the flow rate of the precursor, the concentration of the precursor, the pressure of the compressed air, and the distance between the spray nozzle and the substrate. These parameters produce the most pronounced effects on the microstructures and properties of the deposited films. The main factors which are investigated from this set of results are the microstructures and the adhesion of the films. More detailed discussion of the chemical reactions, are considered later in this chapter, and compared with a process simulation model in Chapter 7.

As explained in Chapter 3, a precursor solution of desired ratio and concentration is delivered to the spray nozzle at a certain flow rate. The solution is sprayed through the nozzle by means of a compressed air at a fixed pressure to form fine aerosol droplets. When the aerosol droplets pass through the flame, the decomposition and combustion reactions occur. As a result, an oxide film is deposited at the substrate.

The deposition process can be categorised into three main groups according to the shapes of a combustion zone (A, B, and C), Fig. 4.1, which can be varied by varying the processing parameters. The combustion zone is an area where the combustion of droplets takes place and all species are covered in flame. The deposition temperature mentioned in this thesis refers to the temperature at the substrate surface during deposition. d is the distance between the spray nozzle and the substrate.

The shape of a combustion zone closely relates to the microstructure of the deposited film. In general, shape A results in a precipitate or flaky film and the

deposition temperature is relatively low (< 500°C). A dense film can be obtained from a combustion zone of shape B where the deposition temperature is intermediate ~ 500°C-700°C. The combustion zone of shape C typically yields a powdery film at relatively high deposition temperature of > 700°C.

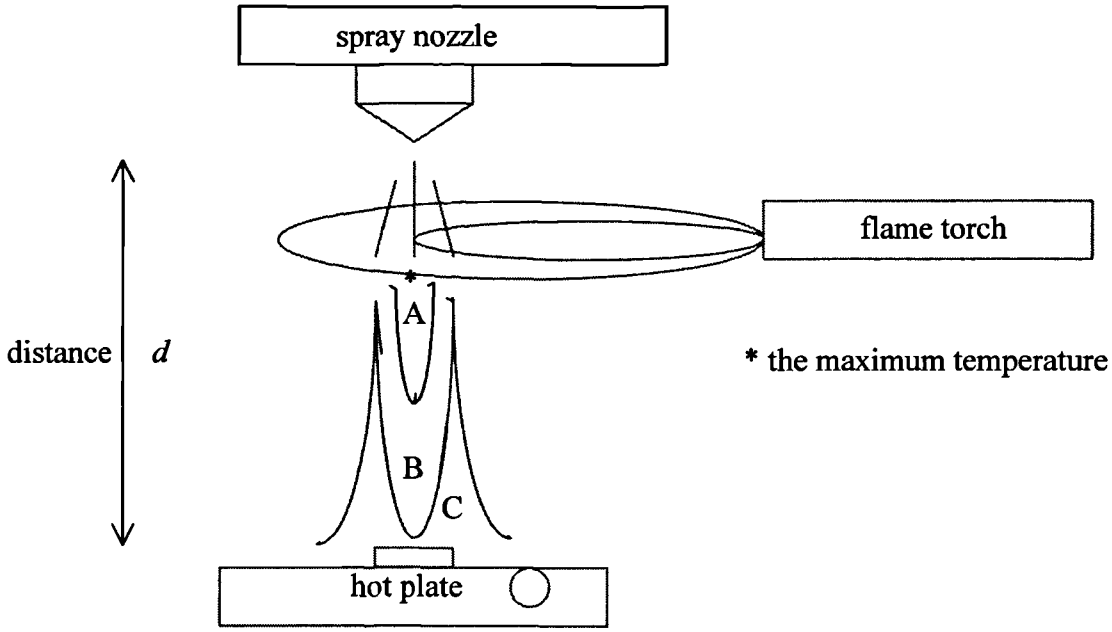


Fig. 4.1 : A sketch of various combustion zones in the FAVD method.

The deposition process related to microstructures of deposited films are discussed in each variation of processing parameters.

4.1 RATIO OF ETHANOL/WATER IN THE PRECURSOR SOLUTION

The aim of these experiments, was to obtain the optimum ratio of ethanol/water, to be able to produce a film of $La_{0.82}Sr_{0.18}MnO_3$. The ratio of ethanol/water was varied from 60% ethanol to 80% ethanol in water solution. By varying the ratio of ethanol to water, the deposition temperature, which was monitored at the substrate surface, changed accordingly as described in Table 4.2. All other parameters were kept constant as shown in Table 4.1.

Table 4.1 : Fixed parameters in the effect of ethanol/water ratio depositions

Concentration of the precursor solution	0.05 Molar
Distance between the spray nozzle and the substrate	12 cm
Flow rate of the precursor solution	12 ml/min
Pressure of the compressed air	22 psi

Table 4.2 : Deposition of $La_{0.82}Sr_{0.18}MnO_3$ at various ethanol/water ratios.

Ethanol/water ratio	Deposition temperature (°C)	Comments
80/20	770-810	Powdery film with fine particles (1μm)
75/25	720-780	Porous film of fine particles (1μm)
70/30	650-690	Uniform porous film of large particles (10-20 μm)
60/40	470-520	Nearly dense film with large particles (10-20 μm)

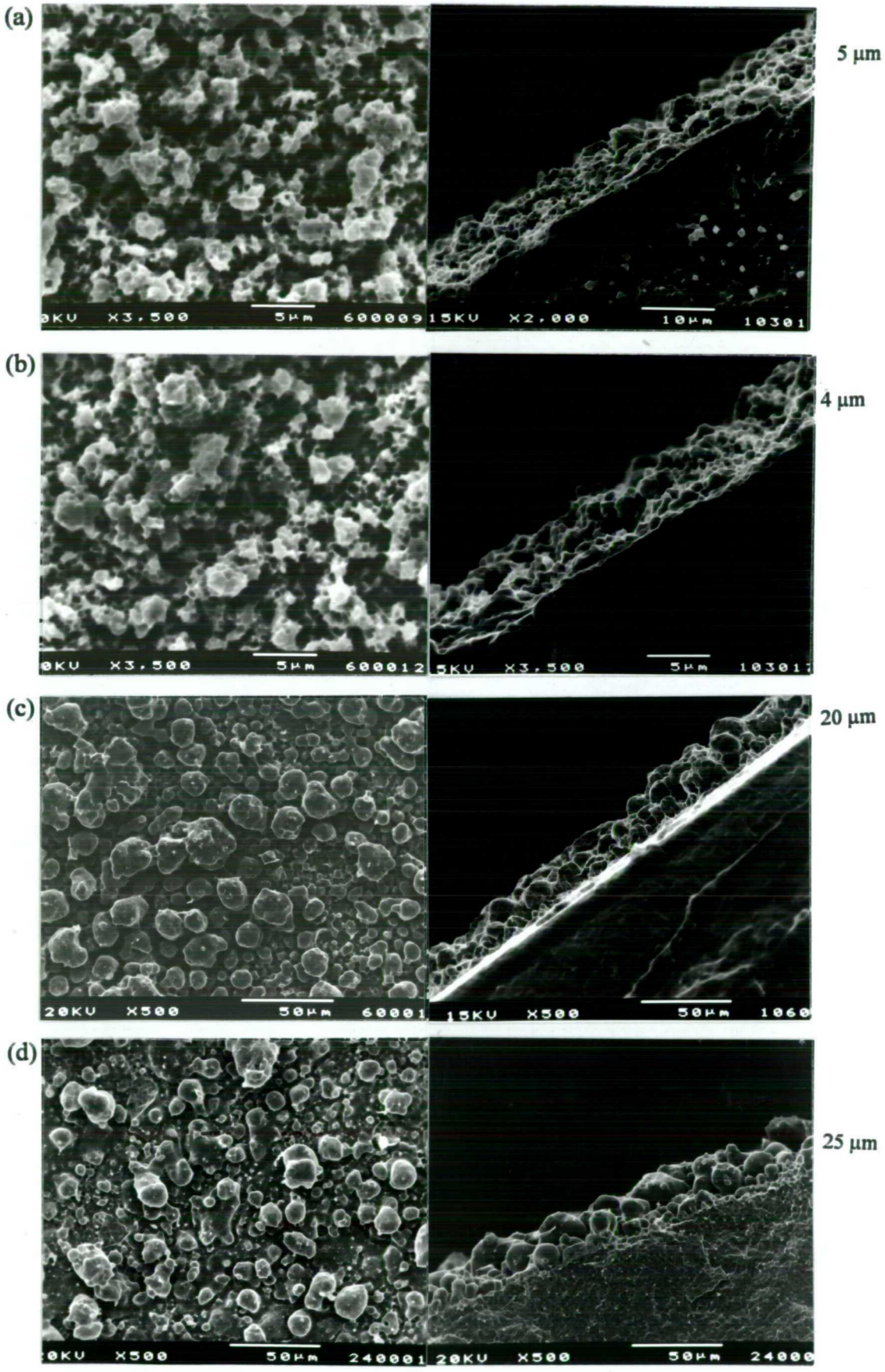


Fig. 4.2 : Surface morphology and cross-sectioned films deposited at various ratios of ethanol to water ; (a) 80/20, (b) 75/25, (c) 70/30, and (d) 60/40.

Fig 4.2 (a)-(d) shows clearly the surface morphology and the cross-section of as-deposited films produced using various ethanol/water ratio 80/20, 75/25, 70/30, and 60/40 respectively. The 80/20 film is very powdery and the film can be removed easily. However, the powder produced is very fine of size, ~1 micron. The film from 75/25 ratio also has fine particle size of ~1 micron, but they are packed together better than the film produced by 80/20 ratio. This creates a porous film of fine particles with some pores. When the ratio is reduced to 70/30, the film produced has uniform porosity, with larger size of particles of around 10-20 microns. This film adheres to the substrate better than 80/20 and 70/30 ratios. At very low ethanol/water ratio of 60/40, the film deposited is nearly fully dense. However, large individual particles are still visible (~10-20 microns). The deposition rate is fairly high of around 1-2 microns per minute.

The effect from the thermal environments has been reported by Wiedmann et al. [182] and Viguie et al. [183] to show the similar phenomena from the shape of a combustion zone. They are summarised in Fig. 4.3. At high ethanol ratio, the range of deposition temperature is high since ethanol acts as a fuel for combustion. Comparing the same distance between the spray nozzle and the substrate, the combustion range of the high ethanol/water ratio deposition is over a longer distance as in *Shape C*. By the time all the combusting species reach the substrate, the temperature is high, since the combustion process still continues. The difference of temperatures in the combustion and the substrate is fairly low. Since the ratio of ethanol/water is high, the fuel is rich, most of species combust and react readily before reaching the substrate; as a result, the deposited particles have very fine sizes. At high substrate temperature, all the chemical reaction takes place in the gas phase, this process is called homogeneous gas phase nucleation.

When the ratio of ethanol/water is low enough to yield the combustion zone of *Shape B*, the deposition temperature is lowered. This also corresponds to the lower substrate temperature where the heterogeneous reaction occurs at the vicinity of the substrate resulting in a dense film.

In case the ratio of ethanol/water is in between the ratios mentioned above, the combustion due to ethanol occurs at a much shorter length of distance, between *Shape B* and *Shape C*. The maximum temperature in the combustion zone is approximately the same as that of the high ethanol ratio, which is around 1000°C, where the maximum temperature at the tip of the flame torch is around 1200°C. However, the heat convected/radiated to the substrate, is lower, since the distance between the combustion range and the substrate is higher than at the high ethanol/water ratio. The combustion is not complete within the combustion zone, therefore some aerosol droplets agglomerate and deposit as a porous film. During the deposition, particles grow and form a more densely packed film as the ratio of ethanol/water is reduced.

The combustion zone of *Shape A* only occurs when the ratio of ethanol/water is very low that the fuel is not sufficient to combust all the droplets. The droplets then splash on the heated substrate. The solvent evaporates and leaves a dry precipitate, producing a flaky, amorphous film as the decomposition is not complete. The deposition temperature is very close to the temperature at the hot plate.

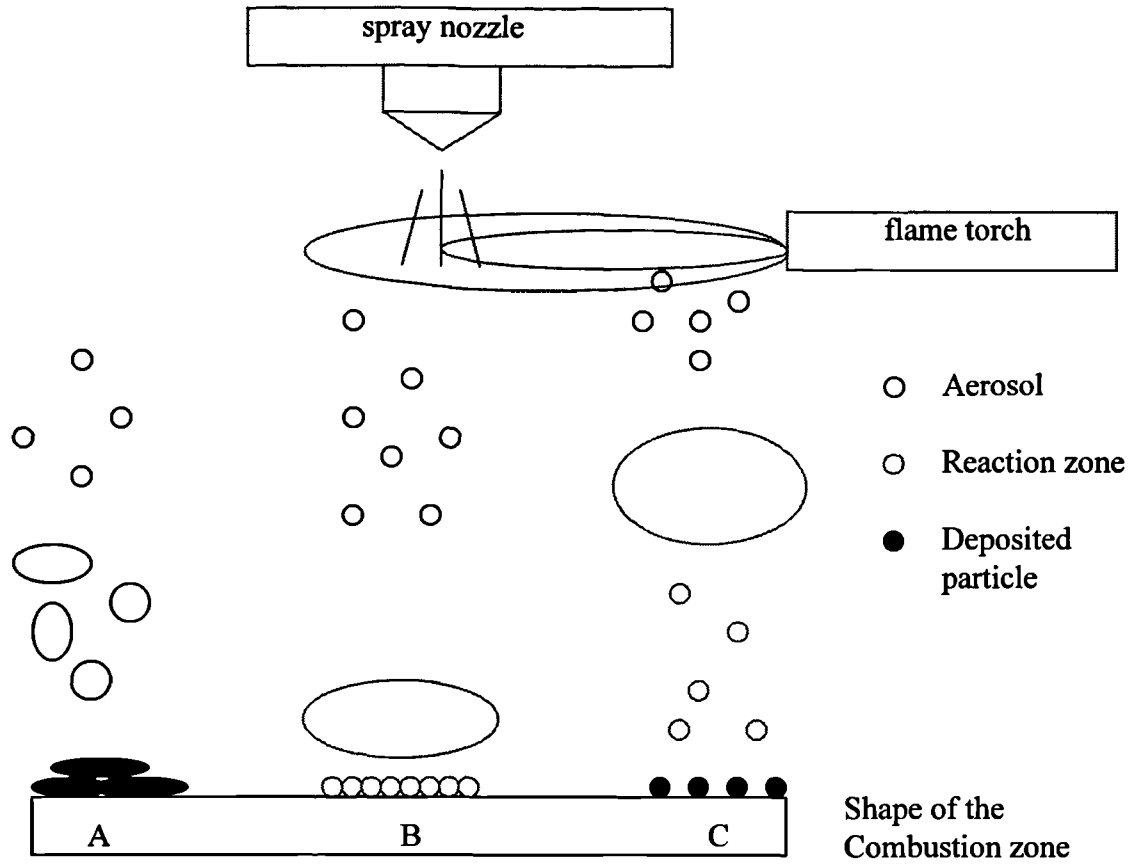


Fig. 4.3 : A sketch of the relationship between the combustion zone and the deposition process.

The same precursor solutions as those used previously, were delivered at a flow rate of 10 ml/min. All other parameters were kept constant as outlined in Table 4.1. Table 4.3 gives a summary of the results.

Table 4.3 : Deposition of $La_{0.82}Sr_{0.18}MnO_3$ at various ethanol/water ratios at the flow rate of 10 ml/min.

Ratio of ethanol/water	Deposition temperature (°C)	Comments
80/20	680-720	Powdery
75/25	670-700	Porous film of fine particles (1-2 μm)
70/30	480-540	Densely packed big particles (10-20 μm)
50/50	300-350	Dense but flaky film

This set of results, shows the same trend as those mentioned above. However, the deposition temperatures are lowered as the overall amount of fuel and aqueous solution are reduced. It is obvious from Fig. 4.4 (a) that the particles are finer than those in Fig. 4.2 (a), i.e. < 1 μm, due to lower flow rate but follows the same trend of the combustion zone of *Shape C*. Fig. 4.4 (b) also shows a lower degree of agglomeration in the microstructure, than in Fig. 4.2 (b). The film in Fig. 4.4 (c) is more densely packed than that in Fig. 4.2 (c), although the sizes of particles are similar. This is because the deposition temperature was brought down nearly 150°C and the deposition process has become the heterogeneous reaction or the combustion zone of *Shape B*. For the low ethanol/water ratio, Fig. 4.4 (d), a flaky film was obtained as the amount of ethanol in the solution was not sufficient and the aerosol then splashed on the substrate, followed the combustion zone of *Shape A*. The difference between the combustion temperature and the substrate temperature was slightly greater than 500°C so that as soon as the film was deposited on the substrate, cracks due to thermal shock formed.

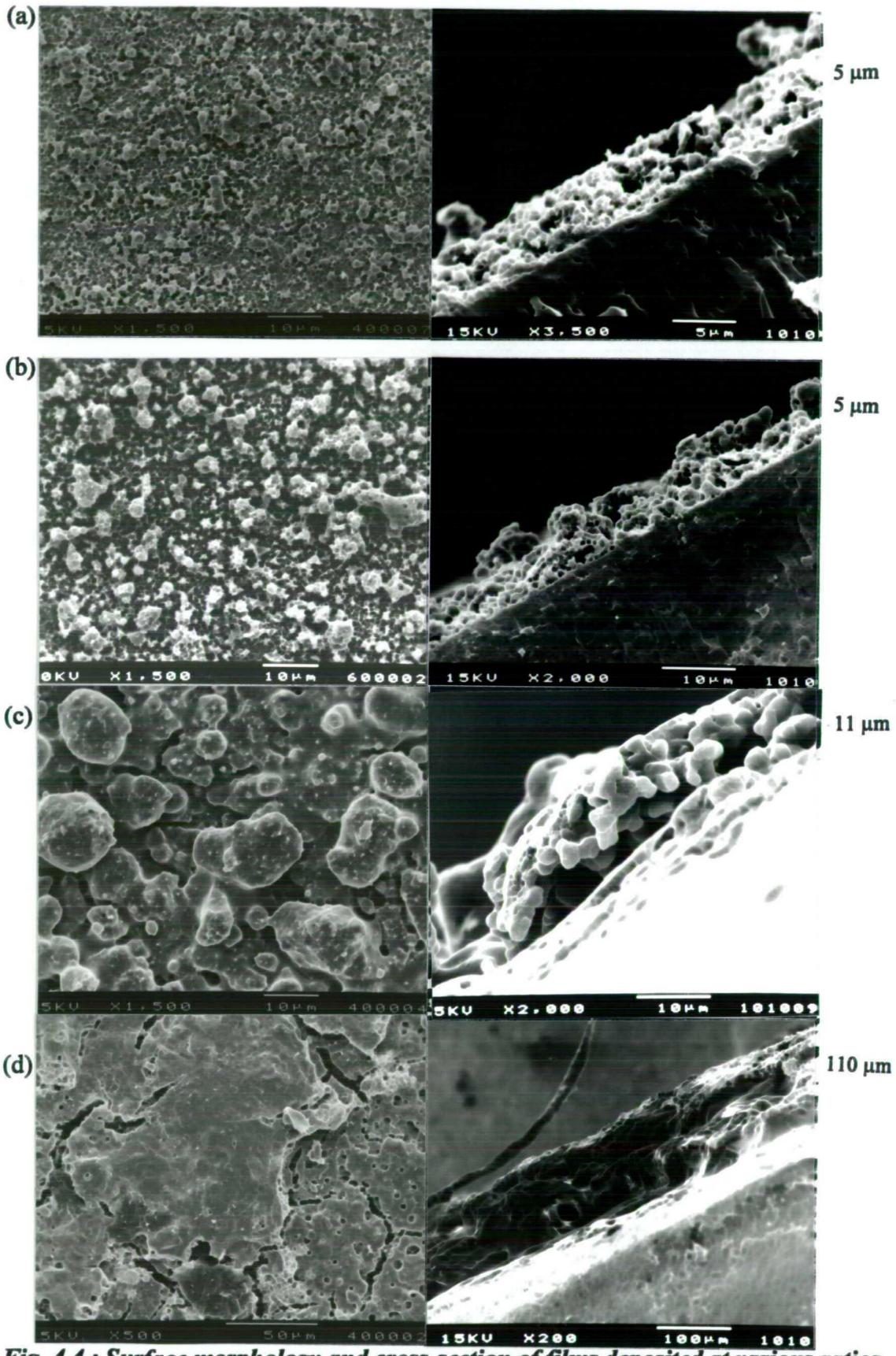


Fig. 4.4 : Surface morphology and cross-section of films deposited at various ratios of ethanol to water ; (a) 80/20, (b) 75/25, (c) 70/30, and (d) 50/50. The flow rate of the precursor solution was 10 ml/min.

4.1.1 CRYSTAL STRUCTURE

Films deposited at various deposition temperatures as discussed above were examined using X-ray diffractometer to identify phases present. The LSM peaks detected refer to the phase of $La_{0.8}Sr_{0.2}MnO_3$ from the standard powder diffraction file [184] (for details see the appendix). Table 4.13 shows a summary of the results.

Table 4.4 : Phases identification of films deposited at various temperatures.

Deposition temperature (°C)	Phases and comments
680-710	sharp crystalline peaks of LSM
650-690	sharp crystalline peaks of LSM
480-530	a few peaks of LSM on broad haloes
300-350	no peaks

Each peak indicates the d-spacing of a specific plane in the crystal structure. In a polycrystalline structure, peaks from various planes are detected, since grains are randomly oriented. For an amorphous structure, a diffuse background is present since there is no specific orientation or crystal structures. Phases present in these films are dependent on the deposition temperature. Crystalline peaks were only present at high deposition temperature, while an amorphous film was obtained at very low deposition temperatures (< 350°C). For deposition between 480°C-530°C, there are only few peaks indicating that the LSM phase are present. However, these are present on broad haloes, which specifies that the film is not fully crystalline. Fig. 4.5 compares the above XRD patterns from high deposition temperature and low deposition temperature.

It is important to note that peaks from the YSZ substrate are detected when the films are not very thick and quite porous or powdery.

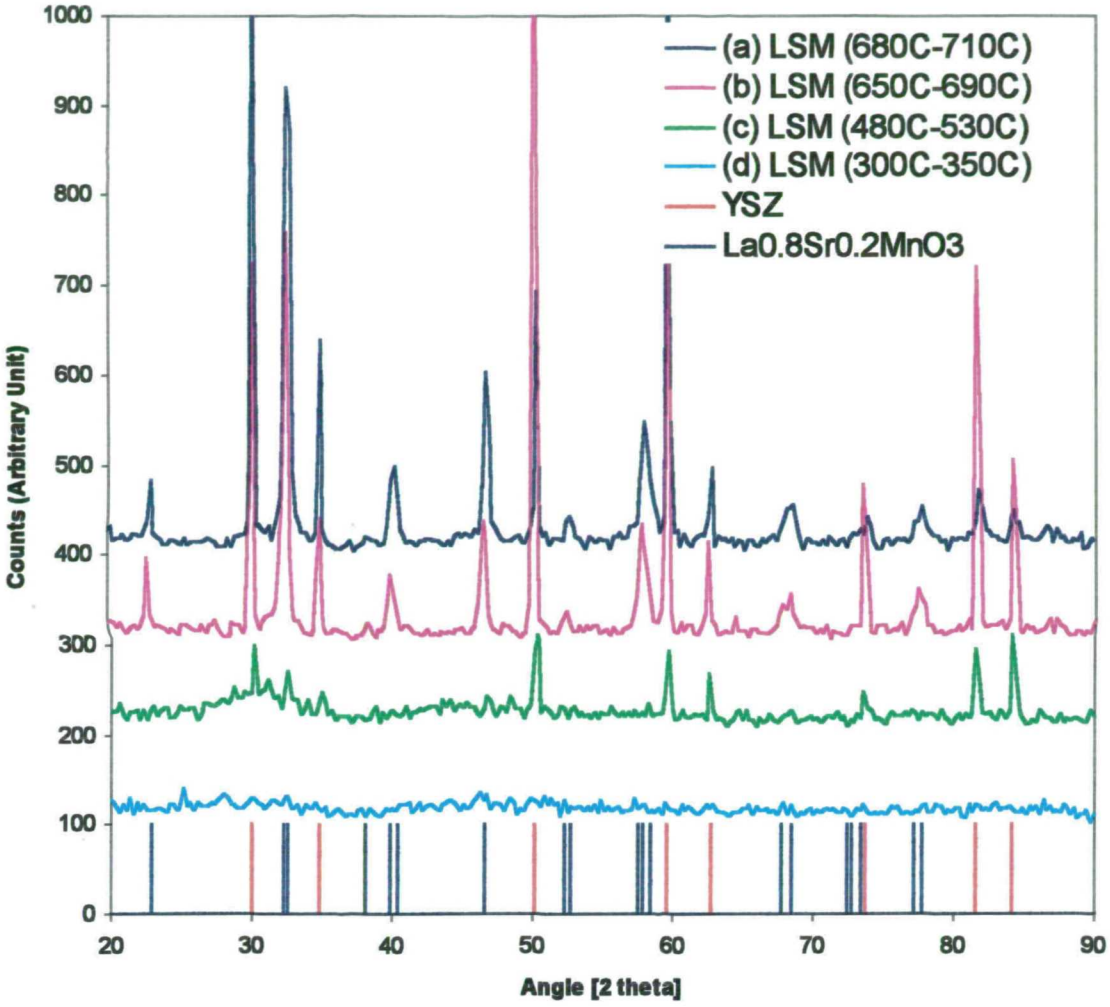


Fig. 4.5 : XRD patterns of LSM films deposited at (a) 680°C-710°C, (b) 650°C-690°C, (c) 480°C-530°C, and (d) 300°C-350°C.

4.2 FLOW RATE OF PRECURSOR SOLUTION

The effect of flow rate of the precursor solution on the deposition of LSM was investigated using two sets of experiments. Two A-site deficient LSMs used in this investigation as they are more stable in contact with YSZ as discussed in Chapter 2. $La_{0.61}Sr_{0.18}MnO_3$ and $(La_{0.82}Sr_{0.18})_{0.9}MnO_3$ were designated as LSM0.61 and LSM0.9 respectively. Investigations on the flow rate, were carried out using two ratios of ethanol/water, 80/20 and 70/30.

4.2.1 $La_{0.61}Sr_{0.18}MnO_3$

In this set of experiments, a wide range of flow rates was investigated. All three experiments were carried out at a fixed deposition temperature (700°C-800°C) by varying the position of the flame torch. Other parameters were kept constant (section 4.1). The ratio of ethanol/water used was 80/20. A summary of the results is listed in Table 4.5 below.

Table 4.5 : Results of LSM0.61 films deposited at various flow rates.

Flow rate (ml/min)	Comments
5.5	Powdery of fine particles
10	Uniform porous film with agglomeration
17	Nearly dense film with cracks

The morphology and cross-section of these films are shown in Fig. 4.6 (a)-(c). At a low flow rate, the film tends to be more powdery, and at higher flow rate, films are more densely packed. The reason is as discussed earlier in section 4.1. At the low flow rate (5.5 ml/min), the combustion and decomposition reactions were completed in the gas phase, therefore, the deposited film was powdery (the combustion zone of *Shape C*). At the high flow rate (17 ml/min), the reactions

mentioned earlier have not been completed at the time the droplets reached the substrate but reacting at the vicinity of the substrate, resulting in a relatively dense film (the combustion zone of *Shape B*). Nevertheless, some cracks were present in the dense film due to a thermal stress on a thin dense film, which is not as tolerant as a thin porous film.

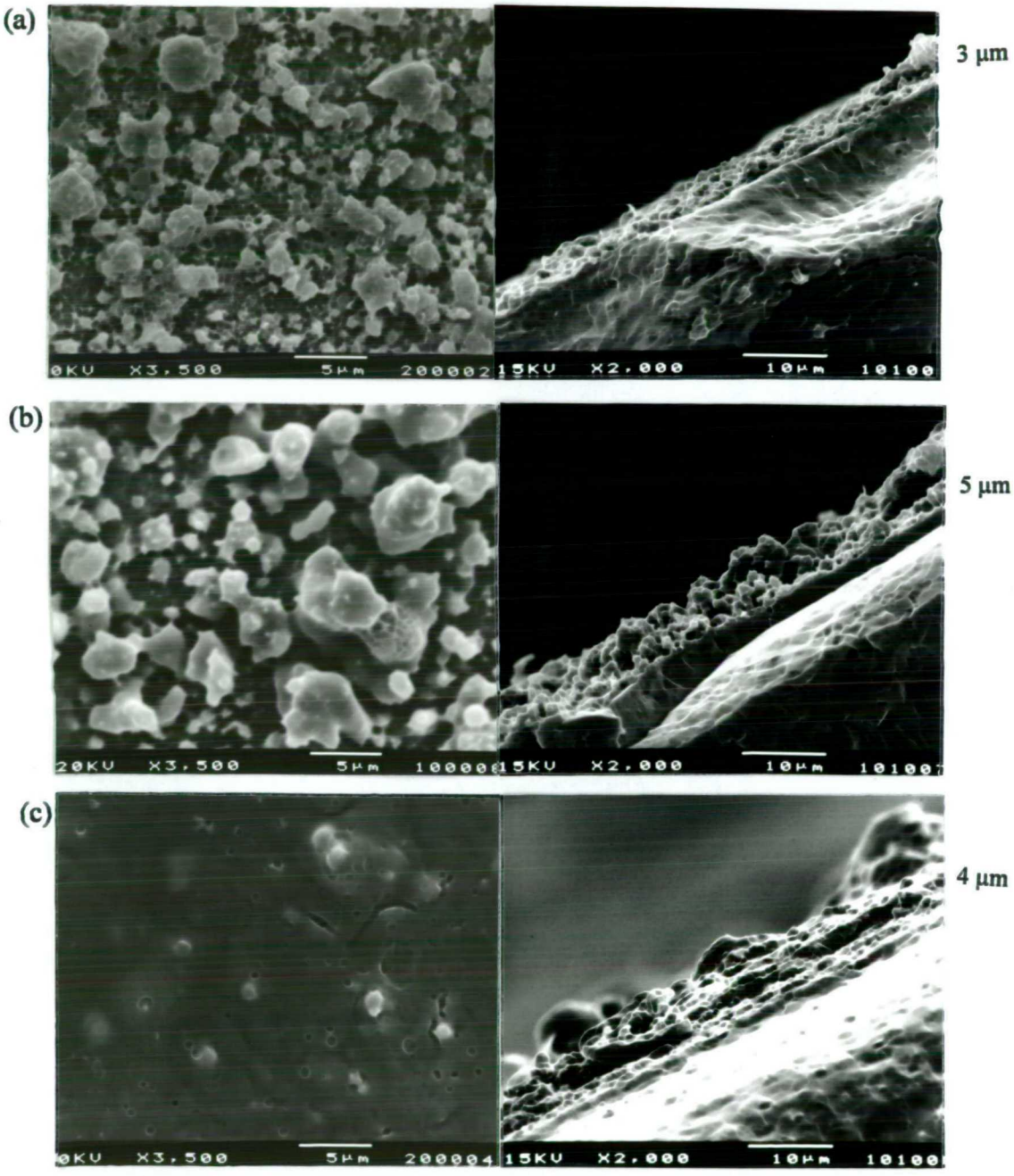


Fig. 4.6 : Surface morphology and cross-sectioned of LSM0.61 films deposited at a) 5.5 ml/min, b) 10 ml/min, and c) 17 ml/min.

4.2.2 CRYSTAL STRUCTURE

When the flow rate varies in a wide range as in section 4.2.1, the XRD patterns are different although the deposition temperature is controlled in the same range from 700°C-800°C. The major difference is the substrate peaks. As the film produced from the high flow rate (17 ml/min) deposition is much denser and thicker, than the film produced at the low flow rate (5.5 ml/min), which is a thin powdery layer. As a result, the substrate peaks are more easily detected and the film is more crystalline than the film deposited at the high flow rate. The LSM peaks are very similar in the shapes and degree of crystallinity. Both patterns are compared in Fig. 4.7. At the low flow rate (5.5 ml/min), traces of $La_2Zr_2O_7$ are detected in addition to LSM peaks.

$La_2Zr_2O_7$ is not desirable in the application of an SOFC cathode. However, it is commonly detected for low dopant concentration as manganese diffuses to YSZ and the remaining lanthanum reacts with YSZ. This acts as an insulating layer and creates thermal stresses at the interface [7]. $La_2Zr_2O_7$ has poor electrical conductivity and the coefficient of thermal expansion is not compatible with that of YSZ [111,115,185].

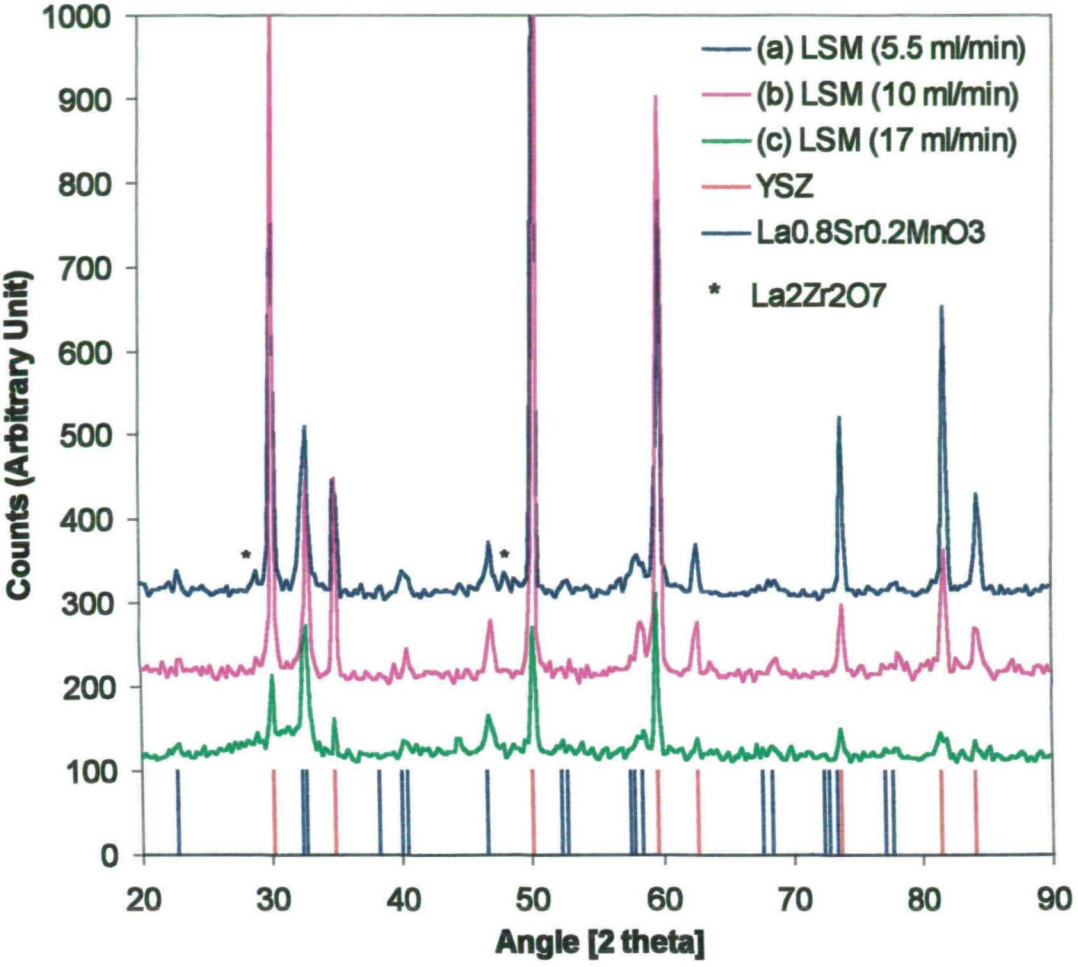


Fig. 4.7 : XRD patterns of LSM films deposited in section 4.2.1 at flow rate (a) 5.5 ml/min, (b) 10 ml/min, and (c) 17 ml/min.

4.2.3 $(La_{0.82}Sr_{0.18})_{0.9}MnO_3$

From the wide range of flow rate examined in section 4.2.1, a smaller range of flow rate is indicated if a porous film is desirable in additional to the desirable crystal structure studied from section 4.2.2. The flow rate of the precursor solution in this section was varied from 10 ml/min. to 15 ml/min using two ratios of ethanol/water; 80/20 and 70/30. Other parameters are kept constant as detailed in section 4.1. The results are summarised in Table 4.6.

Table 4.6 : Results of LSM0.9 films deposited at various flow rates.

Ratio of ethanol/water	Flow rate (ml/min)	Deposition temperature (°C)	Comments
80/20	10	700-750	Powdery with very fine particles (< 1 μm)
80/20	12	850-900	Powdery film
80/20	15	870-920	Porous film with agglomeration (2-5 μm)
70/30	10	700-730	Porous film with agglomeration and powdery (5-10 μm)
70/30	12	700-750	Porous film with agglomeration and powdery (1-5 μm)
70/30	15	740-800	Porous film with agglomeration and powdery (5 μm)

As the flow rates increased, the deposition temperatures increased. For the 80/20 ratio, films were powdery when deposited at relatively low flow rate. At higher flow rate, particles tended to agglomerate, and form a good adhesion film with a porous microstructure (Fig. 4.8 (c)). In the case of 70/30 ethanol/water ratio solution, the effect of flow rate is not as obvious as the 80/20 ratio. Nevertheless, the more desirable uniform porous structure, is obtained when the flow rate is high (15 ml/min), instead of some particle agglomeration at low flow rate (10 ml/min). In addition, at the flow rate of 15 ml/min, the deposited film is less powdery than those deposited at 10 and 12 ml/min.

All the films obtained in this section, the deposition process corresponds to the combination of the combustion zones of *Shape B* and *C* is dominant. At low flow rate, amount of aerosol containing LSM ionic species per unit area is lower when considered in 2 dimensions. When the droplets reach the substrate and react, the deposited film incorporates more dispersed particles per unit area than in the high flow rate solution, where the droplets are closer together, resulting in a film of packed particles. Furthermore, the deposition temperature depends on the amount of ethanol in the solution. At high flow rates, the amount of ethanol in solution per unit volume is greater than at low flow rate, therefore, the deposition temperature is higher. From this reason, the microstructure patterns should follow those in the previous sections. Although, these two processes are counteracting, the effect due to the amount of vapour species in a unit area is much more dominant in this set of investigation judging from the morphology of deposited films.

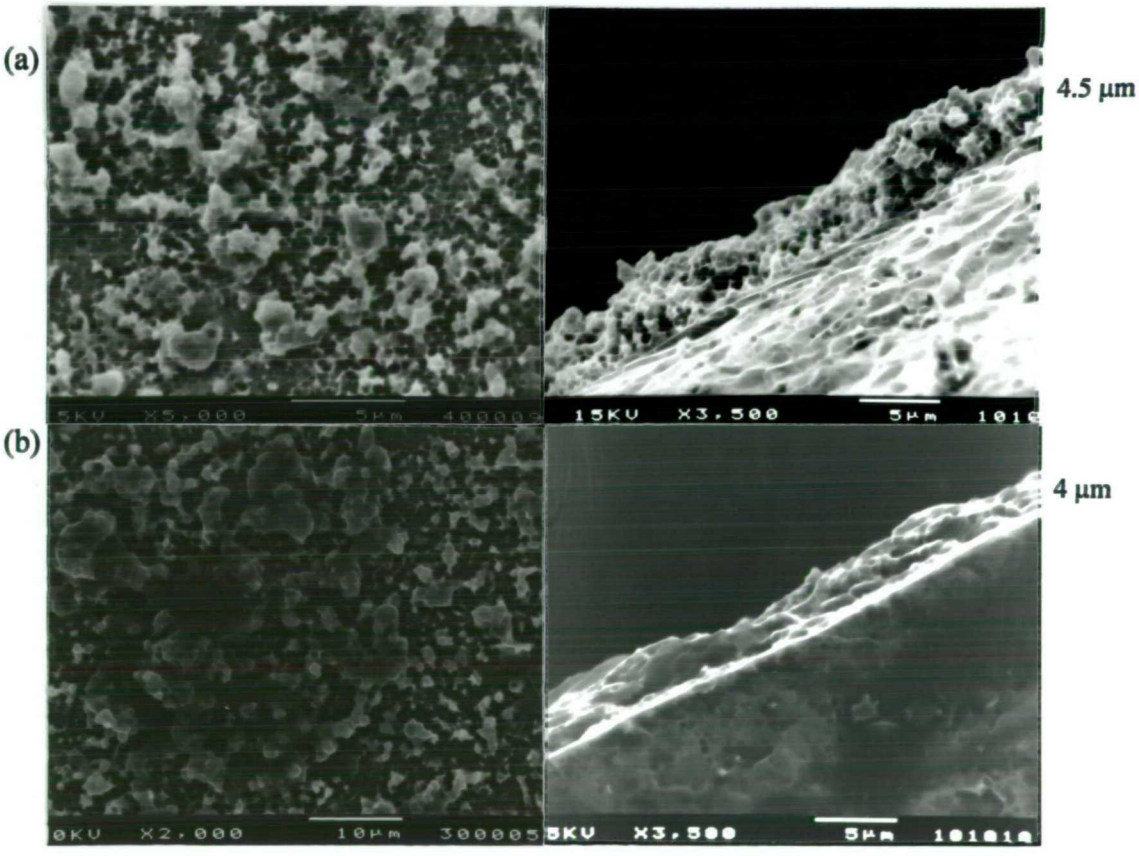


Fig. 4.8 : Surface morphology and cross-sectioned LSM0.9 films deposited using 80/20 ethanol/water ratio at (a) 10, (b) 12 ml/min (cont.).

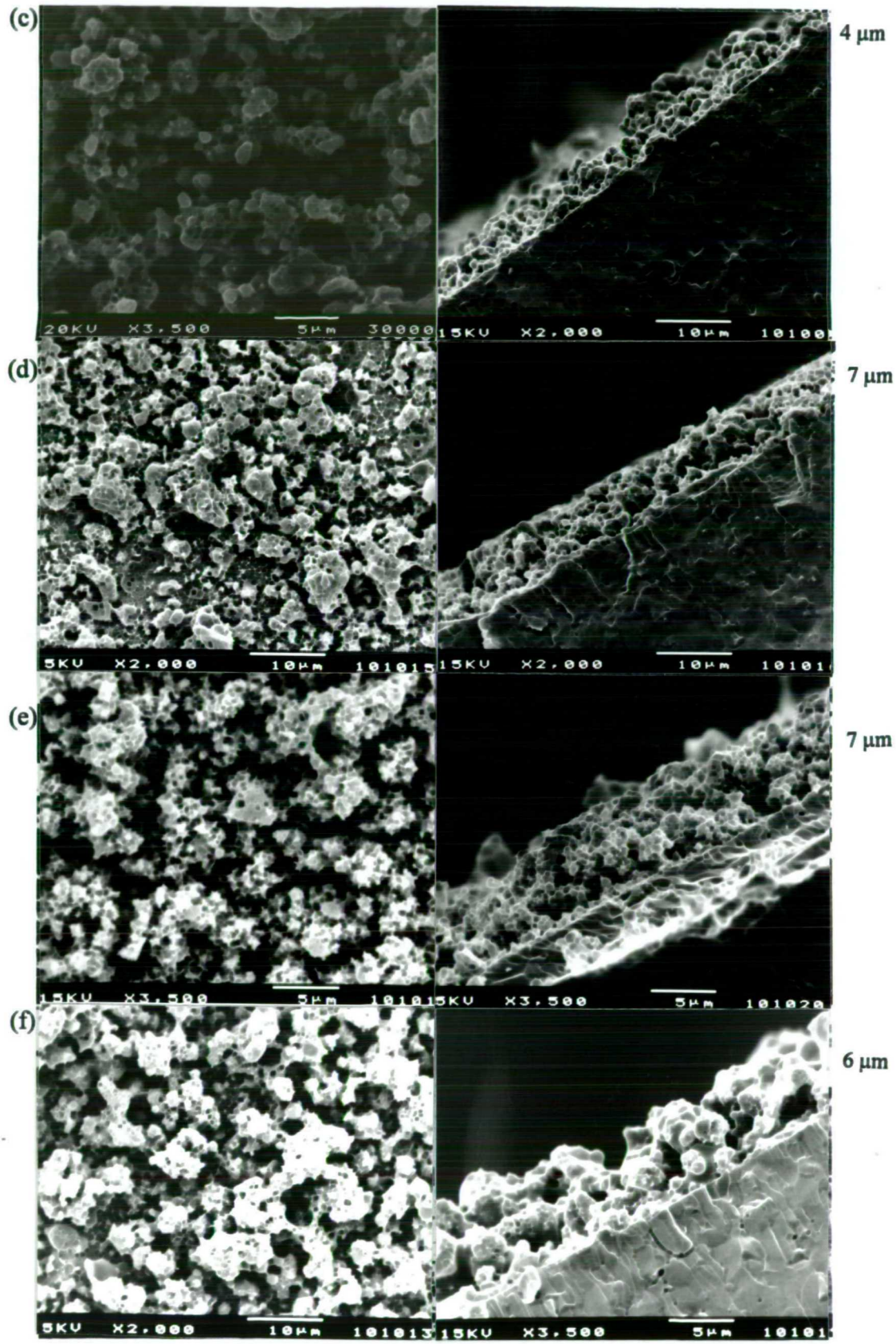


Fig. 4.8 : Surface morphology and cross-sectioned LSM0.9 films deposited using 80/20 ethanol/water ratio at, (c) 15 ml/min, and 70/30 ethanol/water ratio at (d) 10, (e) 12 , and (f) 15 ml/min.

4.2.4 CRYSTAL STRUCTURE

The XRD patterns of films deposited in section 4.2.3, where the flow rate varies from 10-15 ml/min and the deposition temperature varies from 700°C-920°C, are very similar. A typical XRD pattern is shown in Fig. 4.9. All of them show characteristic LSM peaks. This may lead to a conclusion that at relatively high deposition temperatures, the deposited LSM films are crystalline and the slight variation of the flow rate does not affect the crystal structure of deposited films.

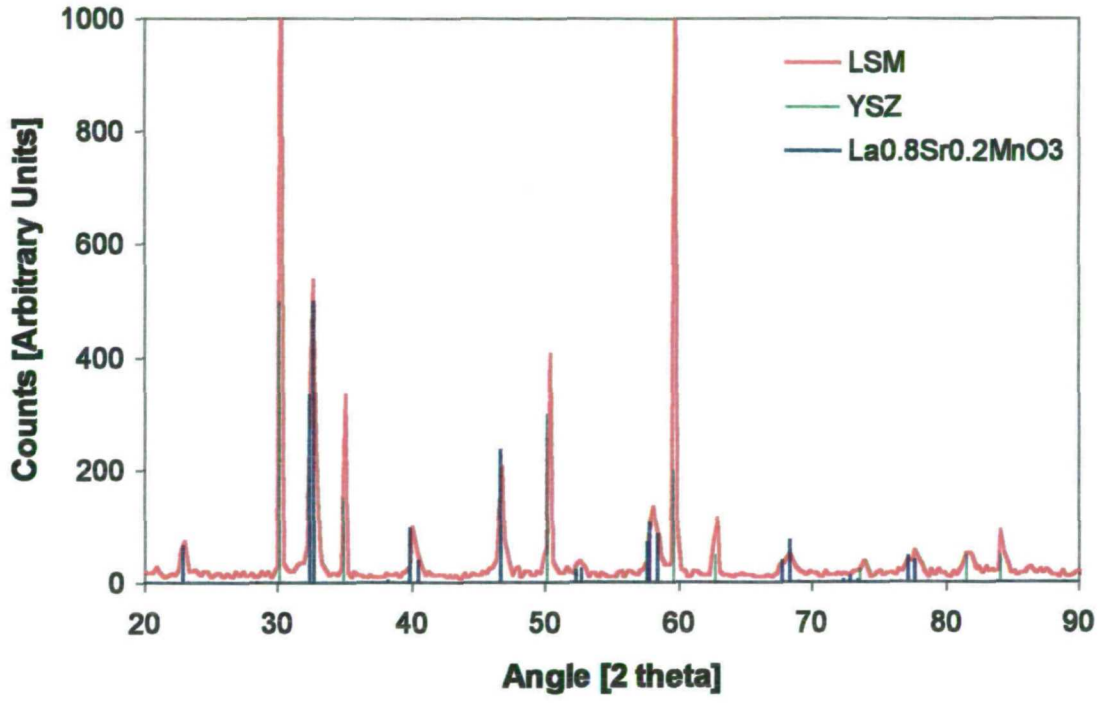


Fig. 4.9 : A typical XRD pattern of LSM film deposited in section 4.2.3.

4.3 PRESSURE OF THE COMPRESSED AIR

The pressure of the compressed air which was used to atomise the precursor solution was varied. The system can only operate efficiently within a narrow pressure range, 17-30 psi. The precursor solution used was for the deposition of $La_{0.82}Sr_{0.18}MnO_3$. The controlled process parameters are listed in Table 4.7.

Table 4.7 : Controlled parameters for the investigation of the pressure of the compressed air.

Concentration of the precursor solution	0.05 Molar
Ratio of ethanol/water	70/30
Distance between the spray nozzle and the substrate	12 cm
Flow rate of the precursor solution	12 ml/min.

Results of each film deposited at various pressures are summarised in Table 4.8. This includes results identified from X-ray diffraction patterns of the as deposited films.

Table 4.8 : Results of $La_{0.82}Sr_{0.18}MnO_3$ films deposited at various pressures.

Pressure (psi)	Deposition temperature (°C)	Comments
17	720-770	Quite powdery with fine particles
22	680-730	Uniform porous
26	450-500	Packed particles

Fig 4.10 (a)-(c) shows large variations in the microstructure, due to the changes of compressed air pressures. At low pressure, the film was powdery of fine

particle sizes, smaller than 2 microns. When pressure was increased, the film was more densely packed with larger particle sizes of up to 20 microns. For the film deposited using 26 psi compressed air, the LSM film was not electrically conducting. However, after annealing at 900°C for 2 hours, it became an electrical conductor. The electrical conductivities are discussed in the next chapter.

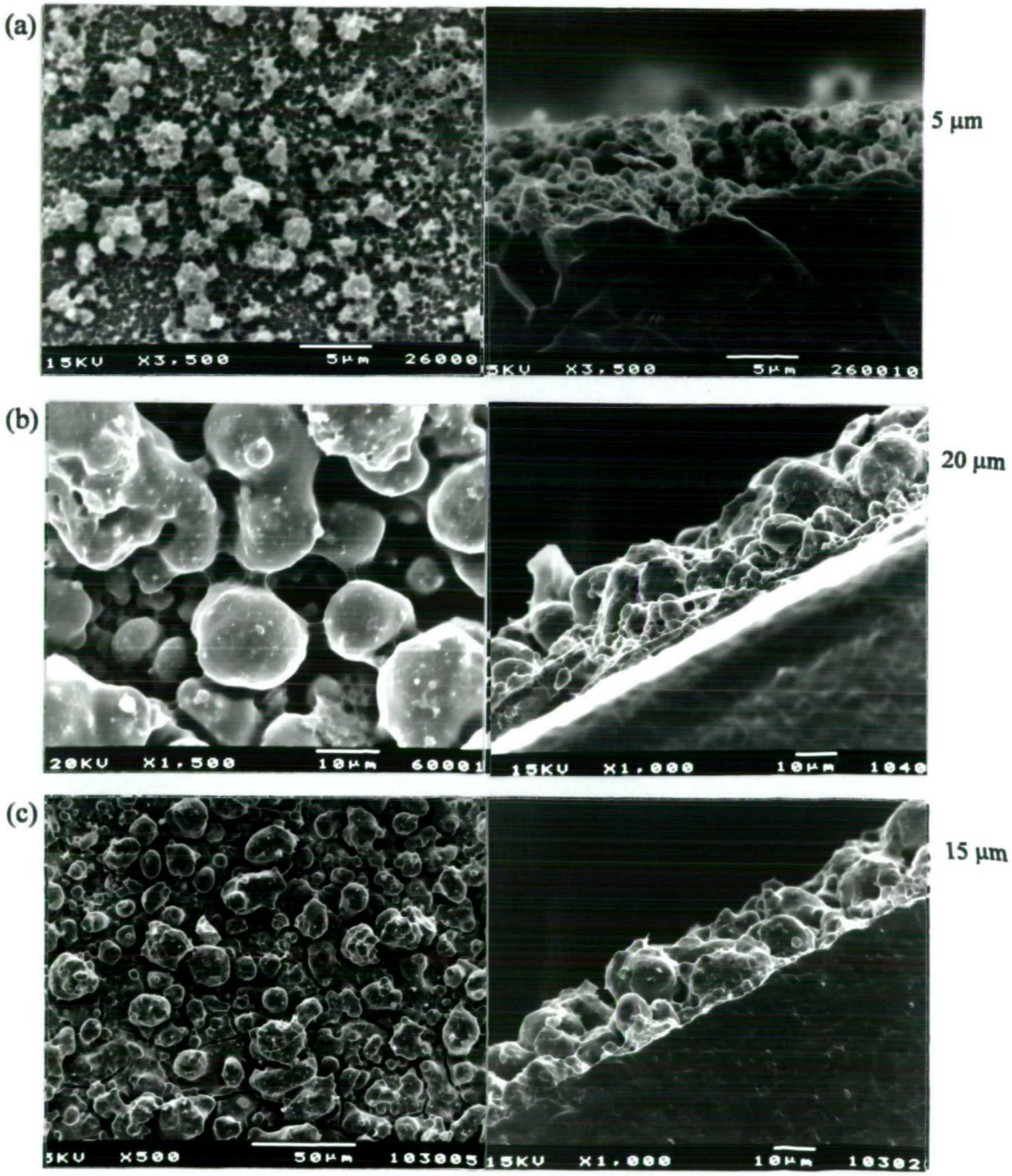


Fig. 4.10 : Surface morphology and cross-sectioned of $La_{0.82}Sr_{0.18}MnO_3$ films deposited at (a) 15 psi, (b) 22 psi, and (c) 26 psi.

The total mass flow, is the sum of the precursor solution and the compressed air. When the compressed air pressure is lowered, the amount of compressed air is also lowered, but it raises the ratio of the precursor solution to the total mass flow. As a result, the deposition temperature is increased, but increasing the compressed air pressure lowers the deposition temperature dramatically. Moreover, the compressed air was at room temperature, therefore, it was acting as a stream of cool air and hence lowered the deposition temperature. The effect of deposition temperatures on the microstructures of the films is similar to the effect of ethanol/water ratio in the precursor solution. Fig. 4.11 shows the sketch of deposition processes at various compressed air pressures. At low air pressure, the deposition process is similar to the combustion zone of *Shape C* and at high air pressure, it is similar to the combination of combustion zone of *Shapes B* and *C*.

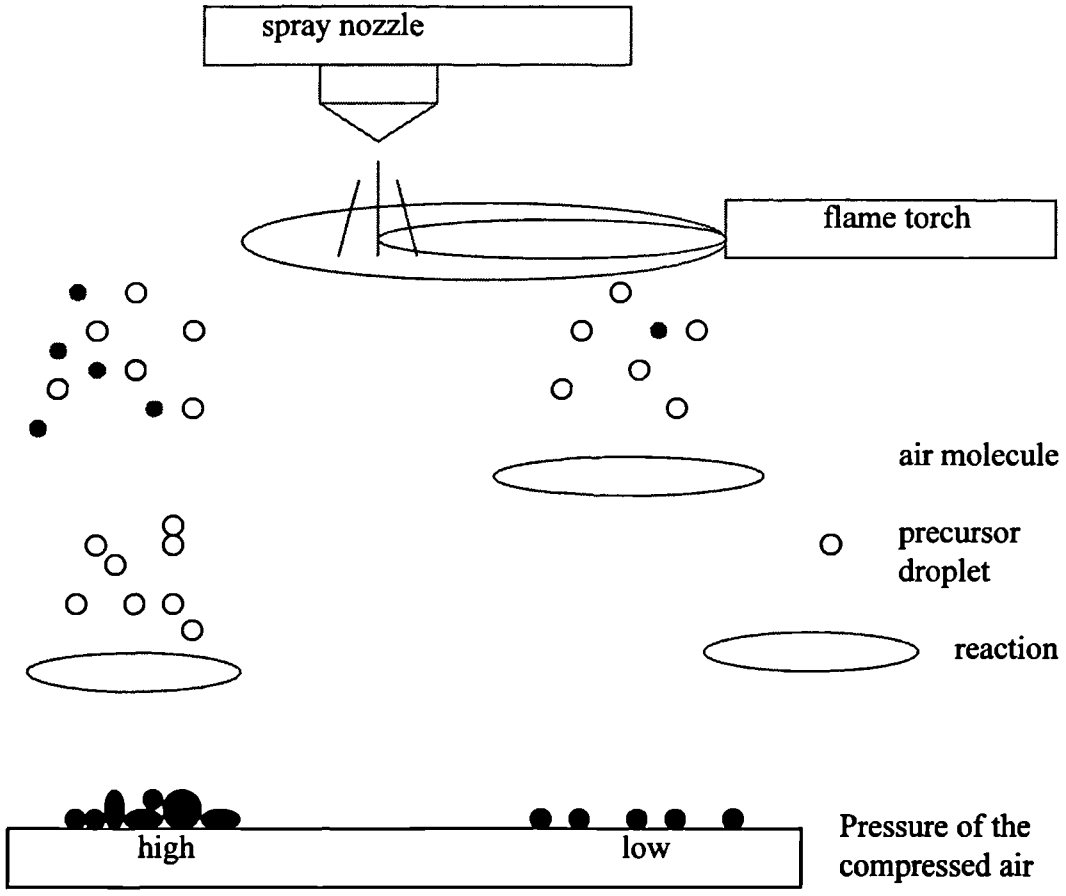


Fig. 4.11 : A sketch of deposition processes at various compressed air pressures.

4.3.1 CRYSTAL STRUCTURE

When the pressure of compressed air was altered, the deposition temperature varied and so did the microstructure. The crystallinity of films was seen to be similar from the XRD patterns in Fig. 4.12. The substrate peaks from the deposition at 17 psi were more obvious, due to the film being a thin powdery layer. The LSM film deposited at 26 psi was not electrically conducting as it was showing amorphous noise background. After annealing at 900°C for 2 hours, this film was more crystalline. The film deposited at 17 psi shows traces of $La_2Zr_2O_7$ phase. This reaction product is undesirable for the SOFC cathode as discussed earlier.

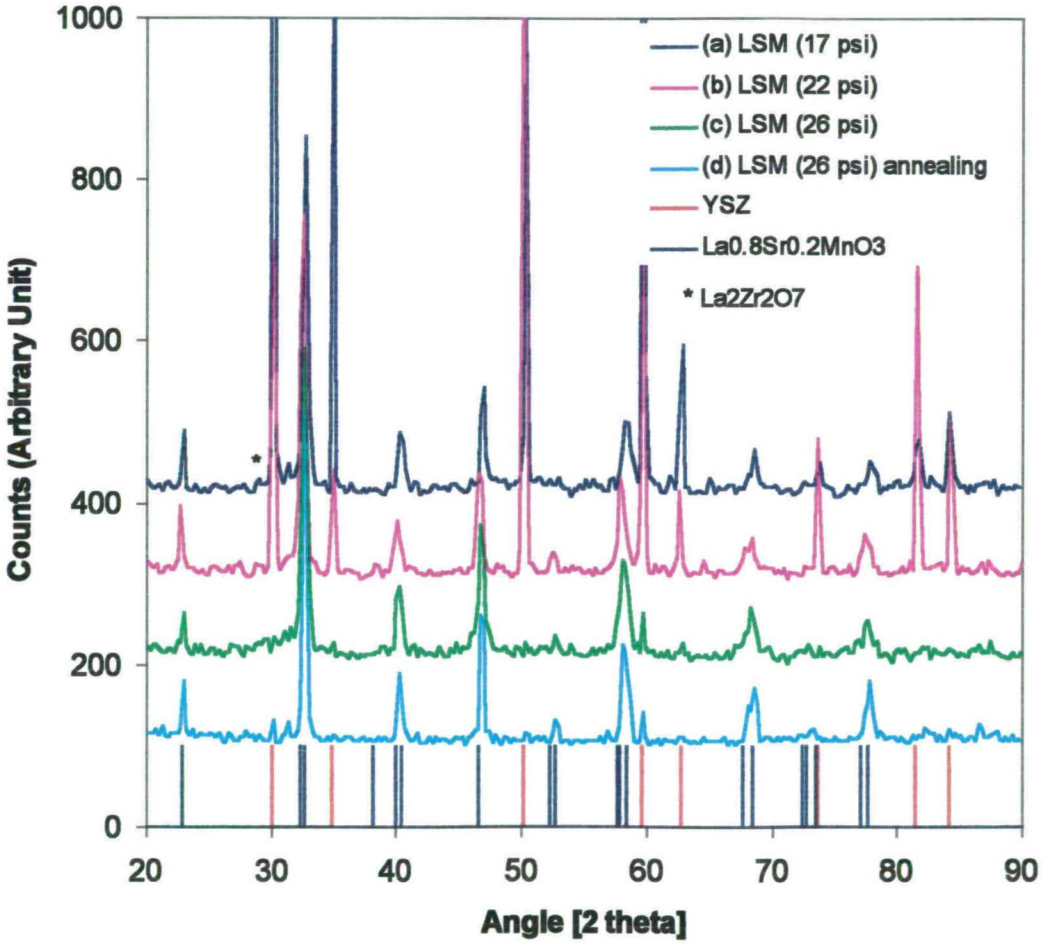


Fig. 4.12 : XRD patterns of LSM films deposited at (a) 17 psi, (b) 22 psi, (c) 26 psi, and (d) 26 psi after annealing.

4.4 DISTANCE BETWEEN THE SPRAY NOZZLE AND THE SUBSTRATE

The aim of these experiments was to deposit two different compositions of LSM over a wide range and a short range of distances between spray nozzle and substrate, *d*. They are $La_{0.61}Sr_{0.18}MnO_3$ and $La_{0.82}Sr_{0.18}MnO_3$, designated LSM0.61 and LSM, respectively. Other controlled process parameters are listed in Table 4.9.

Table 4.9 : Controlled process parameters in the deposition of $La_{1-X}Sr_XMnO_3$ at various distances

Parameters	LSM0.61	LSM
Concentration of the precursor solution (Molar)	0.05	0.05
Pressure of the compressed air (psi)	22	22
Flow rate of the precursor solution (ml/min)	10	10 and 12
Ratio of ethanol/water of the precursor solution	80/20	75/25

4.4.1 $La_{0.61}Sr_{0.18}MnO_3$

Table 4.10 is a summary of the results of LSM0.61 films deposited at a wide range of distances.

Table 4.10 : Results of LSM0.61 films deposited in the investigation of the effect of d.

Distance *d* (cm)	Deposition temperature (°C)	Comments
8	500-830	Smooth film with fine pores and lots of cracks poor adhesion
12	700-800	Uniform porous with some agglomeration (1-5 μm)
16	560-730	Powdery with fine particles (1-2 μm)

The microstructure of the film deposited at a distance of 8 cm, shows a lot of cracks on a smooth film. The cracks are due to the large temperature fluctuation during deposition (Fig 4.13 (a)). On the smooth surface itself, some fine pores are visible due to the rapid cooling process. The adhesion between the film and the substrate was very poor. Fig 4.13 (b) shows the typical microstructure of a film with uniform porosity and some agglomeration, as explained earlier. When *d* was set at 16 cm, fine particles were deposited on the substrate. The sizes of particles were fairly uniform, ranging between 1-2 microns in diameter.

At the distance 8 cm, the substrate was very close to the combustion zone and as a result, the droplets were deposited as a dense film. This was because the combustion and decomposition reactions took place at or near the surface of the substrate. However, when the distance was too low, cracks were obvious from thermal shock effects due to the pulsations. When *d* was at 16 cm, the combustion

process was complete before reaching the substrate. The dominant reaction was the homogenous gas phase nucleation. Moreover, by the time the droplets reached the substrate, their momentum was reduced and then the particles did not pack, resulting as a powdery surface. The relationship between d and the deposition process in the combustion zone is shown in Fig. 4.14.

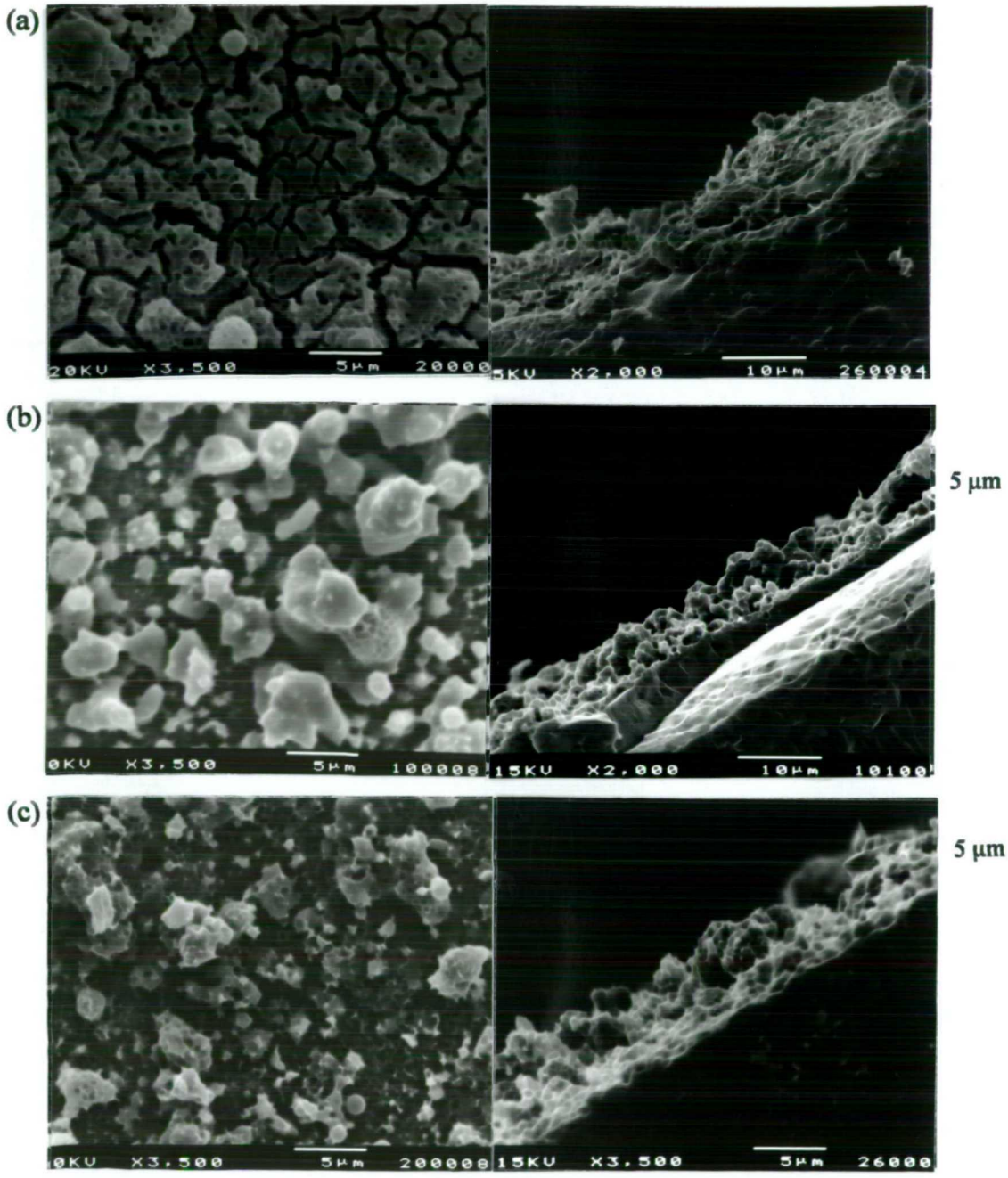


Fig. 4.13 : Surface morphology and cross-sectioned LSM0.61 films deposited at distance (a) 8 cm, (b) 12 cm, and (c) 16 cm between the spray nozzle and the substrate.

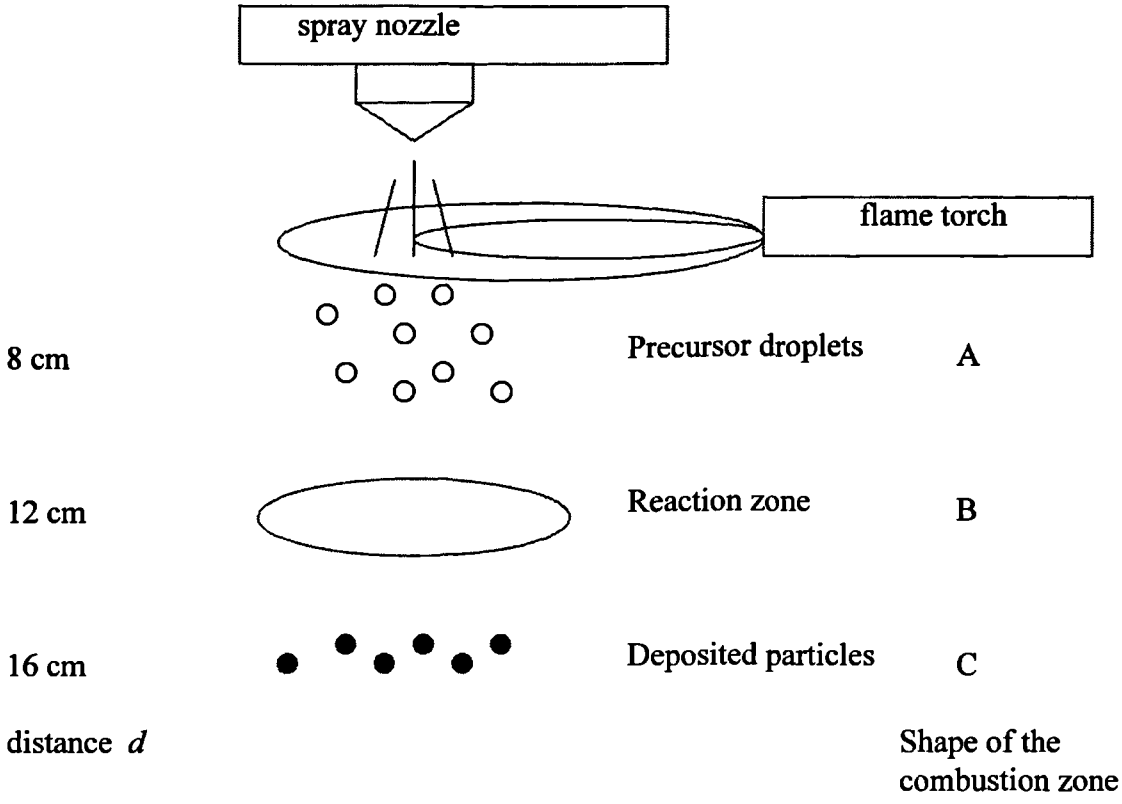


Fig. 4.14 : A sketch of the deposition process at various distances in the combustion zone.

From Table 4.10, it can be clearly seen that at 8 cm and 16 cm distances, the deposition temperatures were too difficult to control within a range of ± 50°C as in previous sections. It is important to remember that the combustion range is the same for both distances. However, due to the greater distance between spray nozzle and the substrate, amount of heat convected/radiated will be lower for the greater distance and vice versa. The combustion zone is fixed, since the flame torch was at a fixed distance from the spray nozzle. While other controlled parameters are kept constant throughout the investigations, the distance *d* is the only variable factor. A peristaltic pump was used to control the flow rate of a precursor solution, the solution was sprayed in regular pulses. Between any two pulsations, only compressed air was sprayed through the nozzle and there was no solution present. This resulted in temperature fluctuation during deposition. This problem from pulsations seems to be pronounced when the distance *d* is at the two extreme ends.

4.4.2 CRYSTAL STRUCTURE

Films from section 4.4.1 were analysed and $La_{0.8}Sr_{0.2}MnO_3$ phase was detected in all deposited film, however, traces of impurities were different. The XRD pattern of the film from distance 8 cm, shows an amorphous phase and LSM phase of low degree of crystallinity, while the pattern of longer distances shows more crystalline films. Peaks representing $La_2Zr_2O_7$ phase were detected in the pattern, for the distance 16 cm film. These two patterns are displayed in Fig. 4.15.

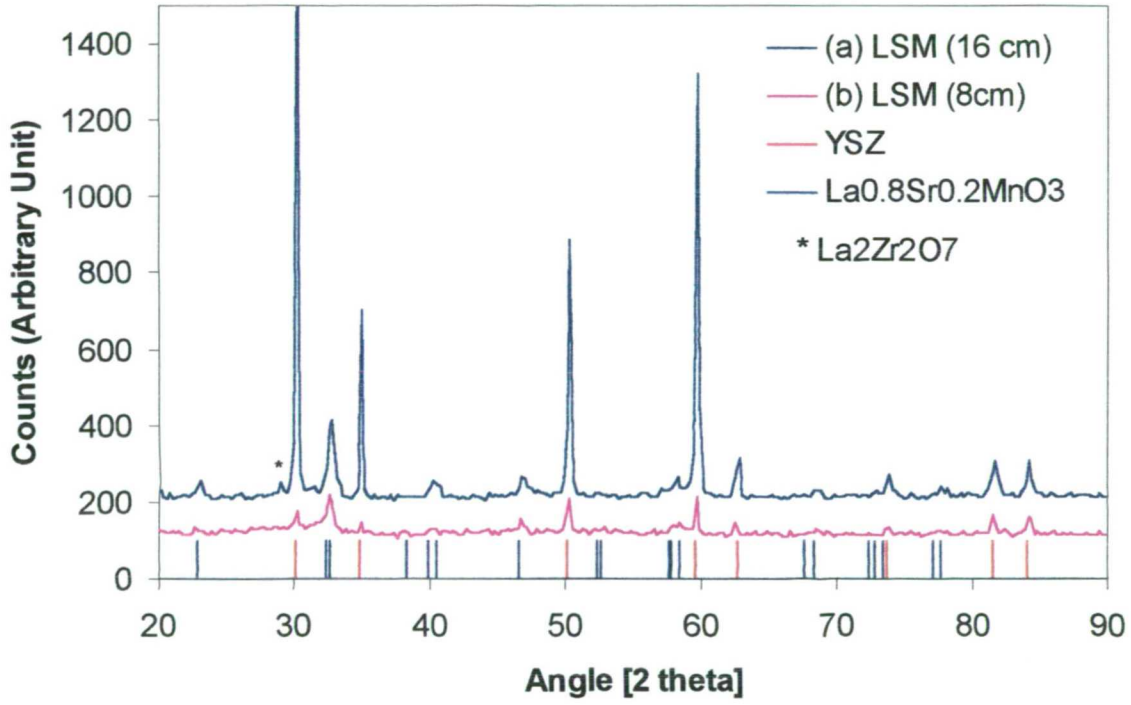


Fig. 4.15 : XRD patterns of films deposited at distance (a) 16 cm and (b) 8 cm between the spray nozzle and the substrate.

4.4.3 LSM

Results from the previous section have clearly shown that the optimum distance is around 12 cm. Further investigation was carried out for a more desirable ratio of ethanol/water at 75/25 judging from the results in previous investigations in section 4.1 and at shorter range of *d*. Two flow rates of precursor solution were selected for the comparison purpose. Table 4.11 is a summary of details and comments for this set of experiments.

Table 4.11 : Results of LSM films deposited in the investigation of the effect of d.

Distance (cm)	Flow rate (ml/min)	Deposition temperature (°C)	Comments
10	12	750-780	Uniform large particles porous film (5-10 μm)
12	12	700-800	Uniform porous film (~1 μm)
10	10	680-750	Porous fine particles film (< 1 μm)
12	10	670-730	Porous fine particles film (< 1 μm)

The film produced, at the flow rate of 12 ml/min and distance of 10 cm has a uniform porosity, where the sizes of particles are 5-10 microns (Fig. 4.16 (a)). When the distance is increased to 12 cm, sizes of particles were reduced to 1-2 microns, with some agglomeration and as a result, the film is more porous (Fig. 4.16 (b)). At a low flow rate, the microstructure of deposited films, are similar for both distances of 10 cm and 12 cm (Fig. 4.16 (c) and (d)). They are very porous and the sizes of particles are the same, <1 micron for particles and 1-5 microns for agglomerations.

For the low flow rate, *d* can also be used as an indication of the distance between combustion zone and substrate, since all other parameters are kept constant. The deposition temperature then follows the same pattern as discussed in section

4.4.1. Nevertheless, when the flow rate is increased, the results do not obey the same pattern. Combining this set of results with those in section 4.4.2, it may be concluded that the combustion zone has extended to some distance beyond the substrate. As the heat generated by combustion, flows in the direction towards the substrate, the end of the combustion zone tends to increase the temperature at that position. At a distance of 10 cm, the deposition temperature is slightly lower than that at 12 cm, therefore the particles in the deposited film grow faster, which results in larger particles than those deposited at 12 cm for the same deposition time. A higher flow rate promotes the effect, whilst there is no indication of this at lower flow rate.

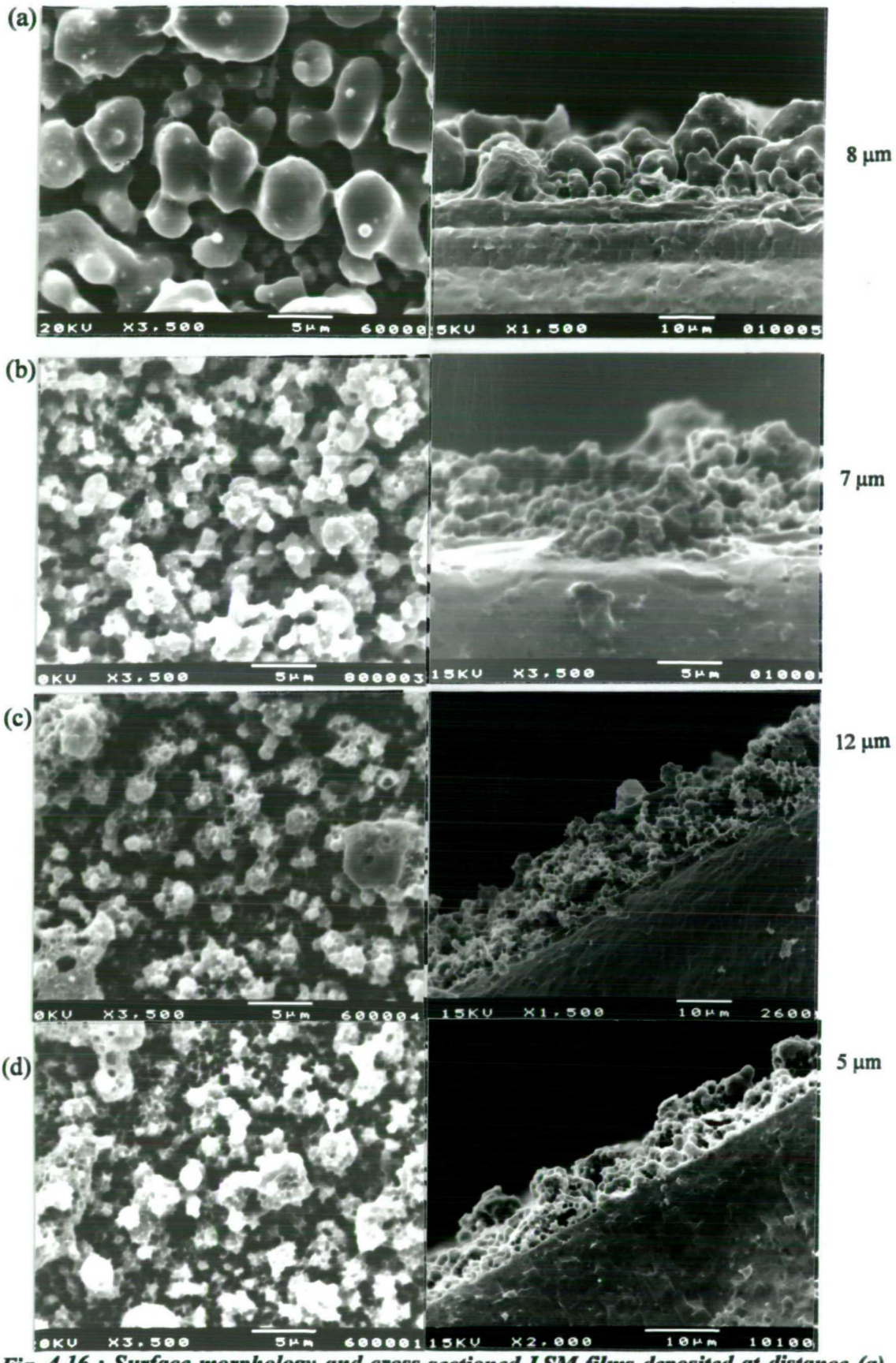


Fig. 4.16 : Surface morphology and cross-sectioned LSM films deposited at distance (a) 10 cm, and (b) 12 cm and the flow rate 12 ml/min. (c) and (d) are at distance 10 cm and 12 cm at the flow rate 10 ml/min.

4.5 CONCENTRATION OF THE PRECURSOR SOLUTION

In previous sections, many variable parameters have been discussed. The remaining parameter of a significant effect, is the concentration of the precursor solution. As the nitrate powders of La, Sr, and Mn are dissolved in water and ethanol to make a solution of a desired concentration. The concentration variation influences the deposited films.

The composition of LSM in this set of experiments was $La_{0.82}Sr_{0.18}MnO_3$. The concentration was varied from 0.01 Molar to 0.1 Molar. At each concentration, a range of ethanol/water ratios was used. The controlled process parameters were kept constant throughout the investigation as specified in Table 4.1. Results of each deposition are summarised in Table 4.12.

Table 4.12 : Descriptions and comments of LSM film in the investigation of precursor concentration.

Concentration (Molar)	Ratio of ethanol/water	Deposition temperature (°C)	Comments
0.1	80/20	750-780	Powdery with agglomeration
0.1	75/25	700-750	Uniform porous with agglomeration
0.1	70/30	690-730	Uniform porous with agglomeration
0.1	60/40	270-300	Dense film with lots of cracks
0.075	80/20	750-785	Fine particles with agglomeration
0.075	75/25	680-720	Porous with agglomeration
0.075	70/30	670-710	Uniform porous with some necking
0.05	80/20	770-810	Powdery of fine particles
0.05	75/25	700-800	Uniform porous with agglomeration
0.05	70/30	650-690	Uniform porous with agglomeration
0.05	60/40	470-520	Densely packed large particles
0.025	80/20	890-950	Very fine particles
0.025	75/25	800-840	Fine particles with agglomeration
0.025	70/30	690-740	Uniform porous
0.025	65/35	650-720	Porous with some necking
0.01	80/20	800-850	Powdery of very fine particles
0.01	70/30	720-750	Powdery of very fine particles
0.01	60/40	500-550	Porous of fine particle with agglomeration

Figs 4.17, 4.18, 4.19, 4.20, and 4.21 show the microstructures of the deposited films with varying concentration. In Fig. 4.17, only at the ratio of 80/20 produces a film that is powdery, and has the agglomeration size of 1-5 microns. When the ratio of ethanol/water is decreased, the microstructure seems to have uniform porous, with 5-10 microns agglomeration. A dense, amorphous film was obtained at 60/40 ratio, but the temperature was too low (270°C-300°C), and as a result cracks, due to thermal shock.

In Fig. 4.18, where the concentration was 0.075 mol, finer particle size was obtained, even the agglomeration sizes are reduced. At 70/30 ratio, necking process occurs resulting in more densely packed particles.

When the concentration was equal to 0.05 mol, the deposited films were powdery for both 80/20 and 75/25 ratios (Fig. 4.19 (a) and (b)). The film is porous only for the 70/30 ratio, with particles of size 2 microns and some agglomeration (Fig. 4.19 (c)). At the ratio 60/40, large particles are packed together as shown in Fig. 4.19 (d).

Fig. 4.20 shows the microstructure of deposited films when the concentration was set at 0.025 mol. At 80/20 and 75/25 ratios, very fine particles are present, however, at 75/25 ratio, there is some agglomeration. The film is porous only when the ratio is at 70/30, with 1-2 microns size particles (Fig. 4.20 (c)). The microstructure is porous with agglomerated particles at the ratio of 65/35. Particle size is also large, ranging from 2-5 microns in diameter (Fig. 4.20 (d)).

Very fine particles of a size smaller than 1 micron are obtained for the ratios of 80/20 and 70/30, when the concentration is 0.01 mol, Fig. 4.21 (a) and (b). Porous structure with agglomeration is observed at lower ethanol/water ratio of 60/40 in Fig. 4.21 (c).

The overall trend is that the deposition temperature increases as the concentration is reduced. In the combustion reaction, sufficient heat from the combustion of ethanol, is required to combust the species in the aerosol droplets.

The heat provided by the ethanol combustion triggers the combustion of these species, which on its own is an exothermic reaction. When the amount of aerosol species is reduced, the total heat generated by the ethanol combustion and from the exothermic reaction of species is increased. Therefore, the deposition temperature of the same ethanol/water ratio is increased, by decreasing the concentration. Nevertheless, at very low concentration, 0.01 mol, the heat released from the exothermic reaction of metal species is negligible, thus reducing the total heat generated and therefore the deposition temperature drops.

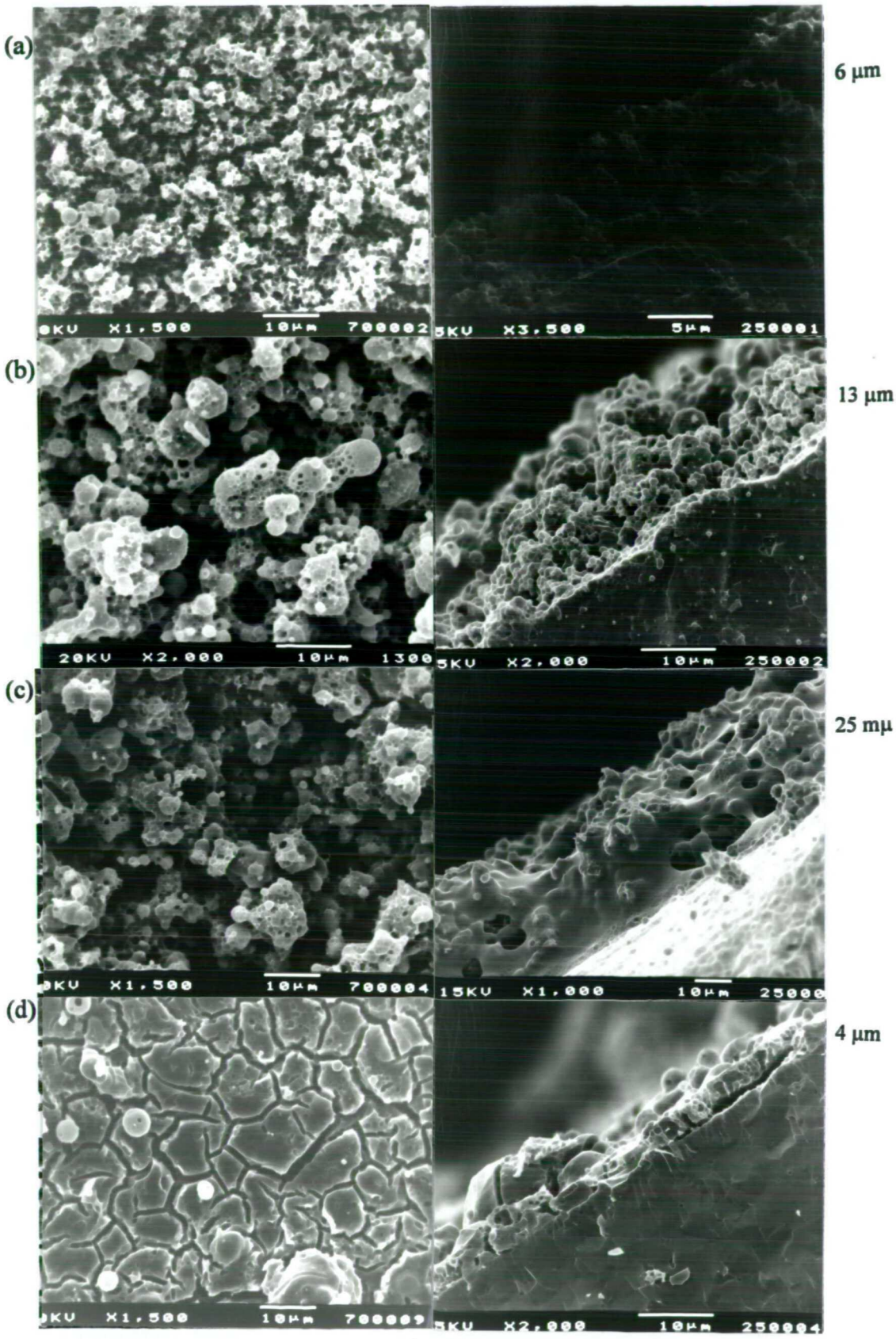


Fig. 4.17 : Surface morphology and cross-sectioned LSM deposited from 0.1 Molar precursor solution at ethanol/water ratio (a) 80/20, (b) 75/25, (c) 70/30, and (d) 60/40.

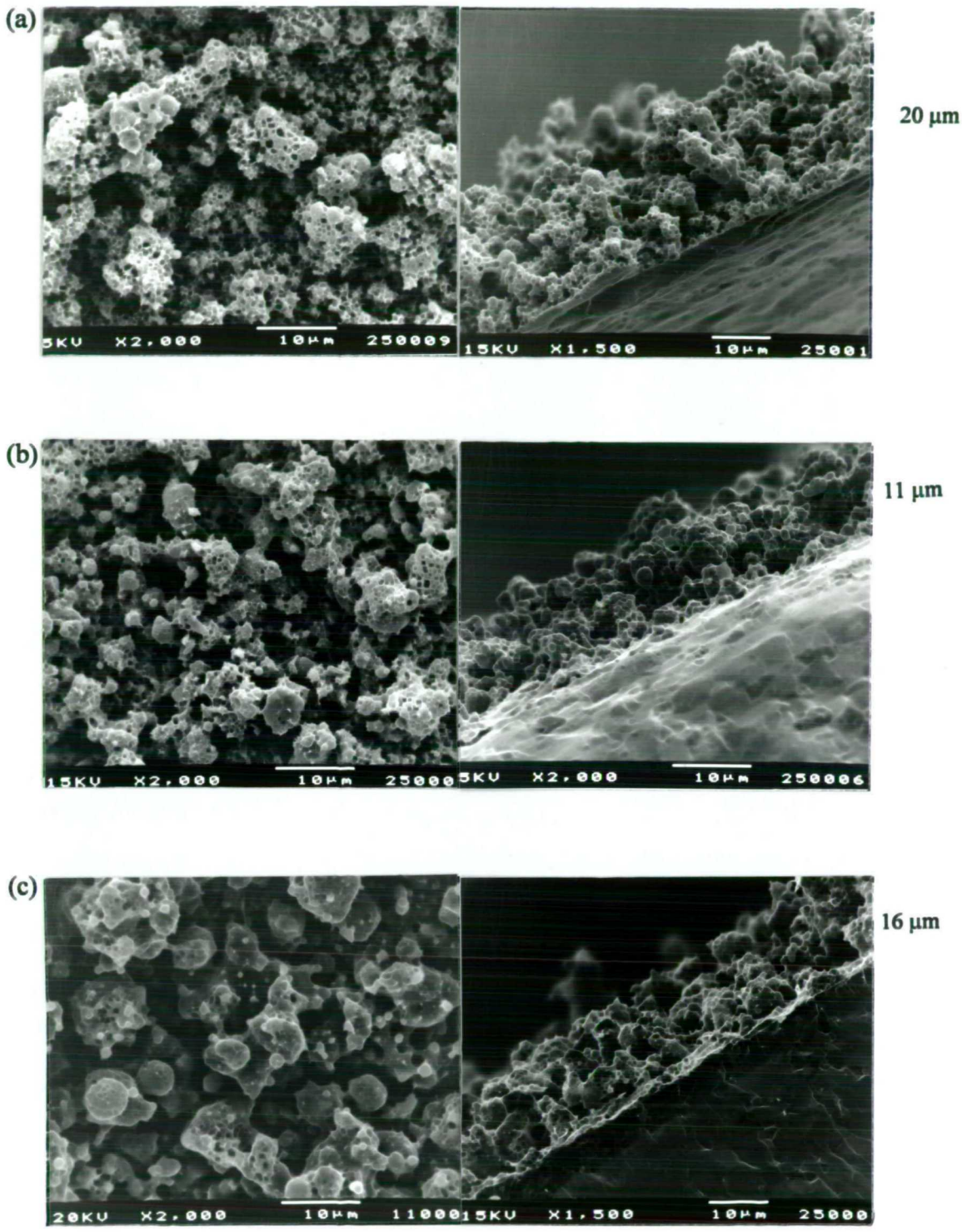


Fig. 4.18 : Surface morphology and cross-sectioned LSM deposited from 0.075 Molar precursor solution at ethanol/water ratio (a) 80/20, (b) 75/25, and (c) 70/30.

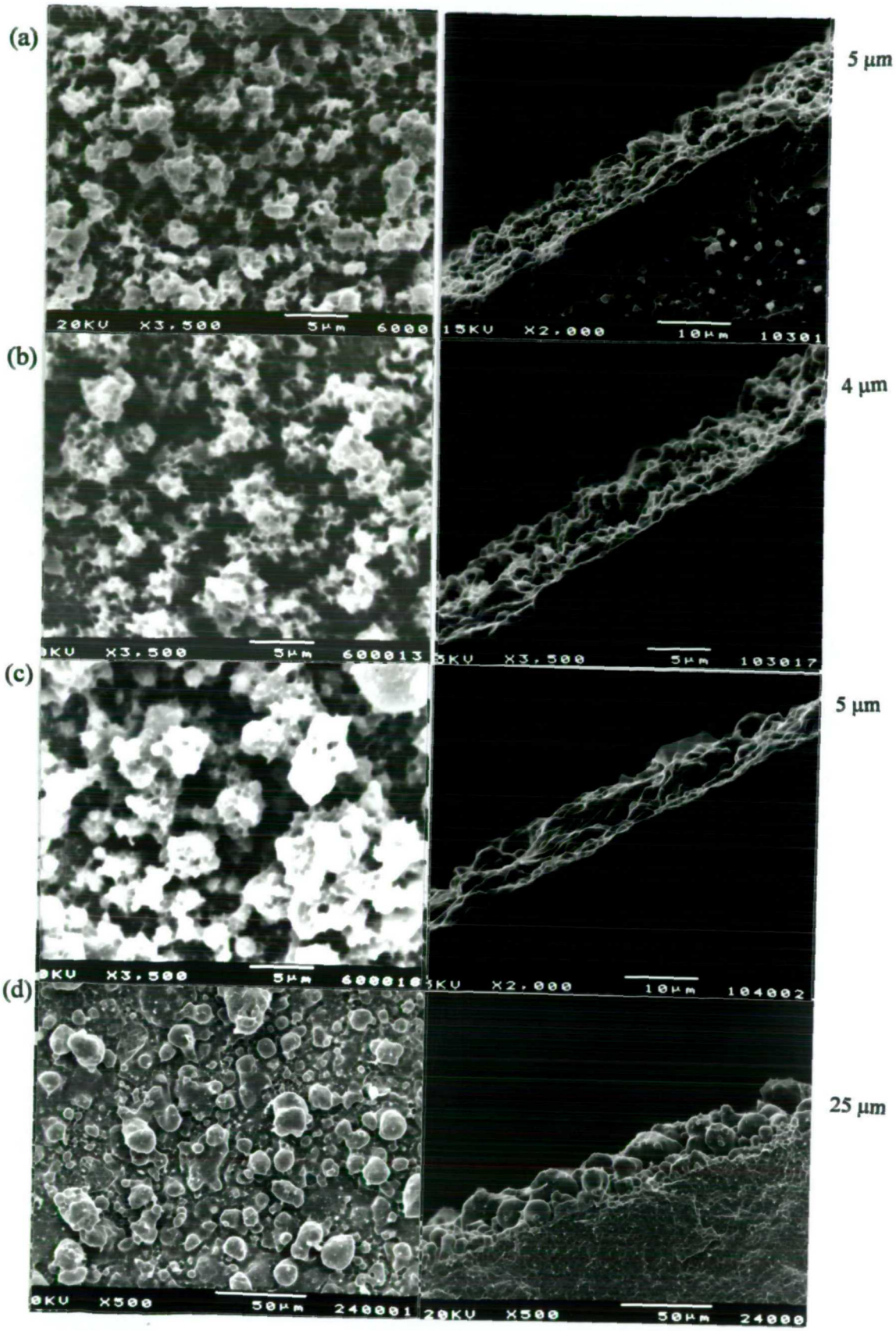


Fig. 4.19 : Surface morphology and cross-sectioned LSM deposited from 0.05 Molar precursor solution at ethanol/water ratio (a) 80/20, (b) 75/25, (c) 70/30, and (d) 60/40.

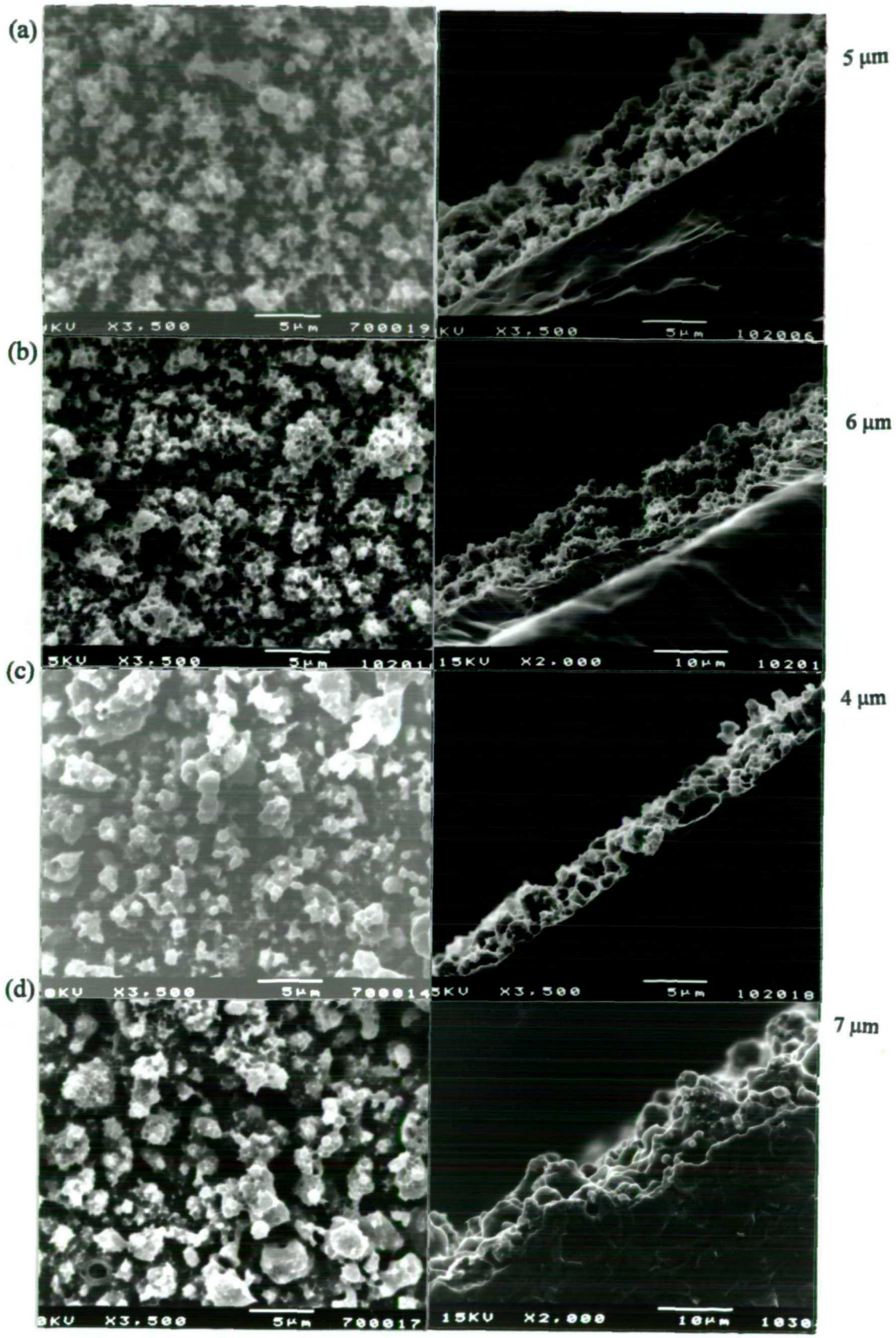


Fig. 4.20 : Surface morphology and cross-sectioned LSM deposited from 0.025 Molar precursor solution at ethanol/water ratio (a) 80/20, (b) 75/25, (c) 70/30, and (d) 65/35.

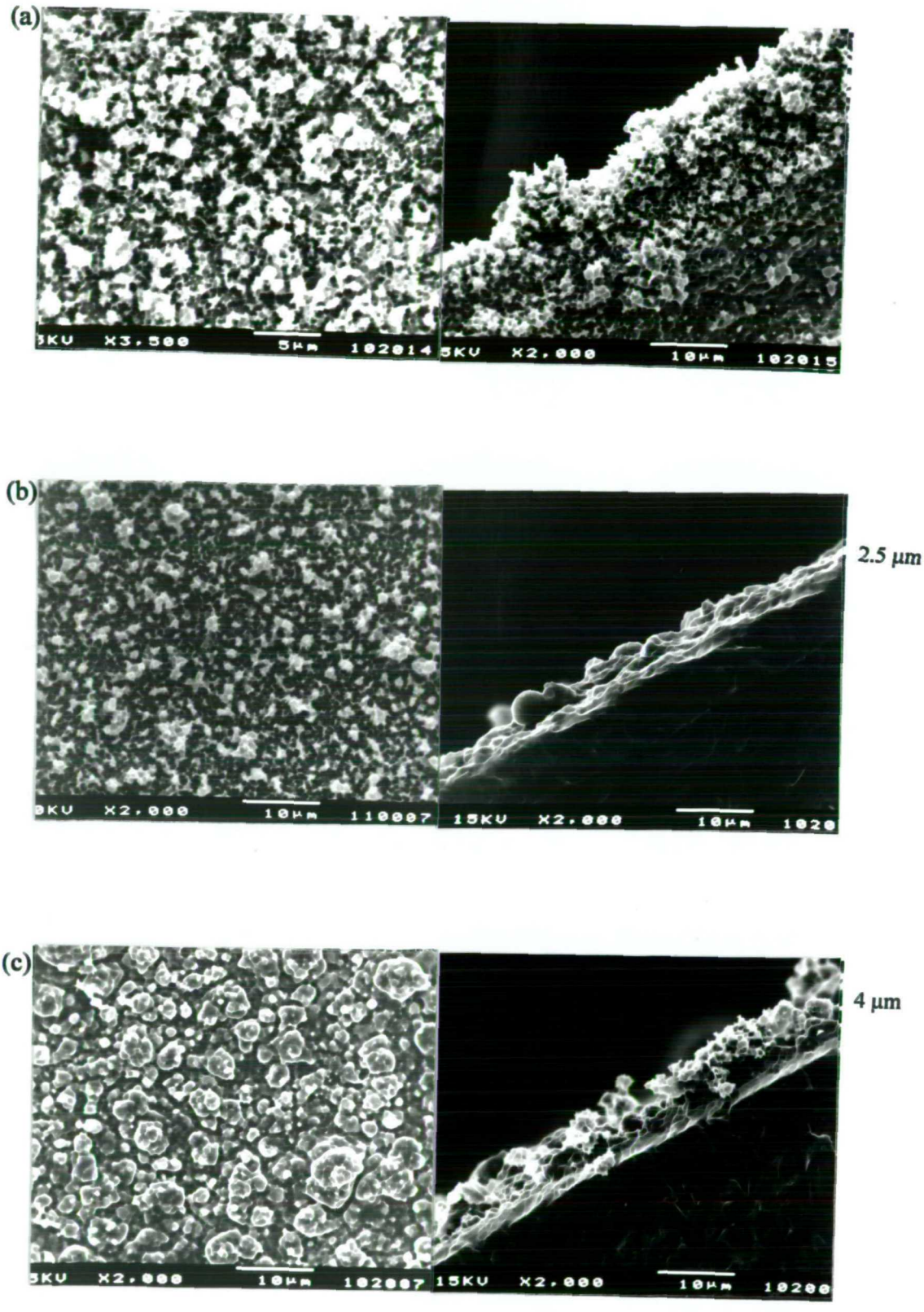


Fig. 4.21 : Surface morphology and cross-sectioned LSM deposited from 0.01 Molar precursor solution at ethanol/water ratio (a) 80/20, (b) 70/30, and (c) 60/40.

The sizes of particles were varied with the concentration, although they were deposited at the same ratio of ethanol/water. The size of particles was largest at high concentration and smallest at low concentration. The degree of agglomeration also depended on the precursor concentration. More agglomeration was obtained at high precursor concentration, which also produced large particles. The porosity is influenced by these parameters forming large particle size together with high degree of agglomeration, associated with a high porosity fraction.

A similar influence has also been observed by S.C. Zhang and G.L. Messing [186] in that the size of particle formed depended on the concentration of the solution using a spray pyrolysis technique to produce zirconia particles. The size of particle was smaller when the concentration of a solution was reduced.

The effect of precursor concentration variation on the microstructure can be seen in the proposed mechanism in Fig. 4.22.

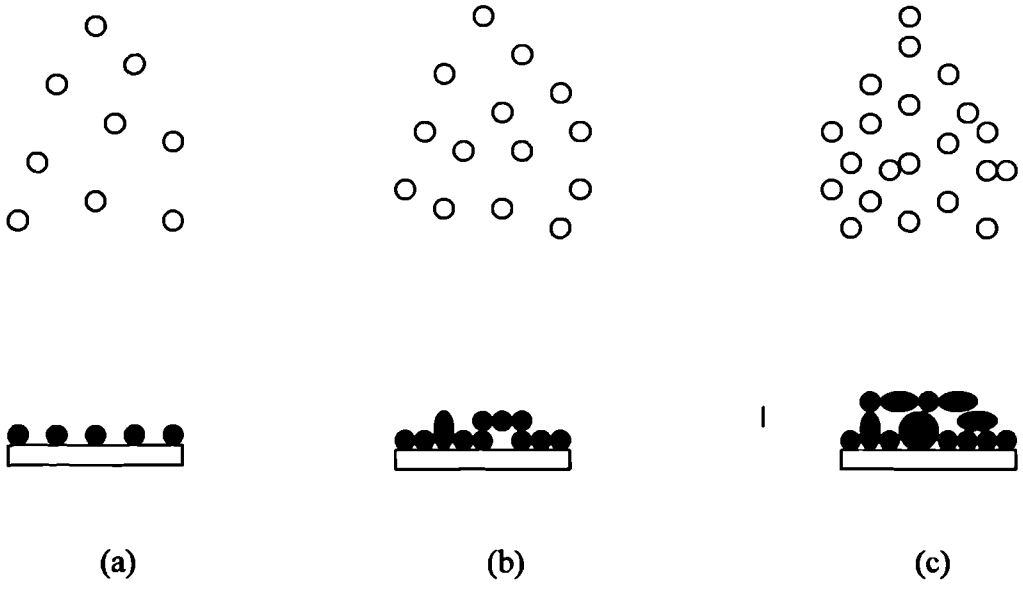


Fig. 4.22 : A sketch of particle agglomerations when the concentration of the precursor is (a) low, (b) moderate, and (c) high.

4.5.1 CRYSTAL STRUCTURE

XRD patterns of LSM films deposited using different concentrations of precursor solution, were analysed. The comparison was made between films deposited at the same range of deposition temperature, since this is more critical than the same ratio of ethanol/water. The range used was from 680°C-750°C. All of them showed similar patterns of $La_{0.8}Sr_{0.2}MnO_3$ phase. Since their microstructures, were not the same, the XRD line broadening method was used to calculate the crystallite size. Assuming that no line broadening due to residual stress occurred, the broadening was attributed to the crystallite size solely. There was no significant difference in the crystallite size and the size was around 200 A° ±10%. Impurity traces were detected from the XRD patterns. They are summarised in Table 4.13.

Table 4.13 : Impurity phases in different concentration of the precursor solution.

Concentration (mol)	Deposition temperature (°C)	Impurity phase
0.1	700-750	-
0.075	680-720	-
0.05	680-730	-
0.025	680-710	$La_2Zr_2O_7$
0.01	720-750	$La_2Zr_2O_7$

From this trend, $La_2Zr_2O_7$ phase is more favourable at low concentration of precursor solution and the deposition temperature is not as important as the microstructure of the film.

4.6 STOICHIOMETRY STUDY OF LSM

$La_{0.82}Sr_{0.18}MnO_3$ powder from 80/20 and 70/30 ethanol/water ratio precursors, were deposited using the same conditions listed in Table 4.1. The deposition temperatures of the substrate, where powder was collected from, was 900°C-1000°C.

The amount of elements contained in these two kinds of LSM powder was analysed using an atomic absorption spectrometry. This analysis was carried out in the Geology Department by Mr. P. Watkins. The method is based on the absorption of ultraviolet or visible light by gaseous atoms. The sample atomic vapour was produced by spraying the sample solution into a flame. The typical light source used was a hollow-cathode lamp containing the element to be determined. The unexcited, neutral atoms of this element within the flame absorb at precisely the wavelength emitted by the light source. Both the emission lines (wavelengths) of the light source and the absorption lines of the same element in the flame, have a narrow wavelength spread. Interference from the spectral lines of other elements is almost impossible. The sensitivity for most elements is about 1 ppm (1 micro gram per ml of solution) or less.

The deposition temperatures at the substrate and results from this analysis are summarised in Table 4.15.

Table 4.14 : Deposition temperatures and stoichiometry of La : Sr : Mn.

Ratio of ethanol/water	Deposition temperature (°C)	Stoichiometry of solution	Stoichiometry of powder
70/30	900	0.80 : 0.18 : 1	0.78 : 0.18 : 1
80/20	1000	0.80 : 0.18 : 1	0.77 : 0.18 : 1

The error involved in this method is ±0.01 mol %. XRD patterns show that both powders predominantly consist of $La_{0.8}Sr_{0.2}MnO_3$ phase. However, traces of $LaMnO_3$ were present in the powder deposited at 1000°C and 900°C, respectively as shown in Fig. 4.23 (a) and (b). The powder deposited from a higher ethanol/water ratio precursor, 1000°C, shows a large number of characteristic peaks and is more crystalline. Although these powders were deposited at high temperature and of powdery forms, impurity phases were not detected. This confirms that the $La_2Zr_2O_7$ phase present in other high deposition temperature and powdery films is the reaction product when YSZ was in contact during deposition.

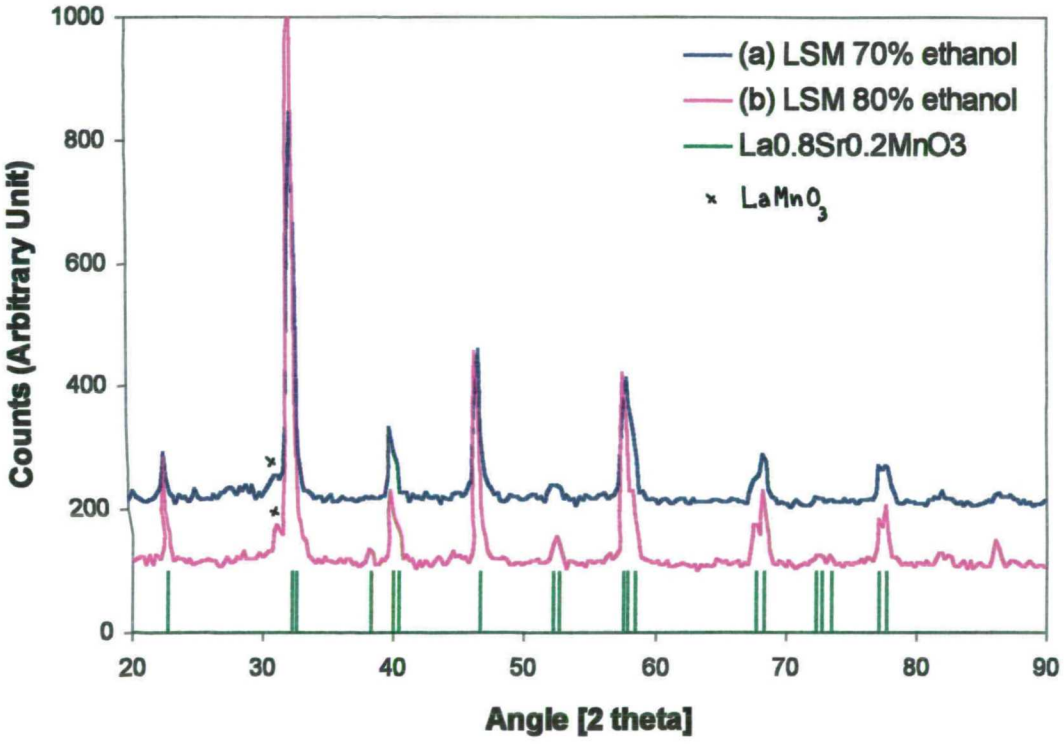


Fig. 4.23 : XRD patterns of LSM powder from (a) 70% and (b) 80% ethanol/water.

4.7 CHEMICAL REACTIONS

As described earlier in Chapter 3, on the experimental procedures, the precursor solution consists of many chemicals, in order to tailor a multi-component oxide. In this section, only an example of LSM deposition is discussed, as a case study.

The precursor solution for LSM deposition consists of :

$La(NO_3)_3 \cdot xH_2O$

$Sr(NO_3)$

$Mn(NO_3)_2 \cdot 6H_2O$

(x in general equals to 6, therefore, x is assumed to be 6 for the discussion)

These nitrates are naturally combustible when ignited, thus, they are suitable for the combustion reaction. These three nitrate powders were measured to the molar ratio of 0.82:0.18:1 to yield the final $La_{0.82}Sr_{0.18}MnO_3$ film. The mixed powder was then dissolved in deionised water. All the chemicals readily dissolved in water as they are hygroscopic. The dissociation reaction can be written as

$$La(NO_3)_3 \cdot 6H_2O_{(s)} \xrightarrow{H_2O} La^{3+}_{(aq)} + 3(NO_3)^-_{(aq)} + 6H^+_{(aq)} + 6OH^-_{(aq)} \quad \text{-----} \quad 4.1$$

The dissociation reaction 4.1 can be applied to $Sr(NO_3)$ and $Mn(NO_3)_2 \cdot 6H_2O$. Therefore, only La^{3+} will be discussed but is applicable to other cations too.

Ethanol was added to the dissolved solution to make a required concentration solution. The role of ethanol is to increase the flammability of the solution and act as a fuel for the combustion reaction.

When the precursor solution was atomised through the air atomiser, the pressure applied in this pneumatic atomiser, broke the solution into fine mist, *aerosol.* The size of droplets atomised from this spray nozzle is in between 10-120 microns depending on the air pressure.

The atomised droplets were ignited using a flame torch (methane), causing a combustion reaction. The processes involved during the rapid combustion, are combustion and decomposition of aerosol. The heat of combustion of ethanol provides the energy for the overall reaction; therefore, the ratio of ethanol in the precursor solution is vital. Many reactions occurred simultaneously, but they are written separately to avoid confusion. The combustion reaction of ethanol occurs provided that there is sufficient oxygen in air :

$$C_2H_5OH_{(l)} + 3O_{2(g)} \xrightarrow{ignited} 2CO_{2(g)} + 3H_2O_{(g)} \quad \text{-----} \quad 4.2$$

and the aerosol from reaction 4.1 can be written as :

$$La^{3+}_{(aq)} + 3(NO_3)^-_{(aq)} + 6H^+_{(aq)} + 6OH^-_{(aq)} \xrightarrow{combustion} \tfrac{1}{2}La_2O_{3(s)} + \tfrac{3}{2}N_{2(g)} + 6H_2O_{(g)} + \tfrac{15}{2}O_{2(g)} \quad \text{-----} \quad 4.3$$

From reaction 4.3, there is an abundance of oxygen gas produced, which can then enhance the combustion of ethanol in reaction 4.2 and continue the cycle of reactions.

Since three metal cations (La^{3+}, Sr^{+}, Mn^{2+}) were mixed together, the oxide component deposited was not La_2O_3, though this phase could be detected. The reaction forming perovskite is :

$$0.82La^{3+}_{(aq)} + 0.18Sr^{+}_{(aq)} + Mn^{2+}_{(aq)} + \frac{3}{2}O_{2\ (g)} \xrightarrow{combustion} La_{0.82}Sr_{0.18}MnO_{3(s)} \quad \text{-----} \quad 4.4$$

The overall reaction can then be written as :

$$0.82[La(NO_3)_3 \cdot 6H_2O]_{(s)} + 0.18[Sr(NO_3)]_{(s)} + Mn(NO_3) \cdot 6H_2O_{(s)} \rightarrow La_{0.82}Sr_{0.18}MnO_{3(s)} + 2.32N_{2(g)} + 10.92H_2O_{(g)} + 5.46O_{2(g)} \quad 4.5$$

The phase present in reaction 4.5, is for an ideal situation. Practically, other phases of reaction products could be detected from XRD patterns as mentioned in the previous chapters. At this composition of LSM, a typical phase that coexists with LSM, is La_2O_3 [187], however the phase of $La_2Zr_2O_7$ was constantly detected as a reaction between lanthanum and YSZ.

4.8 TEMPERATURE DISTRIBUTION

Two precursor solutions consisting of 80% ethanol and 70% ethanol for the deposition of LSM were used for this investigation. Both depositions were set at the same parameters except for the ratio of ethanol to water. The controlled parameters are summarised in Table 4.15.

Table 4.15 : Parameters used for the temperature distribution investigation.

Concentration of the precursor solution	0.05 mol
Distance between the spray nozzle and the substrate	12 cm
Flow rate of the solution	12 ml/min
Compressed air pressure	22 psi

The temperature distribution results are sketched in Figs. 4.24 and 4.25. There were measured using a type K thermocouple (-50°C - 1300°C). During the measurements, the temperature at the flame fluctuated around ± 50°C due to the pulsation from the peristaltic pump and because this deposition process was carried out in an open air.

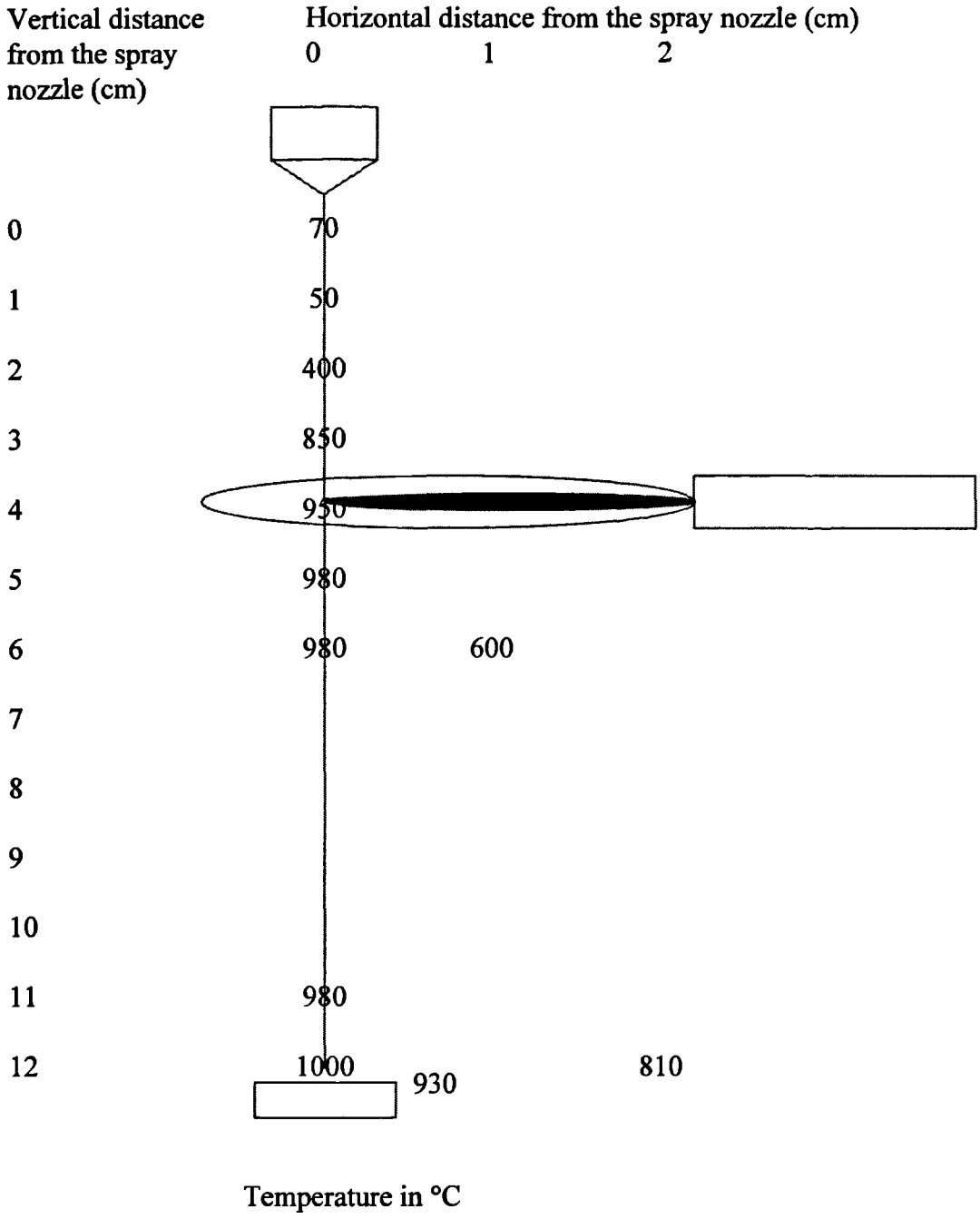


Fig. 4.24 : A sketch of a temperature distribution of FAVD technique for the 80 % ethanol precursor solution

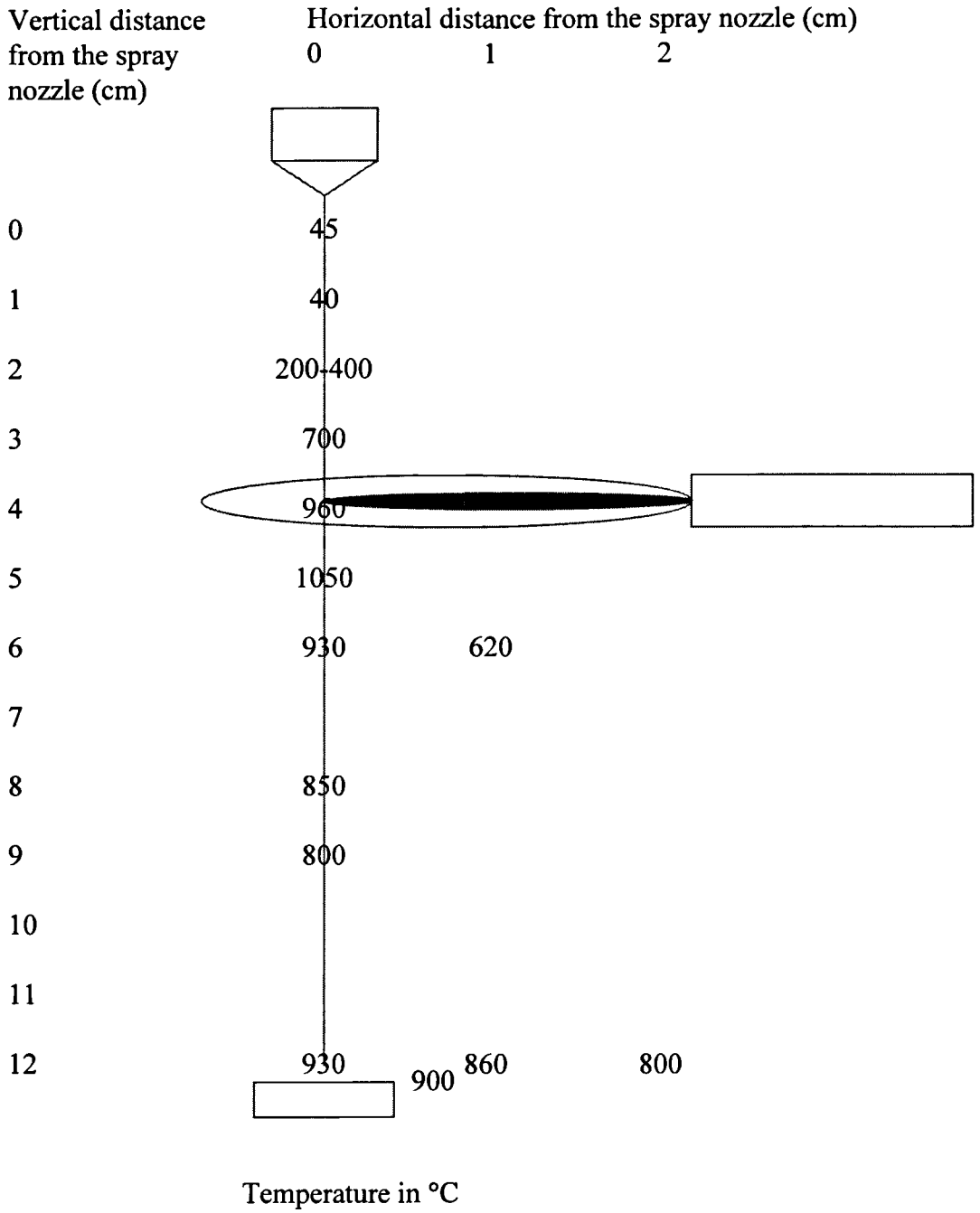


Fig. 4.25 : A sketch of a temperature distribution of FAVD technique for the 70 % ethanol precursor solution

From Figs. 4.24 and 4.25, the temperature distribution varies with the amount of fuel (ethanol) in the precursor solution. However, characteristics are similar. The temperatures measured at the substrate surface and on the side are consistent with the results mentioned earlier in this chapter, the deposition temperature increases with the ratio of ethanol to water.

The position in which the deposition temperature is measured, must be accurately controlled within the range of ± 10°C, so that the results are consistent. The position where the deposition temperatures were monitored in this thesis, was next to the substrate, slightly below the surface.

These two sketches are comparable with the temperature contours obtained from the computer modeling in Chapter 7, which confirms the accurate trend of the modeling results.

4.9 SUMMARY

The investigations of various deposition parameters have shown significant changes in both microstructures and phases of LSM films produced. Desirable microstructures could be obtained simply by adjusting these deposition parameters accordingly.

In conventional CVD reactions, the deposition temperature is the critical variable for the control of microstructure irrespective of whether they are homogeneous reactions or heterogeneous reactions. However, in FAVD there are more variables and the deposition temperature alone cannot produce a change in the reactions without varying at least one other parameter.

In FAVD, a film deposited at high temperature is more powdery and crystalline than that deposited at lower temperature as the dominant reaction is governed by gas phase nucleation as in Fig. 4.2 (a) and 4.4 (a). The temperature can be raised either by increasing an amount of ethanol in the precursor solution or increasing the mass fraction of ethanol, or adjusting the position of the flame torch. For powder product at high temperature, the homogeneous gas phase reactions are dominant, which means that decomposition, combustion, and chemical reactions of the reactants are completed within the gas phase, leading to the formation of nucleated powders and the shape of combustion zone is in category C. Assuming the reactant concentration is high enough, these reactions lead to gas phase nucleation, by which a fine powder is produced. At lower temperatures where heterogeneous reactions are dominant, the decomposition and combustion reactions occur in the gas phase, but the reactions take place at or near the heated substrate as the combustion zone is of shape B. Therefore, the deposited film is dense. A porous film could be obtained by varying the parameters to lie somewhere between those of the homogeneous and heterogeneous reactions, thus causing some particles to be formed in the gas phase and some aerosol to react at the substrate. This yields connected particle films. Fig 4.26 shows the first layer deposition as individual particles as well

as the overall surface morphology of connected particle films after the complete deposition.

The impurity phase of $La_2Zr_2O_7$ has been detected from many LSM films deposited mainly at high temperature but with only powdery films and not porous or dense films. As this reaction product occur at the interface between LSM and YSZ, it is difficult to detect using XRD technique from the top surface as the X-ray penetrates through a layer of LSM. This explains why the reaction product can only be detected when the LSM film is very thin and porous, or powdery. In other films with dense or thick porous LSM layers, there is a possibility that a reaction product phase is present however it cannot be detected.

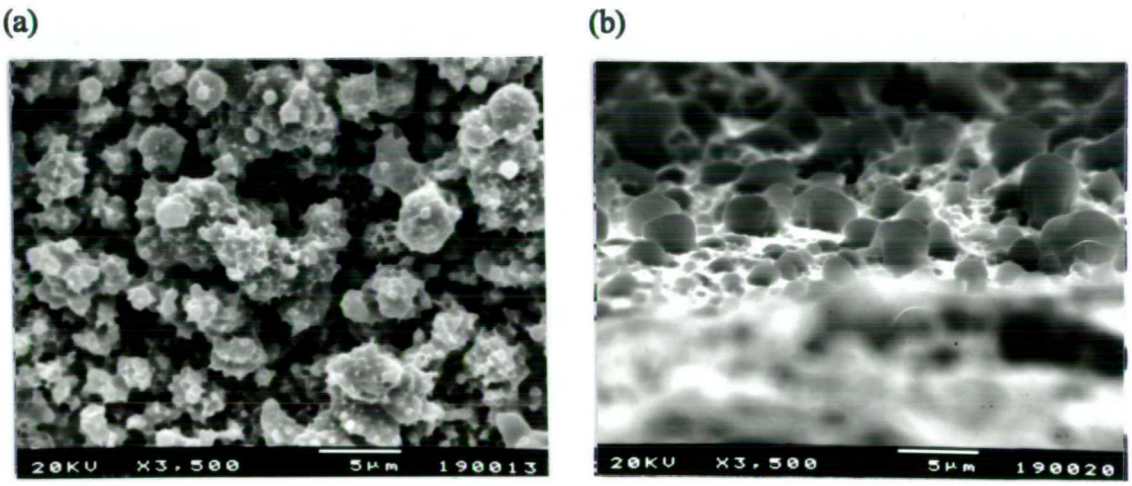


Fig. 4.26 : (a) surface morphology and (b) cross-section of FAVD film showing the change from individual particles to connected particles.

All the processing parameters are influenced by the amount of fuel, the total mass to be combusted and the position of combustion. When one parameter is varied, at least one other parameter must be adjusted in order to maintain the original microstructure and properties. Powdery films can be fabricated not only by having a high ethanol/water ratio but also by using high air pressure, or by increasing the height between the spray nozzle and the substrate. The combustion reaction was confirmed to be completed in the deposition of this powder from the XRD spectra.

At very low deposition temperature, especially at a low ratio of ethanol/water, the energy provided from the combustion of ethanol is not sufficient to combust the entire droplets, and the combustion zone is of shape A. Consequently, the droplets were not readily combusted but splashed onto the substrate. Fig. 4.4 (d), 4.6 (c), 4.13 (a) clearly show flaky films with many pores, due to the incompleteness of the reactions. In addition, these films have high deposition rate, and are amorphous according to the XRD traces.

For application as cathodes in SOFCs, the film has to be porous and crystalline, and have an appropriate electrical conductivity. The conductivity could be improved by modifying the processing parameters and the microstructures. With careful control over the processing parameters, the desired microstructure could be obtained to give a film which performs as a good electrical conductor, as will be discussed in Chapter 5.

Chapter 5 : ELECTRICAL PROPERTIES OF $La_{1-X}Sr_xMnO_3$

In Chapter 4, the relationship between microstructures of LSM and FAVD process parameters has been discussed. This chapter presents the electrical properties related to LSM from some deposition conditions. Additional XRD results are included to support the electrical and electrochemical observations. The electrical conductivity values are compared for various compositions of LSM. In addition, a modified structure of LSM has been deposited and electrical properties have been measured.

5.1 ELECTRICAL CONDUCTIVITY

The electrical conductivity is measured using the dc 4-point (Van der Pauw) technique, as explained in Chapter 3. Voltages and currents across the 4 points on a sample surface are measured at each temperature interval from room temperature to around 800°C. The conductivity is then calculated according to the equation described earlier in Chapter 3. The conductivity is plotted against the reciprocal of temperature (in degree Kelvin). It follows the Arrhenius equation, from which the activation energy of the conductivity process is then quantified from the slope of a straight line.

5.1.1 $La_{0.82}Sr_{0.18}MnO_3$

There are two experimental variations in this investigation; the concentration of the precursor solution and the pressure of the compressed air. The microstructures of these have been discussed in sections 4.3 and 4.5. The lateral electrical conductivity (planar or in plane) was compared at 800°C and 900°C which represent the operating temperatures of SOFCs. It is important to note that these values are not the measured values but extrapolated from the Arrhenius plots.

5.1.1.1 Effect of Concentration of the Precursor Solution

All films have been deposited in the same range of temperature, however the ratios of ethanol/water might have been varied. The controlled parameters are; the distance between the spray nozzle and the substrate (12 cm), the flow rate of the precursor (12 ml/min) and the pressure of the compressed air (22 psi). The process parameters and resistivities are summarised in Table 5.1.

Table 5.1 : Lateral electrical resistivities of $La_{0.82}Sr_{0.18}MnO_3$ from dc 4-point (Van der Pauw) technique at various precursor concentrations.

Precursor concentration (mol)	Deposition temperature (°C) *	Resistivity 800°C (ohm cm)	Resistivity 900°C (ohm cm)	Activation energy (eV)
0.1	750-780 (80)	0.0526	0.0458	0.25
0.1	690-730 (70)	0.0972	0.0763	0.36
0.075	680-720 (75)	0.0917	0.0769	0.29
0.05	680-730 (70)	0.0610	0.0497	0.32
0.025	680-710 (70)	0.0495	0.0327	0.54

* The values in brackets are the percentage of ethanol in the solution.

Fig. 5.1 shows the plot of conductivity (σ) versus the reciprocal of temperature. Comparing the resistivities with the microstructures in Fig. 4.17 (a) and c), the microstructures are not much different but the deposition temperature difference is about 50°C. From the general trend of XRD results in section 4.1.1, a film deposited at higher temperature is more crystalline than the one deposited at lower temperature. This can be used to explain the resistivities of the 0.1 mol concentration films. As the particle sizes and the pore sizes in the 70/30 ethanol/water ratio film are greater than those in the 80/20 ratio film due to the lower deposition temperature as explained in section 4.1. Since a higher energy is required

for electrons to travel across a more porous film (more gaps and less pathways), the activation energy is then raised. These may be due to impurities such as silica forming at the grain boundaries or around particles, which increase the activation energy.

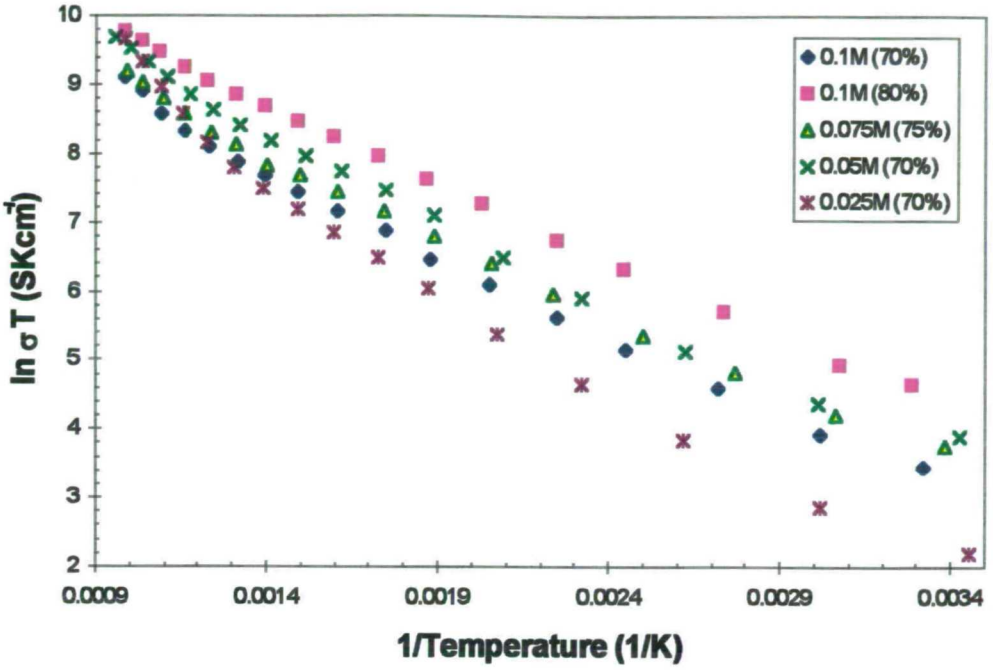


Fig. 5.1 : Conductivity of LSM films deposited at various precursor concentrations.

The effect of the variation in concentration of the precursor solution, the microstructures from Fig. 4.17-4.20 reveal the variation in particles and pore sizes. When the concentration is decreased, the particles and pores sizes decrease, and so does the resistivity, since particles are finer and more uniformly packed. However, when films are powdery, as a result, the activation energy is raised as the particles are loosely in contact. In principle, the activation energy is assumed to be independent of the degree of porosity.

5.1.1.2 Effect of Pressure of the Compressed Air

Further from section 4.3, the electrical resistivities have been measured and compared. The deposition parameters are the same as in section 4.3 and the deposition conditions and resistivities are listed in Table 5.2.

Table 5.2 : Lateral electrical resistivities of $La_{0.82}Sr_{0.18}MnO_3$ from dc 4-point (Van der Pauw) technique at various air pressures.

Pressure (psi)	Deposition temperature (°C)	Resistivity 800°C (ohm cm)	Resistivity 900°C (ohm cm)	Activation energy (eV)
17	720-770	0.0685	0.0487	0.47
22	680-730	0.0610	0.0497	0.32
26*	450-500	0.1102	0.0876	0.35

* The resistivity values were measured after annealing at 900°C for 2 hours in air.

The resistivity is the lowest when the pressure is at 22 psi, as the particles are too small at 17 psi. The activation energy at 17 psi is then very high, with the powdery deposition. The reason of the high activation energy is as explained in section 5.1.1.1. At 26 psi, the film consists of large particles of size 10-20 microns and some cracks observed under an SEM. The film after deposition did not act as an electrical conductor until after annealing in which the film became more crystalline. The resistivity is still high compared with at lower pressures. However, the activation energy is higher than that of 22 psi, since the gaps between particles are large and cracks are present. The plots of conductivity (σ) versus the reciprocal of temperature are shown in Fig. 5.2.

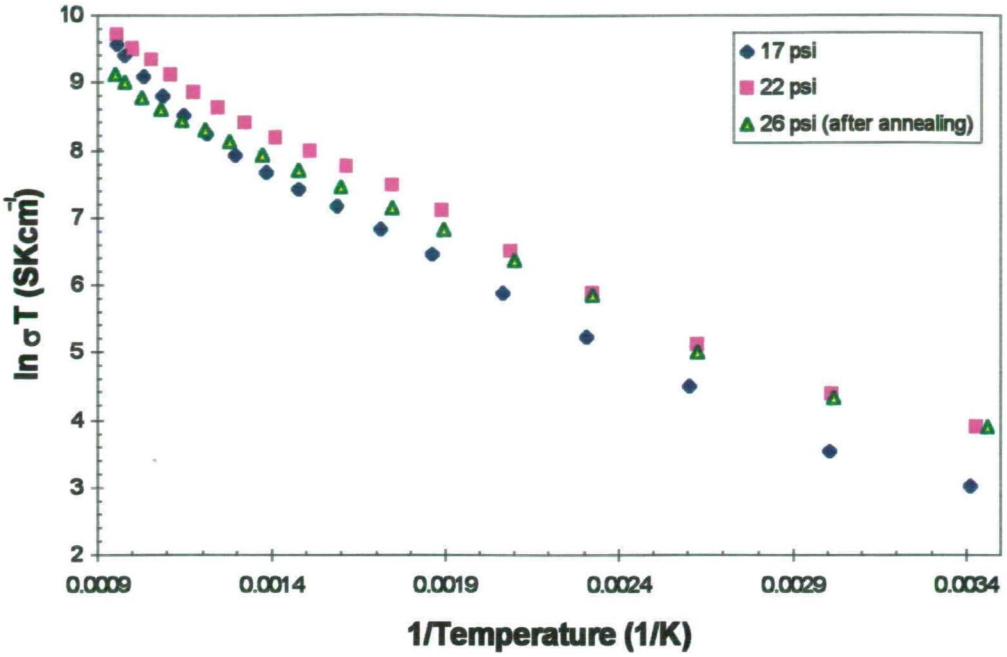


Fig. 5.2 : Conductivity of LSM films deposited at various air pressures.

5.1.2 $(La_{0.82}Sr_{0.18})_{0.9}MnO_3$

In this set of results, they are designated as LSMA (analogous to sections 4.2.2). The resistivities at various flow rate and ethanol/water ratios are listed in Table 5.3. The distance between the spray nozzle and substrate is at 12 cm.

Table 5.3 : Lateral electrical resistivities of $(La_{0.82}Sr_{0.18})_{0.9}MnO_3$ from dc 4-point (Van der Pauw) technique.

Ethanol/water ratio	Deposition temperature (°C)	Flow rate (ml/min)	Resistivity 800°C (ohm cm)	Resistivity 900°C (ohm cm)	Activation energy (eV)
80/20	870-920	15	0.0418	0.0357	0.27
80/20	700-750	10	0.0831	0.0569	0.51
70/30	740-800	15	0.0468	0.0384	0.31
70/30	700-730	10	0.0476	0.0388	0.32

From the microstructures in Figs. 4.8, it is obvious that the film deposited at 10 ml/min flow rate and 80/20 ethanol/water ratio yields a high resistivity value because of the very fine particle sizes which are not as crystalline as those deposited at higher temperatures. In addition, the powdery nature of this film results in particles which are loosely in contact leading to a poor conductivity and also the activation energy of the electrical conductivity is rather high as explained earlier. All other depositions show the values of resistivity very close to each other within the range of ± 0.004 ohm cm and the activation energies are in the same range of ±0.03 eV as they have quite similar microstructures observed under an SEM. The conductivity (σ) versus reciprocal of temperature, of this set of results, is plotted in Fig. 5.3.

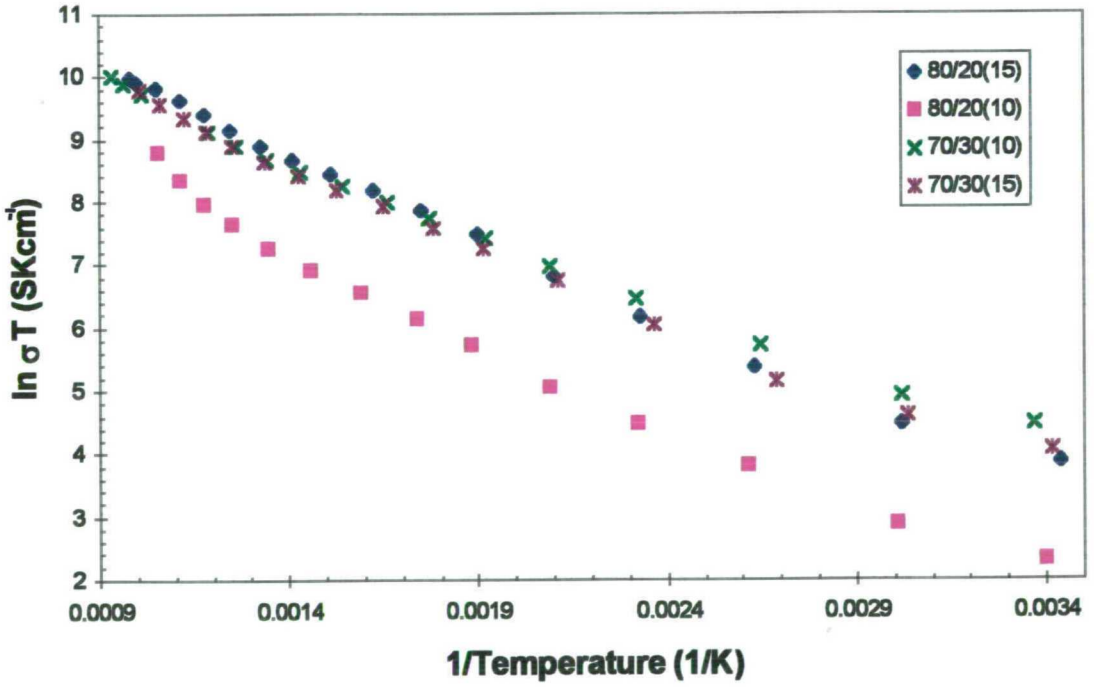


Fig. 5.3 : Conductivity of LSM films deposited at various flow rate and ethanol/water ratios.

5.1.3 IMPROVED LSM

The lateral electrical resistivity of LSM has been improved by two methods in this research. Firstly, it is improved by modification of the composition which yields lower resistivity, and secondly, by modification of the microstructure.

5.1.3.1 $La_{0.61}Sr_{0.18}MnO_3$

In Chapter 2, a lanthanum deficiency LSM has been proposed to have a better electronic conductivity than a conventional stoichiometric LSM. Therefore, a selected composition of $La_{0.61}Sr_{0.18}MnO_3$ was investigated for a comparison purpose. This composition of LSM is designated as LSM0.61. The deposition conditions are listed in Table 5.4.

Table 5.4 : Deposition conditions of LSM0.61.

Concentration of precursor solution (mol)	0.05
Ratio of ethanol/water	80/20
Deposition temperature (°C)	600-750
Distance between the spray nozzle and substrate (cm)	12
Flow rate (ml/min)	12
Pressure of compressed air (psi)	22

The microstructure and cross-sectioned of this film are shown in Fig. 5.4 (a) and (b). The film has low porosity, with large particle sizes, that have gaps in between them. The wide deposition temperature range results in densely packed large particles with no agglomerations. The high deposition temperature yields a highly crystalline film, whilst the low deposition temperature contributes a close packed microstructure and good adhesion.

(a) (b)

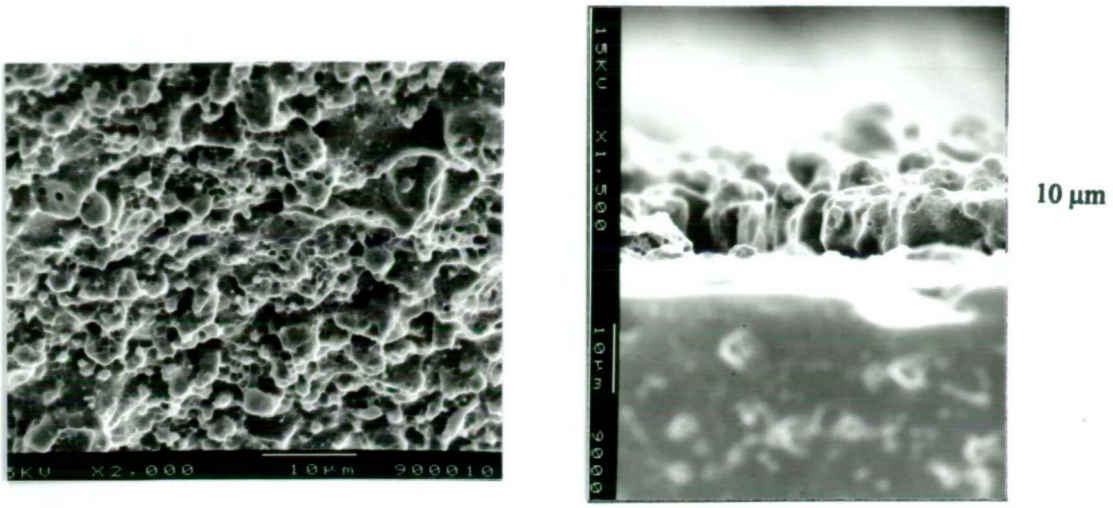


Fig. 5.4 : An improved LSM with composition, LSM0.61, (a) surface morphology and (b) cross-section.

5.1.3.2 $La_{0.82}Sr_{0.18}MnO_3$ Duplex Structure

This type of film is designated as LSM-du. The idea of this LSM duplex structure is to have two porous layers; a thin layer of small particles next to the electrolyte to increase the TPBs area and a thicker layer of large particles to improve an oxygen gas diffusion process from air to the TPBs. The microstructure of this film has been modified by depositing the first few microns, with small particle size (~1 micron) of LSM, followed by a layer of large particle (~5 microns). The deposition details are listed in Table 5.5. All other parameters are the same as in Table 5.4.

Table 5.5 : Deposition conditions of LSM duplex structure.

Parameters	Small particles layer	Large particles layer
Ratio of ethanol/water	75/25	70/30
Deposition temperature (°C)	740-770	680-720
Particle sizes (microns)	1	2-10
Thickness (microns)	5	15

Fig. 5.5 reveals the surface morphology and cross-sectioned of this LSM-du film. The cross-section clearly shows a packed layer of small particles next to the substrate and a layer of larger particles on top.

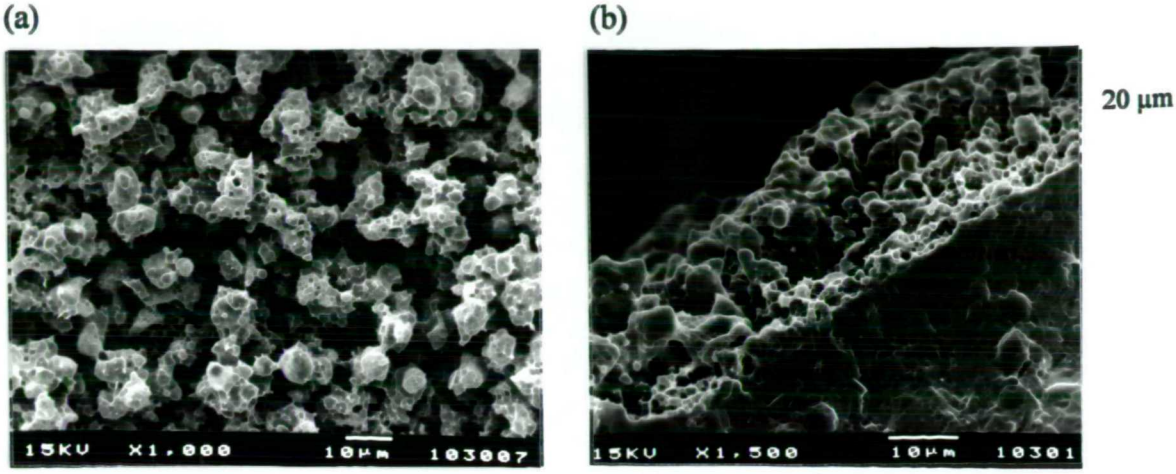


Fig. 5.5 : An improved LSM with microstructure, LSM-du, (a) surface morphology and (b) cross-section.

Lateral electrical resistivities of these improved LSM films have been measured using the same technique (dc 4-point Van der Pauw). The results are compared in Table 5.6.

Table 5.6 : Lateral electrical resistivities of improved LSM.

Sample	Resistivity 800°C (ohm cm)	Resistivity 900°C (ohm cm)	Activation energy (eV)
LSM0.61	0.0348	0.0321	0.19
LSM-du	0.0280	0.0260	0.18
LSM	0.0610	0.0497	0.32
LSM0.8	0.02	-	0.07*

* $La_{0.8}Sr_{0.2}MnO_3$ pellet sintered at 1150°C from ref. [188].

The results from Table 5.6 clearly show that the LSM-du sample is a better electrical conductor than LSM0.61, and both of them are even better conductors than LSM film deposited using the same processing parameters (from section 5.1.1.1 = 0.05 mol) at SOFC operating temperature. Nevertheless, both LSM films have the resistivities in the same order of magnitude as those LSM films fabricated from sintering routes which is shown as LSM0.8. The activation energy of these LSM films are in the same range as for other compositions of LSM (0.15-0.35 eV), prepared from a sintering route by Hammouche et al. [189]. However, the activation energy of LSM0.8 is very low compared to others even prepared from conventional ceramic routes. Therefore, the electrical conductivity of LSM prepared from our FAVD technique is comparable with those prepared from a sintering route within the same range and can be explained by the conductivity between particles and within the particles. The duplex structure provides a better conductivity than an ordinary porous LSM of the same composition and the La deficiency LSM.

5.2 ELECTROCHEMICAL PROPERTY OF LSM

An electrochemical property investigated in this section is an Electrode Polarisation or an Area Specific Resistivity (ASR) of LSM in this case. It is measured using an AC-impedance spectroscopy in air, from 300°C to 800°C. The experimental details are described in Chapter 3.

Selected LSM compositions and deposition conditions have been used to deposit a symmetrical cell for this AC-impedance measurement. All films have been deposited at the distance 12 cm, between the spray nozzle and substrate, flow rate of 12 ml/min, pressure of the compressed air 22 psi, and 0.05 mol precursor solution. The deposition conditions and ASRs are listed in Table 5.7. The ASR values at 800°C and 900°C were from an extrapolation of the straight line. All LSM films have the same composition apart from LSM0.61, which has been explained in a previous section. Plots of conductivity against the reciprocal of temperature are shown in Fig. 5.6.

Table 5.7 : Deposition conditions and Area Specific Resistivity (ASR) of LSM.

Sample	Deposition temperature (°C)	ASR 800°C (ohm cm^2)	ASR 900°C (ohm cm^2)	Activation energy (eV)
LSMX	650-730 (70)	11.316	7.585	0.53
LSMY	680-730 (70)	2.867	1.086	1.15
LSMZ	720-780 (75)	7.647	3.909	0.82
LSM-du	740-770 (75)	11.542	4.910	1.02
LSM0.61	600-750 (80)	3.903	1.356	1.24
LSM0.8❋	1100	140	30	1.41
LSM0.8/YSZ*	1350	1	0.15	1.8
LSM0.8/YSZ*	1500	18.7	3.16	1.7

❋ $La_{0.8}Sr_{0.2}MnO_3$ prepared from a slurry painting technique sintered at 1100°C [121].

*$La_{0.8}Sr_{0.2}MnO_3$ /YSZ at the molar ratio of 8:2 prepared from a screen printing technique and sintered at 1350°C and 1500°C as indicated [190].

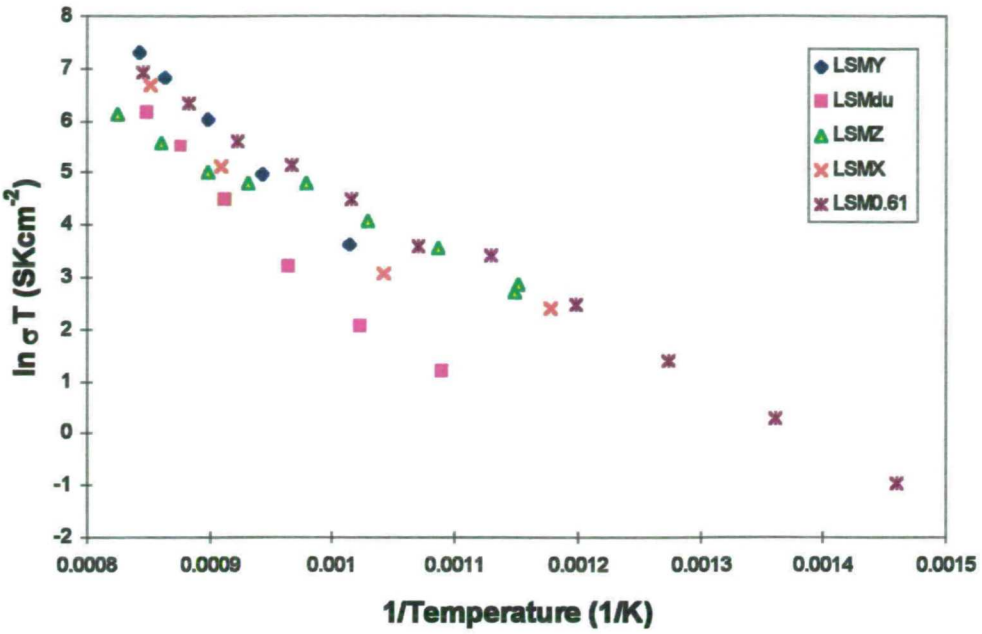


Fig. 5.6 : Conductivity vs 1/Temperature of LSM

From the microstructure, in Fig. 4.1 (c), LSMX consists of large particles of size 5-20 microns. The microstructures of LSMX, LSMY, and LSMZ are shown in Fig. 5.7. Gaps between particles are also large which provide a pathway for oxygen diffusion to the TPBs, but result in smaller electrode contact area. LSMZ and LSM-du have similar microstructure, but the thickness of LSMZ is about half of LSM-du. Therefore, the pathways of the diffusion of gaseous oxygen from air to the TPBs have been shortened by approximately half way, which is obviously better, and hence it has a lower ASR. LSMY has a porous structure of particles size around 1-5 microns and some agglomerates but these particles are well connected. This microstructure indicates the best performance LSM film with the lowest ASR. LSM0.61 shows a good sign of low ASR, as the film is crystalline and porous which provides pathways for oxygen gas diffusion.

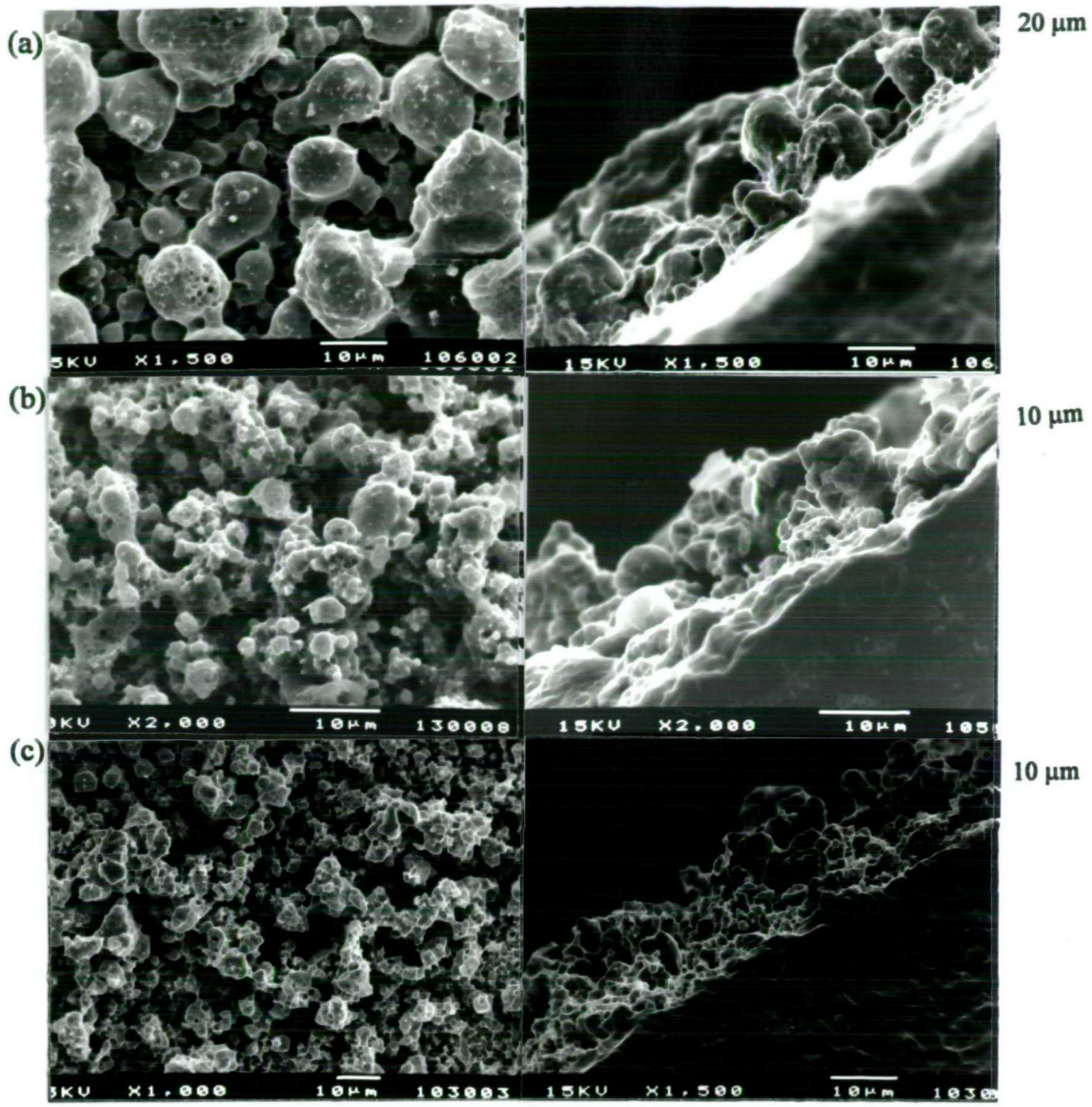


Fig. 5.7 : Microstructures of (a) LSMX, (b) LSMY, and (c) LSMZ.

A La deficient LSM has been reported by Weber et al [191] to show lower cell resistance than a $La_{0.8}Sr_{0.2}MnO_3$ cathode cell without a sign of $La_2Zr_2O_7$ reaction product. However, this reaction phase was not detected in our investigations. The XRD patterns of LSMY, LSM-du and LSM0.61 are shown in Fig. 5.8. The ASR obtained are still high compared with the target set by Steele [63] that it should be targeted at 0.15 Ωcm^2. This has been achieved in commercial laboratories such as at ECN [191].

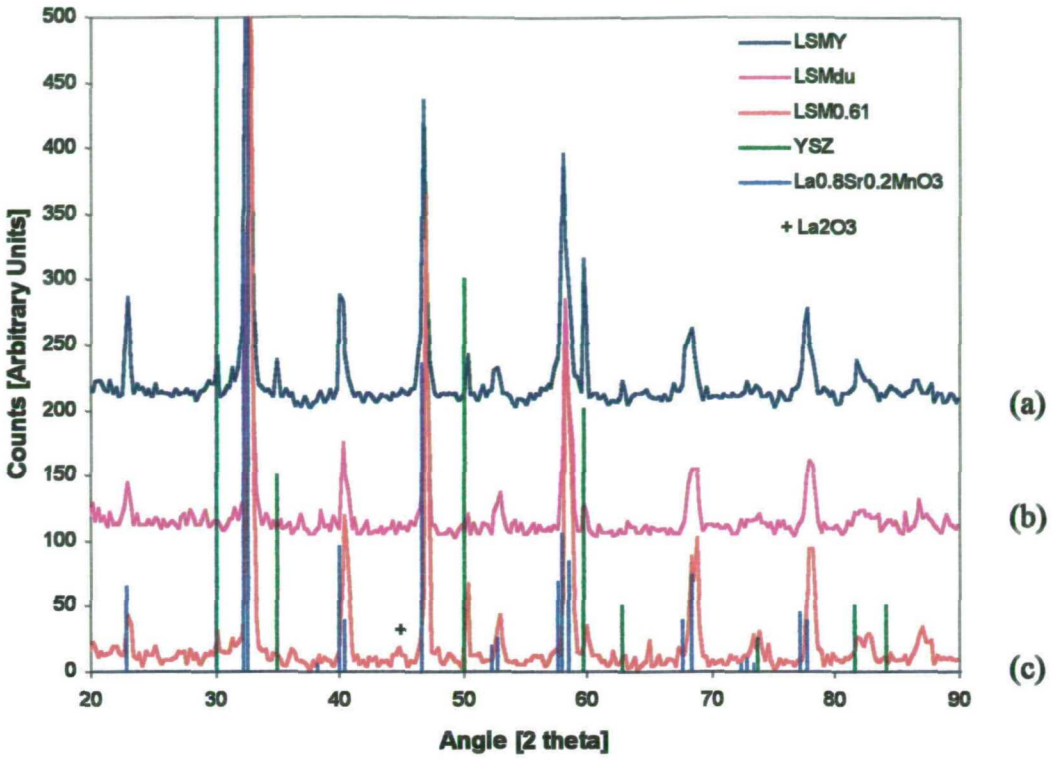


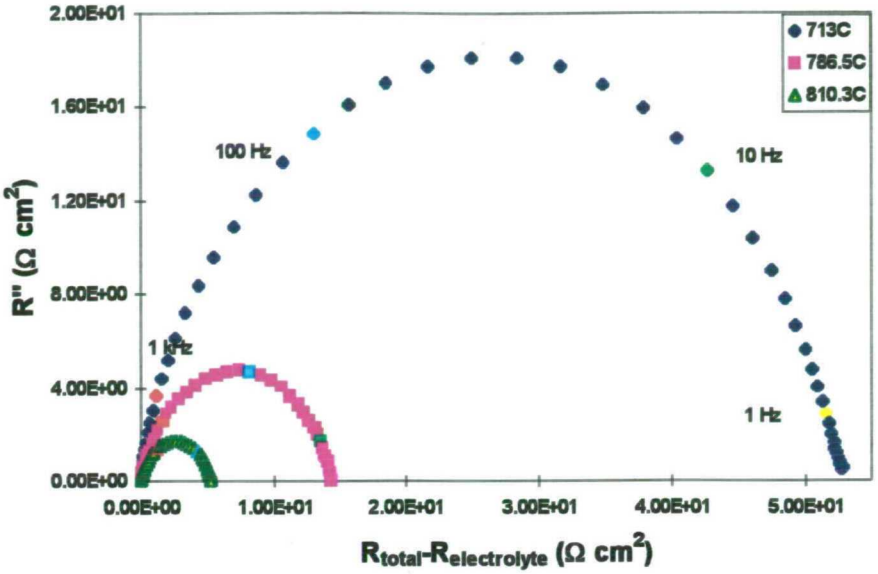
Fig. 5.8 : XRD patterns of (a) LSMY, (b) LSM-du, and (c) LSM0.61

The $La_2Zr_2O_7$ reaction product at the LSM/YSZ interface is not desirable as it hinders the reactions at the TPB from its low electronic and ionic conductivity [89]. This lanthanum zirconate phase forms at the interface when sintered at 1100°C [89,192]. Mizusaki et al [193] have suggested that the rate determining reaction process of the electrode reaction takes place at the interface of the electrode materials and the formed oxide layer in which increases the bulk resistance of the cell remarkably. From our study, it seems that the effect of a reaction product of La_2O_3 is not as pronounced as the effect of microstructures and contact areas. This agrees with the work reported by Sasaki et al. [92] which suggests that homogeneously distributed long TPBs, high lateral conductivity, and a narrow contact spacing of the current collectors are required to maximise the effective electrode area.

LSMY and LSM0.61 show relatively high activation energy compared with other films. These are comparable with a literature reported by Chen et al. [121] that the activation energy for $La_{0.8}Sr_{0.2}MnO_3$/YSZ interface is 1.4 eV. The surface reaction can be the rate-determining step as the activation energy of the surface exchange coefficient (k cm/s) is 1.4 eV [62]. The difference in the activation energy can be as a result of different processing techniques and hence, the different surface structure and mechanisms for oxygen reduction. The activation energies of those from sintering routes are greater than from FAVD technique as they were sintered at higher temperature than our deposition temperature.

AC-impedance response from LSM-du and LSMY are plotted in Fig. 5.9 (a) and (b). Note that the real axis resistance is the value of the total resistance minus the resistance due to the electrolyte, current collector contact resistance and ohmic loss through wiring. The resistance is for a symmetrical cell of two-sided cathode, therefore the real ASR is half of the semi-circle. All of them show a perfect semi-circle which refers to only one rate-determining step. Attention is drawn to the fact that in some of the impedance diagrams, the axes do not have the same scales.

(a)



(b)

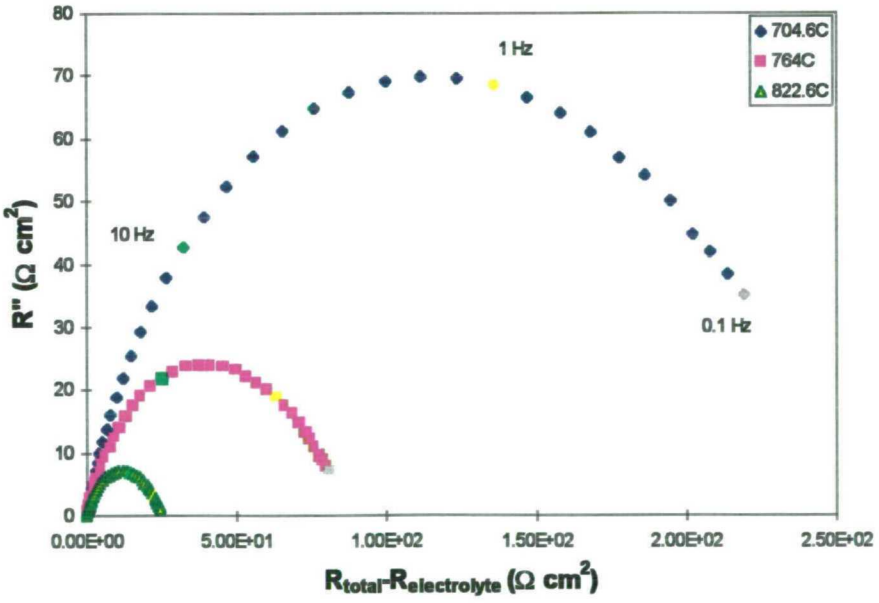


Fig. 5.9 : AC-impedance responses of (a) LSMY and (b) LSM-du at various temperatures.

LSM is regarded as an electronic conductor since the oxygen conductivity is very low that can be considered as negligible in air at atmospheric pressure [62]. The oxygen reduction is taking place at the triple phase boundary (TPB) between gas, electrolyte, and electrode only. There are many models proposed to explain the reactions involved at TPBs. Some of the reactions have been described in Chapter 2.

As there are many reactions involved, the slow reaction is considered as the rate-determining step, however, there has not been any concrete conclusion for this argument.

Van Heuveln et al. [194] have proposed three models to explain this phenomena. Nevertheless, in aid of experimental results, one particular model seems to yield the best fit. This involves four reaction steps :

1) Oxygen adsorption

$$O_{2(g)} \rightarrow 2O_{ad} \qquad \text{-----} \quad 5.1$$

2) Oxygen adsorption charge transfer

$$O_{ad} + e^{-} \rightarrow O_{ad}^{-} \qquad \text{-----} \quad 5.2$$

3) Diffusion of adsorbed oxygen

$$O_{ad}^{-} \rightarrow O_{TPB}^{-} \qquad \text{-----} \quad 5.3$$

4) Charge transfer at the TPB

$$O_{TPB}^{-} + e^{-} + V_O^{\cdot\cdot} \rightarrow O_O^{x} \qquad \text{-----} \quad 5.4$$

Van Heuveln et al [194] suggest that reactions 5.2 and 5.3 are the rate-determining steps in their investigations with voltage losses. However, reaction 5.2 is a fast process in general. One possible rate-determining step in the LSM series can be the oxygen adsorption, when the LSM particles are not homogeneous, and as a result, this process is slow. If LSM particles are not connected well, charge transfer process is slow down, and reactions 5.2 and 5.4 may be the rate-determining steps. Reaction 5.3 is dominant if the diffusion of oxygen adsorbed species along the LSM

is slow which is supported by Mitterdorfer et al [89]. The reaction products play an important role in the charge transfer process at the TPB, reaction 5.4, as they reduce the TPB area. This reaction then occurs over a smaller area. As reaction 5.1 is sensitive to oxygen partial pressure therefore it can be identified. However, reaction 5.4 is insensitive to oxygen partial pressure.

Takeda et al. [195] and Siebert et al. [196] have suggested that the rate-determining step is the dissociation of adsorbed oxygen molecules to oxygen atoms. This reaction is shown below as reaction (5.5)

$$O_{2,ad} \rightarrow 2O_{ad} \qquad \text{-----} \quad 5.5$$

Ostergard and Mogensen [197] have proposed three reaction mechanisms as the rate-determining step according to the frequency of the semi-circle. At high frequencies, the charge transfer of oxygen ions from the TPB to the oxygen vacancies in the electrolyte process, reaction 5.4, is slow. The semi-circle at intermediate frequencies is attributed to reaction 5.5 and that at low frequencies is responsible to the diffusion of oxygen ions to the TPB which is reaction 5.3.

For LSMY, the microstructure reveals a porous layer of LSM which is well connected. The layer is thin enough (5 microns) that the diffusion of oxygen to the TPB is not the rate-determining step. The remaining step is thus the charge transfer process. Investigations on the reaction products can be carried out using a high-resolution electron microscopy technique. Due to the nature of research, this work has not been studied in this thesis.

At high cathodic polarisation (>160 mV), LSM behaves as a mixed conductor at high temperature [198]. The diffusion limitation disappears at high cathodic overpotential [194].

5.3 SUMMARY

The electrical conductivity of LSM deposited at various process parameters has been examined. The relationship between process/microstructure/property can be established that the powdery film deposited at high temperature show a high electrical conductivity while the activation energy is also high. The lower deposition temperature results in a porous film which has lower electrical conductivity but low activation energy.

Two modifications of LSM have been proposed by improving the microstructure and composition. The lateral electrical conductivity of LSM has been improved by depositing a duplex structure which has thin fine particles next to the electrolyte interface and thick large particles on top using FAVD technique. This type of improved LSM shows better conductivity than the La deficiency LSM, $La_{0.61}Sr_{0.18}MnO_3$ at high temperature. The activation energy varies with the change in microstructure. However, this duplex LSM has greater ASR than the La deficiency LSM. The rate-determining step that dominates the interfacial reaction cannot be concluded at this state without further investigations.

The electrical properties examined from the improved LSM deposited using FAVD technique are compared favourably with LSM films fabricated from conventional sintering routes.

Chapter 6 : IMPROVED CATHODE

In this chapter, the main concentration is on an improvement of a cathode for SOFCs. In stead of using the conventional cathode material, LSM, a mixed ionic-electronic conductor such as $La_{0.8}Sr_{0.2}CoO_3$ (LSC) was introduced. It has been reported by several researchers that this material exhibits a larger ionic and electronic conductivity than LSM [110,126,130,199]. LSC has been reported to react with YSZ electrolyte, therefore, an interlayer of either $Ce_{0.8}Gd_{0.2}O_{1.9}$ (CGO) or $Ce_{0.74}Y_{0.26}O_{1.87}$ (YDC) was deposited as a thin layer on YSZ substrate prior to the deposition of porous LSC layer. The YSZ substrate was the same substrate used in the previous chapters. These two types of interlayer are a good ionic conductor at high temperatures (> 500°C) and also, the coefficients of thermal expansion are in between those of YSZ and LSC [177]. These help to minimise the thermal mismatch in a cell and moreover, act as a diffusion barrier between YSZ and LSC.

An interlayer of YDC between YSZ and LSM has been reported to improve the interfacial performance and hence improving the overall power density of a cell [200]. Chen et al [121], Horita et al [201], Jacobson et al [202], and Bauza et al [203] have suggested an improved YSZ electrolyte by using an interlayer of thin dense doped-ceria film in between cathode and electrolyte. It was appropriate, therefore to investigate the behaviour of CGO and YDC interlayers prepared by FAVD.

Five combinations of cathodes and interlayers of LSC on CGO, LSC on YSZ, LSC/CGO on YSZ, LSC/YDC on YSZ, and LSM/YDC on YSZ prepared using FAVD have been investigated using SEM for the microstructure, XRD for phases present, dc 4-point (Van der Pauw) for lateral electronic resistivity, and AC-impedance for area specific resistivity (ASR). They have been compared after deposition and after certain periods of annealing at 900°C in air.

6.1 CGO INTERLAYER ON YSZ

There are two ways for the deposition of two layers on both sides of a pellet substrate to form a symmetrical cell. If one side of a pellet is designated *a*, and the other side is designated *b*, the deposition either follows pattern CGO*a*-CGO*b*-LSC*b*-LSC*a*, (abba), or pattern CGO*a*-LSC*a*-CGO*b*-LSC*b*, (aabb). When there is a change from side *a* to side *b*, the substrate was physically turned over *in situ*.

The near optimum deposition conditions of CGO and LSC were investigated and tested. The deposition parameters are summarised in Table 6.1. The flow rate of the precursor for the deposition of CGO was fixed at 12 ml/min, but that of LSC was varied between 10 and 12 ml/min. In addition, the deposition temperatures were controlled by varying the flame distance from the substrate whereby varying the distance of the combustion zone from the substrate.

Table 6.1 : Deposition parameters of CGO and LSC.

Parameters	CGO	LSC
Ratio of ethanol/water	70/30	75/25
Distance between the spray nozzle and substrate (cm)	12	12
Pressure of compressed air (psi)	22	22
Concentration of the precursor in the solution (mol)	0.05	0.05

The deposition descriptions and comments of CGO/LSC interlayer combination are listed in Table 6.2.

Table 6.2 : Descriptions and comments of CGO/LSC films.

Sample	Pattern	Deposition temperature of CGO (°C)	Deposition temperature of LSC (°C)	Flow rate of precursor* (ml/min)
CG/LC10	*abba*	690-750	700-780	10
CG/LC30	*abba*	670-740	600-680	10
CG/LC97	*abba*	680-750	640-700	10
CG/LC11	*abba*	700-800	730-800	12
CG/LC14	*aabb*	680-730	650-730	10
CG/LC17	*aabb*	670-730	700-750	12

* This flow rate is for the precursor for the deposition of LSC.

The deposition temperature of CGO layers were in the same range for all the samples, however, those for the deposition of LSC were increased as the flow rate increased. The results from dc 4-point and AC-impedance measurements were plotted using the same procedure as explained in Chapter 5, in which the values at 800°C and 900°C were extrapolated from the straight lines obtained according to an Arrhenius type equation. These values are summarised in Table 6.3. The figures after 'CG/LC' are only the sample code and they have no difference in the compositions.

Table 6.3 : Electrode ASRs and lateral electrical resistivities (ρ) of CGO/LSC films.

Samples	ASR 800°C (Ω cm^2)	ASR 900°C (Ω cm^2)	Activation energy (eV)	ρ800°C (Ω cm)	ρ900°C (Ω cm)	Activation energy (eV)
CG/LC10	0.0173	0.0036	1.81	0.0094	0.0083	0.22
CG/LC30	0.0365	0.0113	1.36	0.0192	0.0177	0.18
CG/LC97	0.0602	0.0173	1.45	0.0251	0.0217	0.26
CG/LC11	0.7290	0.3660	0.84	0.0690	0.0590	0.27
CG/LC14	0.0472	0.0180	1.14	0.0142	0.0127	0.21
CG/LC17	0.0340	0.0104	1.38	0.0320	0.0265	0.30

The interpretations of these results have to be taken into consideration together with the microstructures and phases including any reaction products present between the interlayers. All LSC films were porous. Nevertheless, a slight change in deposition temperature caused changes in microstructure and leading to significant changes in the electrical properties, especially the ASR. As mentioned in the last chapter, the ASR is sensitive to any changes at the TPBs. Therefore, the change in microstructure and any reaction products at the TPBs have to be determined. In addition, the thickness of the interlayers affected the diffusion of oxygen gas to the TPB and it is summarised in Table 6.4 together with phases detected from XRD patterns. Surface morphology and cross-section of these samples are shown in Fig. 6.1. Amount of the precursor solution used was varied according to the required thickness of the film.

The distinctive difference between the two patterns of deposition is that those films deposited from pattern *aabb* have a trace of La_2O_3 phase in the film. However, the presence of this phase does not change the electrical properties significantly as the main contrubution is from the microstructure. In general, the LSC layer consists

of combinations of LSC compositions; $La_{0.8}Sr_{0.2}CoO_3$ (LSC0.8), $La_{0.9}Sr_{0.1}CoO_3$ (LSC0.9), $La_{0.6}Sr_{0.4}CoO_3$ (LSC0.6), $La_{0.2}Sr_{0.8}CoO_3$ (LSC0.2), and $LaCoO_3$, although the precursor solution was made up to the ratio of La:Sr:Co = 0.8:0.2:1.

Table 6.4 : Phases present and thickness of CGO/LSC interlayers.

Samples	Phases	Thickness of LSC (μm)
CG/LC10	LSC0.8 LSC0.2	5
CG/LC30	$LaCoO_3$ LSC0.2 LSC0.6	5
CG/LC97	LSC0.8 LSC0.9	10
CG/LC11	-	13
CG/LC14	LSC0.9 LSC0.6 LSC0.2 La_2O_3	6
CG/LC17	LSC0.9 LSC0.6 LSC0.2 La_2O_3	7

Numbers after LSC refer to the value of 1-X from $La_{1-X}Sr_XCoO_3$.

The thickness of CGO layer is around 1 micron, apart from sample CG/LC11 which is about 3 microns thick.

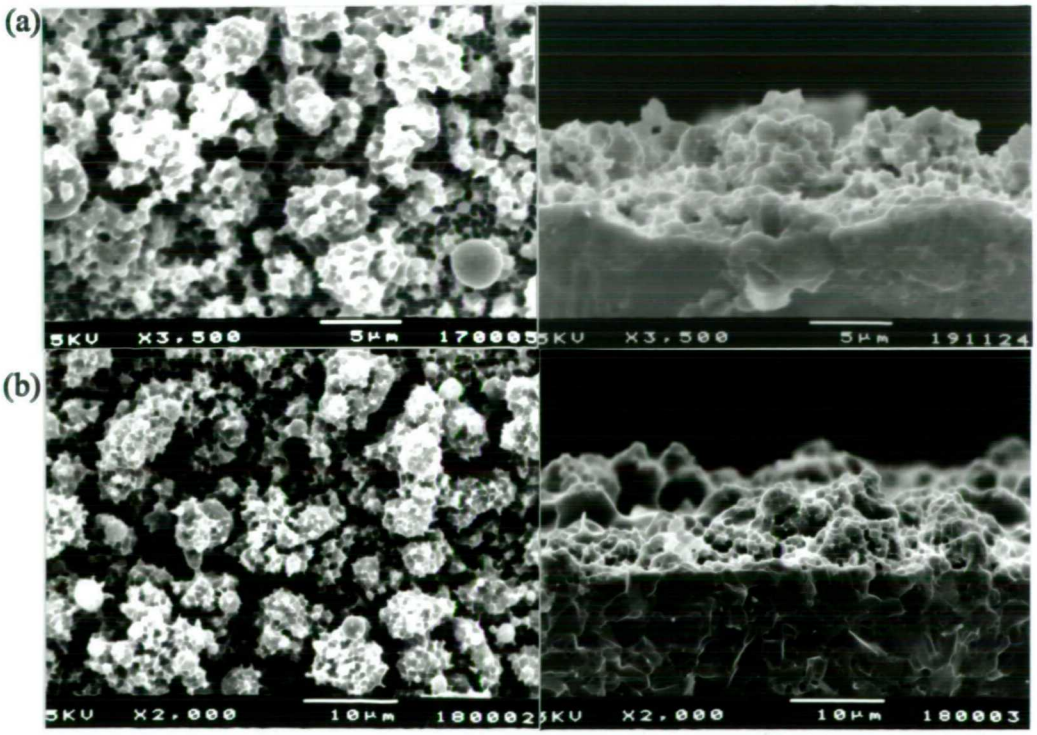


Fig. 6.1 : Surface morphology and cross-sections of (a) CG/LC10 and (b) CG/LC30.

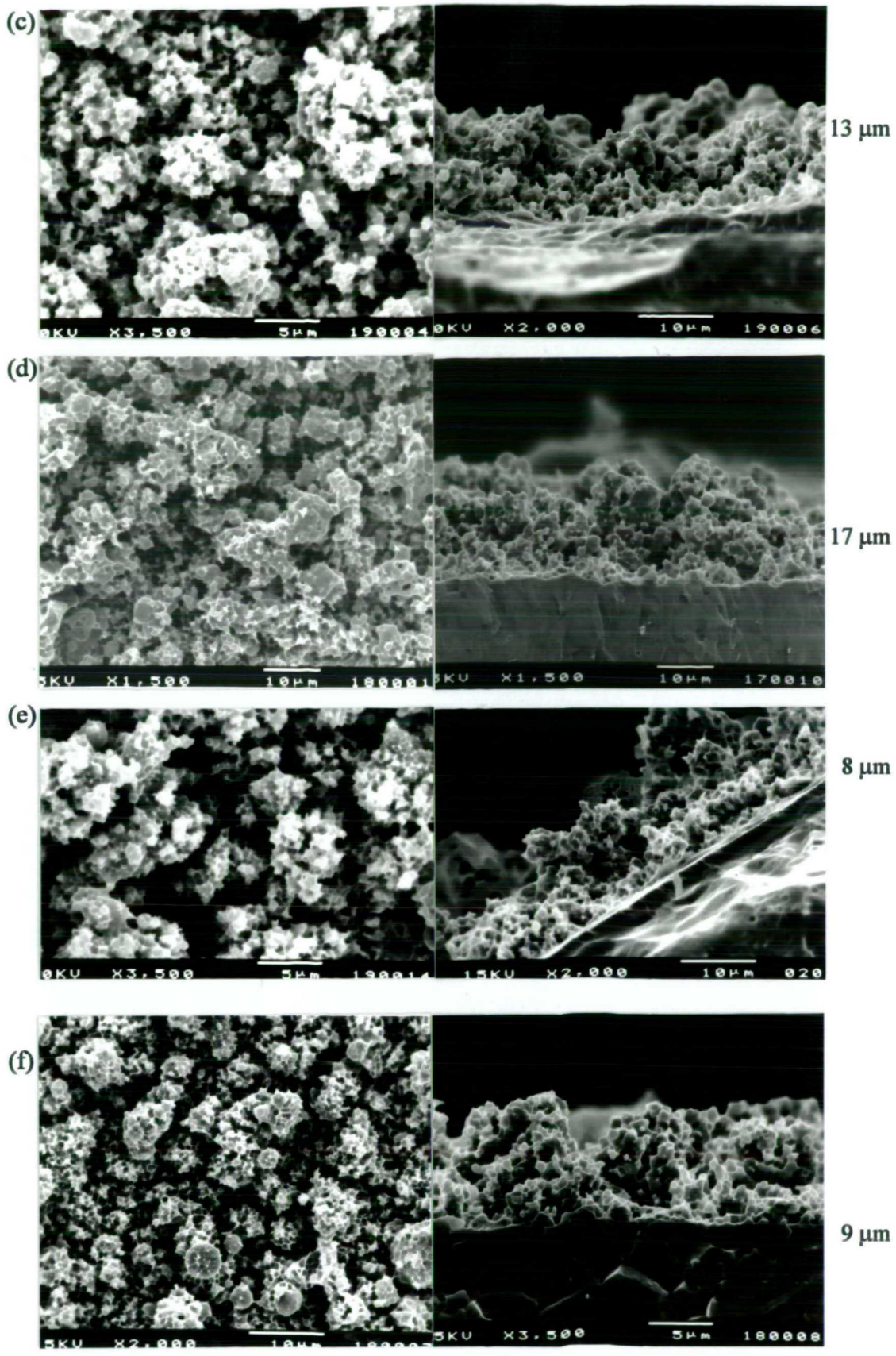


Fig. 6.1 : Surface morphology and cross-sections of (c) CG/LC97, (d) CG/LC11, (e) CG/LC14, and (f) CG/LC17.

Films of this combination did not show any cracks or spallation between layers. The adhesion was also very good.

It is obvious that the best performance was obtained from sample CG/LC10. It had a uniform porous structure and 5 microns size agglomerates of fine particles (0.5 microns). As the LSC film was relatively thin (5 microns), the diffusion of gaseous oxygen to the TPBs was fast, then the ASRs were small. The LSC layer was uniformly connected, therefore, the lateral electrical resistivity was very low. The poorest result was from sample CG/LC11, which had the thickest layers of CGO (around 3 microns) and LSC (around 13 microns). The large size of agglomerates (10 microns) reduced the TPB area tremendously, yielding very high ASRs. Moreover, large gaps between agglomerates resulted in a poor planar connection; therefore, the lateral electrical resistivity was high. The activation energies of these samples are comparable with the reported value of 1.45 eV from the system of $La_{0.6}Sr_{0.4}CoO_3$/ceria/$La_{0.6}Sr_{0.4}CoO_3$ [204].

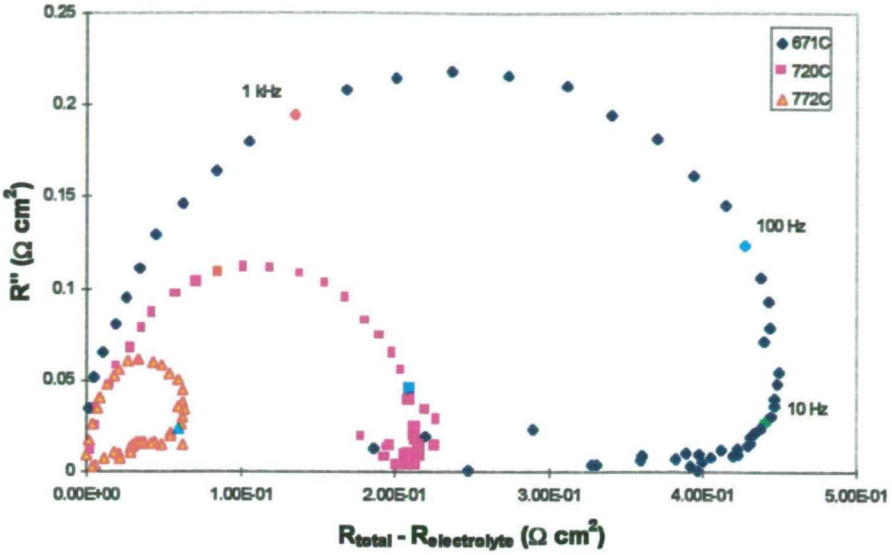
All other samples seemed to be in the same range of lateral electrical resistivity, depending on the connection between LSC particles. Low activation energy also indicated a good planar conductor. Sample CG/LC14 showed uniform porous structure but not very well connected from the cross-section view. As a result, the lateral electrical resistivity was higher than that of CG/LC10 with similar activation energy.

Samples with scattered LSC particles, such as CG/LC30 and CG/LC17, did not agglomerate as others. This type of microstructure help the diffusion of gaseous oxygen from air to the TPBs. Hence, the ASRs were relatively lower than others with agglomerates. The presence of La_2O_3 may contribute to the high ASR values of CG/LC17 and CG/LC14 as compared to the others that this phase around the TPB area reduces the reaction sites as it is a poor conductor. The activation energies of these two samples were very low.

Slight variations of deposition parameters yield a wide range of electrical properties films. Films must be deposited under well-controlled parameters. However, some parameters proved to be very difficult to control, which reduced the reproducibility of the films. This leads to errors in experiments from temperature fluctuation, resistance fluctuations and errors in calculations which influenc the reproducibilities of films. Nevertheless, films in the same range of electrical and microstructural properties could be reproduced.

AC-impedance plots of samples CG/LC10 and CG/LC11 at different temperatures are shown in Fig. 6.2 (a) and (b). All the plots for other samples are shown in The appendix. They have been plotted as a function of frequency when the y-axis refers to the imaginary resistance and the x-axis refers to the real resistance. The values on both axes are for a symmetrical cell, therefore, the actual ASR value is half that of the x-axis intercepts. These Real resistances are from the total resistance subtracted by the resistance due to the electrolyte and ohmic loss.

(a)



(b)

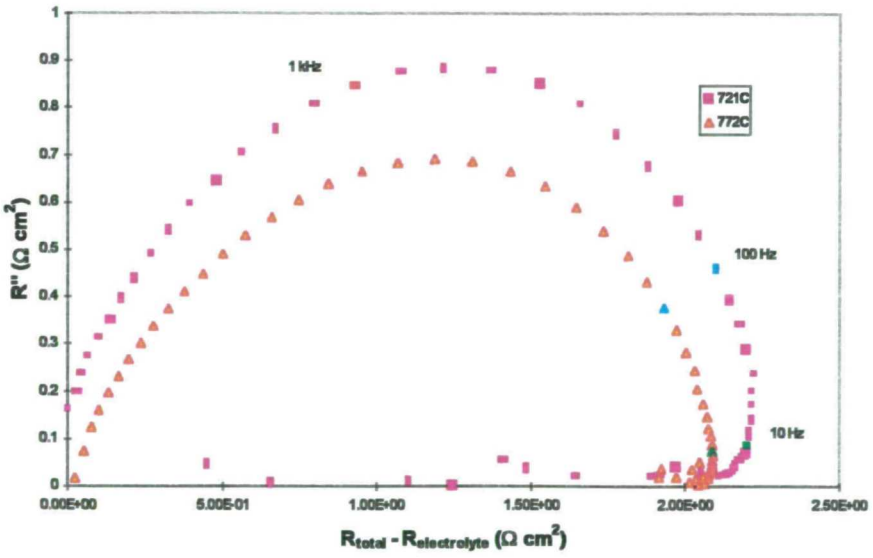


Fig. 6.2 : AC-impedance responses of (a) CG/LC10, (b) CG/LC11.

The semi-circles represent the number of rate-determining steps involved in the conductivity process. Traditionally, it is believed that the major contribution of the rate-determining reaction is the charge transfer process at the TPBs [205,206,207]. However, it is obvious that the AC responses from samples CG/LC30

and CG/LC14 show two semi-circles at high temperatures which refer to at least two rate-determining steps. The second semi-circle at low frequency end becomes more distinguished at higher temperature. Adler [204] has proposed that the oxygen adsorption and transport in the bulk of the mixed ionic-electronic conductor, may play a significant role in the electrode polarisation. The large faradaic capacitances (up to 1 F/cm^2) support this argument [208,209].

Samples CG/LC30 and CG/LC14 had relatively thin layers of LSC cathode, which was responsible for a low overall planar conductivity. In addition, the deposition temperatures were slightly lower than other samples. This may lead to the poor bulk ionic and electronic conductivity from the less crystalline phases (according to the general observations from Chapter 4), which results in poor oxygen adsorption and transport after all. The extrapolated ASRs for these two samples were from the contribution of both semi-circles. Nevertheless, if only the first semi-circle at the high frequency end is taken into account, these ASRs would be reduced by at least 10 %.

Equivalent circuits can be obtained from impedance data by using a suitable programme e.g. Boukamp. However, detailed analysis is not appropriate at this stage because a) complexity of microstructures, and b) model proposed by Adler suggests that splitting impedance values into separate circuits are not appropriate because the chemical and mass transport processes are coupled and interdependent.

6.2 YDC INTERLAYER ON YSZ

Tsai et al. [200] have reported an improvement of a cell power density for LSM cathode using an interlayer of YDC on both sides of YSZ. It is interesting to study whether this type of interlayer can improve the interfacial performance of LSC cathode system. An interlayer of YDC was deposited on YSZ substrate, then followed by a cathode layer of either LSM or LSC. The deposition parameters are listed in Table 6.5. The pattern of deposition was *aabb*.

Table 6.5 : Deposition parameters of YDC interlayer.

Process Parameters	YDC/LSM	YDC/LSC
Concentration of the precursor solution (mol)	0.05	0.05
Distance between the spray nozzle and substrate (cm)	12	12
Pressure of compressed air (psi)	22	22
Flow rate of precursor solution (ml/min)	12	12
Ratio of ethanol/water for YDC layer	75/25	75/25
Deposition temperature of YDC layer (°C)	830-890	850-920
Ratio of ethanol/water for cathode layer	70/30	75/25
Deposition temperature of cathode layer (°C)	750-800	740-810
Thickness of cathode layer (microns)	10	15

The thickness of the YDC layer in both samples is around 1 micron. The surface morphology and cross-section of these films indicated porous cathode layers in Fig. 6.3 (a), (b), (c), and (d). A back-scattered EM was used to analyse the phases present in the films qualitatively. This showed a homogenous layer in both YDC/LSM (YC/LM) and YDC/LSC (YC/LC).

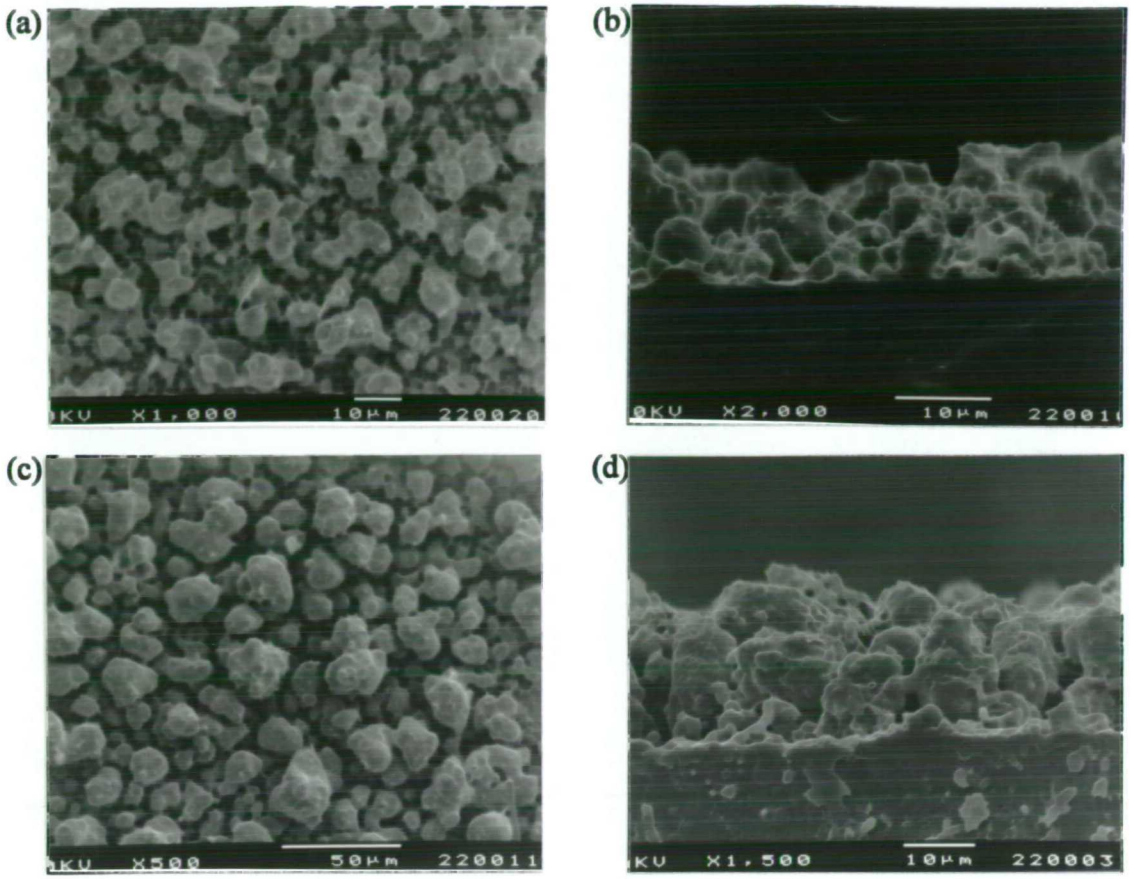


Fig. 6.3 : (a) Surface morphology and (b) cross sections of YC/LM. (c) and (d) are as above for YC/LC.

The lateral electrical resistivities and ASRs for electrode were measured for both samples and plotted in the same manner as described previously for LSMs and CG/LCs. The data are summarised in Table 6.6.

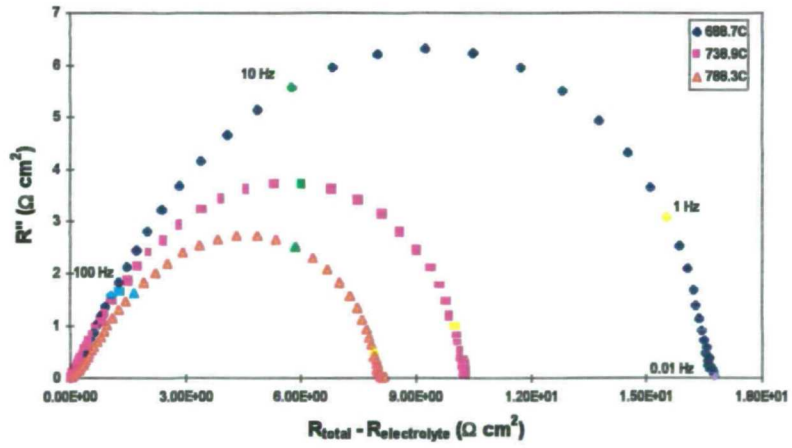
Table 6.6 : Lateral electrical resistivities and ASRs of YC/LM and YC/LC.

Samples	YC/LM	YC/LC
ASR 800°C (Ω cm^2)	2.9585	0.0267
ASR 900°C (Ω cm^2)	1.3275	0.0097
$\rho_{800°C}$ (Ω/cm)	0.0597	0.0148
$\rho_{900°C}$ (Ω/cm)	0.0480	0.0135

The sample YC/LM was comparable with other unmodified LSMs for the lateral electrical resistivity while the ASR values have been improved. However, when LSC was used as a cathode material instead of LSM, the ASRs was improved 2 orders of magnitude, whilst ρ have been reduced at least 3 fold. These results are expected, as LSC is a better electronic and ionic conductor than LSM.

AC-impedance responses of YC/LM and YC/LC are shown in Fig. 6.4 (a) and (b). For YC/LM, only one semi-circle is present at each temperature, which refers to only one rate determining step as discussed in a previous chapter. Nevertheless, two semi-circles are present at each temperature for YC/LC. They become more distinguishable and dominant at high temperatures. It was suggested that the second semi-circle at the low frequency end corresponds to the gas phase diffusion [204]. This will be discussed later in section 6.3.

(a)



(b)

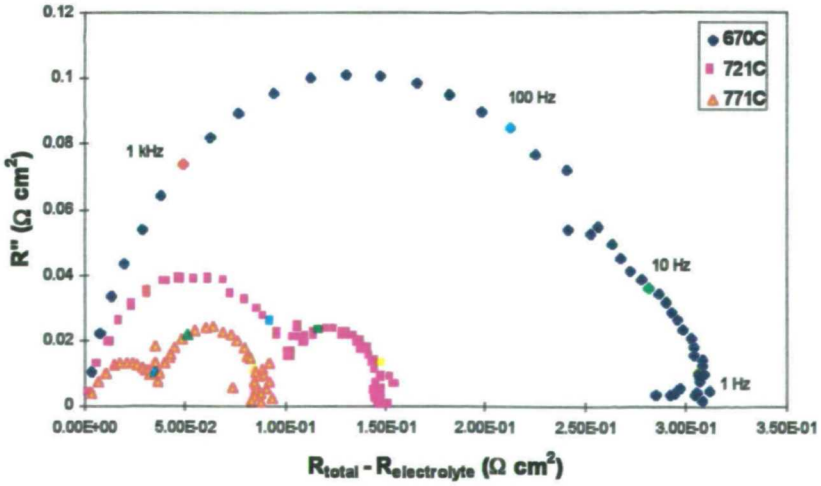


Fig. 6.4 : AC-impedance responses of (a) YC/LM and (b) YC/LC.

6.3 EFFECT OF ANNEALING TIME

All the aforementioned samples were annealed in air at 900°C for certain hours in which the ASRs were measured using an AC-impedance spectroscopy. The temperature 900°C was selected as this temperature is slightly higher than a high temperature fuel cell operating temperature (700°C - 850°C); therefore, any deleterious effects could be visualised over a shorter period of time. In addition to an AC-impedance measurement, all films were analysed using an XRD to examine any phases of reaction products present.

For comparison, porous LSC films were deposited on CGO and YSZ substrates to make two symmetrical cells. They are designated LSC12 and LSC30 for the CGO and YSZ substrates, respectively. Deposition parameters are the same as those for the deposition of LSC in sample YC/LC, but the deposition temperature of LSC12 was 660°C-720°C and LSC30 was 700°C-760°C. All samples mentioned in this section are the best performance sample of each batch. They were annealed for 10, 20, 36, and 100 hours for all samples apart from the CG/LC10 which was annealed for 4, 14, 30, and 96 hours.

6.3.1 LATERAL ELECTICAL RESISTIVITY

The lateral electrical resistivities of each sample were measured before and after annealing for 10 hours at 900°C. The data provided in Table 6.7 are those extrapolated at 800°C and 900°C. The activation energy are listed in Table 6.8.

Table 6.7 : Lateral electrical resistivities, ρ, (Ω/cm) of selected combinations of cathode/interlayer films.

Annealing time (hours)	Samples	LSC30	LSC12	CG/LC10	YC/LC	YC/LM
0	$\rho_{800°C}$	-	0.0097	0.0095	0.0148	0.0597
0	$\rho_{900°C}$	-	0.0086	0.0085	0.0135	0.0480
10	$\rho_{800°C}$	0.0200	0.0133	0.0149*	0.0235	0.0749
10	$\rho_{900°C}$	0.0186	0.0105	0.0120*	0.0204	0.0595

* The annealing time for CG/LC10 is 4 hours instead of 10 hours.

Table 6.8 : Activation energy of the reciprocal of ρ in eV, of selected combinations of cathode/interlayer films.

Annealing time (hours)	LSC30	LSC12	CG/LC10	YC/LC	YC/LM
0	-	0.23	0.22	0.20	0.33
10	0.18	0.36	0.34*	0.25	0.35

* The annealing time for CG/LC10 is 4 hours instead of 10 hours.

All the microstructures of these five samples are shown in Fig. 6.5.

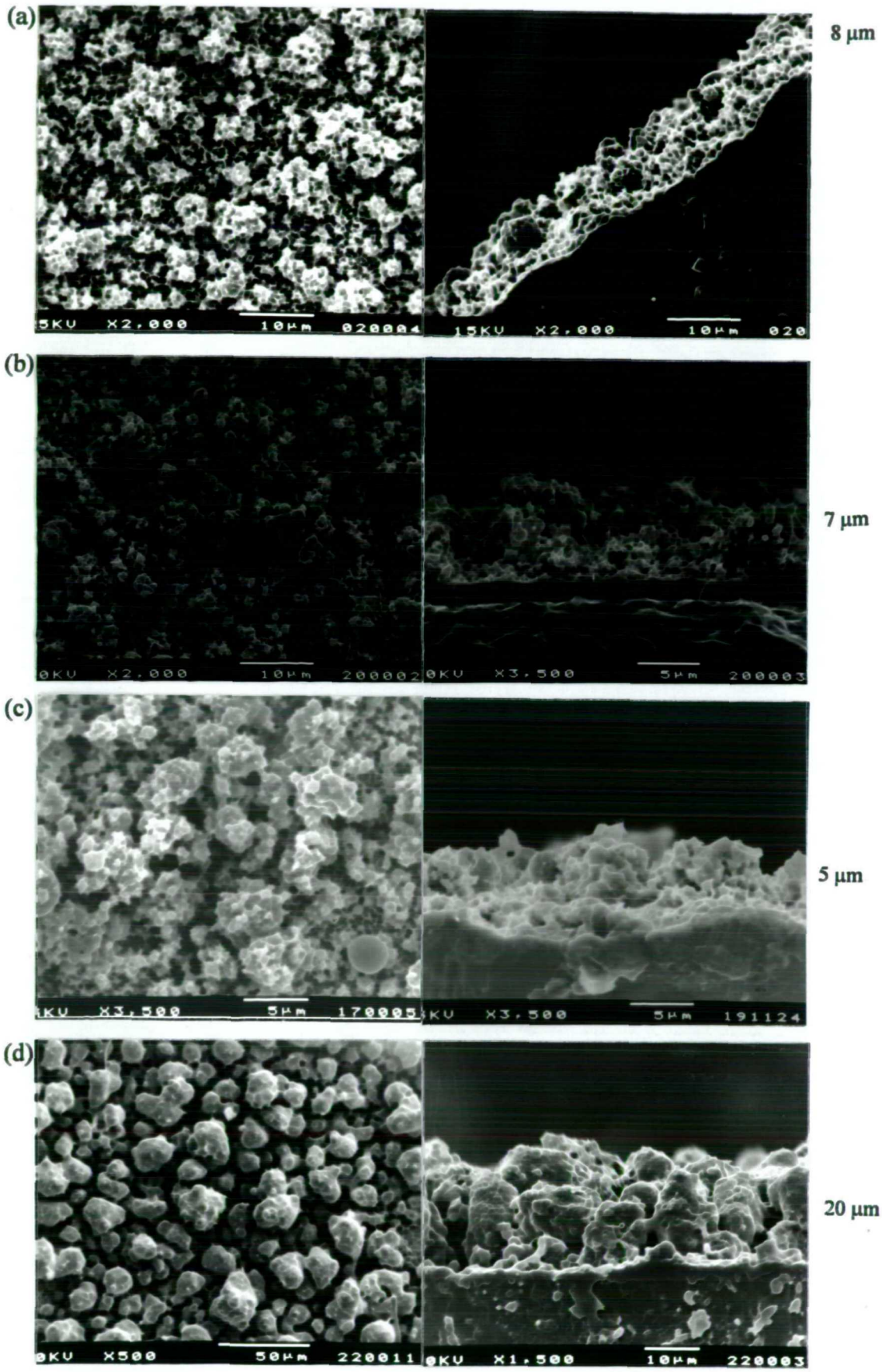
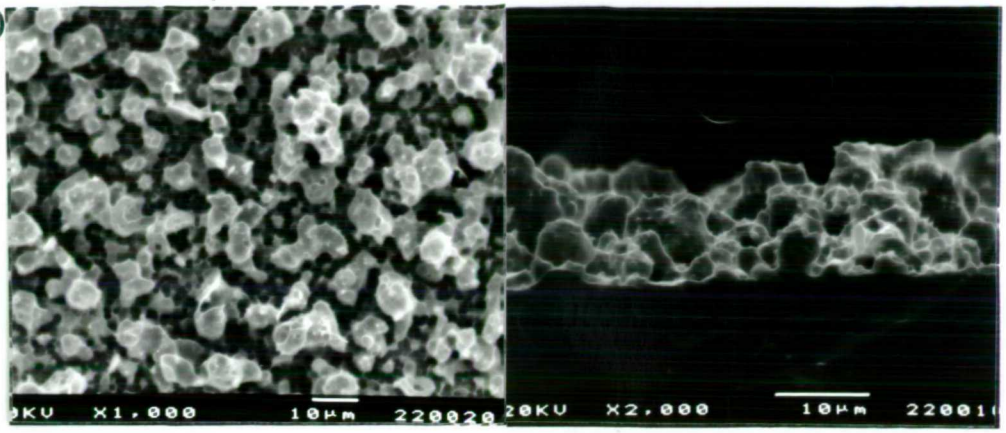


Fig. 6.5 : Surface morphology and cross-section of (a) LSC30, (b) LSC12, (c) CG/LC10, (d) YC/LC, and (e) YC/LM (see overleaf).

(e)



12 µm

Fig. 6.5 : Surface morphology and cross-section of (e) YC/LM.

From Table 6.7 and Fig. 6.5, the values of ρ depended on the microstructure of the cathode layer. Among the LSC cathode, the LSC layer from sample YC/LC consisted of large particles (10-20 microns), therefore, the connection between particles and the conductivity were rather poor. The values of ρ from sample CG/LC10 were very similar to those from sample LSC12 which refered to the similarity in microstructures. After annealing, all samples exhibited increased resistivities. These may be due to the microstructure that after annealing, films have been scratched from the mechanical pressure of AC and dc measurements. The microstructures of films after annealing at certain hours are shown in Fig. 6.6. In general, all the films are more porous. The mechanical damage is obvious for sample YC/LC that particles are not uniformly distributed. Sample LSC12 (LSC on CGO substrate) shows the least effect of annealing on the microstructure as both before and after annealing are very similar. However, as expected from the high thermal expansion mismatch between LSC and YSZ, the LSC film from sample LSC30 (LSC on YSZ substrate) was very powdery after annealing and the particles were finer than before (~0.5 microns compared with ~5-10 microns agglomerates).

The XRD patterns for all samples before annealing have indicated only peaks from various compositions of $La_{1-X}Sr_XCoO_3$ and $LaCoO_3$. After annealing, traces of La_2O_3 have been detected in every sample except YC/LM which shows no reaction products at all throughout the annealing process. However, the La_2O_3 phase

disappeared after annealing for 30 hours for all samples, only for LSC30 which it was present until after 100 hours annealing and disappeared after 600 hours while a phase of $SrZrO_3$ was detected instead. The XRD patterns are shown in the appendix.

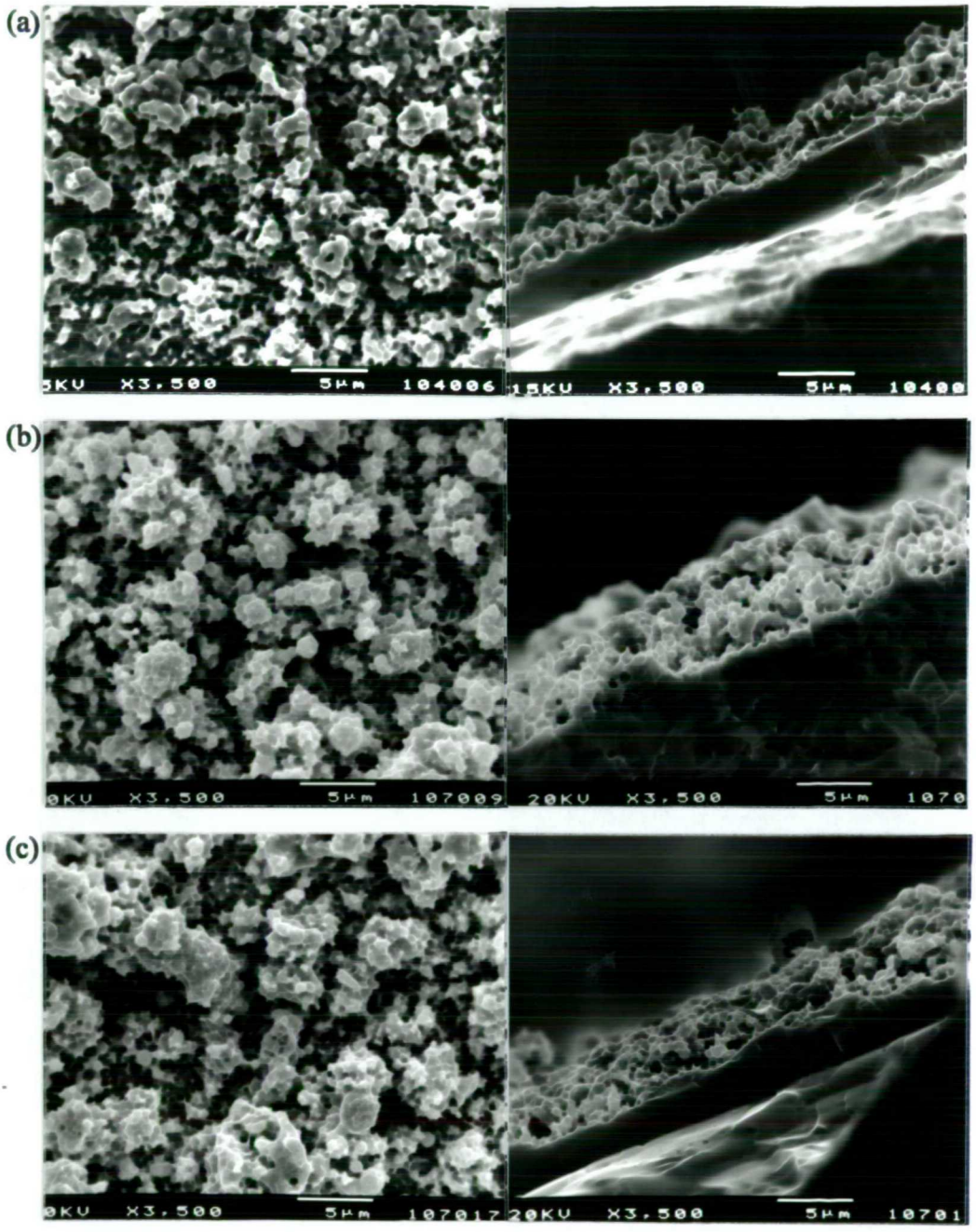


Fig. 6.6 : Surface morphology and cross-section of (a) LSC30, (b) LSC12, (c) CG/LC10, (d) YC/LC and (e) YC/LM after annealing (see overleaf).

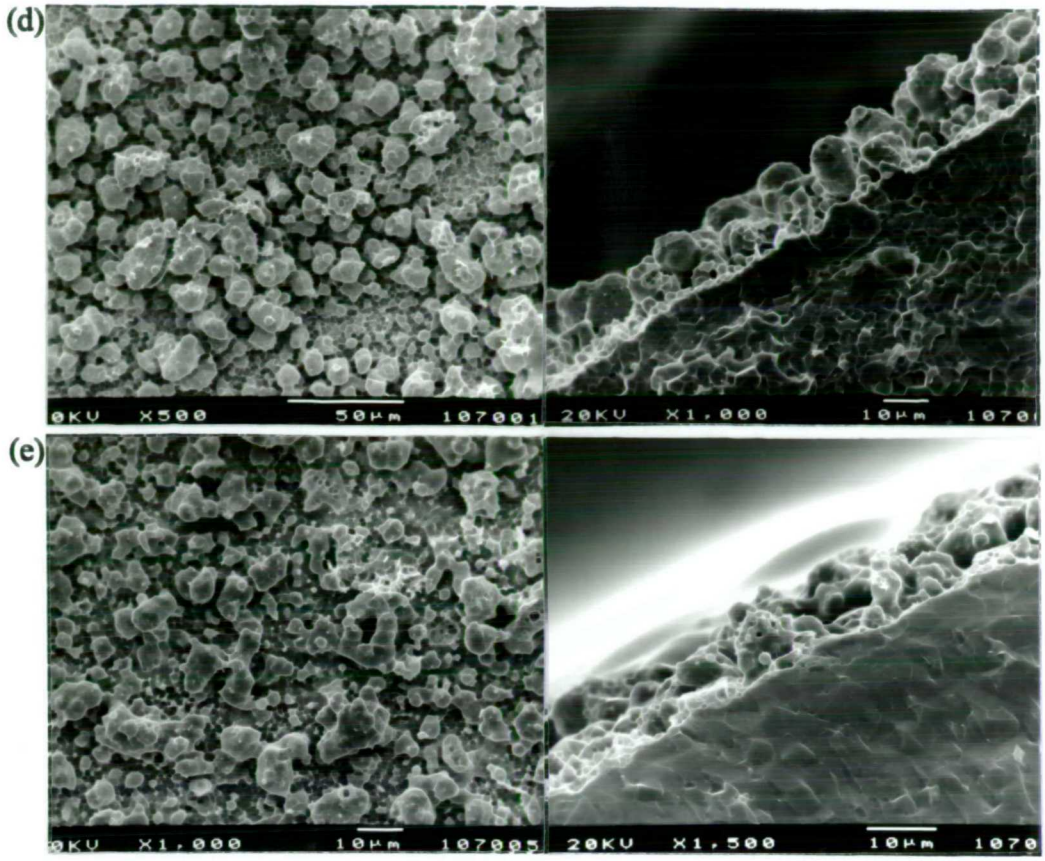


Fig. 6.6 : Surface morphology and cross-section of (d) YC/LC and (e) YC/LM after annealing.

6.3.2 AREA SPECIFIC RESISTIVITY

The ASRs of all samples were measured after each annealing for electrode, bulk and grain boundary to enable comparisons to be made about the behaviour of the electrode. The electrode ASRs are separated from those bulk and grain boundary ASRs as the electrolyte material influences the latter cases.

6.3.2.1 Electrode ASR

The values of ASRs at 800°C and 900°C were plotted in Fig. 6.7 (a) and (b) for LSC30, LSC12, CG/LC10, YC/LC, and YC/LM.

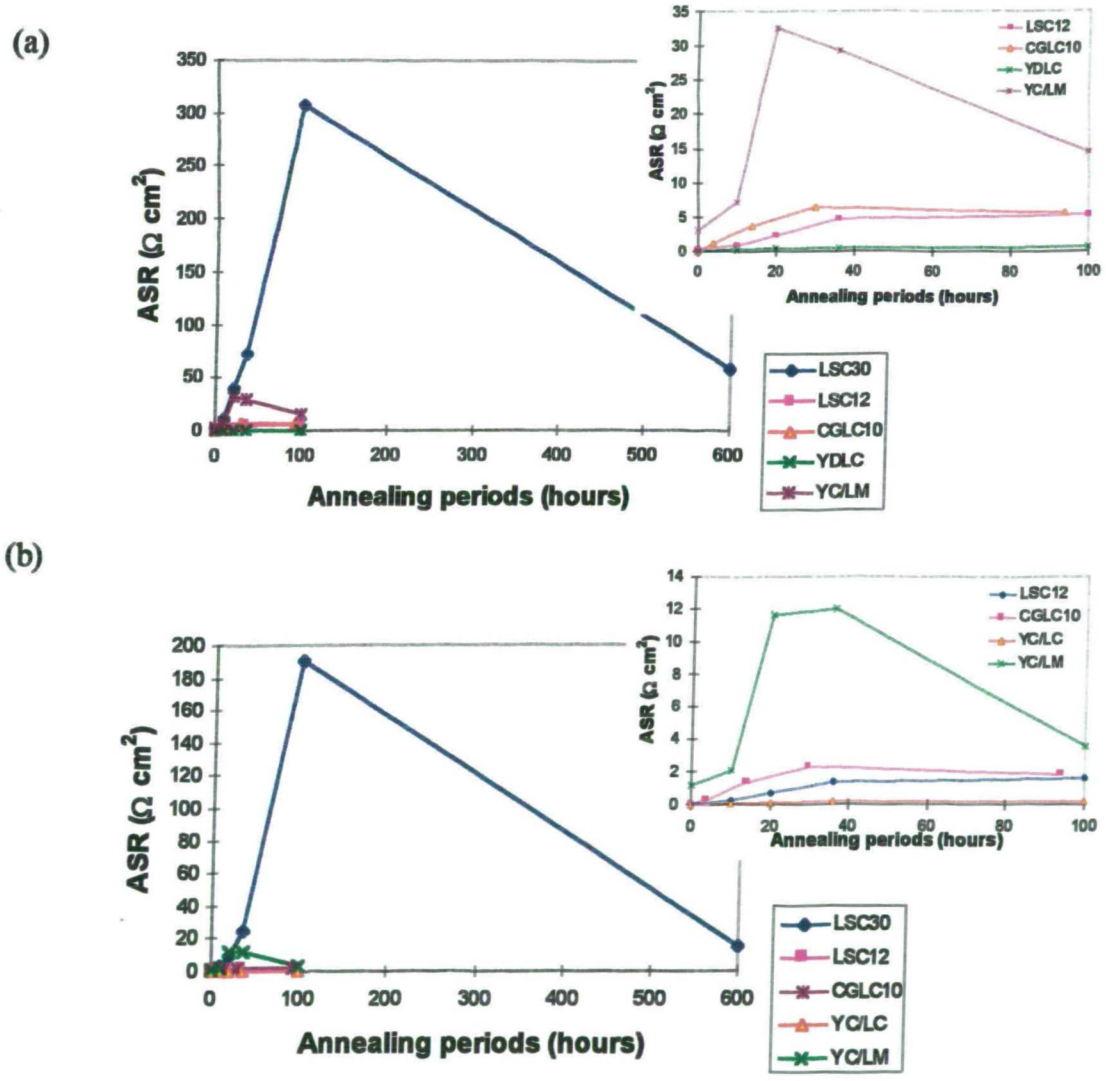


Fig. 6.7 : Plots of electrode ASRs after certain annealing periods at (a) 800°C and (b) 900°C for LSC30, LSC12, CG/LC10, YC/LC, and YC/LM.

From the plots in Fig. 6.7, it is obvious that the most incompatible combination is between LSC and YSZ as the ASR increases many fold with annealing time, although it drops after 600 hours. This may be due to the reaction products at the interface and also the very high thermal mismatch between these two materials. La_2O_3 phase, which is detected after annealing, might play a great role in this part that many peaks are detected after 100 hours in which the sample shows the highest ASR. After 600 hours, this phase no longer exists but many peaks of $SrZrO_3$ phase are detected instead although this material is used as a protonic conductor. This may correspond to the drop of ASR. The same reason is applicable to explain the drop of ASR for sample YC/LM after annealing for 100 hours.

The sample CG/LC10 has higher ASR than LSC12. The reaction products detected from XRD might not be sufficient to explain this effect. Although, LSC is very reactive with YSZ, a layer of thin dense CGO plays a great role as a diffusion barrier and hence the ASRs after 100 hours for LSC12 and 94 hours for CG/LC10 are very close. The most compatible combination is the LSC/YDC/YSZ system. The ASRs after 100 hours of annealing are still acceptable for the SOFC application that the target set by Steele is 0.15 Ωcm^2 [63]. Undesirable reaction products have not been detected at all. However, any traces of reaction product phases below 5% of the total amount in the film cannot be detected using XRD technique. This tiny amount of reaction products may contribute to the increase of the ASRs after annealing.

Selected AC impedance responses of each sample after certain hours of annealing are shown in Figs. 6.8, 6.9, 6.10, 6.11, and 6.12 which represent samples LSC30, LSC12, CG/LC10, YC/LC, and YC/LM, respectively. The complete responses are shown in the appendix.

In Fig. 6.10 (a), the observation of abnormal fluctuations at low frequencies and very low resistance could be associated with the impedance response of the measuring equipment.

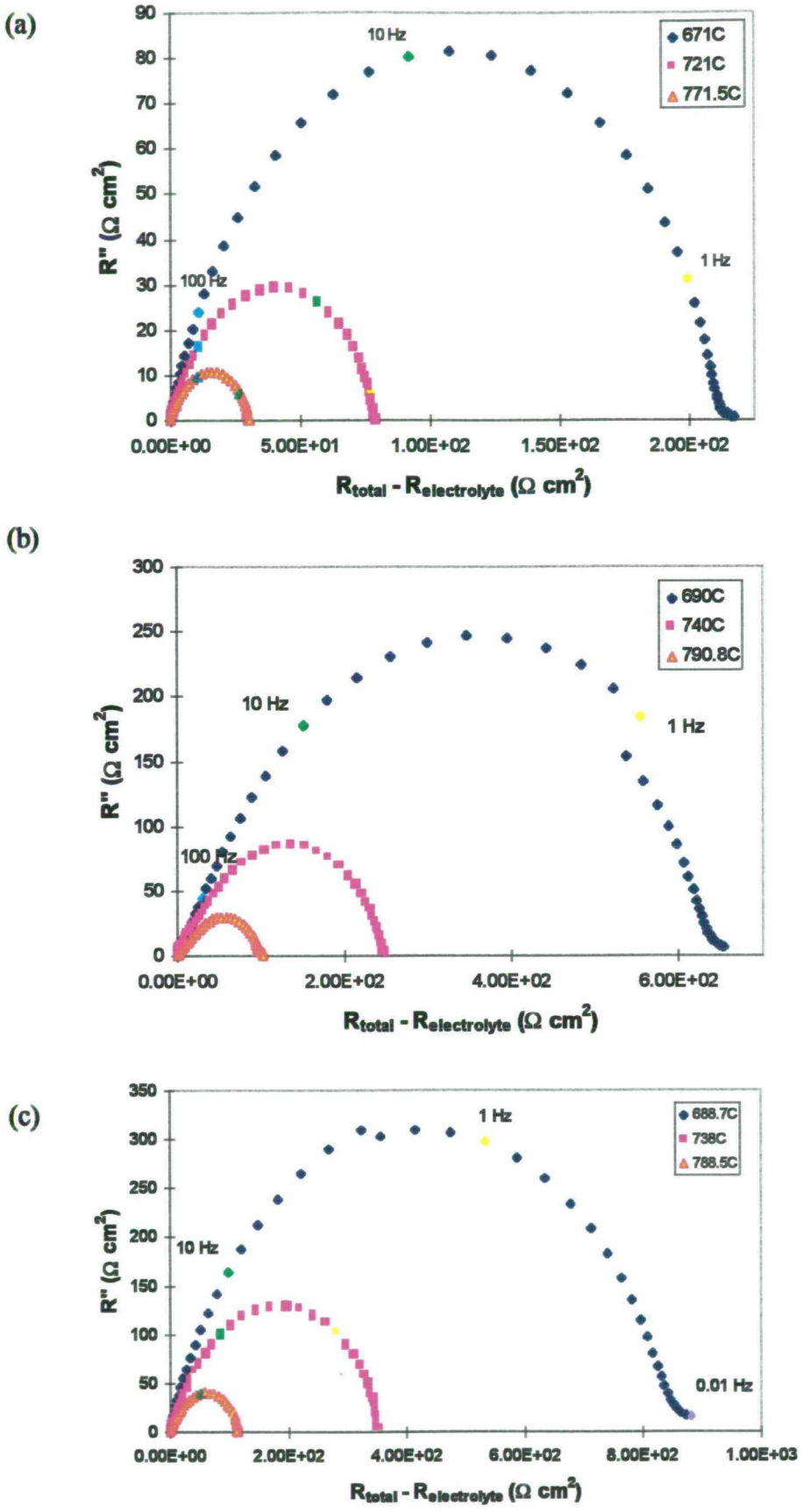


Fig 6.8 : AC-impedance responses of sample LSC30 after annealing for (a) 10 hours, (b) 100 hours, and (c) 600 hours.

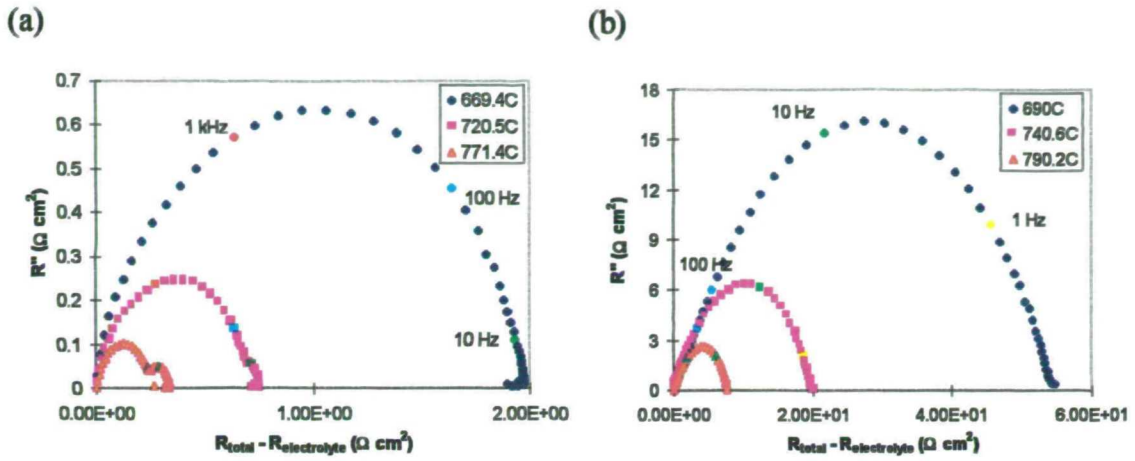


Fig 6.9 : AC-impedance responses of sample LSC12 (a) as deposited and (b) after annealing for 100 hours.

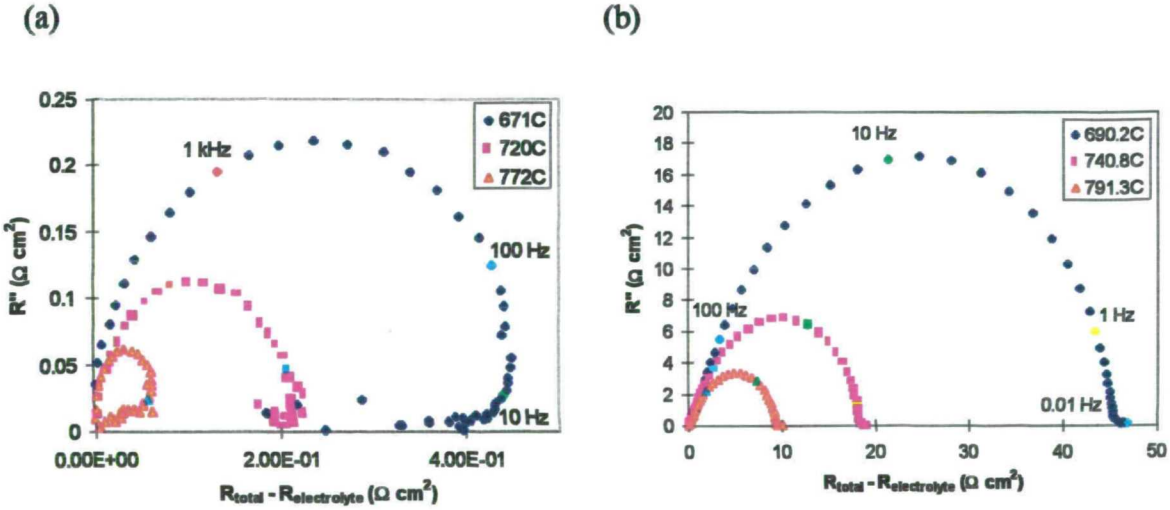


Fig 6.10 : AC-impedance responses of sample CG/LC10 (a) as deposited and (b) after annealing for 94 hours.

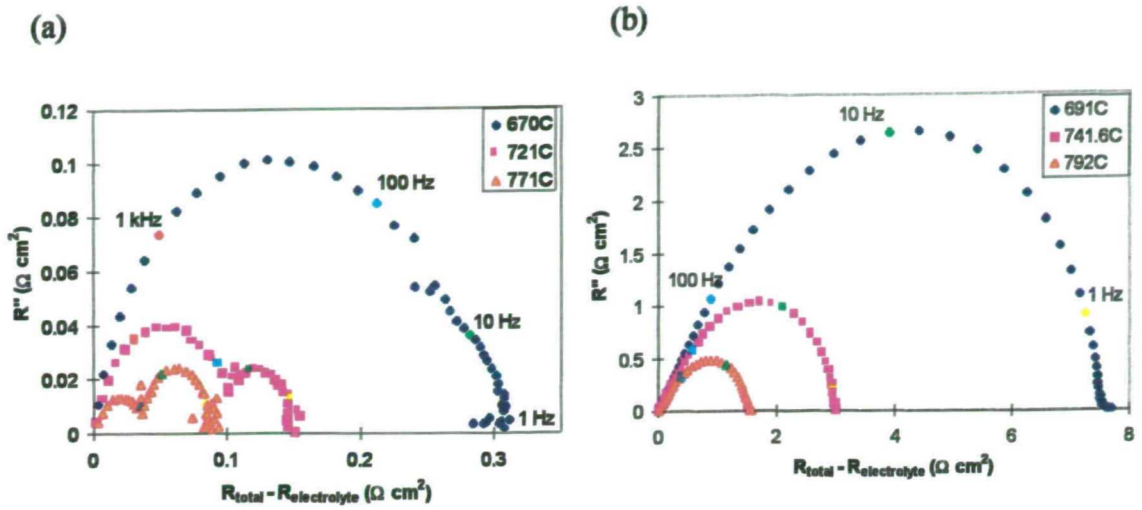


Fig 6.11 : AC-impedance responses of sample YC/LC (a) as deposited and (b) after annealing for 100 hours.

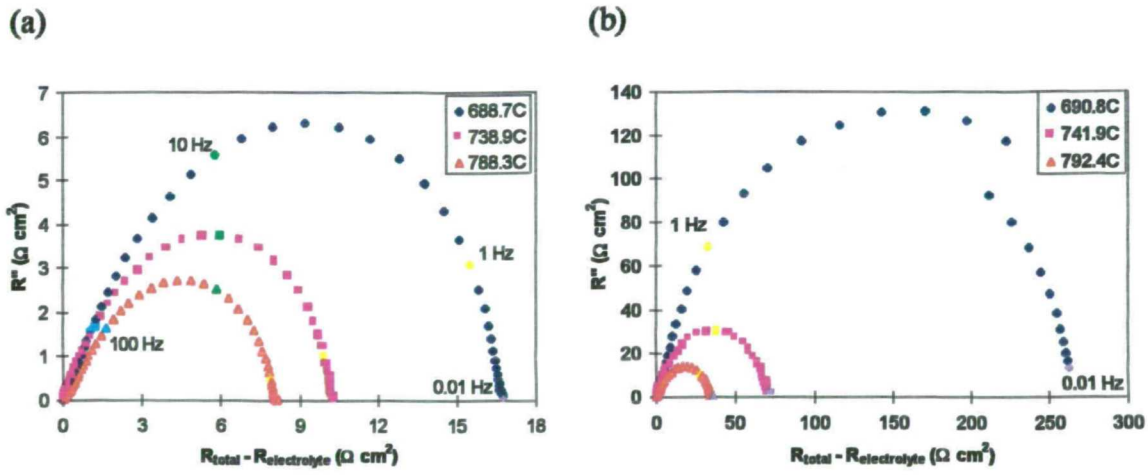


Fig 6.12 : AC-impedance responses of sample YC/LM (a) as deposited and (b) after annealing for 100 hours.

The number of semicircles in the AC-impedance response indicates the rate determining steps involved in the oxygen reduction between cathode, electrolyte and gas phase. There is only one semi-circle present in most cases from Fig. 6.8 - 6.12. The capacitance from each semi-circle can be used to indicate the type of reaction process that dominates the overall reaction. These capacitance and ASR values may

vary with different electrolyte materials. Since the capacitances are in the range of microfarad/cm^2, the rate-determining step is believed to be dominated by the charge transfer process at the interface. However, as deposited samples LSC12 and YC/LC show the second semi-circle at high temperature at the low frequency end. The capacitances are in the range of farad/cm^2 which suggests the diffusive process. For these two particular samples, the conclusion can be drawn that the charge transfer process dominate the rate determining step at relatively low temperature, and the oxygen diffusive process becomes dominant at high temperature (approximately 800°C). Nevertheless, this diffusive process is no longer dominant after annealing and the charge transfer remains the only rate-determining step for all samples. The responses from sample YC/LM show a 45° angle interception at the real axis at the high frequency end. This refers to the Warburg semi-infinite diffusion effect. The as deposited sample CG/LC10 shows an inductance loop at high temperature. There is no conclusive evidence for this phenomenon reported so far.

From these figures, the increase of ASRs after annealing cannot be attributed solely from the reaction products formed at the interface. Changes in microstructure can also occur during the annealing process due to the incompatibility in the coefficients of thermal expansion between layers. During the thermal cycling process, particles could be dislodged and the interface weakened, leading to reduced surface area contact. At the same time, after repeated mechanical pressure from the AC-impedance and dc 4-point measurements, the porous layers have been crushed at the surface, which decreases the thickness of films. As the film is relatively thinner than before annealing, oxygen diffusion through the bulk cathode layer is easier.

The activation energies of the reciprocal of ASRs of each sample after certain hours of annealing are listed in Table 6.9.

Table 6.9 : Activation energies (eV) of the reciprocal of ASRs after several annealing periods.

Annealing (hours)	LSC30	LSC12	CG/LC10	YC/LC	YC/LM
0	-	1.27	1.81	1.19	0.97
10	1.56	1.26	1.48	1.34	1.26
20	1.59	1.40	1.21	1.36	1.22
36	1.24	1.46	1.20	1.42	1.07
100	0.62	1.43	1.30	1.53	1.64

* The annealing periods of CG/LC10 are 0, 4, 14, 30, and 96 hour.

The activation energy of $La_{0.6}Sr_{0.4}CoO_3$/ceria/$La_{0.6}Sr_{0.4}CoO_3$ was reported by Adler [204] to be equal to 1.45 eV. This value is comparable with our observations for most of the LSC systems. The activation energy of YC/LM is also in the same range as those from Chapter 5 (activation energy of LSM0.61 is 1.24 eV). The most pronounced affect of annealing on the activation energy was observed for sample LSC30 that it decreased more than 2 fold. The change in the microstructure to be more powdery may correspond to this change. However, the ASR data vary with the electrolyte material used as well as the cathode microstructure. The activation energy was also shown to depend on the microstructure that it was 1.35 eV for a porous electrode and 1.66 eV for a dense electrode of $La_{0.6}Sr_{0.4}Co_{0.2}Fe_{0.8}O_{3-\delta}$ on CGO [210]. Our values for LSC12 are well within this range.

6.3.2.2 Electrolyte ASR

There are two main ASRs generated from the electrolyte which are from the grain boundary (gb) and the grain interior or bulk. These two aspects are discussed briefly in this section for the comparison between a single layer electrolyte (samples LSC30 and LSC12), and a double layer electrolyte (samples CG/LC10, YC/LC, and YC/LM). The semi-circles referring to these bulk and gb ASRs are apparent at relatively low temperatures, below 500°C. The bulk semi-circle is at the very high frequency end and the capacitance is in the range of below picofarad, whilst the gb semi-circle is at lower frequency (between bulk and electrode semi-circles) region and the capacitance is in the range of nanofarad.

AC-impedance responses of these samples before annealing and after 100 hours annealing are shown in the appendix for comparison at low temperatures. Note that sample LSC30 was annealed after deposition, thus the responses are after 10 hours and 100 hours annealing. The annealing time for CG/LC10 was 94 hours instead of 100 hours.

All the semi-circles behave in the same manner both before annealing and after 100 hours annealing. Therefore, the rate-controlling step remains the same throughout. However, there is not enough evidence to identify what reaction is responsible for this process as the investigations in the surface kinetics and formation of reaction products involved are necessary.

The gb and bulk ASRs of the five samples investigated previously have been measured at various temperatures in air. The values are taken from the straight lines at 400°C, and plotted against annealing periods in hours. These are shown in Fig. 6.13 and Fig. 6.14.

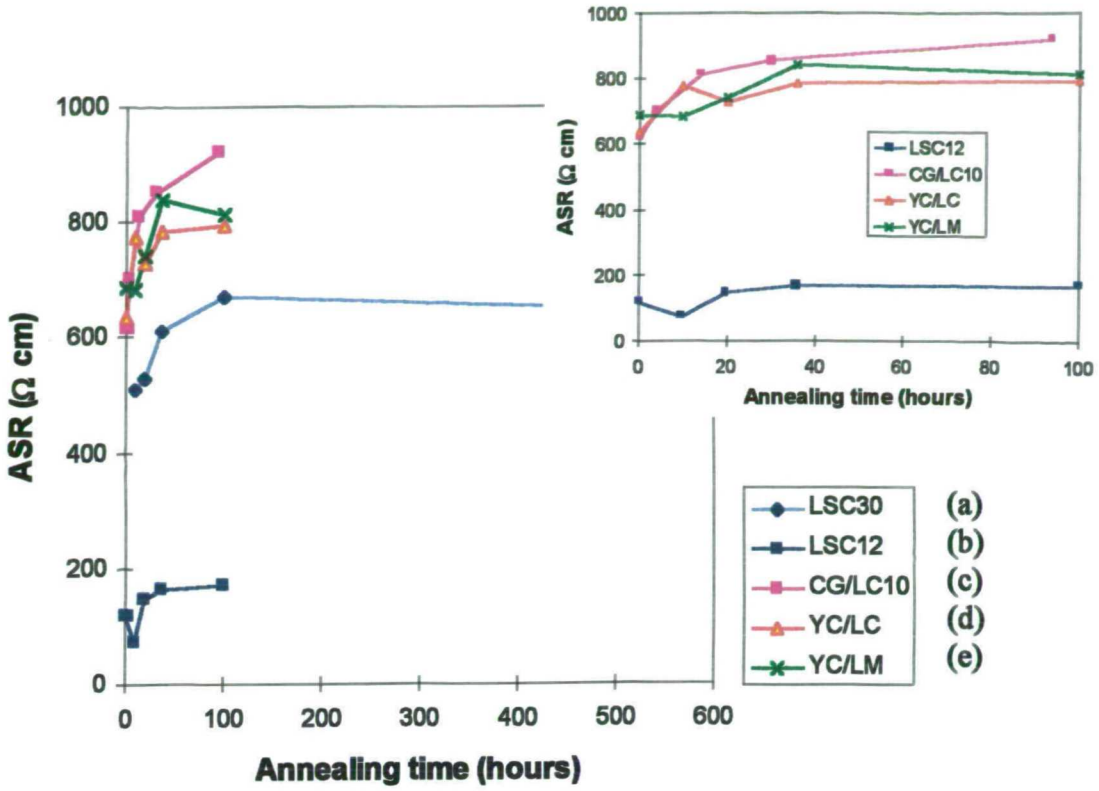


Fig. 6.13 : Plots of gb ASRs after certain annealing periods at 400°C for (a) LSC30, (b) LSC12, (c) CG/LC10, (d) YC/LC, and (e) YC/LM.

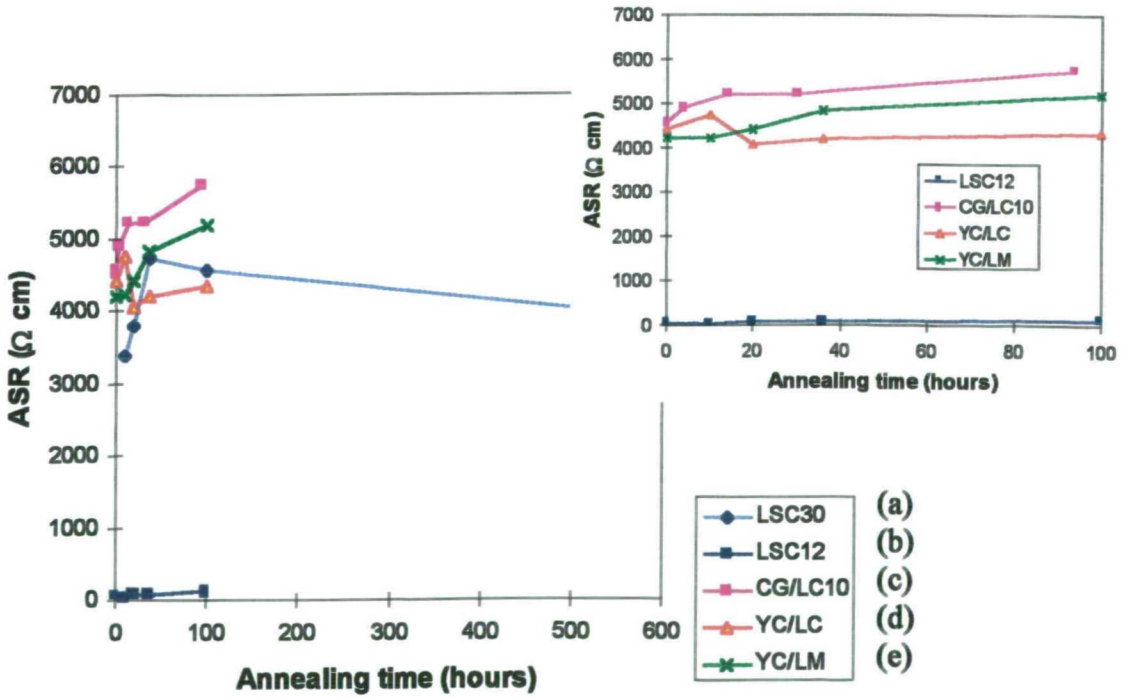


Fig. 6.14 : Plots of bulk ASRs after certain annealing periods at 400°C for (a) LSC30, (b) LSC12, (c) CG/LC10, (d) YC/LC, and (e) YC/LM.

In all samples, the gb ASRs are relatively constant after annealing for 30 hours. However, the bulk ASRs slightly increase with annealing time. The gb ASRs for LSC12 and LSC30 do not vary much with annealing time and are lower than those with interlayers. The bulk ASRs of LSC12 remain relatively constant over the period of 100 hours annealing. The bulk ASR of LSC30 after annealing for 600 hours is lowered which might confirm the stabilisation process of the electrolyte with annealing time.

For the gb ASR, all samples with an interlayer show even greater values than without the interlayer (LSC30). This can be explained by a reaction phase between doped ceria and YSZ as investigated by Horita et al [201]. This phase has been reported to decrease the ionic conductivity of the electrolyte.

The bulk ASRs of all samples with YSZ substrate are in the same range that is consistent with the fact that most of conductivity in the electrolyte is attributed from the YSZ substrate itself which is much higher than those from the interlayer. For comparison, the thickness of the substrate was greater than 300 microns while the interlayers were around 1-2 microns. The ionic conductivity of YSZ is much lower than that of doped ceria and this results in the low ASRs of sample LSC12.

The system with YDC interlayer performs better than the sample with CGO interlayer. Sample LSC/YDC/YSZ showed an improvement in the bulk ASRs over the system without an interlayer of LSC/YSZ over an annealing period of 100 hours. The reaction which might have occured between the YDC and LSM from the system LSM/YDC/YSZ still caused less pronounced effect than between CGO an YSZ on the bulk and gb ASRs from LSC/CGO/YSZ.

6.4 EFFECT OF OXYGEN PARTIAL PRESSURE

The ASRs of sample LSC30 after annealing for 600 hours and sample LSC12 after annealing for 100 hours were measured at various oxygen atmosphere which were at 0.21, 0.10, and 0.05 atm, respectively. The electrode, gb, and bulk ASRs of LSC30 and LSC12 are compared in Fig. 6.15 and 6.16 .

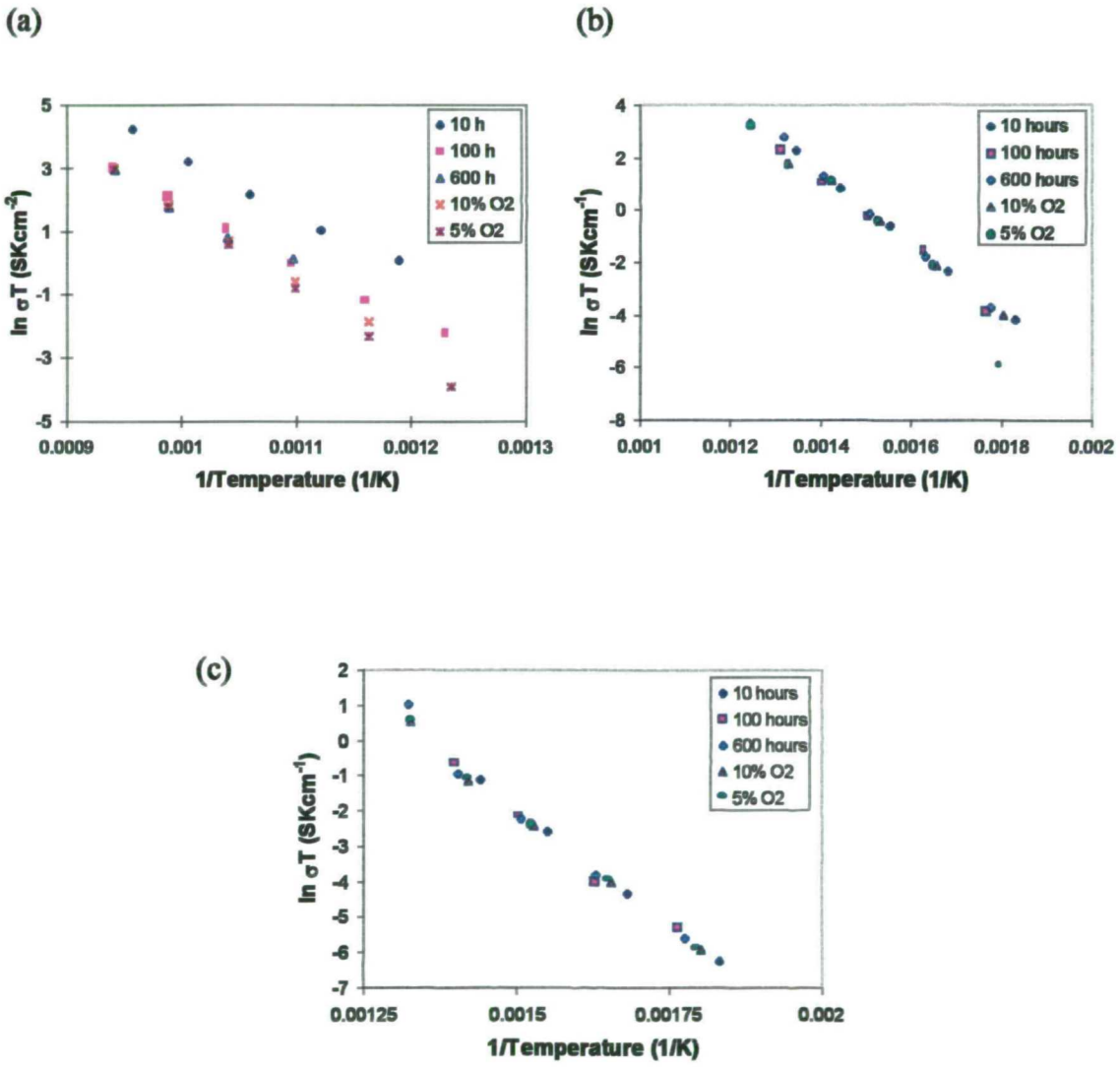


Fig. 6.15 : Plots of (a) electrode ASRs, (b) gb ASRs, and (c) bulk ASRs of LSC30 at various oxygen partial pressures.

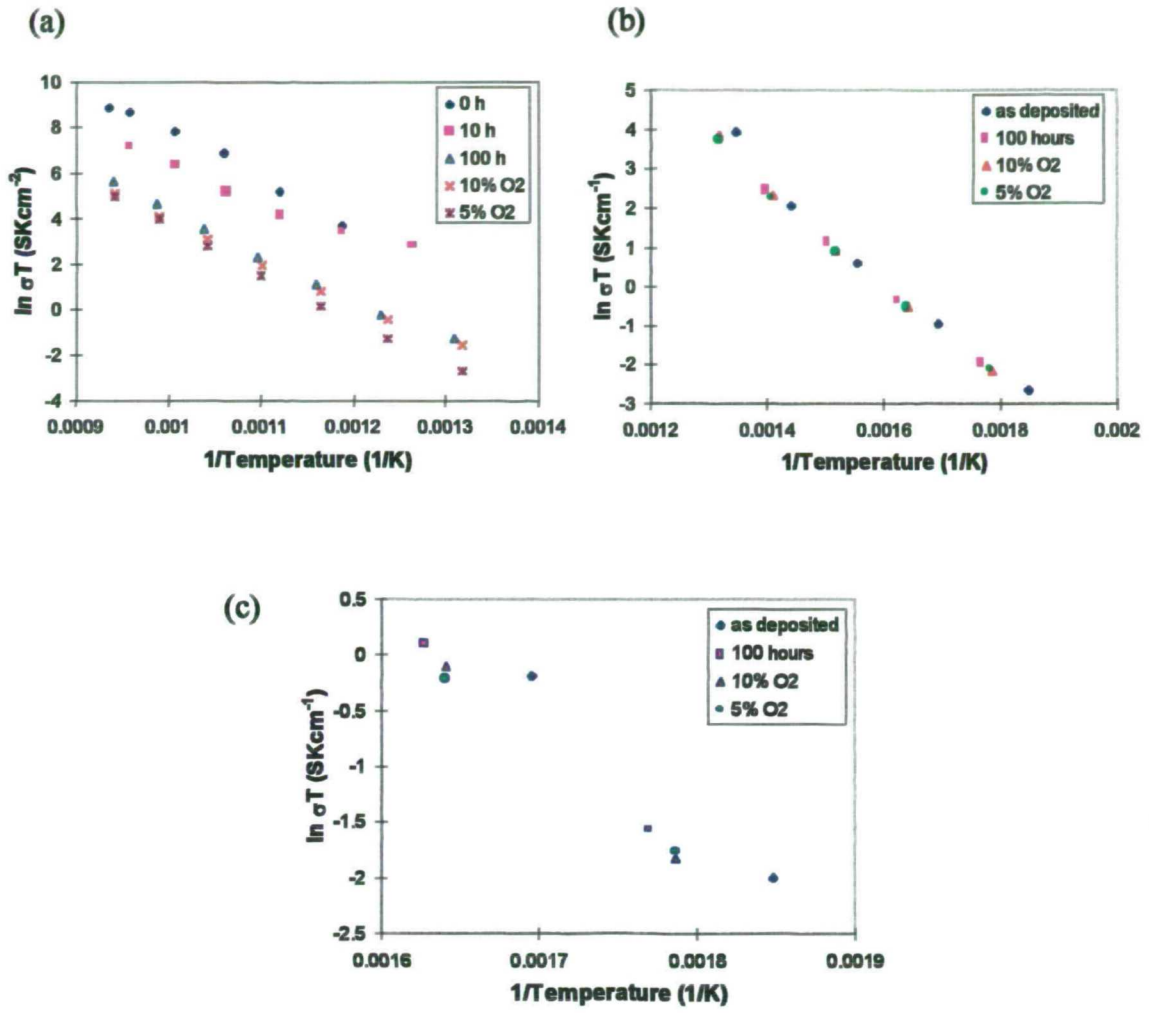


Fig. 6.16 : Plots of (a) electrode ASRs, (b) gb ASRs, and (c) bulk ASRs of at various oxygen partial pressures.

From these two figures, the range of oxygen partial pressure is not wide enough to distinguish the difference in the bulk and gb ASRs for both samples. However, the electrode ASRs increase when the oxygen partial pressure is decreased. When the oxygen partial pressure is decreased, the oxygen diffusivity is increased while the surface exchange decreases [211]. As the overall ASRs increase with decreasing oxygen partial pressure, this means the surface exchange of oxygen dominates the electrode interfacial resistance and not the oxygen diffusion. AC-impedance responses of samples LSC30 and LSC12 for different oxygen partial pressure at high temperature are shown in the the appendix.

Sample LSC30 has very similar semi-circles throughout the change in oxygen partial pressure. However, when the oxygen partial pressure is reduced, the Warburg semi-infinite diffusion effect could be detected at the high frequency end. Sample LSC12 shows more pronounced phenomenon that a hump occurs at the high frequency end of the semi-circle when the oxygen partial pressure is reduced. This corresponds to the charge transfer process as the rate-determining step. Such behaviour agrees well with the observation made by Lane et al. [212] and Chen et al. [121] but with $La_{0.6}Sr_{0.4}Fe_{0.8}Co_{0.2}O_{3-\delta}$ instead of LSC.

6.5 CALCULATED ELECTRODE ASR

A chemical resistance (R_{chem}) represents the electrode ASR which can be calculated from the equation (2.13) in section 2.4.2.2,

$$R_{chem} = \left(\frac{RT}{2F^2}\right)\sqrt{\frac{\tau}{(1-\varepsilon)D^* a c_{mc} k}} \qquad \text{-----} \quad (2.13)$$

where R = gas constant (8.314 J/molK),

T = temperature (K),

F = Faradaic constant,

τ = solid phase tortuosity,

ε = porosity,

a = surface area per unit volume (cm^{-1})

c_{mc} = the concentration of oxygen sites in the cathode material which is obtained from the lattice parameter,

k = surface exchange coefficient of oxygen (cm/s), and

D* = self-diffusion coefficient of oxygen (cm^2/s).

The chemical resistance therefore depends on the microstructural parameters of the surface area, porosity, and tortuosity of the porous cathode for the same type of material. Table 6.10 shows some of the calculated R_{chem} based on the data of $La_{0.8}Sr_{0.2}CoO_{3-\delta}$ when the microstructural parameters are varied. The calculation is based on the kinetics data at 800°C from literature in chapter 2 while the microstructural parameters are estimated from SEM images. The results given then act as guidelines only.

Table 6.10 : Calculated R_{chem} for $La_{0.8}Sr_{0.2}CoO_{3-\delta}$

Tortuosity (τ)	Porosity (ε)	Particle size (μm)	R_{chem}
1	0.3	1	0.05226
1	0.3	1.5	0.06401
1	0.3	2	0.07391
1	0.3	3	0.09052
1	0.3	5	0.11686
1	0.4	1	0.05645
1	0.4	1.5	0.06914
1	0.4	2	0.07983
1	0.4	3	0.09777
1	0.4	5	0.12622
1.2	0.3	1	0.05725
1.2	0.3	1.5	0.07012
1.2	0.3	2	0.08096
1.2	0.3	3	0.09916
1.2	0.3	5	0.12802
1.2	0.4	1	0.06184
1.2	0.4	1.5	0.07573
1.2	0.4	2	0.08745
1.2	0.4	3	0.10711
1.2	0.4	5	0.13827
1.5	0.3	1	0.06401
1.5	0.3	1.5	0.07839
1.5	0.3	2	0.09052
1.5	0.3	3	0.11086
1.5	0.3	5	0.14313
1.5	0.4	1	0.06914
1.5	0.4	1.5	0.08467
1.5	0.4	2	0.09777
1.5	0.4	3	0.11975
1.5	0.4	5	0.15459

The parameters, which yield R_{chem} close to the extrapolated ASRs from the measured data of YC/LC and CG/LC10, are in Table 6.11.

Table 6.11 : Microstructural parameters for CG/LC10 and YC/LC.

Parameters	CG/LC10	YC/LC
Tortuosity	1	1
Porosity	0.1	0.2
Particle size (μm)	0.3	0.3
Calculated R_{chem}	0.02524	0.02678
Measured ASR (Ω cm^2)	0.01728	0.0267

Using these parameter values, the values of the surface exchange coefficient (k), the self-diffusion coefficient of oxygen (D^*) and the combination of k and D^* of systems CG/LC10 and YC/LC can then be calculated from the electrode ASRs after certain periods of annealing. In order to perform this calculation, it is assumed that other parameters are constant that is the microstructure, which corresponds to the tortuosity, porosity, and particle size. These are plotted in Figs. 6.17, 6.18, and 6.19.

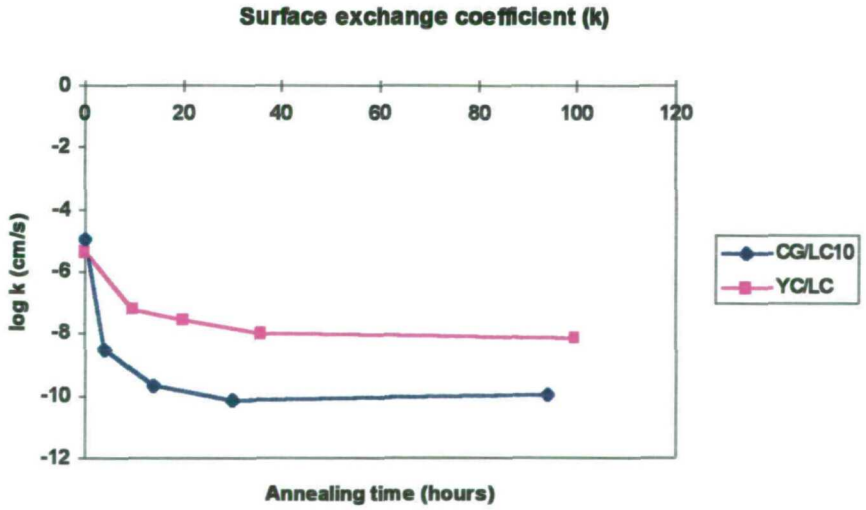


Fig. 6.17 : Surface Exchange Coefficient (k) of CG/LC10 and YC/LC with annealing time.

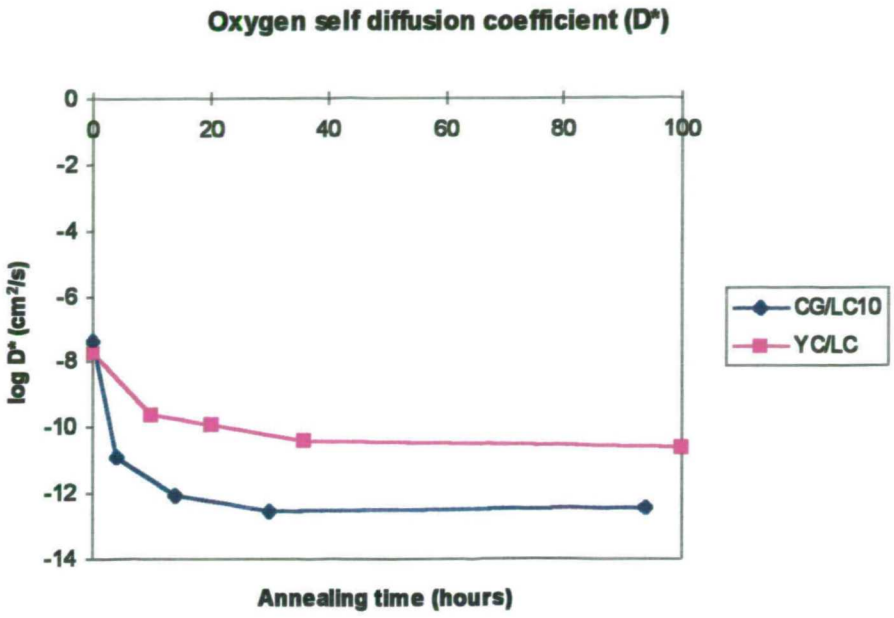


Fig. 6.18 : Self-Diffusion Coefficient of Oxygen (D) of CG/LC10 and YC/LC with annealing time.*

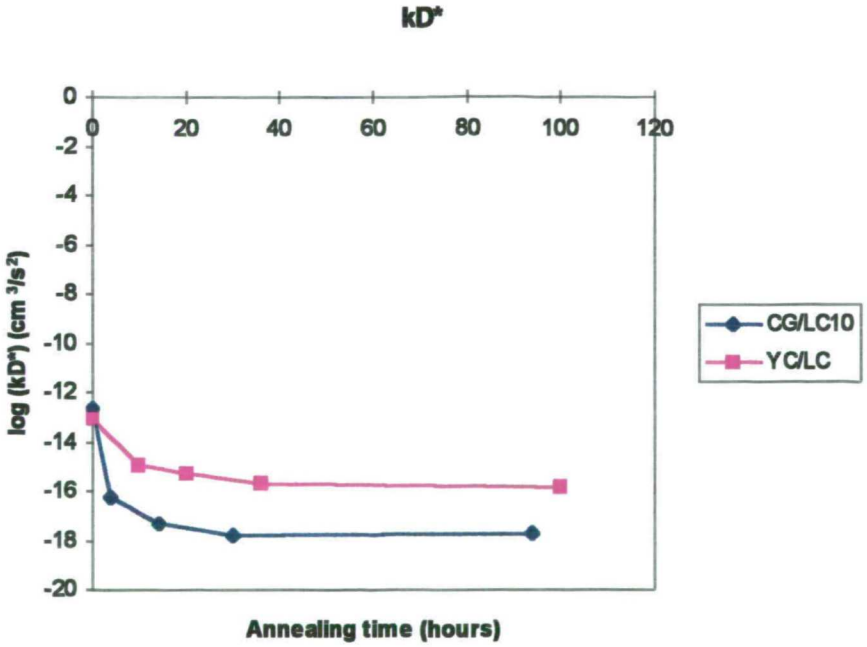


Fig. 6.19 : Combination of k and D of CG/LC10 and YC/LC with annealing time.*

From Figs. 6.17, 6.18, and 6.19, k, D^* and kD^* drop with increasing the annealing time for both systems and then remains constant after 36 hours. Nevertheless, the k and D^* values of sample YC/LC are still greater than that of sample CG/LC10 about 2 orders of magnitude. This trend agrees well with the experimental data measured and discussed in section 6.3. It can be concluded that the system LSC/YDC/YSZ has better surface exchange coefficient and/or oxygen diffusion coefficient than the system LSC/CGO/YSZ as both values may vary with annealing time. From the microstructures of these two systems after annealing for 94 hours for LSC/CGO/YSZ system and 100 hours for LSC/YDC/YSZ system, there is a slight change mainly in porosity and tortuosity. However, these changes are still minor compared with the increase of calculated k and D^*.

6.6 SUMMARY

The microstructure and electrical conductivities of cathode films depend on the careful control of processing parameters as shown in sections 6.1, 6.2, and 6.3. The lateral resistivity of the cathode layer is not affected by an interlayer between the cathode and YSZ electrolyte. However, it depends on the microstructure of the cathode layer itself which is a consequence of different processing parameters used in the deposition. The lateral resistivity is generally low for films deposited at high temperature, yielding a crystalline but powdery film. The SEM micrographs indicate that these films have fine particles (~ 1 micron). The activation energy of powdery films tend to be greater than those with porous films due to the loose contact between particles.

The cathode/electrolyte systems with an interlayer have demonstrated the improvement in the electrode ASR but unfortunately the bulk and gb ASRs deteriorate after annealing at 900°C over a period of 94-100 hours. For electrode ASR, the system of LSC on YSZ substrate shows the greatest resistivity even greater than the LSM/YDC/YSZ system. The system of LSC/CGO/YSZ shows a better performance than these two systems, however the ASRs are still greater than the LSC on CGO and LSC/YDC/YSZ systems. The LSC/YDC/YSZ system has lower ASRs than LSC on CGO, which means YDC is a better electrolyte than CGO and systems with an interlayer definitely have lowered the electrode ASRs.

The electrode ASRs measured from AC-impedance method are comparable with the calculated values using the measured data on the oxygen self-diffusion coefficient (D^*) and oxygen surface exchange coefficient (k). The ASRs after annealing at certain period of time of two systems, LSC/YDC/YSZ and LSC/CGO/YSZ, have been used to predict the values of k and D^* assuming that the microstructure has not changed. This suggests that k and/or D^* decreases with increasing annealing time until after 30 hours that they remain relatively constant.

Further work on bulk and gb ASRs indicates the opposite effect that over the same annealing period, the bulk ASRs of interlayer systems are in the same range as

those of the same substrate material (YSZ) but without an interlayer. This effect is as expected, as the major contribution of the bulk ASR is from the substrate, which is much thicker than the interlayer by more than 100 times. The systems with an interlayer show a negative effect on the gb ASRs that when doped ceria is in contact with YSZ, the ionic conductivity is lowered. The solid solution of this mixture normally has lower ionic conductivity than YSZ, YDC, and CGO therefore this can explain the higher ASRs.

The electrode ASRs of LSC on CGO and YSZ substrates increased with decreasing the oxygen partial pressure from 0.21 atm down to 0.05 atm. This phenomenon is attributed from the increase in oxygen diffusivity but decrease in surface exchange coefficient with decreasing oxygen partial pressure. As the overall ASRs increase with decreasing oxygen partial pressure, this means surface exchange of oxygen plays a major role in the interfacial resistance.

Chapter 7 : MODELLING

The Flame Assisted Vapour Deposition (FAVD) method is currently used to deposit ceramic films for use as the cathode component in Solid Oxide Fuel Cells (SOFCs). The properties and microstructures of the deposited films vary with the deposition conditions. These conditions are influenced by many parameters such as the deposition temperature, the ratio of alcohol to water in the precursor solution, the distance between the spray nozzle and the substrate, and the flow rate of the precursor solution. Experiments described in previous chapters have shown the effect of varying these parameters. In this chapter, the results of a computer simulation of some process parameters are described. As FAVD involves a combination of heat transfer and fluid flow, the software called FLUENT* has been used. This software package uses the finite volume method to model various types of physical phenomena involved in heat transfer and fluid flow.

7.1 EXPERIMENTAL SETUP

FAVD involves many processes and the apparatus consisted of many components such as a flame source, spray nozzle, precursor flow control, air compressor, air flow control, hot plate, and temperature measurement unit. A liquid precursor, mainly ethanol and water mixed with some soluble metal salts, is atomised through the spray nozzle by means of compressed air. The atomised precursor is in the form of fine droplets, which can be assumed to be aerosol. These droplets then combust when ignited by a flame source. In this case, a natural gas (CH_4) bunsen burner was used as the flame source. The heat of combustion provides thermal energy during the decomposition and vapourisation of these droplets, which undergo vapour phase reactions, resulting in an oxide film being deposited on a substrate surface underneath the spray nozzle. The substrate is placed on a hot plate, which provides a thermal environment in addition to the flame source.

*** FLUENT is a trademark of Fluent Inc.**

All these experiments were carried out in an open atmosphere with no physical barriers apart from the substrate located on a hot plate underneath the spray nozzle. The flow rates of the compressed air and the liquid precursor were measured. The temperature at the substrate surface was monitored throughout the deposition. The ratio of ethanol to water in the liquid precursor was varied together with the pressure of the compressed air.

7.2 OVERVIEW

The model was set up in the form of an axi-symmetrical cylinder with a fuel (methanol and water) inlet at the centre to represent the spray nozzle. Note that methanol was used as one of the fuel components in the model because values of its properties are available in the package's database, but this is not the case for ethanol. This will affect the details of the temperature distribution, but not the qualitative results and overall trends. The fuel inlet was combined together with the oxidiser (nitrogen and oxygen gases) inlet. At the opposite side of the inlet was the hot plate, which was set to a temperature of 227°C at its centre. Any boundary other than those described above was considered to be an outlet. Fig. 7.1 shows the computational grid (25 x 20 cells) used for this setup. Each cell is equal to 1 cm in distance or less, so the entire grid represents the size of 25 cm x 15 cm, which is slightly larger than the real setup.

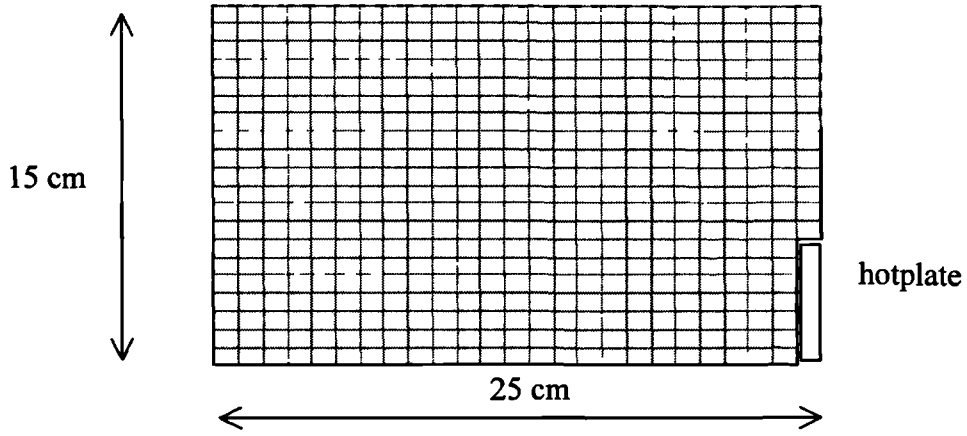


Fig. 7.1 : A grid of the model setup.

As the precursor is atomised in the real system on exit from the spray nozzle, the fuel spray coming out of the inlet was treated as a dispersed secondary phase of liquid droplets. It was treated as evaporating into the primary gas phase and undergoing combustion when ignited by the flame source.

The flow of the droplets and the air was turbulent and this influences the combustion reaction, which requires inter-diffusion of the mixtures. The combustion reaction was modelled using a preprocessor program called preProbability Density Function, or "prePDF".

7.3 BASIC EQUATIONS IN MODELLING

In this model, the system was considered to be a 2-dimensional axi-symmetrical cylinder where the spray nozzle was regarded as the centre of the cylinder on one end. Standard Cartesian geometry was used throughout, where the subscripts *i, j,* and *k* are the coordinate directions. Note that all the equations are shown in one direction but are expanded to three directions in the model. Dashed subscripts refer to the various chemical species involved.

7.3.1 HEAT TRANSFER AND FLUID FLOW GOVERNING EQUATIONS IN THE GAS PHASE

The basic conservation equations considered in this model were:

- Conservation of mass,
- Conservation of momentum,
- Conservation of energy,
- Conservation of species.

7.3.1.1 The Mass Conservation Equation

$$\frac{\partial \rho}{\partial t} + \frac{\partial}{\partial x_i}(\rho u_i) = S_m \qquad \text{-----} \quad (7.1)$$

where ρ is the density of fluid,

t is the time,

∂x_i is the distance of the cell in the i direction,

u_i is the velocity of fluid in the i direction, and

S_m is the mass transferred to the primary phase from the dispersed second phase due to the vapourisation of liquid droplets.

It should be noted that equation 7.1 is a scalar equation, where the second term is a summation over the three components (as indicated by the repeated subscripts).

7.3.1.2 The Momentum Conservation Equation

The i^{th} direction of the momentum conservation equation is given by:

$$\frac{\partial}{\partial t}(\rho u_i) + \frac{\partial}{\partial x_j}(\rho u_i u_j) = -\frac{\partial p}{\partial x_i} + \frac{\partial \tau_{ij}}{\partial x_j} + \rho g_i + F_i \qquad \text{-----} \quad (7.2)$$

where p is the static pressure,

τ_{ij} is the stress tensor,

g_i is the gravitational acceleration,

F_i is the external body forces in the i direction.

The stress τ_{ij} is calculated from:

$$\tau_{ij} = \left[\mu\left(\frac{\partial u_i}{\partial x_j} + \frac{\partial u_j}{\partial x_i}\right)\right] - \frac{2}{3}\mu\frac{\partial u_l}{\partial x_l}\delta_{ij} \qquad \text{-----} \quad (7.3)$$

where μ is the molecular viscosity and

$\frac{2}{3}\mu\frac{\partial u_l}{\partial x_l}\delta_{ij}$ is the effect of volume dilation.

7.3.1.3 The Species Conservation Equation

The equation describing the conservation of species i' is:

$$\frac{\partial}{\partial t}(\rho m_{i'}) + \frac{\partial}{\partial x_i}(\rho u_i m_{i'}) = \frac{\partial}{\partial x_i}(J_{i',i}) + S_{i'} \qquad \text{-----} \quad (7.4)$$

where $m_{i'}$ is the mass fraction of species i',

$J_{i',i}$ is the diffusive mass flux of species i' in the ith direction, and

$S_{i'}$ is the net rate of production of species i' per unit volume due to the contribution from the dispersed phase.

The overall mass conservation equation is the summation of conservation equations of all the species present in the continuous phase.

The diffusion due to the concentration gradients and thermal effects are considered in the diffusive mass flux as follows:

$$J_{i',i} = -\rho D_{i',m}\frac{\partial m_{i'}}{\partial x_i} - D_{i'}^{T}\frac{1}{T}\frac{\partial T}{\partial x_i} \qquad \text{-----} \quad (7.5)$$

where $D_{i',m}$ is the diffusion coefficient for species i', and

$D_{i'}^{T}$ is the thermal diffusion coefficient.

7.3.1.4 The Energy Conservation Equation

The conservation of energy is solved in terms of conservation of the static enthalpy, h, as:

$$h = \sum_{i'} m_{i'} h_{i'} \qquad \text{-----} \quad (7.6)$$

where

$$h_{i'} = \int_{T_{ref}}^{T} c_{p,i'} dT \qquad \text{-----} \quad (7.7)$$

T_{ref} is a reference temperature, and

$c_{p,i'}$ is the specific heat at constant pressure of species i'.

Species diffusion due to pressure and external forces is assumed to be negligible. Therefore, the energy equation in terms of h becomes [213]:

$$\frac{\partial}{\partial t}(\rho h) + \frac{\partial}{\partial x_i}(\rho u_i h) = \frac{\partial}{\partial x_i}\left(k \frac{\partial T}{\partial x_i}\right) - \frac{\partial}{\partial x_i} \sum_{j'} h_{j'} J_{j'} + \frac{\partial p}{\partial t} + u_i \frac{\partial p}{\partial x_i} + \tau_{ij} \frac{\partial u_i}{\partial x_j} + S_h \qquad (7.8)$$

where T is the temperature,

τ_{ij} is the viscous stress tensor,

$J_{j'}$ is the flux of species j' , and

k is the mixture thermal conductivity.

7.3.1.5 Conservation Equations in Cylindrical Form

As the model is treated as a 2-D axi-symmetrical cylinder, the conservation equations are expressed in cylindrical co-ordinates (x, r, θ) as follows:

Continuity:

$$\frac{\partial \rho}{\partial t} + \frac{\partial (\rho u)}{\partial x} + \frac{1}{r} \frac{\partial (r \rho v)}{\partial r} = S_m \qquad \text{-----} \quad (7.9)$$

Axial Direction Momentum:

$$\frac{\partial}{\partial t}(\rho u)+\frac{\partial}{\partial x}(\rho u u)+\frac{1}{r}\frac{\partial}{\partial r}(r\rho v u)+ = -\frac{\partial p}{\partial x}+\frac{\partial \tau_{xx}}{\partial x}+\frac{1}{r}\frac{\partial(r\tau_{xr})}{\partial r}++\rho g_x + F_x \qquad (7.10)$$

Radial Direction Momentum:

$$\frac{\partial}{\partial t}(\rho v)+\frac{\partial}{\partial x}(\rho u v)+\frac{1}{r}\frac{\partial}{\partial r}(r\rho v v)= \\ -\frac{\partial p}{\partial r}+\frac{\partial(\tau_{xr})}{\partial x}+\frac{1}{r}\frac{\partial(\tau_{rr})}{\partial r}-\frac{\tau_{\theta\theta}}{r}+\rho g_r + F_r \qquad \text{-----} \quad (7.11)$$

where u is the axial velocity component and v is the radial velocity component.

The stress tensor in cylindrical coordinates is:

$$\tau_{xx} = 2\mu\frac{\partial u}{\partial x}-\frac{2}{3}\mu\left(\frac{\partial u}{\partial x}+\frac{1}{r}\frac{\partial(rv)}{\partial r}\right) \qquad \text{-----} \quad (7.12)$$

$$\tau_{rr} = 2\mu\frac{\partial v}{\partial r}-\frac{2}{3}\mu\left(\frac{\partial u}{\partial x}+\frac{1}{r}\frac{\partial(rv)}{\partial r}\right) \qquad \text{-----} \quad (7.13)$$

$$\tau_{\theta\theta} = 2\mu\left(\frac{v}{r}\right)-\frac{2}{3}\mu\left(\frac{\partial u}{\partial x}+\frac{1}{r}\frac{\partial(rv)}{\partial r}\right) \qquad \text{-----} \quad (7.14)$$

$$\tau_{xr} = \mu\left(\frac{\partial u}{\partial r}+\frac{\partial v}{\partial x}\right) \qquad \text{-----} \quad (7.15)$$

This formulation provides direct calculation of curvature related terms, yielding more accurate numerical results in this model.

7.3.2 SECONDARY PHASE EQUATIONS

The dispersed phase droplets undergo vapourisation and then combustion when ignited.

7.3.2.1 Droplet Vapourisation

This reaction occurs when the temperature of the dispersed phase droplet reaches the vapourisation temperature, T_{vap}, and continues until the boiling temperature, T_{bp}, is reached or the droplet has completely evaporated. Once vapourisation is initiated, it will continue even if the droplet temperature falls below T_{vap}.

The rate of vapourisation is governed by gradient diffusion, with the flux of droplet vapourises into the gas phase relates to the gradient of the vapour concentration between the droplet surface and the bulk gas:

$$N_{i'} = k_c(C_{i',s} - C_{i',\infty}) \qquad \text{-----} \quad (7.16)$$

where $N_{i'}$ is the molar flux of vapour (mol/m^2-s)

k_c is the mass transfer coefficient (m/s)

$C_{i',s}$ is the vapour concentration at the droplet surface (mol/m^3)

$C_{i',\infty}$ = vapour concentration in the bulk gas (mol/m^3).

This mass transfer coefficient is calculated from a Nusselt correlation [214,215]

The heat change in the droplet during vapourisation includes the convective and latent heat transfer between the droplet and the gas:

$$m_p c_p \frac{dT_p}{dt} = hA_p(T_\infty - T_p) + \frac{dm_p}{dt} h_{fg} \qquad \text{-----} \quad (7.17)$$

where c_p is the droplet heat capacity (J/kg K)

T_p is the droplet temperature (K)

T_∞ is the temperature of continuous phase (K)

h is the convective heat transfer coefficient (W/m^2 K)

$\frac{dm_p}{dt}$ is the rate of evaporation (kg/s)

h_{fg} is the latent heat between the droplet and the gas (J/kg)

(i) Trajectory Calculations

The trajectory of a dispersed phase droplet is predicted by integrating the force balance on the particle, in a Lagrangian reference frame. The force balance equates the particle inertia with the forces acting on the particle [216].

(ii) Integration of the Trajectory Equations

The trajectory equations, and any auxiliary equations describing heat or mass transfer to/from the particle, are solved by step-wise integration over discrete time steps [217]. During the integration, the fluid phase velocity, u, is considered to be the cell-based velocity for all positions within the cell or the velocity at the particle position.

(iii) Dispersed Phase Boundary Condition

If a droplet migrates into a boundary cell, the entire droplet instantaneously flashes to vapour (a 'trap' boundary condition).

(iv) Turbulent Dispersion of Particles

The turbulent dispersion of particles is predicted by integrating the trajectory equations for individual particles [218].

7.3.3 MODELS FOR TURBULENT FLOW

7.3.3.1 Reynolds Averaging of the Conservation Equations

The conservation equations for turbulent flow are treated by a time averaging procedure known as Reynolds averaging.

The Reynolds averaging procedure can be illustrated by following the general transport equation:

Accumulation + Convection = Diffusion + Source

If ϕ is a conserved scalar quantity, it is comprised of a mean value and a fluctuating part in turbulent flow as follows:

$$\phi = \bar{\phi} + \phi' \qquad \text{-----} \quad (7.18)$$

where $\bar{\phi}$ is the time averaged value of ϕ defined as:

$$\bar{\phi} = \frac{1}{\Delta t}\int_{t}^{t+\Delta t}\phi dt \qquad \text{-----} \quad (7.19)$$

and Δt is a time scale much larger than the largest time scale of turbulent fluctuations. The turbulent fluctuations are assumed to be random so that the mean value equals zero. Combining equation 7.18 with the general scalar conservation equation and then time integrating over a sufficiently large time interval yields:

$$\frac{\partial}{\partial t}\left(\overline{\rho\phi}\right)+\frac{\partial}{\partial x_i}\left(\overline{\rho u_i\phi}\right)=-\frac{\partial}{\partial x_i}\left(\overline{\rho u_i'\phi'}\right)+\overline{D_\phi}+\overline{S_\phi} \qquad \text{-----} \quad (7.20)$$

The correlation $\overline{u_i'\phi'}$ multiplied by the density represents the transport or diffusion of ϕ due to turbulent fluctuations.

The species conservation, $\overline{u_i'm_{i'}'}$, and the enthalpy correlation, $\overline{u_i'h'}$, are modelled using the gradient transport analogy as:

$$\overline{\rho u_i'm_{i'}'} = -\frac{\mu_t}{\sigma_m}\frac{\partial m_{i'}}{\partial x_i} \qquad \text{-----} \quad (7.21)$$

$$\overline{\rho u_i'h'} = -\frac{\mu_t}{\sigma_h}\frac{\partial h}{\partial x_i} \qquad \text{-----} \quad (7.22)$$

where σ_m and σ_h are the turbulent Schmidt and Prandtl numbers, respectively.

The enthalpy equation in turbulent flow contains an additional contribution from viscous heating, with the viscous dissipation, $\tau_{ij}\frac{\partial u_i}{\partial x_j}$, augmented by the dissipation of turbulence, $\rho\varepsilon$. This represents the effect of the dissipation of turbulent eddies on the heating of the fluid.

7.3.3.2 Reynolds Averaging of the Momentum Equations

The velocity at a point is considered to be the sum of the mean (time averaged) and fluctuating components:

$$u_i = \bar{u}_i + u_i' \qquad \text{-----} \quad (7.23)$$

Substituting equation 7.23 into equation 7.2 for the momentum balance yields the ensemble-averaged momentum equations for predicting turbulent flow [219] :

$$\frac{\partial}{\partial t}(\rho u_i) + \frac{\partial}{\partial x_j}(\rho u_i u_j) =$$
$$\frac{\partial}{\partial x_j}\left(\mu\left[\frac{\partial u_i}{\partial x_j} + \frac{\partial u_j}{\partial x_i}\right] - \left(\frac{2}{3}\mu\frac{\partial u_l}{\partial x_l}\right)\right) - \frac{\partial p}{\partial x_i} + \rho g_i + F_i + \frac{\partial}{\partial x_j}(\rho\overline{u_i' u_j'}) \quad \text{----- (7.24)}$$

The velocities now represent the time-averaged values and the effect of turbulence is incorporated through the Reynolds stresses, $\rho\overline{u_i' u_j'}$. To close this new system of equations, a specific turbulence model is required. In this work, the k-ε turbulence model was used.

7.3.3.3 The k-ε Turbulence model

The k-ε model is a semi-empirical model which provides accurate predictions in many types of turbulent flow including shear flow and wall-bounded flow. It is suitable for isotropic turbulence. This model is an eddy-viscosity model in which the Reynolds stresses are assumed to be proportional to the mean velocity gradients, with the constant of proportionality being the turbulent viscosity, μ_t. This assumption is know as the Boussinesq hypothesis with the following expression for the Reynolds stresses [220]:

$$\rho\overline{u_i' u_j'} = \rho\frac{2}{3}k\delta_{ij} - \mu_t\left(\frac{\partial u_i}{\partial x_j} + \frac{\partial u_j}{\partial x_i}\right) + \frac{2}{3}\mu_t\frac{\partial u_l}{\partial x_l}\delta_{ij} \quad \text{----- (7.25)}$$

where k is the turbulent kinetic energy:

$$k = \frac{1}{2}\sum_i \overline{u_i'^2} \quad \text{----- (7.26)}$$

The turbulent viscosity, μ_t, plays the same role as the molecular viscosity, μ, from equation 7.3. However, μ is replaced by an effective viscosity, μ_{eff}:

$$\mu_{eff} = \mu + \mu_t \qquad \text{-----} \quad (7.27)$$

The turbulent viscosity is assumed to be proportional to the product of a turbulent velocity scale and length scale. These velocity and length scales are obtained from two parameters: k, the turbulent kinetic energy, and ε, the dissipation rate of k. The velocity scale is $\sqrt{k}$ and the length scale is $\frac{\sqrt{k^3}}{\varepsilon}$. μ_t then becomes:

$$\mu_t = \rho C_\mu \frac{k^2}{\varepsilon} \qquad \text{-----} \quad (7.28)$$

where C_μ is an empirically derived constant of proportionality (FLUENT's default value of 0.09 was used).

7.3.4 CHEMICALLY REACTING FLOW MODELS

7.3.4.1 Mixture Fraction/PDF Formulation

In this approach, transport equations of individual species are not solved. Instead, a single conserved scalar, the mixture fraction, is calculated and individual component concentrations are derived from the predicted mixture fraction distribution. This model has been specifically developed for the simulation of turbulent diffusion flow, for which it offers many benefits. The turbulence effects in the conserved scalar approach are accounted for with the help of a probability density function, or PDF. The reacting system is treated via chemical equilibrium calculations. Physical properties of chemical species and equilibrium data are obtained from a chemical database.

As the spray combustion involves a turbulent diffusion flow, the mixture fraction/PDF approach is appropriate. The mixture fraction method allows intermediate species formation, dissociation effects, and the coupling between turbulence and chemistry to be accounted for in a rigorous way. It allows quite accurate estimation of the flow field mean density.

7.3.4.2 Mixture Fraction

The basis of this modelling approach is that under a certain set of simplifying assumptions the instantaneous thermo-chemical state of the fluid is related to a single conserved scalar quantity known as the mixture fraction, f:

$$f = \frac{Z_k - Z_{kO}}{Z_{kF} - Z_{kO}} \qquad \text{-----} \quad (7.29)$$

where Z_k is the element mass fraction for an element k. Subscript O denotes the value at the oxidant stream inlets and subscript F denotes the value at the fuel stream inlets. For simple fuel/oxidiser systems, the mixture fraction can be stated more simply in terms of the local fuel mass fraction:

$$f = \frac{\dot{m}_F}{\dot{m}_F + \dot{m}_O} \qquad \text{-----} \quad (7.30)$$

The conserved quantity of the mixture fraction at each point in the flow domain is computed through solution of the following conservation equation for the mean (time averaged) value $\bar{f}$ of f in the turbulent flow field:

$$\frac{\partial}{\partial t}\left(\rho \bar{f}\right) + \frac{\partial}{\partial x_i}\left(\rho u_i \bar{f}\right) = \frac{\partial}{\partial x_i}\left(\frac{\mu_t}{\sigma_t}\frac{\partial \bar{f}}{\partial x_i}\right) + S_m \qquad \text{-----} \quad (7.31)$$

The source term S_m is due solely to transfer of mass into the gas phase from liquid fuel droplets.

In addition to solving for the mean mixture fraction, FLUENT solves a conservation equation for the mixture fraction variance, $\bar{f}^2$:

$$\frac{\partial}{\partial t}\left(\rho \overline{f'^2}\right) + \frac{\partial}{\partial x_i}\left(\rho u_i \overline{f'^2}\right) = \frac{\partial}{\partial x_i}\left(\frac{\mu_t}{\sigma_t}\frac{\partial \overline{f'^2}}{\partial x_i}\right) + C_g \mu_t \left(\frac{\partial \bar{f}}{\partial x_i}\right) - C_d \rho \frac{\varepsilon}{k}\overline{f'^2} \qquad (7.32)$$

where the constants σ_t, C_g, and C_d take the values 0.7, 2.86, and 2.0, respectively [221]. This mixture fraction variance is used in the closure model describing turbulence-chemistry interactions.

Through the calculation of a single conserved scalar field f, other important scalars of interest can be derived without solving individual transport equations. The mixture fraction value at each point in the flow field can be used to compute the instantaneous values of individual species mole fractions, density, and temperature with a given description of the reacting system chemistry.

In non-adiabatic systems:

$$\phi_i = \phi_i(f, h^*) \qquad \text{------} \quad (7.33)$$

where ϕ_i represents the instantaneous species concentration, density or temperature

h^* is the instantaneous enthalpy:

$$h^* = \sum_{j'} m_{j'} \left(h_{j'} + h_{j'}^o \right)$$

$$= \sum_{j'} m_{j'} \left[\int_{T_{ref}}^{T} c_{p,j'} dT + \frac{h_{j'}^o}{M_{j'}} + \int_{T_{ref,j'}}^{T_{ref}} c_{p,j'} dT \right] \qquad \text{-----} \quad (7.34)$$

7.3.4.3 Non-Adiabatic Extensions of the Mixture Fraction/PDF Approach

The local thermo-chemical state is no longer related only to the mixture fraction, f, but also to h^* in reacting systems involving heat transfer to the wall boundaries or to the dispersed phase because the heat from the combustion reaction is partially transferred to the vapourised droplets and out of the system, respectively. The system enthalpy impacts the chemical equilibrium calculation and the temperature of the reacted flow in which the change in enthalpy due to heat loss must be considered when computing scalars from the mixture fraction. This scalar dependence was described earlier in equation 7.33. Turbulent fluctuations should be accounted for by means of a joint PDF $p(f, h^*)$. The model can be simplified by assuming that the enthalpy fluctuations are independent of the enthalpy level. Therefore, the heat losses do not significantly impact the turbulent enthalpy fluctuations. Hence, $p = p(f)$ and

$$\overline{\phi_i} = \int_0^1 \phi_i(f, \overline{h^*}) p(f) df \qquad \text{-----} \quad (7.35)$$

Determination of $\overline{\phi_i}$ in this non-adiabatic system requires solution of the modelled transport equation for enthalpy:

$$\frac{\partial}{\partial t}(\rho \overline{h^*}) + \frac{\partial}{\partial x_i}(\rho u_i \overline{h^*}) = \frac{\partial}{\partial x_i}\left(\frac{\mu_t}{\sigma_h}\frac{\partial \overline{h^*}}{\partial x_i}\right) + S_h' \qquad \text{-----} \quad (7.36)$$

where S_h' accounts for source terms due to radiation and heat exchange with the second phase.

To minimise the computation time, the calculation for the mixture fraction/PDF model is performed in the preprocessor, prePDF. The chemistry model is used in conjunction with the known shape of the PDF to perform the integration given earlier. The integration performed and stored relate the mean flow variables $\overline{\phi_i}$ to the values of $\overline{f}$, $\overline{f'^2}$ and $\overline{h^*}$. Equations 7.31, 7.32 and 7.36 are solved to obtain local values for these unknowns.

7.3.5 MODELS DESCRIBING THE SYSTEM CHEMISTRY

Equilibrium Assumption

The model assumes that the chemistry is rapid enough for chemical equilibrium to always exist at the molecular level. An algorithm based on the minimisation of Gibbs free energy [222] is used to compute species mole fractions from f. It can predict the formation of intermediate species without the requirements of the detailed chemical kinetic rate data. Relevant property data for the species involved in the chemical system are accessed from a chemical database.

7.3.6 PDF MODELLING OF TURBULENCE-CHEMISTRY INTERACTION

The prediction of the turbulent reacting flow is concerned with prediction of the time averaged values of the scalars, f and $\overline{f'^2}$. These time-averaged values are related to the instantaneous values in a manner which depends on the turbulence-

chemistry interaction model. The probability density function (PDF) approach is introduced as a closure model in combination with the mixture fraction approach.

The probability density function, $p(f)$, describes the fraction of time that the fluctuating variable f takes on a value between f and $f + \Delta f$:

$$p(f)\Delta f = \lim_{T\to\infty} \frac{1}{T} \sum_{i} \tau_i \qquad \text{-----} \quad (7.37)$$

where τ_i is the fraction of time that f spends in the Δf band.

The shape of the function $p(f)$ depends on the nature of the turbulent fluctuations in f. In practice, $p(f)$ is expressed as a mathematical function that approximates the PDF shapes that have been observed experimentally. Here, a β-function with two parameters, the mean mixture fraction, $\bar{f}$, and its variance, $\overline{f'^2}$, was used. This allows the calculation of time-averaged values of those variables, which depend on f [223].

7.4 PROPERTIES OF FLUIDS

7.4.1 DENSITY

The mixture density is described as a function of temperature, pressure and composition in ideal gases. When compressibility effects are negligible, the density, ρ, is:

$$\rho = \frac{p_{op} + p'}{\bar{R}T\sum_{i'} \frac{m_i}{M_i}} \qquad \text{-----} \quad (7.38)$$

where $\bar{R}$ is the universal gas constant,

M is the molecular weight of species I',

$m_{i'}$ is the mass fraction of species i',

p_{op} is the operating pressure

p' is the local static pressure relative to p_{op}.

7.4.2 SPECIFIC HEAT CAPACITY

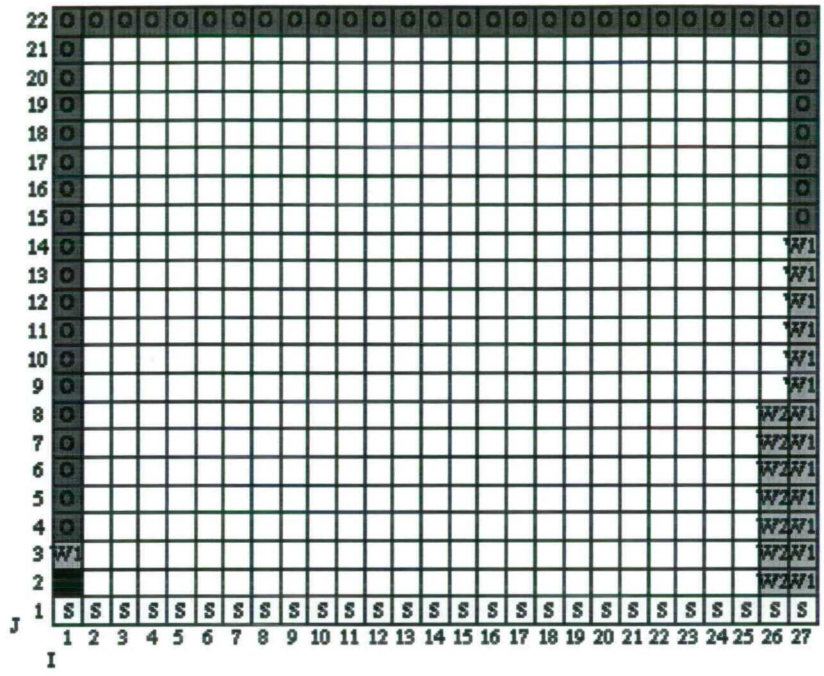
The specific heat capacity of fluid, c_p, is defined as a function of temperature in single component flow while the mixture heat capacity is computed as a mass fraction weighted average of the individual component heat capacities.

7.4.3 TRANSPORT PROPERTIES

The viscosity (μ), thermal conductivity (κ), and mass diffusion coefficients (D) are used as constant values for air at 300 K. This simplified choice of values is not important, because the turbulent transport is greater than the classical transport. The viscosity, the thermal conductivity, and the mass diffusion coefficients are the significant variables in the governing conservation equations of momentum, energy and chemical species, respectively.

7.5 BOUNDARY CONDITIONS

The boundary is divided into sections designated as wall, inlet, outlet, and symmetry boundaries, as shown in Fig. 7.2. The conditions applied at each of these boundaries are described in detail below.



O	=	Outlet	I1	=	Inlet 1
W1	=	Wall 1 (room temp.)	W2	=	Wall 2 (hotplate 500K)
S	=	Symmetrical axis			

Fig. 7.2 : Boundary conditions of the model used in this Chapter.

7.5.1 SPECIFIED VELOCITY BOUNDARY CONDITIONS

An inlet is treated as a specified velocity boundary condition, as the flow of spray droplets enter the cell at a known velocity, composition and temperature. In turbulent flow, the k and ε values at the inlet boundary are specified from inputs of turbulence intensity and characteristic length. The diffusion of all scalars at this inlet boundary is assumed to be zero.

7.5.2 OUTLET BOUNDARIES

At the outlet, combusted vapours come out at atmospheric pressure. Values for all variables are extrapolated at an outlet boundary condition from the interior cells adjacent to the outlet.

7.5.3 SYMMETRY BOUNDARIES

As this model is considered as a 2-dimensional axi-symmetrical cylinder, a zero normal gradient condition is applied for all variables at the axis of symmetry, except for the radial velocity component, which vanishes.

7.5.4 WALL BOUNDARIES

At wall boundaries, the normal velocity component is constrained to zero. For turbulent flow, it is standard practice to use empirical 'wall functions' at the near wall grid point to estimate the effect of the wall on the turbulent flow. This eliminates the need to fully resolve all regions of a turbulent boundary layer and allows the near wall grid point to be placed relatively far from the wall. This approach helps saving the computational resources in turbulent flow simulations for the standard high-Reynolds-number. The standard wall function used in the model is explained further in the appendix.

7.6 PARAMETERS AND CONDITIONS

7.6.1 PDF MODEL

Species: CH_3OH, O_2, N_2, H_2O, CO_2, CO and H_2.

Composition (mass fraction)

Percentage of methanol in the precursor by volume		50%	70%	80%
fuel stream	CH_3OH	0.44	0.64	0.76
	H_2O	0.56	0.36	0.24
oxidiser stream	0.21 O_2 : 0.79 N_2 for all cases.			

Operating Conditions:

Pressure	101000	Pa
Min. Temperature	280	K
Max. Temperature	2800	K
Inlet Temperature	300	K (fuel)
	300	K (oxidiser)

The solution Parameters:

These values are defaults in prePDF

Interpolation tolerance	0.001
Enthalpy discretization mode	1
Enthalpy points	41
Variance points per enthalpy curve	3
Mean mixture fraction points	25
Distribution centre point	0.2
Mixture fraction variance points	15
Rich flammability limit	0.4

7.6.2 FLUENT

This model is created based on the turbulence k-ε model with PDF combustion, which calculates temperature, cylindrical velocities, and species.

Domain 2-D axi-symmetry of length 0.25 m,
outer radius 0.15 m, and
sector angle 6.28 radians.

Boundary conditions:

Wall 1 temperature	300	K
Wall 2 temperature	500	K (acts as a hot plate)
Outlet temperature correction	1	
Effective emissivity	1	

At inlet 1 (as the spray nozzle)

Initial velocity	4.2	m/s	(as measured experimentally)
Static temperature	300	K	
Turbulence intensity	10%		(assumption)
Characteristic length	0.01	m	(assumption)

Physical constants:

These are set at the values for air:

Viscosity	$2x10^{-5}$	kg/s-m
Thermal conductivity	0.025	W/m-K
Binary diffusivity	$2.88x10^{-5}$	m^2/s

The second phase constants are set at the values for water:

Initial density	$1x10^{-3}$	kg/m^3
Latent heat of vapourisation	$2.25x10^{6}$	J/kg
Vapourisation temperature	300	K
Boiling point	373	K
Specific heat, Cp	4180	J/kg-K
Binary diffusivity	$2.6x10^{-5}$	m^2/s

Fraction volatiles				1.0						
Vapour pressure				-10 for piecewise linear fit						
T(K)	256	275	285	296	307	315	325	340	356	373
Vp(Pa)	133	664	1329	2658	5316	7974	13289	26579	53158	101000

Droplet setting:

The spray cone was modelled using a range of horizontal velocities for the droplets. These parameters were fixed according to the values measured experimentally and/or estimated.

The initial position of each droplet was at inlet 1 (spray nozzle).

Horizontal velocity	4.2	m/s.
Initial vertical velocity	0.1	m/s
2nd vertical velocity	1.4	m/s.
Initial/2nd temperature	300	K
Min./Max. diameter of each droplet	$1x10^{-5}$	m
Mean diameter of each droplet	$1x10^{-5}$	m
Mass flow rate	$1.65x10^{-4}$	kg/s

7.7 RESULTS

7.7.1 EFFECT OF MIXTURE FRACTIONS

The temperature distribution contours at different mixture fractions (m.f.) from 0.05 to 0.5 for the 70% alcohol containing solution are shown in Fig. 7.3. The temperature contours at different mixture fractions for 50% and 80% alcohol solution are in the appendix.

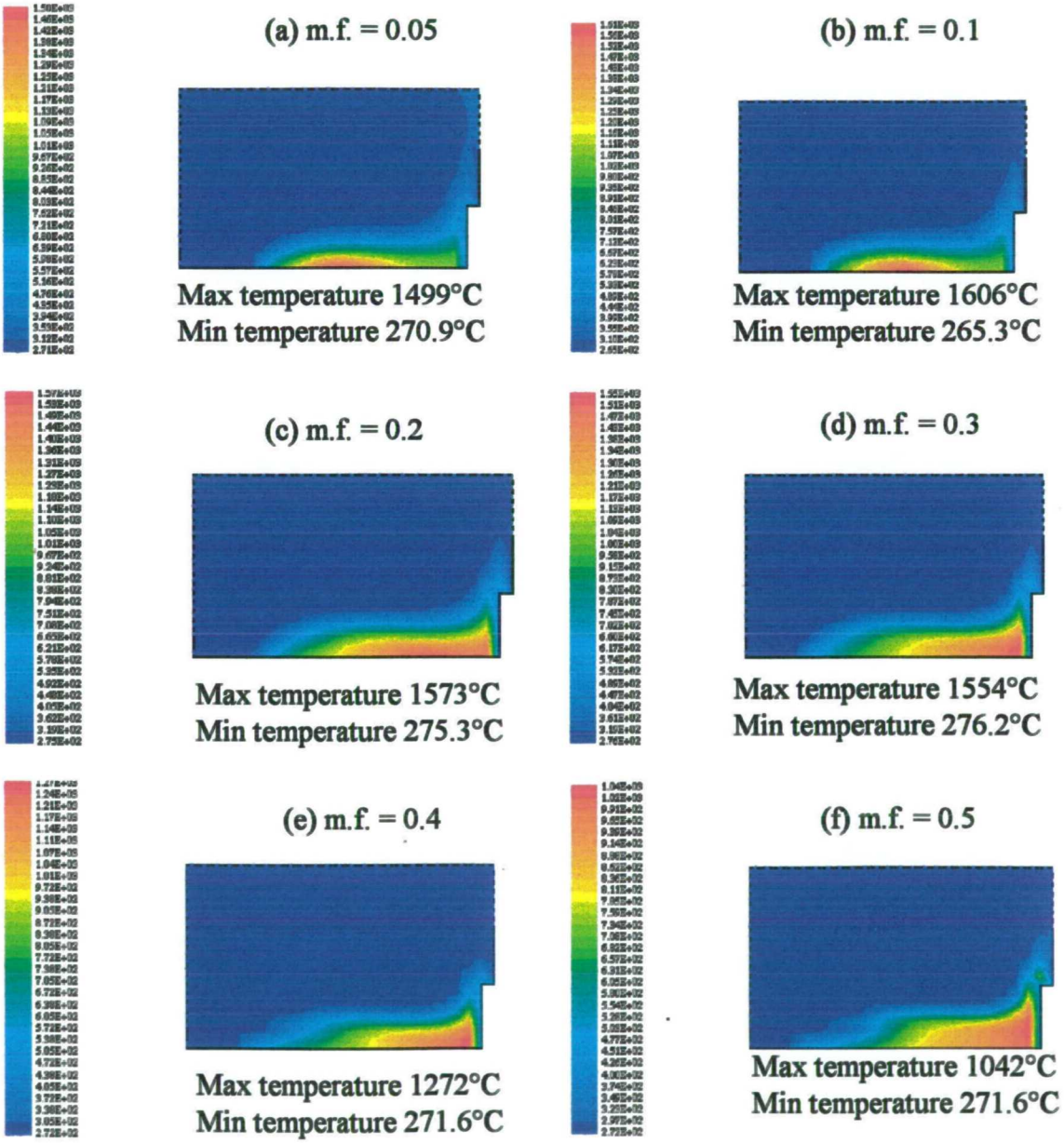


Fig. 7.3 : Temperature distribution contours at different mixture fractions for 70% alcohol solution.

The maximum temperatures of the contours in Fig. 7.3 are plotted in Fig. 7.4.

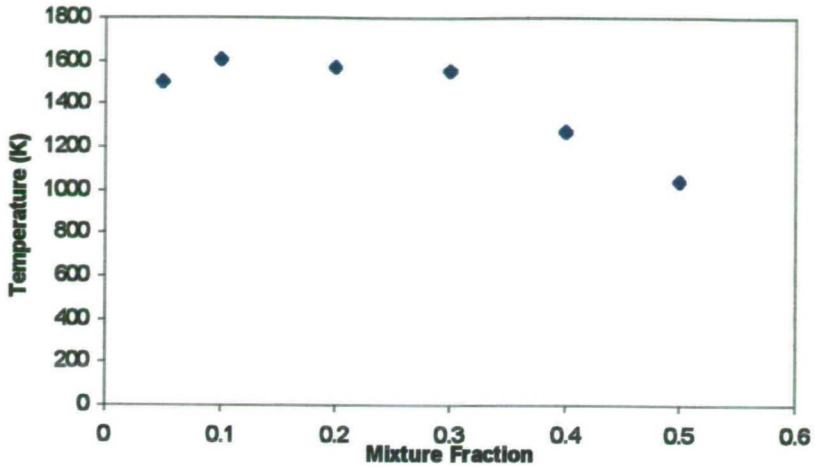


Fig. 7.4 : Maximum Temperature versus Mixture Fraction for the 70% alcohol.

The comparison of maximum temperatures of selected mixture fraction from 50%, 70%, and 80% alcohol solutions are plotted in Fig. 7.5.

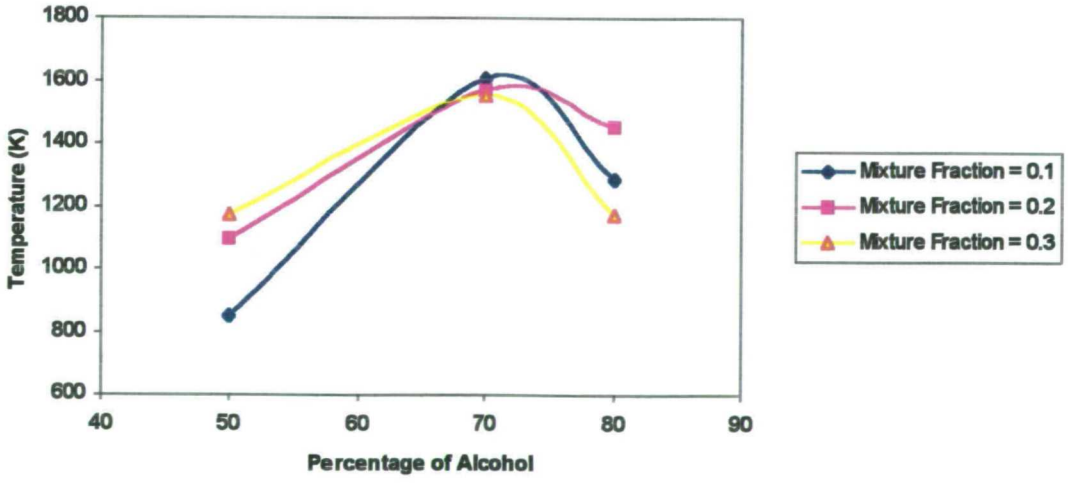


Fig. 7.5 : The Maximum Temperature for Various Percentages of Alcohol and Mixture Fractions.

Fig. 7.6 is a plot of the flow velocity vectors of the model for the 70% alcohol solution and a mixture fraction of 0.2 as this mixture fraction exhibits the greatest maximum temperature as shown in Fig. 7.5.

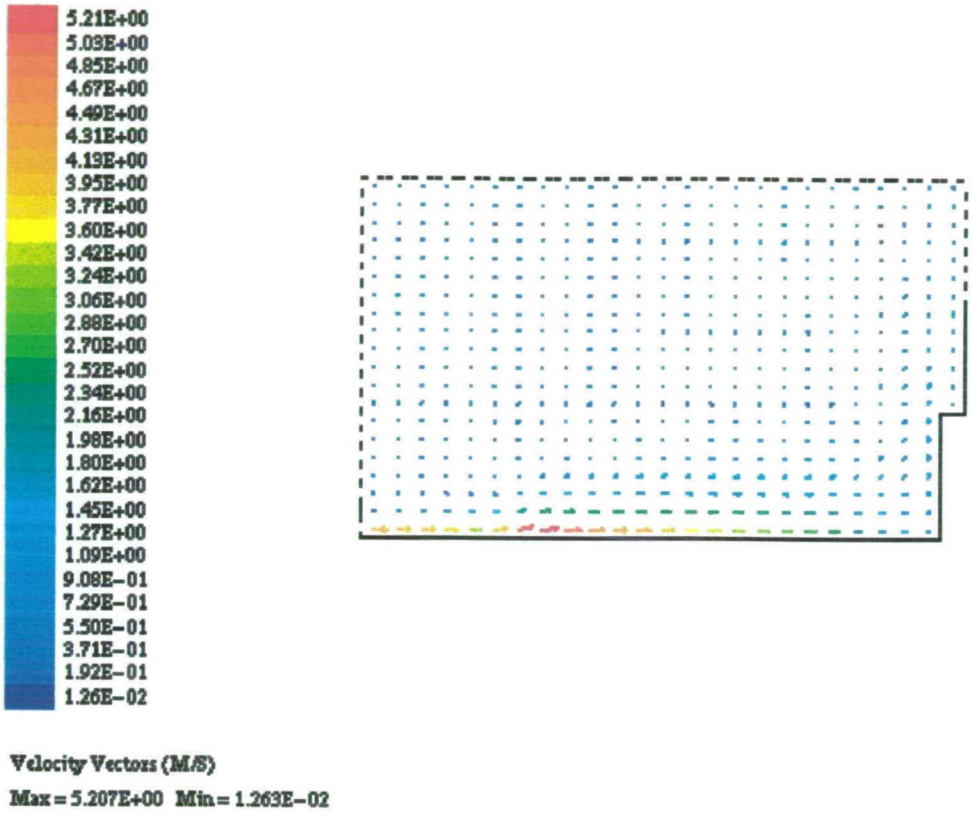


Fig. 7.6 : The flow velocity vectors of a mixture fraction 0.2 for 70% alcohol solution.

The amounts of chemical species from the combustion process are compared for 50%, 70% and 80% ethanol in the precursor. The mixture fraction was fixed at 0.2 for all the chemical species investigated which are oxygen gas, water, carbon monoxide and carbon dioxide. The maximum and minimum mass fractions of each gas are summarised in Fig. 7.7 and the actual contours are shown in the appendix.

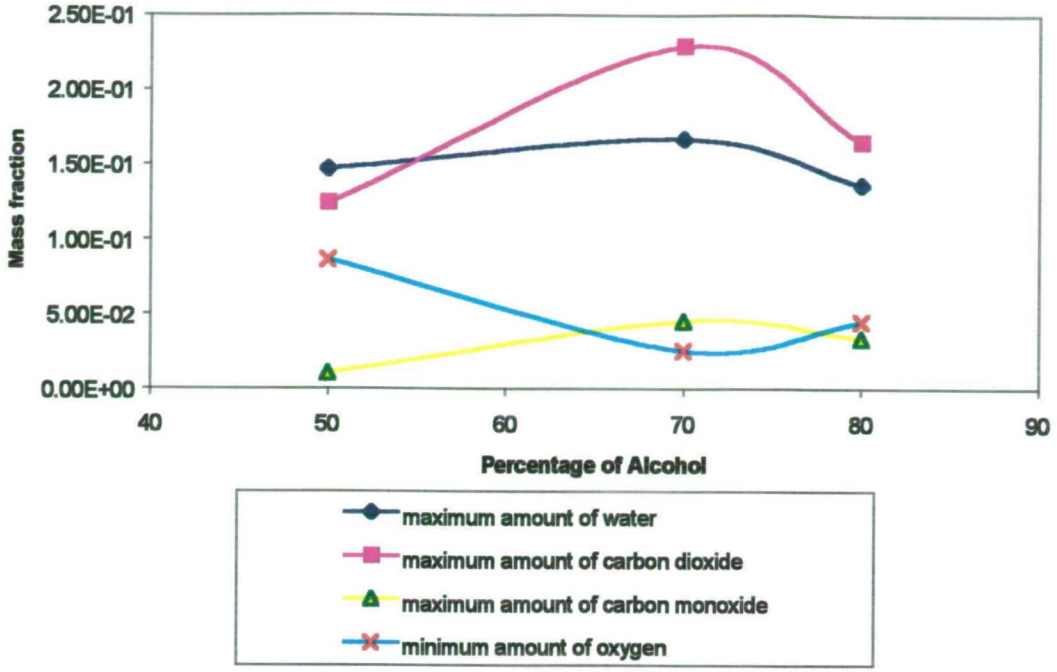


Fig. 7.7 : Mass fraction of chemical species present for 50%, 70%, and 80% alcohol mixtures.

7.7.2 EFFECT OF DROPLET SIZE

Fig. 7.8 shows the temperature distribution contours as a result of different droplet sizes from uniform size at (a) 10 microns, (b) 50 microns, and (c) 100 microns, and ranges of sizes from (d) 10-50 microns, (e) 10-100 microns, and (f) 50-100 microns when the mixture fraction was fixed at 0.2.

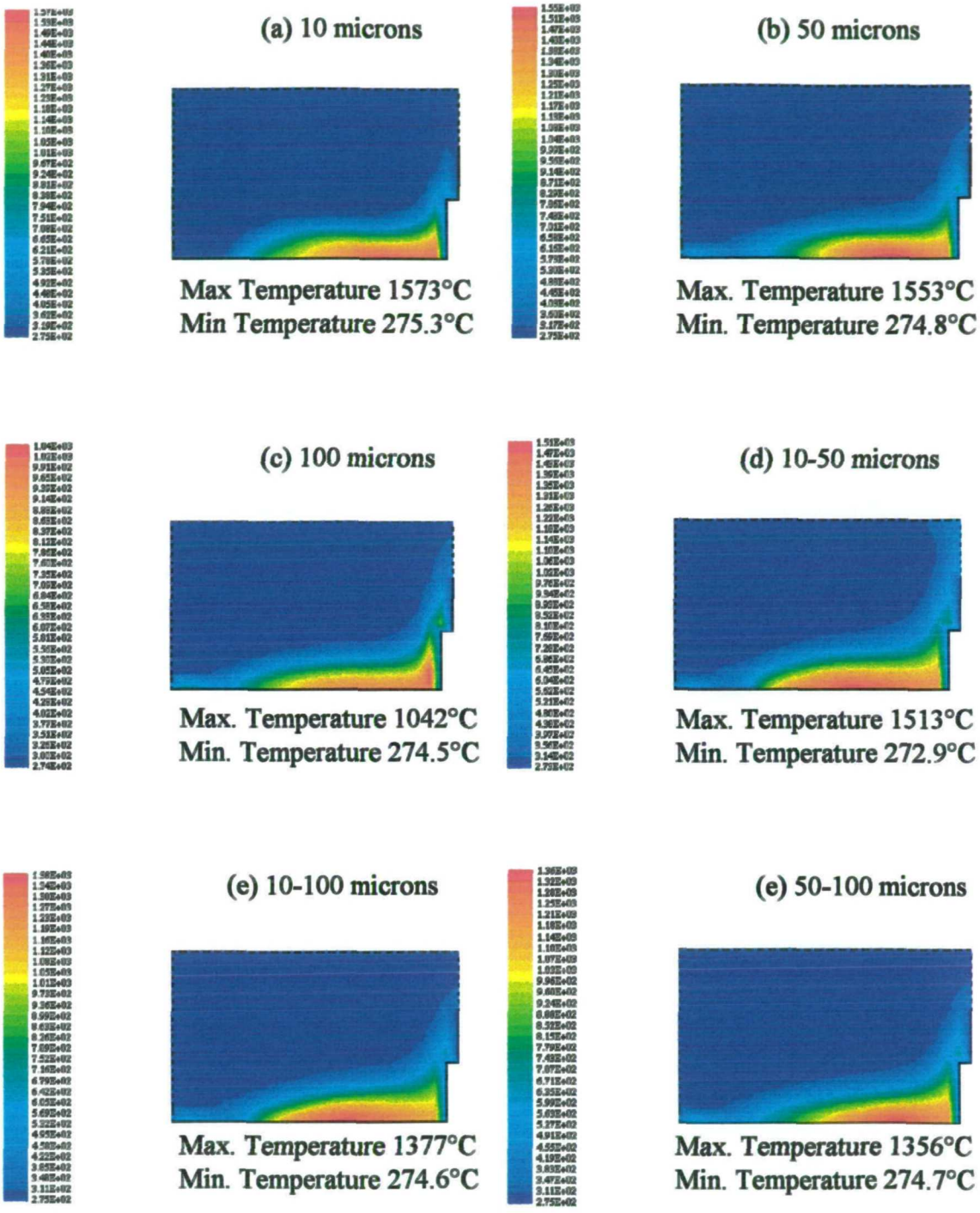


Fig. 7.8 : Temperature distribution contours of various droplets size (a) 10, (b) 50, (c) 100, (d) 10-50, (e) 10-100, and (f) 50-100 microns when the mixture fraction was fixed at 0.2.

7.8 DISCUSSION

The model has been set as close as possible to the actual FAVD experiment to make the results as meaningful as possible. This is the first attempt to model the processing effect for FAVD method. However, in some cases alternative data is used as the exact data is not available or accessible, e.g. thermodynamic data for ethanol, which is not included in the database. In this case, data for methanol is used instead. The difference is not very significant as the main purpose is to identify the trend and the temperature distribution pattern, not the exact numerical values. Physical parameters such as the flow velocity and droplet sizes are more critical and these values were approximated based on the measured values and data given from the manufacturer. A slight change in these parameters could affect the model results more significantly than the change of the thermodynamic data from ethanol to methanol. If exact quantitative results are required, the physical parameters and data and thermodynamic data should be accurately specified.

When the simulations are performed, the flow pattern is viewed from the velocity vector display, which shows both the magnitude and direction of the flow. The temperature distribution is shown as a temperature contour, resulting from the vapourisation and combustion reactions of the mixtures. Different ranges of temperature are represented in different colours.

7.8.1 EFFECT OF MIXTURE FRACTION

The effect in varying the mixture fraction is similar to varying the ratio of fuel to water in the fuel stream. However, the mixture fraction is the ratio of fuel (alcohol + water) to oxidant (air). This clearly identifies the difference in the temperature distribution pattern and the maximum temperature at different mixture fractions in Fig. 7.3 to Fig. 7.5. The optimum condition is where the maximum temperature of the system is the greatest, which indicates the most complete combustion reaction in Fig. 7.3 (b). At this condition, the combustion of the fuel has been completed before reaching the hot plate, i.e. the substrate. This can be taken to be the condition where all species in the vapour phase have undergone a gas phase homogeneous reaction, by which oxide powders are obtained. In Fig. 7.3 (c) - (f),

the combustion of the fuel still continues at the substrate. This signifies that the combustion at the substrate is not complete. Therefore, some non-combusted vapour may reach the substrate as well. This leads to a heterogeneous reaction, which results in either a dense oxide film or a porous film by the interaction between species in the vapour phase and solid phase nucleation.

In addition, the temperature distribution pattern shows the location of the maximum temperature, which can be used to estimate the optimum distance between the substrate and the spray nozzle. The optimum distance is a necessary condition for producing films with the desired properties.

7.8.2 EFFECT OF AMOUNT OF ALCOHOL

Alcohol acts as a fuel in this model. The lower limit of 50% alcohol shows the effect of a low concentration while the 80% alcohol shows the effect of high concentration. The combustion length and temperature are low for the low fuel and much greater for the high fuel. From all the observations, the shapes of the temperature contours at various mixture fractions do not differ much in the low fuel models but show significant changes in the high fuel models. Only at the mixture fraction of 0.3 of 80 % alcohol solution is the maximum combustion temperature reached at the substrate, while in the others it is somewhere before reaching the substrate. These observations can therefore be explained in the same way as for the effect of mixture fractions.

When comparing Fig. 7.3 (c) and Fig. 7.6, from the temperature contour the maximum velocity is at the beginning of the combustion reaction. After the combustion has started, the velocity decreases until the droplet reaches the substrate. At a distance where the velocity of droplets at the substrate is high, a film is difficult to produce because most of the droplets rebound back from the substrate due to the high momentum. When the velocity is not too high, particles (reacted and combusted droplets) can form a packed film on the substrate because the momentum is just enough to pack them together.

The reaction below describes the complete combustion reaction taking place between the spray nozzle and the substrate.

$$CH_3OH + 1.5O_2 \rightarrow 2H_2O + CO_2 \quad \text{-----} \quad 7.1$$

At the same time, CO and CO_2 coexist at equilibrium, as in reaction 7.2.

$$2CO + O_2 \leftrightarrow 2CO_2 \quad \text{-----} \quad 7.2$$

From these two reactions, water and carbon dioxide are the products of the complete combustion process. The combustion process is turbulent, and the reactions involved are not at equilibrium. The amounts of all species involved in the reactions are compared in Figs 7.7. From Fig. 7.5, the model indicates that the optimum combustion reaction should occur when methanol is mixed with water at around 70% alcohol mixture (by volume). The results for the chemical species support the trend above in that the amount of oxygen gas is lowest in the combustion area of 70% alcohol mixture. The products of the combustion process, which are water, carbon monoxide, and carbon dioxide, are found to be richest in the 70% alcohol mixture, not at 80% or above. This leads to the conclusion that at this mixture, the combustion process occurs at the highest efficiency since it consumes the maximum amount of reactant and releases the maximum amount of products. The results from this model agree with the experimental results that a porous film is obtained from a 70% ethanol precursor solution while a powdery film is typically obtained from a higher percentage of ethanol in the precursor solution.

The species contours of carbon monoxide and carbon dioxide (see Appendix) indicate the location of both gases. When all the mixtures have vapourised and combusted, the first intermediate product of carbon is carbon dioxide. This carbon dioxide gas flows towards the substrate while in equilibrium with carbon monoxide gas when the temperature has reached its maximum. Carbon monoxide gas is in equilibrium with carbon dioxide gas over a short distance before being converted

fully to carbon dioxide gas , although some of it reaches the substrate.

7.8.3 EFFECT OF DROPLET SIZE

When different sizes and ranges of droplet size have been modelled, the temperature distribution patterns change as shown in Fig 7.8. If we consider the uniform size droplets in Fig. 7.8 (a), (b), and (c), all have an incomplete combustion shape from the temperature contours for the distance of interest. The smallest droplet size starts combusting at a shorter distance from the spray nozzle to the larger size droplets, and the maximum temperature for smaller droplet sizes is also greater than that for the larger sizes. Therefore, a faster ignition and higher temperature flame can be expected for smaller droplets that the overall combustion complete in a shorter period of time. For the largest droplet size used here (100 microns), the combustion is not complete on reaching the hot plate but continues on the walls, which is not desirable in real experiments.

When ranges of droplet size are considered, the shapes of the temperature contours are different from those of the uniform sizes in that the contour shape is more tapering. The smaller size of droplet initiates the combustion earlier and easier than the larger sizes. In Fig. 7.8 (d) and (e) the combustion starts at about the same distance while the combustion in Fig. 7.8 (f) starts at a distance further from the substrate. The maximum temperature of a droplet with size in the range 10-50 microns is slightly lower than those with uniform sizes of 10 microns and 50 microns. Particle size ranges of 10-100 and 50-100 microns give maximum temperatures in between those of the uniformly small sizes (10 and 50 microns, respectively) and 100 microns.

A few small droplets cause early ignition, which increases the temperature and, hence, increases the evaporation rate for the larger droplets. The whole ignition process then occurs over a longer distance and a longer period of time.

7.9 SUMMARY

The reaction systems in the Flame Assisted Vapour Deposition method have been modelled using a finite volume method based on fluid flow and heat transfer theories. The purpose of the model is to predict the parameter values, which give the best conditions for the deposition process. Although the exact results are not possible to predict at this stage, parameters controlling complete fuel combustion and low droplet momentum at the substrate are suggested. The experiments have been modelled as closely as possible, but some approximations were made where necessary.

The temperature distribution contours and velocity vectors of the particle flow indicate where complete combustion occurs and the predicted products at different distances between the spray nozzle and the substrate. Three parameters have been shown to vary the shapes of the temperature contours significantly; these are the mixture fraction, the amount of fuel and the sizes of droplets. Complete combustion is expected to occur for a combination of suitable mixture fraction that is not too high or too low, amount of fuel and small droplet sizes.

Chapter 8 : CONCLUSIONS AND FUTURE WORK

8.1 : CONCLUSIONS

The investigations of various deposition parameters of the FAVD method in Chapter 4 have shown significant changes in both microstructures and phases of LSM films produced. Desirable microstructures could be obtained by varying these deposition parameters accordingly.

All the processing parameters are influenced by the amount of fuel, the total mass to be combusted and the region of combustion. A film deposited at high temperature is more powdery and crystalline than that deposited at lower temperature as the dominant reaction is governed by gas phase nucleation. This means the decomposition, combustion, and/or chemical reactions of the reactants are completed within the gas phase and the shape of the combustion zone is in category C as explained in Chapter 4. The temperature can be raised either by increasing the amount of ethanol in the precursor solution or increasing the mass fraction of ethanol, or adjusting the position of the flame torch. Powdery films can be fabricated not only by having a high ethanol/water ratio which results in a high deposition temperature but also by using high air pressure, or by increasing the height between the spray nozzle and the substrate. The combustion reaction was confirmed to be complete under these deposition conditions. The deposition rate for powdery film is rather low compared with other types of microstructure.

A dense film is deposited when the deposition temperature is lowered where heterogeneous reactions are dominant. The decomposition and combustion reactions occur in the gas phase, but the reactions take place at or near the heated substrate as the combustion zone is of shape B. A porous film could be obtained by varying the parameters to lie somewhere between those of the homogeneous and heterogeneous reactions, thus causing some particles to be formed in the gas phase and some aerosol to react at the substrate.

At very low deposition temperatures, especially at a low ratio of ethanol/water, the energy provided from the combustion of ethanol is not sufficient therefore the droplets are not readily combusted but splash onto the substrate. These films have high deposition rate but are amorphous.

The effect of processing parameters in the FAVD method have been modelled using a finite volume method based on fluid flow and heat transfer theories. The results support the experimental observation that complete combustion takes place. This allows the microstructure of products at different distances between the spray nozzle and the substrate to be predicted. Complete combustion is suggested to be optimum for a combination of suitable mixture fraction of fuel and oxidant (0.2), amount of fuel (70 % alcohol), and small droplet sizes (10 μm).

Two modifications of LSM have been investigated to improve the electrical properties of SOFC cathodes; La deficient LSM ($La_{0.61}Sr_{0.18}MnO_3$) and LSM with a duplex structure. The duplex structure improved the lateral electrical conductivity of the films but it was not affected by changing the composition. However, the La deficient LSM has a better area specific resistivity (ASR) than duplex structured LSM. The electrical properties of modified LSM deposited using the FAVD technique compare favourably with LSM films fabricated from conventional sintering routes.

For the investigation of improved cathode/electrolyte systems with an interlayer, the lateral resistivity of the cathode depends on the microstructure of the cathode layer itself and is not significantly affected by an interlayer between the cathode and YSZ electrolyte. The lateral resistivity is generally low for films deposited at high temperature, yielding crystalline but powdery film. The activation energy of powdery films tends to be greater than those with porous films due to the loose contact between particles.

The electrode ASRs have been improved with another layer of doped ceria in between cathode and YSZ electrolyte. All the systems of doped ceria in contact with LSC show very low electrode ASRs. After annealing for 94-100 hours, the system of LSC/CGO/YSZ shows a better performance than LSC on YSZ substrate and LSM/YDC/YSZ system, however the ASRs are still greater than the LSC on CGO and LSC/YDC/YSZ systems. The LSC/YDC/YSZ system has even lower ASRs than LSC on CGO, which means YDC is a better interlayer than CGO, and systems with the interlayer definitely have lowered the electrode ASRs.

The bulk and gb ASRs of the systems without an interlayer are lower than those with an interlayer. After annealing, the bulk ASRs of interlayer systems are in the same range as those of the same substrate material (YSZ) due to the higher ionic conductivities of ceria based material. The ionic conductivity of ceria-YSZ solid solution is lower than either the interlayer materials or YSZ. Therefore, the systems with an interlayer show higher gb ASRs.

The electrode ASRs after annealing at certain period of time of LSC/YDC/YSZ and LSC/CGO/YSZ systems have been used to predict the values of k and D^* assuming that the microstructure has not changed. As a result, k and/or D^* decreases with increasing annealing time.

The FAVD method has been proven to produce a cathode for a SOFC with useful properties. Nevertheless, a better control of some of the important processing parameters (e.g. deposition temperature) is sufficient. With the experimental apparatus used, it is difficult to obtain a reproducible film without further investigations.

8.2 : FUTURE WORK

The proposed future work can be divided into two major areas which concern the FAVD method and the electrical properties of cathode films.

8.2.1 FAVD METHOD

In the area of FAVD method, some physical parameters are unknown at this stage due to the lack of characterisation equipment and technology. The droplet size and velocity of the aerosol atomised from the spray nozzle should be quantified using a laser doppler technique. These values are necessary to supply data needed for more accurate computer modelling.

The chemistry involved in FAVD method is still not clear. The deposition mechanisms in the chemical reactions are complex that a thorough study is essential.

The temperature fluctuation can be overcome with an enclosed/controlled environment to reduce the effect of turbulence and air flow inside a fume extraction cupboard. The modified setup has served this purpose adequately but it can be improved further with more modifications of a totally closed unit.

With a better control over the processing parameters, a more accurate effect of each parameter can be quantified which leads to more controlled microstructure and properties.

The surface area and porosity of a porous film can be determined when a larger surface area of film (thicker film and larger substrate size) is used. These will supply more reliable data for the calculation of reactive site at the TPBs and of R_{chem}.

The FAVD method is capable of producing metal oxide powder with a careful control of processing parameters. It is easier to produce powder product rather than a film. This can be useful in a ceramic industry.

8.2.2 ELECTRICAL PROPERTIES

More investigations in the AC-impedance measurements of different cathode materials are necessary as the kinetics behaviour interpretation is still not conclusive at this stage. To determine the rate-determining step(s) for the interfacial reaction, more studies are required including the examination of the surface kinetics of each component and the effect of oxygen partial pressure with the AC response.

Our interlayer system has demonstrated an improvement in the electrode ASRs, however the gb ASRs deteriorate. With a careful selection of electrolyte combinations, these can be improved further.

An improvement by modifying the cathode structure such as a duplex structure has been proven to be advantageous and therefore a further modification can be made in combination with an interlayer. The preferred cathode material is the mixed ionic-electronic conductor (LSC) rather than a purely electronic conductor (LSM). This new combination is expected to perform better in both lateral electrical conductivity and ASR.

The impurity phase of $La_2Zr_2O_7$ has been detected from many LSM films deposited mainly at high temperature but with only powdery films. It is difficult to use XRD technique to detect this phase when it is present at the interface between the electrode and electrolyte when the electrode layer is thick and either porous or dense. There is a possibility that a reaction product phase is present.

A line-scan EDX and Secondary Ion Mass Spectroscopy could be used to identify elements present at the interface between cathode and electrolyte. Hence, any reaction products can be predicted accurately. In addition, a high resolution electron microscope is capable of detecting an impurity phase present at the interface and has been used to identify $La_2Zr_2O_7$ phase between LSM and YSZ [177].

LIST OF PUBLICATIONS

1. K.L. Choy, S. Charojrochkul and B.C.H. Steele, "Fabrication of Cathode for Solid Oxide Fuel Cells Using Flame Assisted Vapour Deposition Technique", Solid State Ionics ***96*** (1997) pp. 49-54.
2. K.L. Choy, S. Charojrochkul and B.C.H. Steele, "Porosity Variation in the Fabrication of Porous Cathode Films for Solid Oxide Fuel Cells Using Flame Assisted Vapour Deposition", in the Proceedings of the Inter. Conf. On Materials Technology – "Recent Developments and Future Potential", January 9-10, 1997, Chiang Mai, Thailand, p. 109.
3. K. Choy, W. Bai, S. Charojrochkul and B.C.H. Steele, J. Power Sources, ***71*** (1998) pp. 361-369.
4. S. Charojrochkul, K-L. Choy and B.C.H. Steele, "Cathode/Electrolyte Systems for Solid Oxide Fuel Cells Fabricated Using Flame Assisted Vapour Deposition Technique", in the 11^{th} Solid State Ionics Conference, November 16-21, 1997, Hawaii, U.S., to be published in Solid State Ionics.

Chapter 9 : REFERENCES

1. B.C.H. Steele, "Materials for Fuel Cells", in Encyclopedia of Advanced Materials, D. Bloor, R.J. Brook, M.C. Flemings and S. Mahajan, (eds.), No. 18616RB007, London, Pergamon Press, 1994.
2. N.Q. Minh, J. Am. Ceram. Soc., *76* (1993), pp. 563-88.
3. H. Iwahara, T. Esaka, H. Uchida and N. Maeda, Solid State Ionics, *3/4* (1981), pp. 359-63.
4. Fuel Cells, A Handbook (Revision 3), U.S. Department of Energy, DOE/METC-94/1006 (DE94004072), January 1994.
5. S.E. Veyo and C.A. Forbes, in Proceedings of the 3rd European SOFC Forum (2-5 June, 1998), U. Bossel, ISBN 3-905592-00-2, Switzerland, pp. 79-86.
6. K. Yamada, J. Mizusaki, H. Sasaki, A. Tsunoda, H. Yokokawa, Y. Yamazaki and K. Nakayama, in the Proceedings of the 4th Inter. Sym. On SOFCs, Yokohama, Japan (1995), Electrochemical Society, Pennington, NJ, p. 33.
7. N.Q. Minh and T. Takahashi, Science and Technology of Ceramic Fuel Cells, Elsevier (1995).
8. A. Hammou, Advances in Electrochemical Science and Engineering, *2* (1992) pp. 87-139.
9. T. Ishihara, H. Matsuda and Y. Takita, Solid State Ionics, *79* (1995) pp. 147-151.
10. K. Huang, M. Feng, J.B. Goodenough and M. Schmerling, J. Electrochem. Soc., 143 (1996) pp. 3630-3636.
11. B.C.H. Steele, in the Proceedings of the 1st European SOFC Forum (October 3-7, 1994), Switzerland.
12. S.S. Liou and W.L. Worrell, Appl. Phys. A, *49* (1989) pp. 25-31.
13. L. Blum, W. Drenckhahn, H. Greiner and E. Ivers-Tiffée, see ref. [6], p. 163.
14. Westinghouse Electric Corp., "Solid Oxide Fuel Cell Power Generation System, The Status of the Cell Technology – A Topical Report", Rept. No. DOE/ET/17089-15, U.S. Dept. of Energy, Washington, DC, 1984.
15. J.T. Brown, IEEE Trans. On Energy Conv., *2* (1988) pp. 193-197.
16. Y. Ohno, S. Nagata and H. Sato, in Proceedings of the 15th IECEC, August 18-22, 1980, Seattle, WA, American Institute of Aeronautics and Astronautics, New York, 1980, p. 881.
17. J.N. Michaels, C.G. Vayenas and L.L. Hegedus, J. Electrochem. Soc., *133* (1986) pp. 522-525.

18. S. Majumdar, T. Claar and B. Flandermeyer, J. Am. Ceram. Soc., ***69*** (1986) pp. 628-33.
19. K.M. Myles and C.C. McPheeters, J. Power Sources, ***29*** (1990) pp. 311-319.
20. D.C. Fee, S.A. Zwick and J.P. Ackerman, in Proceedings of the Conference on High Temperature Solid Oxide Electrolytes, Vol. 1-Anion Conductors, August 16-17, 1983, Brookhaven National Laboratory, Upton, NY, 1983, p. 29.
21. R.T. Dirstine, R.N. Blumenthal and T.F. Kuech, J. Electrochem. Soc., ***126*** (1979) p. 264.
22. R.N. Blumenthal and J.E. Garnier, J. Solid State Chem., ***16*** (1976) pp. 21-34.
23. T. Kudo and H. Obayashi, J. Electrochem. Soc., ***122*** (1975) p. 142.
24. K. Eguchi, T. Setoguchi, T. Inoue and H. Arai, Solid State Ionics, ***52*** (1992) pp. 165-172.
25. I. Riess, D. Braunshtein and D.S. Tannhauser, J. Am. Ceram. Soc., ***64*** (1981) p. 479.
26. D.L. Maricle, T.E. Swarr and S. Karavolis, Solid State Ionics, ***52*** (1992) pp. 173-182.
27. H. Yahiro, Y. Eguchi, K. Eguchi and H. Arai, J. Appl. Electrochem., ***18*** (1988) p 527.
28. M.T. Hernández, J.R. Jurado and P. Durán, in the Proceedings of the 2nd Inter. Sym. On SOFCs, July 2-5, 1991, Athens, Greece, F. Grosz, P. Zegers, S.C. Singhal and O. Yamamoto, eds, Commission of the European Communities, Luxembourg, 1991, p. 421.
29. C. Milliken, S. Elangovan and A.C. Khandkar, in the Proceedings of the 2nd Inter. Sym. Ionics and Mixed Conducting Ceramics, T.A. Ramanarayanan, W.L. Worrell and H.L. Tuller, (eds.), Vol. 94-12, p. 466.
30. K. Eguchi, T. Setoguchi and H. Arai, Energy Conversion and Utilization with High Efficiency, 1990, C01-16, p. 93.
31. H. Arai, K. Eguchi, T. Setoguchi, H. Itoh and T. Ionue, Extended Abstract No. 562, Vol. 89-2, Fall Meeting, Electrochem. Soc., 1989.
32. I. Riess, Solid State Ionics, ***52*** (1992) pp. 127-134.
33. J.F. Jue, J. Jusko and A.V. Virkar, J. Electrochem. Soc., ***139*** (1992) p 2458.
34. R. Draper, Ind. Heat, December (1991) p. 44.
35. T. Takahashi, K. Ito and H. Iwahara, in the Proceedings of Journees Internationales d'Etude des Piles a Combustible III, June 21-24, 1965, Societe d'Etudes de Recherches et d'Application pour l'Industrie, Brussels, Belgium, 1965, p. 42.
36. H. Yahiro, K. Eguchi and H. Arai, Solid State Ionics, ***36*** (1989) p. 71.
37. R. Männer, E. Ivers-Tiffée and W. Wersing, see ref. [28], p. 715.
38. H.L. Tuller and A.S. Nowick, J. Electrochem. Soc., ***122*** (1975) p. 209.

39. H. Yahiro, K. Eguchi and H. Arai, Solid State Ionics, *21* (1986) p. 37.
40. T.H. Etsell and S.N. Flengas, Chem. Rev., *70* (1970) p. 339.
41. T.H. Etsell and S.N. Flengas, J. Electrochem. Soc., *118* (1971) p. 1890.
42. T.M. Gur, I.D. Raistrick and R.A. Huggins, in Fast Ion Transport in Solids, P. Vashishta, J.N. Mundy and G.K. Shenoy, (eds.), Elsevier North Holland, New York, 1979, p. 113.
43. M. Kleitz, P. Farby and E. Schouler, Solid State Ionics, *57* (1992) p. 439.
44. P. Farby and M. Kleitz, J. Electroanal. Chem. Interfacial Electrochem., *57* (1974) p. 165.
45. J. Sasaki, J. Mizusaki, S. Yamauchi and K. Fueki, Bull. Chem. Soc. Jpn., *54* (1981) p. 1688.
46. T. Kenjo, S. Osawa and H. Murahashi, Denki Kagaku, *58* (1990) p. 533.
47. J. Mizusaki, K. Amano, S. Yamaguchi and K. Fueki, Solid State Ionics, *22* (1987) p. 313.
48. J. Mizusaki, K. Amano, S. Yamaguchi and K. Fueki, ibid, p. 323.
49. H. Yanagida, R.J. Brook and F.A. Kröger, J. Electrochem. Soc., *117* (1970) p. 593.
50. R.J. Brook and T.L. Markin, Solid State Ionics, *57* (1992) p.533.
51. R.J. Brook, W.L. Pelzmann and F.A. Kröger, J. Electrochem. Soc., *118* (1971) 185.
52. M.V. Glumov, Sov. Electrochem. (Engl. Transl.), *22* (1986) p. 207.
53. T.M. Gur, I.D. Raistrick and R.A. Huggins, J. Electrochem. Soc., 127 (1980) p. 2620.
54. A.I. Gruzdev, Sov. Electrochem. (Engl. Transl.), *26* (1990) p. 530.
55. A.T. Filayev, S.V. Karpachev and S.F. Pal'guev, in Electrochemistry of Molten and Solid Electrolytes, Vol. 4, A.N. Braboshkin and S.F. Pal'guev, eds, Consultants Bureau, New York, 1967, p. 161.
56. I.V. Murygin and V.N. Chebotin, Sov. Electrochem. (Engl. Transl.), *15* (1979) p. 1415.
57. S. Pizzini, in Fast Ion Transport in Solids, Solid State Batteries and Devices, W. Van Gool, (ed.), North Holland, Amsterdam, The Netherlands, 1973, p. 461.
58. B.C.H. Steele, Phil. Trans. R. Soc. Lond. A, *354* (1996) pp. 1695-1710.
59. F.H. Van Heuveln, F.P.F. Van Berkel and J.P.P. Huijsmans, in the Proceedings of the 14th Risϕ Inter. Sym. On Materials Science, High Temperature Electrochemical Behaviour of Fast Ion and Mixed Conductors, September 6-10, 1993, Roskilde, Denmark, F.W. Poulsen, J.J. Bentzen, T. Jacobsen, E. Skou and M.J.L. Østergård, (eds.), Risϕ National Laboratory, Denmark, 1993, p. 53.
60. L.G.L. de Haart, K.J. de Vries, A.P.M. Carvalho, J.R. Frade and F.M.B. Marques, Mater. Res. Bull., *26* (1991) p. 507.

61. J. Mizusaki, H. Tagawa, K. Tsuneyoshi and A. Sawata, J. Electrochem. Soc., ***138*** (1991) p. 1867.

62. B.C.H. Steele, Solid State Ionics 86-88 (1996) pp. 1223-1234.

63. B.C.H. Steele, Solid State Ionics ***75*** (1995) pp. 157-165.

64. B.C.H. Steele, Mater. Sci. Eng., ***B13*** (1992) p. 79.

65. M. Liu, in Ionics and Mixed Conducting Ceramics, Vol. 91-12, R.A. Ramanarayan and H.L. Tuller, (eds.), Electrochemical Society, NJ, 1991, p. 95.

66. B.C.H. Steele, see ref. [59], p. 423.

67. S.B. Adler, J.A. Lane and B.C.H. Steele, J. Electrochem. Soc., ***143*** (1996) pp. 3554-64.

68. J. van Roosmalen, Some Thermochemical Properties of (La,Sr)$MnO_{3+\delta}$ as a Cathode Material for Solid Oxide Fuel Cells, Netherlands Energy Research Foundation ECN, Petten, The Netherlands, 1993.

69. G.V. Subba Rao, B.M. Wanklyn, C.N.R. Rao, J. Phys. Chem. Solids, ***32*** (1971) p. 345-358.

70. G.H. Jonker, J. Appl. Phys., ***37*** (1966) p. 1424.

71. H. Yokokawa, N. Sakai, T. Kawada and M. Dokiya, J. Electrochem. Soc., ***138*** (1991) pp. 2719-2727.

72. Z. Li, M. Behruzi, L. Fuerst and D. Stoöer, in the Proceedings of the 3rd Inter. Sym. On SOFCs, May 16-21, 1993, Honolulu, HI, S.C. Singhal and H. Iwahara, (eds.), Electrochemical Society, Pennington, NJ, 1993, p. 171.

73. H. Tagawa, J. Mizusaki, H. Nambu, C. nakao, H. Takai and H. Minamiue, in the British Ceramic Proceedings No. 56 (1996) p. 113.

74. M. Kertesz, I. Riess, D.S. Tanhauser, R. Langpape and F.J. Rohr, J. Solid State Chem., ***42*** (1982) pp. 125-129.

75. E. Syskakis, B. Robens and A. Naoumidis, J. de Physique IV, Colloque C7, supp. III, ***3*** (1993) pp. 1429-1434.

76. I.G. Krogh Andersen, E. Kroch Andersen, P. Norby and E. Skou, J. Solid State Chem., ***113*** (1994) pp. 320-326.

77. R. Millini, M.F. Gagliardi and G. Piro, J. Mat. Sci., ***29*** (1994) pp. 4065-4069.

78. P. Kofstad and A. Petrov, see ref. [59], p. 287.

79. I. Yasuda and M. Hishinuma, J. Solid State Chem., ***123*** (1996) pp. 382-390.

80. I. Yasuda and M. Hishinuma, see ref. [29], p. 209.

81. J.H. Kuo, H.U. Anderson and K.M. Sparlin, J. Solid State Chem., ***83*** (1989) p. 52.

82. S. Otoshi, H. Sasaki, H. Ohnishi, M. Hase, K. Ishimaru and M. Ippommatsu, J. Electrochem. Soc., ***138*** (1991) pp. 1519-1522.

83. A. Endo, M. Ihara, H. Komiyama and K. Yamada, Solid State Ionics, ***86-88*** (1996) pp. 1191-1195.

84. T. Pagnier, B. Gharbage and A. Hammou, see ref. [72], p. 575.

85. M.J.L. Østergård and M. Mogensen, Electrochim. Acta, ***38*** (1993) p. 2015.

86. K. Wippermann, U. Stimming, H. Jansen and D. Stöver, see ref. [72], p. 180.

87. Y. Takeda, R. Kanno, M. Noda, Y. Tomida and O. Yamamoto, J. Electrochem. Soc., ***134*** (1987) p. 2656.

88. B.A. van Hassel, T. Kawada, N. Sakai, H. Yokokawa, M. Dokiya and H.J.M. Bouwmeester, Solid State Ionics, ***66*** (1993) p. 295.

89. A. Mitterdorfer and L.J. Gauckler, in the Proceedings of the 17th Risϕ Inter. Sym. On Materials Science, High Temperature Electrochemical Behaviour of Fast Ion and Mixed Conductors, September 2-6, 1996, Roskilde, Denmark, , (eds.), Risϕ National Laboratory, Denmark, 1996, p. 357.

90. M. Ippommatsu, H. Sasaki, S. Otoshi, M. Suzuki, C. Kurusu, A. Kajimura and N. Sugiura, see ref. [72], p. 200.

91. M. Suzuki, H. Sasaki, So. Otoshi, A. Kajimura, N. Sugiura and M. Ippommatsu, in 1992 Fuel Cell Seminar Abstracts, November 29 – December 2, 1992, Tucson, AZ, Courtesy Associates, Washington, DC, 1992, p. 297.

92. K. Sasaki, J.P. Wurth, R. Gschwend, M. Gödickemeier and L.J. Gauckler, J. Electrochem. Soc., ***143*** (1996) pp. 530-543.

93. I. Yasuda, K. Ogasawara, M. Hishinuma, T. Kawada and M. Dokiya, Solid State Ionics, ***86-88*** (1996) pp. 1197-1201.

94. J.H. Kuo, H.U. Anderson and D.M. Sparlin, J. Solid State Chem., ***87*** (1990) p. 55.

95. K. Eguchi, T. Inoue, T. Setoguchi and H. Arai, J. Alloys and Compounds, ***193*** (1993) pp. 59-61.

96. T. Ishihara, T. Kudo, H. Matsuda and Y. Takita, J. Electrochem. Soc., ***142*** (1995) pp. 1519-1524.

97. S. Carter, A. Selcuk, R.J. Chater, J. Kajda, J.A. Kilner and B.C.H. Steele, Solid State Ionics, ***53-56*** (1992) pp. 597-605.

98. A. Mackor, T.P.M. Koster, J.G. Kraaijkamp, J. Gerretsen and J. van Eijk, see ref. [28], p. 463.

99. H. Lauret, E. Caignol and A. Hammou, see ref. [28], p. 479.

100. H. Tagawa, J. Mizusaki, H. Takai, Y. Yonemura, H. Minamiue and T. Hashimoto, see ref. [89], p. 437.

101. H. Yokokawa, N. Sakai, T. Kawada and M. Dokiya, in Science and Technology of Zirconia V, S.P.S. Badwal, M.J. Bannister and R.H.J. Hannink, (eds.), Technomic Publishing Company, Lancaster, PA, 1993, p. 752.

102. G. Stochniol, E. Syskakis and A. Naoumidis, J. Am. Ceram. Soc., *78* (1995) pp. 929-932.

103. A. Weber, R. Männer, B. Jobst, M. Schiele, H. Cerva, R. Waser and E. Ivers-Tiffée, see ref. [89], p. 473.

104. Y. Takeda, Y. Sakaki, T. Ichikawa, N. Imanishi and O. Yamamoto, Solid State Ionics, *72* (1994) pp. 257-264.

105. H. Nishiyama, M. Aizawa, H. Yokokawa, T. Horita, N. Sakai, M. Dokiya and T. Kawada, J. Electrochem. Soc., *143* (1996) pp. 2332-2341.

106. W.J. Quadakkers, H. Greiner, M. Hänsel, A. Pattanaik, A.S. Khanna and W. Mallener, Solid State Ionics, *91* (1996) pp. 55-67.

107. P.M. Raccah and J.B. Goodenough, Phys. Rev., *155* (1967) p. 932.

108. A.N. Petrov and P. Kofstad, see ref [72], p. 220.

109. J. Mizusaki, J. Tabuchi, T. Matsuura, S. Yamauchi and K. Fueki, J. Electrochem. Soc., *136* (1989) p. 2082.

110. V.V. Vashuk, I.F. Kononyuk, Y.G. Zonov and O.N. Golovchan, Inorg. Mater. (Engl. Transl.), *28* (1992) p. 486.

111. J.A. Labrincha, J.R. Frade, F.M.B. Marques, see ref. [28], p. 689.

112. H. Yokokawa, N. Sakai, T. Kawada and M. Dokiya, J. Electrochem. Soc., *138* (1991) p. 2719.

113. H. Yokokawa, N. Sakai, T. Kawaka and M. Dokiya, see ref. [28], p. 663.

114. E. Ivers-Tiffée, M. Schieβl, H.J. Oel and W. Wersing, see ref. [72], p. 613.

115. J.A. Labrincha, J.R. Frade and F.M.B. Marques, J. Mater. Sci., *28* (1993) p. 3809.

116. E.F. Sverdrup, D.H. Archer and A.D. Glasser, Advances in Chemistry Series, R.F. Gould, (ed.), Fuel Cell Systems II, American Chemical Society Publications.

117. K. Sasaki, H.P. Seifert and L.J. Gauckler, J. Electrochem. Soc., *141* (1994) pp. 2759-2768.

118. J.C. Manifacier, Thin Solid Films, *90* (1982) pp. 297-308.

119. Y. Takeda, H. Ueno, N. Imanishi, O. Yamamoto, N. Sammes and M.B. Phillipps, Solid State Ionics, *86-88* (1996) pp. 1187-1190.

120. T. Ishihara, T. Kudo, H. Matsuda and Y. Takita, J. Am. Ceram. Soc., 77 (1994) pp. 1682-1684.

121. C.C. Chen, M.M. Nasrallah and H.U. Anderson, see ref. [72], p. 598.

122. J.A. Lane, P.H.Middleton, H. Fox, B.C.H. Steele and J.A. Kilner, see ref. [29], p. 489.

123. H. Yamada and H. Nagamoto, see ref. [72], p. 213.

124. M.B. Phillipps, N.M. Sammes and O. Yamamoto, J. Mat. Sci., *31* (1996) pp. 1689-1392.

125. Y. Ohno, S. Nagata and H. Sato, Solid State Ionics, ***9-10*** (1983) pp. 1001-1008.

126. A.N. Petrov, O.F. Kononchuk, A.V. Andreev, V.A. Cherepanov and P. Kofstad, ibid, ***80*** (1995) pp. 189-199.

127. M. Sahibsada, B.C.H. Steele, K. Zheng, R.A. Rudkin, J.M. Bae, N. Kiratzis, D. Waller and I.S. Metcalfe, in the Proceedings of the 2nd European Forum, May 6-10, 1996, Oslo, Norway, p. 687.

128. R. Chiba and T. Ishii, see ref. [6], p. 482.

129. K. Eguchi, T. Inoue, M. Ueda, J. Kamimae and H. Arai, see ref. [28], p. 697.

130. A. Endo, S. Wada, C.J. Wen, H. Komiyama and K. Yamada, J. Electrochem. Soc., ***145*** (1998) L35-L37.

131. S. Srilomsak, D.P. Schilling and H.U. Anderson, in the Proceedings of the 1st Inter. Sym. On SOFCs, October 16-18, 1989, Hollywood, FL, S.C. Singhal, (ed.), Electrochem. Soc., Pennington, NJ, 1989, p. 129.

132. M. Fandel, J. Hoschele, W. Schäfer and R. Schmidberger, in Euro-Ceramics Vol. 2, Properties of Ceramics, G. de With, R.A. Lerpstra and R. Metselaar, (eds.), Elsevier Applied Science, London, U.K., 1989, p. 2.236.

133. J. Echigoya, S. Hiratsuka and H. Suto, Mater. Trans. JIM, ***30*** (1989) p. 789.

134. T. Setoguchi, K. Eguchi and H. Arai, in the Proceedings of the Inter. Conf. Thin Film Physics and Applications, p. 74.

135. K. Eguchi, T. Setoguchi, S. Tamura and H. Arai, see ref. [101], p. 694.

136. Handbook of Thin Film Process Technology, D. Glocker, S. Ismat Shah, (eds.), 1997.

137. K.Z. Fung, J. Chen, C. Tanner and A.V. Virkar, see ref. [6], p. 1018.

138. S.P.S. Badwal, see ref. [11], p. 399.

139. M. Prica, K. Kendall and M. Painter, see ref. [6], p. 1056.

140. Y. Aihara, S. Ito and S. Kawasaki, see ref. [6], p. 180.

141. M. Cassidy, G. Lindsay and K. Kendall, see ref. [11], p. 577.

142. T. Setoguchi, M. Sawano, K. Eguchi and H. Arai, Solid State Ionics, ***40/41*** (1990) pp. 502-505.

143. T. Setoguchi, T. Inoue, H. Takebe, K. Eguchi, K. Morinaga and H. Arai, Solid State Ionics, ***37*** (1990) pp. 217-221.

144. N.Q. Minh and R.A. Gibson, see ref. [11], p. 587.

145. E. Scafé, M. Musicanti and S. Mercuri, ibid, p. 789.

146. E. Scafé, M. Musicanti and S. Mercuri, ibid, p. 809.

147. B. Gut, J. Kübler and R. Primas, ibid, p. 781.

148. M. Brocco, G. Cosoli, L. Pilloni, M. Ronchetti and E. Scafé, ibid, p. 767.

149. D. Stolten, L. Winter, W. Schäfer, H. Geier and G. Lindemann, ibid, p. 799.

150. S.K. Lau and S.C. Singhal, in 1985 Fuel Cell Seminar Abstracts, Tucson, AZ, May 19-22, 1985, Countesy Associates, Washington, DC, 1985.

151. S. Majumdar, in 1986 Fuel Cell Seminar Abstracts, October 26-29, 1986, Tucson, AZ, Courtesy Associates, Washington, DC, 1986, p. 60.

152. S. Majundar, T. Claar and B. Flandermeyer, J. Am. Ceram. Soc., ***69*** (1986) p. 628.

153. Ceramatec, Inc., Development of Planar Geometry Solid Oxide Fuel Cell Technology, Phase I Final Report, July 1986 – July 1987, Report No. GRI-87/0297, Gas Research Institute, Chicago, IL, 1987.

154. A. Tintinelli, C. Rizzo, S. Loreti and A. Selvaggi, see ref. [28], p. 747.

155. C.C. McPheeters, U. Balachandran, P.E. Blackburn, D.E. Busch, D.W. Dees, S.E. Dorris, J. Dusek, J.J. Heiberger, H. Leu, S. Majumdar, F.C. Mrazek, K.M. Myles, J.J. Picciolo and R.B. Poeppel, in the Proceedings of the 23rd IECEC, July 31-August 5, 1988, Denver, CO, Vol. 2, American Society of Mechanical Engineers, New York, 1988, p. 279.

156. J.P.P. Huijsmans, E.J. Siewers, F.H. van Heuveln and J.P. de Jong, see ref. [28], p. 113.

157. N.Q. Minh and C.R. Horne, see ref. [59], p. 337.

158. N.Q. Minh, C.R. Horne, F.S. Liu, K.M. Moffatt, P.R. Staszak, T.L. Stillwagon and J.J. Van Ackeren, in the Proceedings of the 25th IECED, August 12-17, 1990, Reno, NV, Vol. 3, American Institute of Chemical Engineers, New York, 1990, p. 230.

159. N.Q. Minh, in the Proceedings of the Inter. Sym. On SOFCs, November 13-14, 1989, Nagoya, Japan, O. Yamamoto, M. Dokiya and H. Tagawa, (eds.), Science House, Tokyo, Japan, 1989, p. 67.

160. N.Q. Minh, T.R. Armstrong, J.V. Guiheen, C.R. Horne, F.S. Liu, D.M. Moffatt, T.L. Stillwagon and J.J. Van Ackeren, in 1990 Fuel Cell Seminar Abstracts, November 25-28, 1990, Phoenix, AZ, Courtesy Associates, Washington, DC, 1990, p. 524.

161. Smithells Metals Reference Book, p. 35.

162. A. Negishi, K. Nozaki and T. Ozawa, Solid State Ionics, ***3/4*** (1981) pp. 443-446.

163. W.A. Bryant, J. Mat. Sci., ***12*** (1977) pp. 1285-1306.

164. A.O. Isenber, in the Proceedings of the Symposium on Electrode Materials and Processes for Energy Conversion and Storage, May 9-12, 1977, Philadelphia, PA, J.D.E. McIntyre, S. Srinivasan and F.G. Will, (eds.), Electrochemical Society, Pennington, NJ, 1977, p. 572.

165. M.F. Carolan and J.N. Michaels, Solid State Ionics, ***25*** (1987) pp. 207-216.

166. C. Wagner, Z. Phys. Chem. B, ***21*** (1933) p. 25.

167. R.J. Bratton, P. Reichner and L.W. Montgomery, see ref. [nt 9-108], p. 80.

168. K. Choy, W. Bai, S. Charojrochkul and B.C.H. Steele, J. Power Sources, *71* (1998) pp. 361-369.

169. K.L. Choy, W. Bai and B.C.H. Steele, in the Proceedings of the 5th Inter. Symp. On SOFCs, Aachen, Germany, June 1997, Electrochemical Society, Pennington, NJ, 1997, p. 1177.

170. A.T. Hunt, *Combustion Chemical Vapor Deposition from Liquid Organic Solutions*, PhD. Thesis, Georgia Institute of Technology, U.S., 1993.

171. J.L. Deschanvres, F. Cellier, G. Delabouglise, M. Labeau and M. Langlet, J. de Physique (1989), C5-695.

172. J.M. Hampikian, A.T. Hunt and W.B. Carter, Processing and Fabrication of Advanced Materials III, 1994, Ch. 60, pp. 345-354.

173. J. McHale, R.W. Schaeffer, A. Kebede, J. Macho and R.E. Salomon, J. of Superconductivity, 5 (1992) p. 511.

174. M. Koguchi, Y. Matsuda, E. Kinoshita and K. Hirabayashi, Jap. J. Appl. Phys., 29 (1990) L33-L35.

175 K.L. Choy, in the British Ceramic Proceedings No. 54, 1995, "Ceramic Films and Coatings", W.E. Lee, (ed.), p. 65.

176. A.T. Hunt, W.B. Carter and J.K. Cochran Jr., Appl. Phys. Lett., *63* (1993) pp. 266-268.

177. M. Mogensen, T. Lindegaard, U.R. Hansen and G. Mogensen, see ref. [29], p. 448.

178. S. Srilomsak, D.P. Schilling and H.U. Anderson, see ref. [131], p. 129.

179. N. Bonanos, B.C.H. Steele, E.P. Butler, W.B. Johnson, W.L. Worrell, D.D. Macdonald and M.C.H. McKubre, "Applications of Impedance Spectroscopy" in Impedance Spectroscopy – Emphasizing Solid Materials and Systems, J.R. Macdonald, (ed.), John Wiley and Sons, 1987, p. 191.

180. J.E. Bauerle, J. Phys. Chem. Solids, *30* (1969) pp. 2657-2670.

181. L.J. van der Pauw, Philips Research Reports, *13* (1958) pp. 1-9.

182. I. Wiedmann, K.L. Choy and B. Derby, British Ceramic Proceedings No. 53, "Novel Synthesis and Processing of Ceramics", F.R. Sale, (ed.), p.133.

183. J.C. Viguié and J. Spitz, J. Electrochem. Soc., *122* (1975) pp. 585-588.

184. Powder Diffraction File, JCPDS, International Centre for Diffraction Data.

185. M. Mori, H. Itoh, N. Mori, T. Abe, O. Yamamoto, Y. Takeda and N. Imanishi, see ref. [101], p. 776.

186. G.L. Messing, S.C. Zhang and G.V. Jayanthi, J. Am. Ceram. Soc., *76* (1993) pp. 2707-26.

187. E. Bergsmark, S. Furuseth, O. Dyrlie, T. Norby and P. Kofstad, see ref. [28], p. 473.

188. T. Tsai and S.A. Barnett, Solid State Ionics, *93* (1997) pp. 207-217.

189. A. Hammouche, E.J.L. Schouler and M. Henault, ibid, ***28-30*** (1988) pp. 1205-1207.

190. H. Kamata, A. Hosaki, J. Mizusaki and H. Tagawa, ibid, ***106*** (1998) pp. 237-245.

191. J.P.P. Huijsmans, J.P. de Jong, F.H. van Heuveln and F.P.F. van Berkel, see ref. [6], p. 94.

192. F.H. van Heuveln, H.J.M. Bouwmeester and F.P.F. van Berkel, J. Electrochem. Soc., ***144*** (1997) pp. 126-133.

193. J. Mizusaki, H. Takawa, M. Katou, K. Hirano, A. Sawata and K. Tsuneyoshi, see ref. [28], p. 487.

194. F.H. Van Heuveln and H.J.M. Bouwmeester, J. Electrochem. Soc., ***144*** (1997) pp. 134-140.

195. Y. Takeda, R. Kanno, M. Noda, Y. Tomida and O. Yamamoto, ibid, ***134*** (1987) p. 2656.

196. E. Siebert, A. Hammouche and M. Kleitz, Electrochimica Acta, ***40*** (1995) pp. 1741-1753.

197. M.J.L. Østergård and M. Mogensen, ibid, ***38*** (1993) pp. 2015-2020.

198. H. Lauret and A. Hammou, J. Euro. Ceram. Soc., ***16*** (1996) pp. 447-451.

199. M. Gödickemeier, K. Sasaki, L.J. Gauckler and I. Riess, Solid State Ionics, ***86-88*** (1996) pp. 691-701.

200. T. Tsai and S.A. Barnett, see ref. [169], p. 274.

201. T. Horita, N. Sakai, H. Yokokawa, M. Dokiya, T. Kawada, J. Van Herle and K. Sasaki, J. Electroceramics ***1*** (1997) pp. 155-164.

202. C.P. Jacobson, S. J. Visco and L.C. De Jonghe, in the Proceedings of the 3rd Inter. Sym. On Ionic and Mixed Conductors, September 1997, Paris, Proc. Vol. PV97-24, Electrochemical Society (in press).

203. D. Bauza, D. Especel and M. Gouet, Novel Ceramic Fabrication Processes and Applications, 1986, British Ceramic Proceedings No. 38, p. 197-201.

204. S.B. Adler, see ref. [202] (in press).

205. M. Liu and J. Winnick, J. Electrochem. Soc., ***144*** (1997) p. 1881.

206. M. Gödickemeier, K. Sasaki, L.J. Gauckler and I. Reiss, J. Electrochem. Soc., ***144*** (1997) p. 1635.

207. I. Riess, M. Gödickemeier and L.J. Gauckler, Solid State Ionics, ***90*** (1996) p. 91.

208. M. Kleitz and F. Petitbon, ibid, ***92*** (1996) p. 65.

209. M. Kleitz, L. Dessemond, T. Kloidt and M.C. Steil, see ref. [6].

210. J.D. Sirman, J.A. Lane and J.A. Kilner, see ref. [202] (in press).

211. S. Benson, R.J. Chater and J.A. Kilner, see ref [202] (in press).

212. J.A. Lane, S. Adler, P.H. Middleton and B.C.H. Steele, see ref. [29], p. 584.

213. R.B. Bird, W.E. Stewart, and E.N. Lightfoot, Transport Phenomena, Chapter 6, John Wiley and Sons, New York, NY, 1960, pp. 180-207.

214. W.E. Ranz, and W.R. Marshall, Jr., 'Evaporation from Drops, Part I', Chem. Eng. Prog., ***48*** [3], (1952) pp. 141-146.

215. W.E. Ranz, and W.R. Marshall, Jr., 'Evaporation from Drops, Part II, Chem. Eng. Prog., ***48*** [4], April 1952, pp. 173-180.

216. Fluent User's Guide, Version 4.3, Fluent Inc., Lebanon, NH, 1995, Section 19, p. 124.

217. Fluent User's Guide, Version 4.3, Fluent Inc., Lebanon, NH, 1995, Section 19, p. 126.

218. Fluent User's Guide, Version 4.3, Fluent Inc., Lebanon, NH, 1995, Section 19, p. 127.

219. Fluent User's Guide, Version 4.3, Fluent Inc., Lebanon, NH, 1995, Section 19, p. 41.

220. J.O. Hinze, Turbulence, McGraw-Hill Publishing Co., New York, NY, 1975.

221. Fluent User's Guide, Version 4.3, Fluent Inc., Lebanon, NH, 1995, Section 19, p. 44.

222. K.K.Y. Kuo, Principles of Combustion, John Wiley and Sons, New York, NY, 1986.

223. Fluent User's Guide, Version 4.3, Fluent Inc., Lebanon, NH, 1995, Section 19, p. 49.

219. B.E. Launder, and D.B. Spalding, 'The Numerical Computation of Turbulent Flows', Imperial College of Science and Technology, London, England, NTIS N74-12066, January 1973.

220. A.J. Appleby, Energy, ***11*** (1986) p. 21.

APPENDIX

A1 LSM DIFFRACTION DATA

$La_{0.8}Sr_{0.2}MnO_3$ 40-1100 [184]

Monoclinic system a = 5.4843 Å,

b = 5.5349 Å,

c = 7.7916 Å, and

β = 90.746°

d spacing (Angstrom)	hkl
3.8983	110
2.7680	020
2.7422	$\bar{2}00$
2.3537	121
2.2563	022
2.2291	202
1.9479	220
1.7487	130
1.7357	222
1.5980	$\bar{1}32$
1.5930	132
1.5782	312
1.3837	040
1.3709	$\bar{4}00$
1.3039	042
1.2985	330
1.2880	402
1.2354	240
1.2285	332

A2 ELECTRODE ASR AND ACTIVATION ENERGY

Table A1 : Electrode ASRs and activation energy (E_A) of the reciprocal of ASR for sample LSC30 at several annealing periods.

Annealing (hours)	ASR 800°C (Ω cm^2)	ASR 900°C (Ω cm^2)	E_A (eV)
10	11.069	2.870	1.56
20	39.248	9.893	1.59
36	71.405	24.916	1.24
100	307.488	190.501	0.62
600	57.864	15.039	1.56

Table A2 : Electrode ASRs and activation energy (E_A) of the reciprocal of ASR for sample LSC12 at several annealing periods.

Annealing (hours)	ASR 800°C (Ω cm^2)	ASR 900°C (Ω cm^2)	E_A (eV)
0	0.263	0.090	1.27
10	0.729	0.250	1.26
20	2.292	0.688	1.40
36	4.765	1.351	1.46
100	5.418	1.580	1.43

Table A3 : Electrode ASRs and activation energy (E_A) of the reciprocal of ASR for sample CG/LC10 at several annealing periods.

Annealing (hours)	ASR 800°C (Ω cm^2)	ASR 900°C (Ω cm^2)	E_A (eV)
0	0.017	0.0036	1.81
4	1.024	0.285	1.48
14	3.738	1.343	1.21
30	6.418	2.330	1.20
94	5.578	1.833	1.30

Table A4 : Electrode ASRs and activation energy (E_A) of the reciprocal of ASR for sample YC/LC at several annealing periods.

Annealing (hours)	ASR 800°C (Ω cm^2)	ASR 900°C (Ω cm^2)	E_A (eV)
0	0.027	0.0097	1.19
10	0.248	0.079	1.34
20	0.337	0.105	1.36
36	0.569	0.169	1.42
100	0.690	0.185	1.53

Table A5 : Electrode ASRs and activation energy (E_A) of the reciprocal of ASR for sample YC/LM at several annealing periods.

Annealing (hours)	ASR 800°C (Ω cm^2)	ASR 900°C (Ω cm^2)	E_A (eV)
0	2.959	1.328	0.97
10	5.257	1.791	1.26
20	32.620	11.632	1.22
36	29.247	11.968	1.07
100	14.592	3.517	1.64

Table A6 : ASRs of sample LSC30 after annealing for 600 hours.

Oxygen partial pressure (atm)	0.21	0.10	0.05
Electrode ASR 800°C (ohm cm^2)	57.864	48.077	48.165
Electrode ASR 900°C (ohm cm^2)	15.039	9.252	8.304
gb ASR 800°C (ohm cm)	0.018	0.045	0.054
gb ASR 900°C (ohm cm)	0.006	0.018	0.022
bulk ASR 800°C (ohm cm)	0.129	0.223	0.289
bulk ASR 900°C (ohm cm)	0.046	0.085	0.113

Table A7 : ASRs of sample LSC12 after annealing for 100 hours.

Oxygen partial pressure (atm)	0.21	0.10	0.05
Electrode ASR 800°C (ohm cm^2)	5.418	6.578	6.446
Electrode ASR 900°C (ohm cm^2)	1.580	1.747	1.358
gb ASR 800°C (ohm cm)	0.014	0.009	0.011
gb ASR 900°C (ohm cm)	0.006	0.0036	0.0045
bulk ASR 800°C (ohm cm)	0.0112	0.0106	0.0278
bulk ASR 900°C (ohm cm)	0.0048	0.0045	0.0130

A3 AC IMPEDANCE RESPONSES

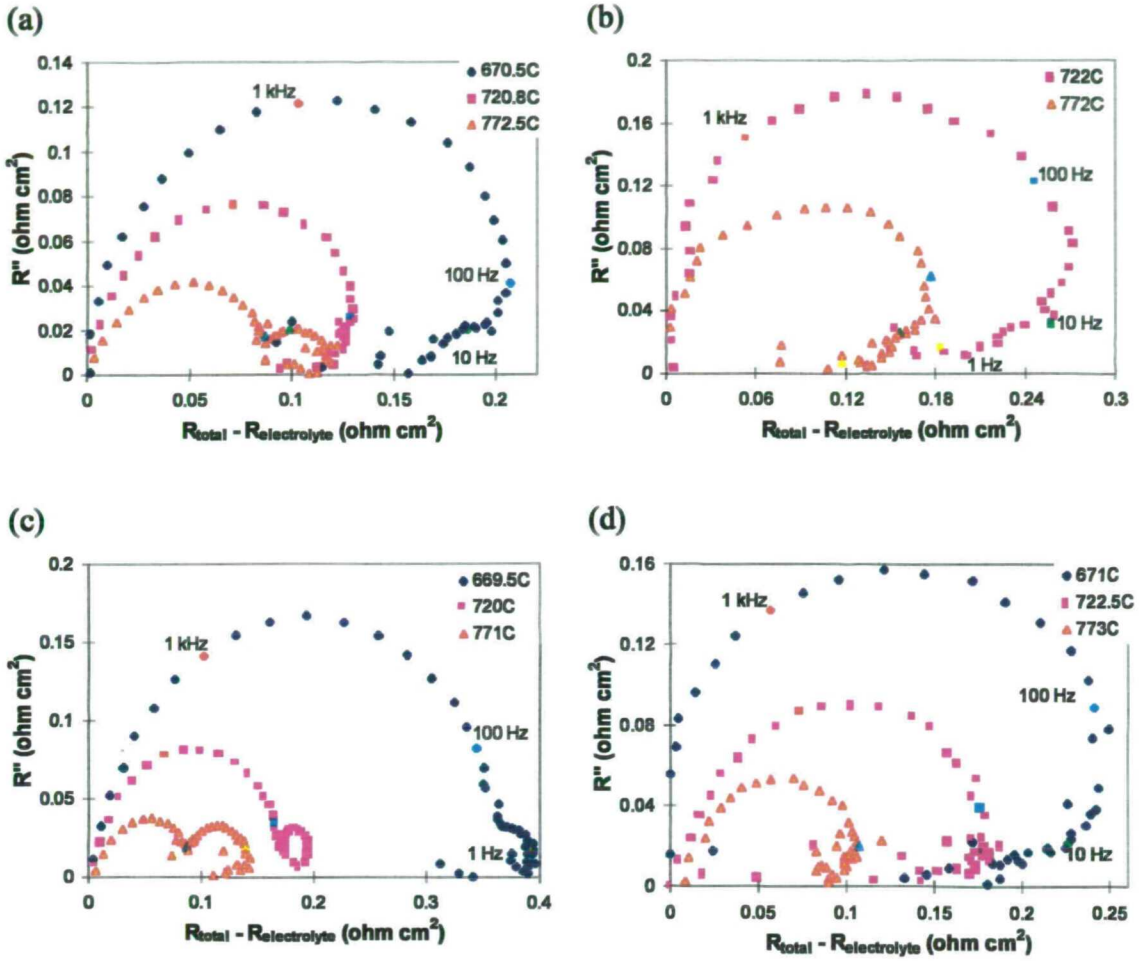


Fig. A1 : AC-impedance responses of (a) CG/LC30, (b) CG/LC97, (c) CG/LC14, and (d) CG/LC17.

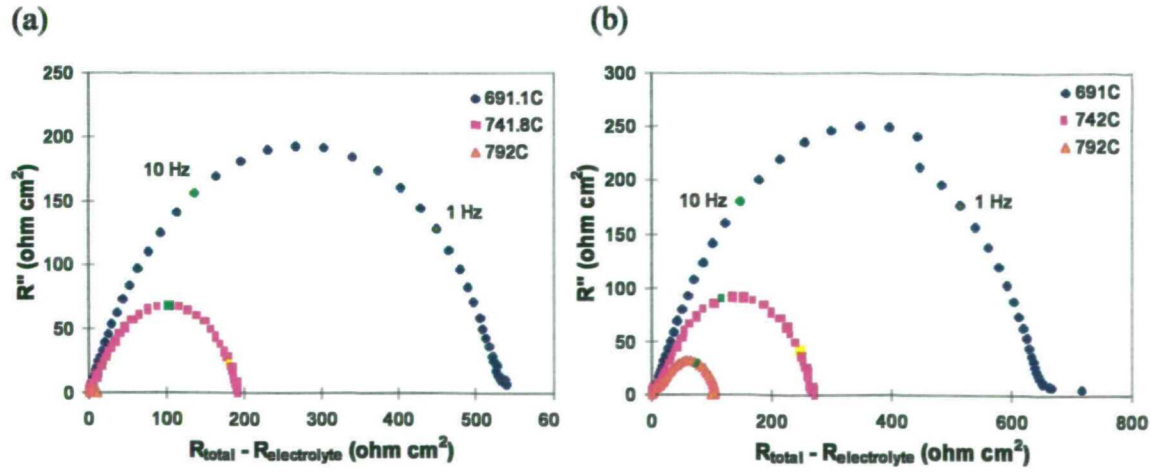


Fig. A2 : AC-impedance responses of sample LSC30 after annealing for (a) 20 hours and (b) 36 hours.

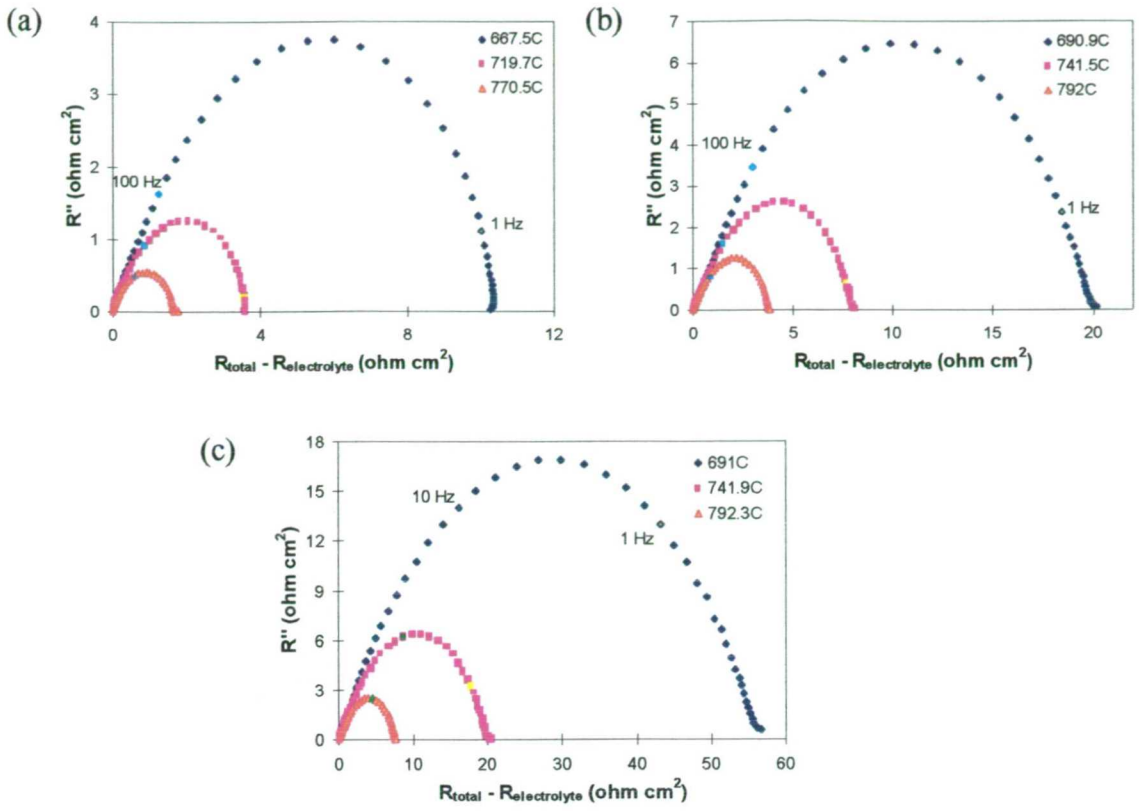


Fig. A3 : AC-impedance responses of sample LSC12 after annealing for (a) 10 hours, (b) 20 hours, and (c) 36 hours.

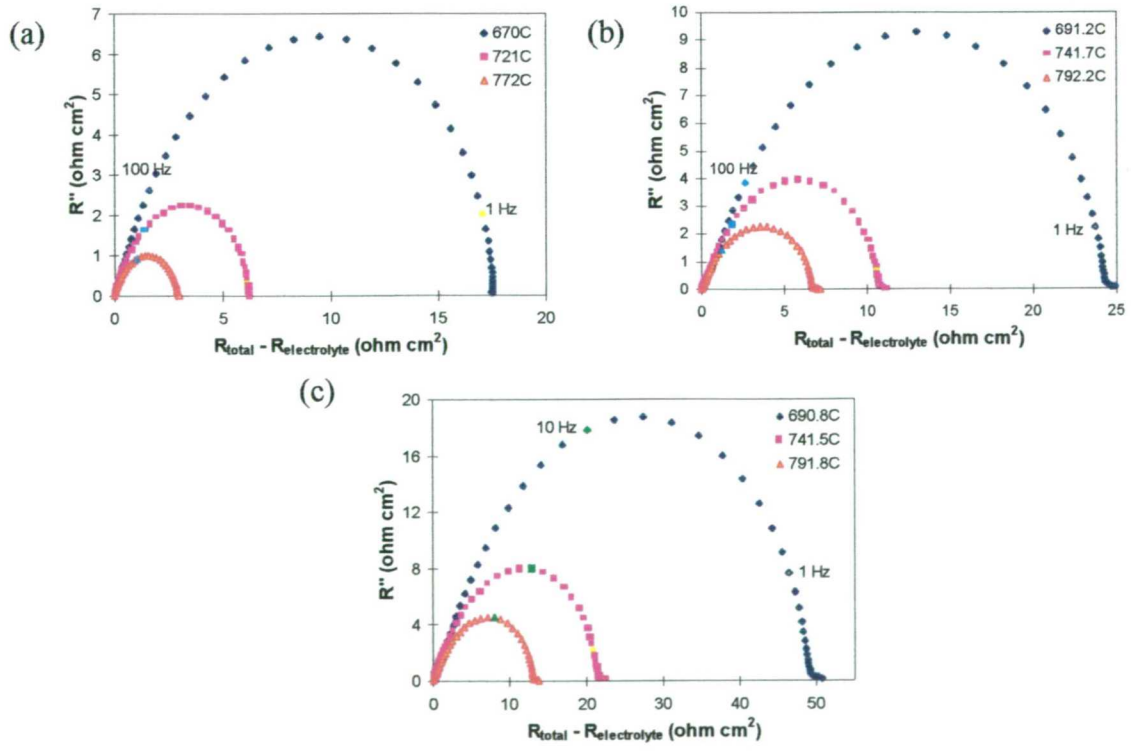


Fig. A4 : AC-impedance responses of sample CG/LC10 after annealing for (a) 4 hours, (b) 14 hours, and (c) 30 hours.

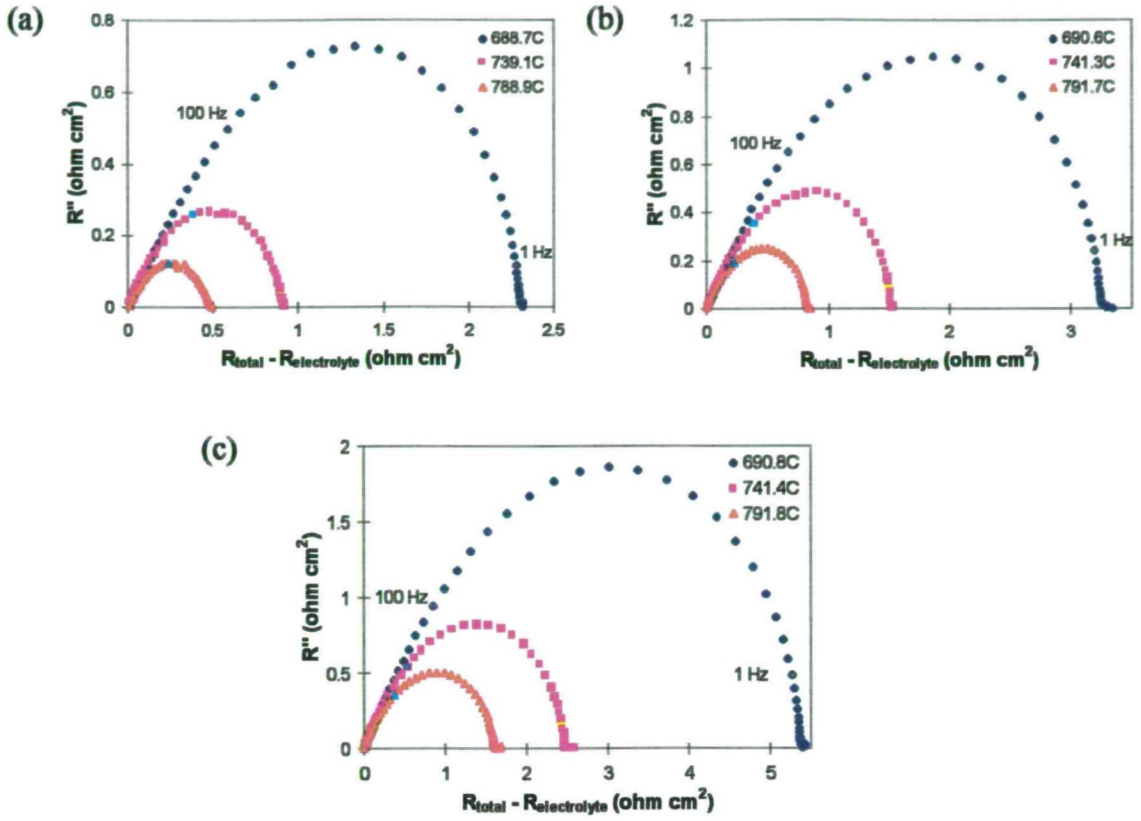


Fig. A5 : AC-impedance responses of sample YC/LC after annealing for (a) 10 hours, (b) 20 hours, and (c) 36 hours.

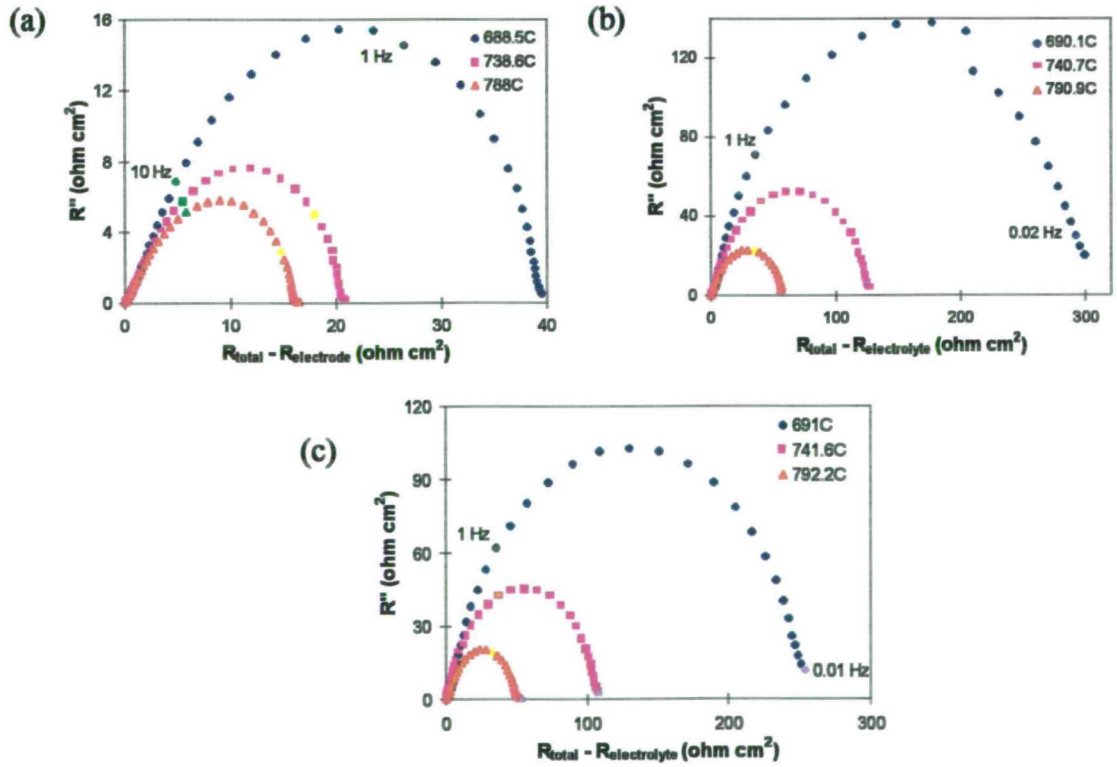


Fig. A6 : AC-impedance responses of sample YC/LM after annealing for (a) 10 hours, (b) 20 hours, and (c) 36 hours.

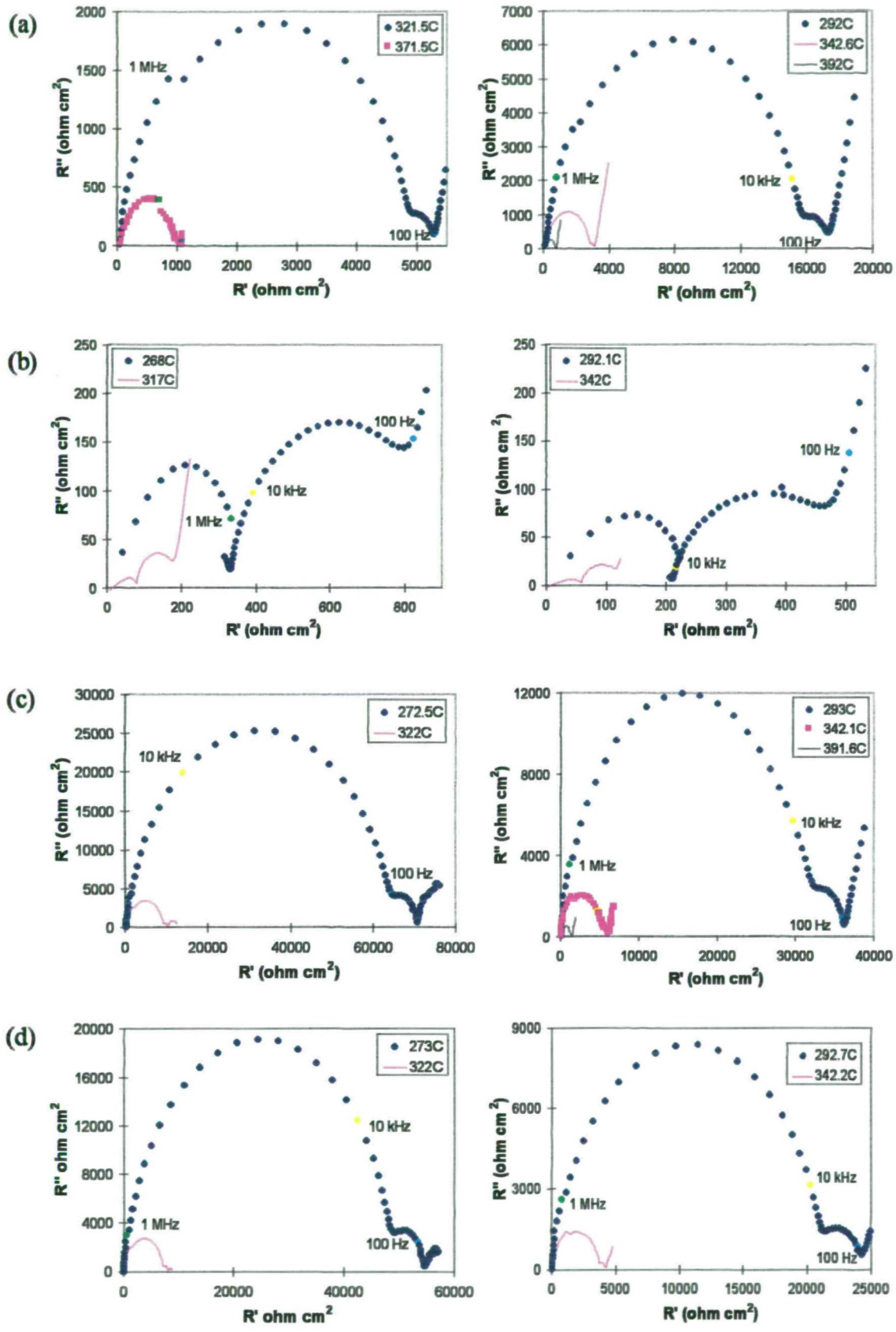


Fig. A7 : AC-impedance responses before annealing and after 100 hours annealing in the range of low temperature for (a) LSC30, (b) LSC12, (c) CG/LC10 (94 hours), (d) YC/LC, and (e) YC/LM (see overleaf).

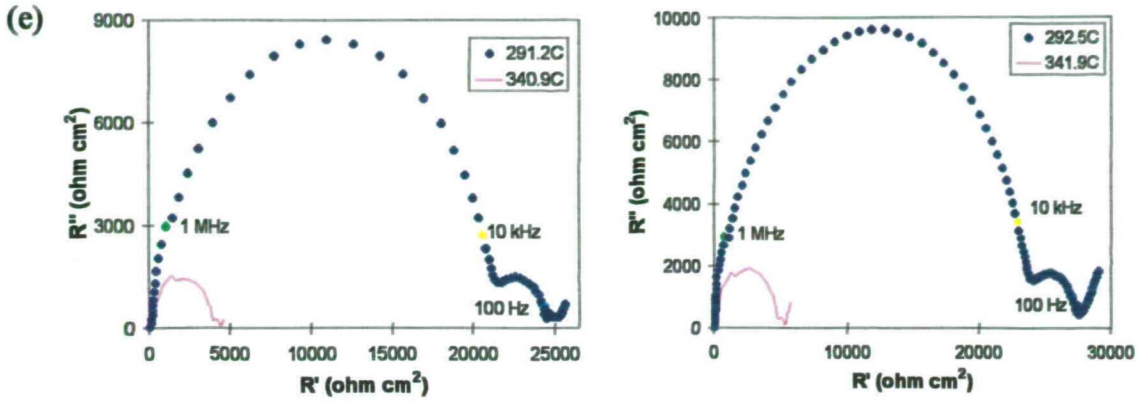


Fig. A7 : AC-impedance responses before annealing and after 100 hours annealing in the range of low temperature (e) YC/LM.

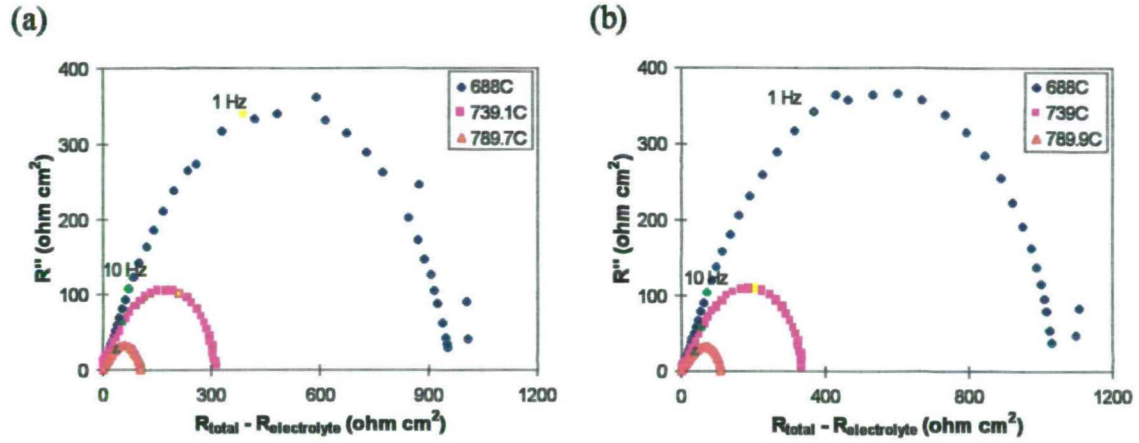


Fig. A8 : AC-impedance responses of sample LSC30 in oxygen partial pressure (a) 0.10 atm and (b) 0.05 atm.

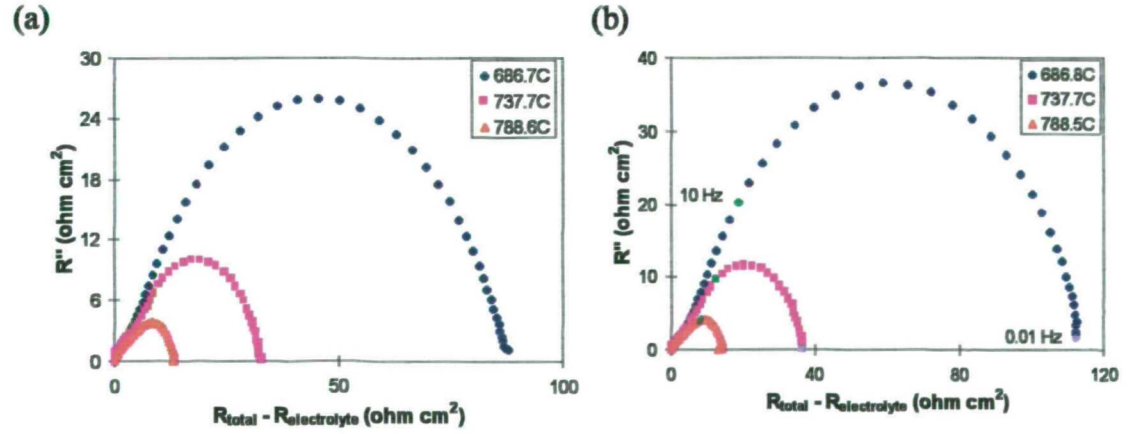


Fig. A9 : AC-impedance responses of sample LSC12 in oxygen partial pressure (a) 0.10 atm and (b) 0.05 atm.

A4 XRD PATTERNS

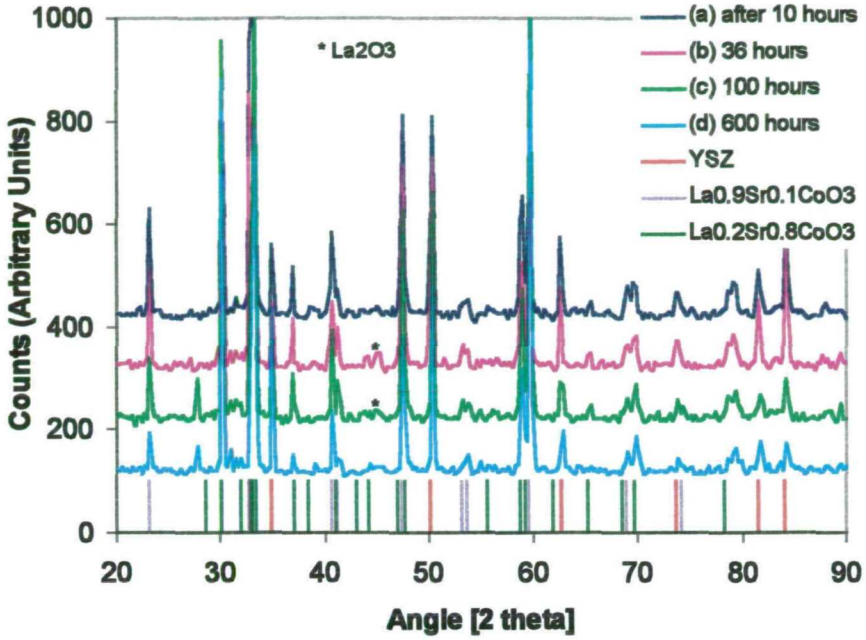


Fig A10 : XRD patterns of sample LSC30 after annealing for (a) 10 hours, (b) 36 hours, (c) 100 hours, and (d) 600 hours.

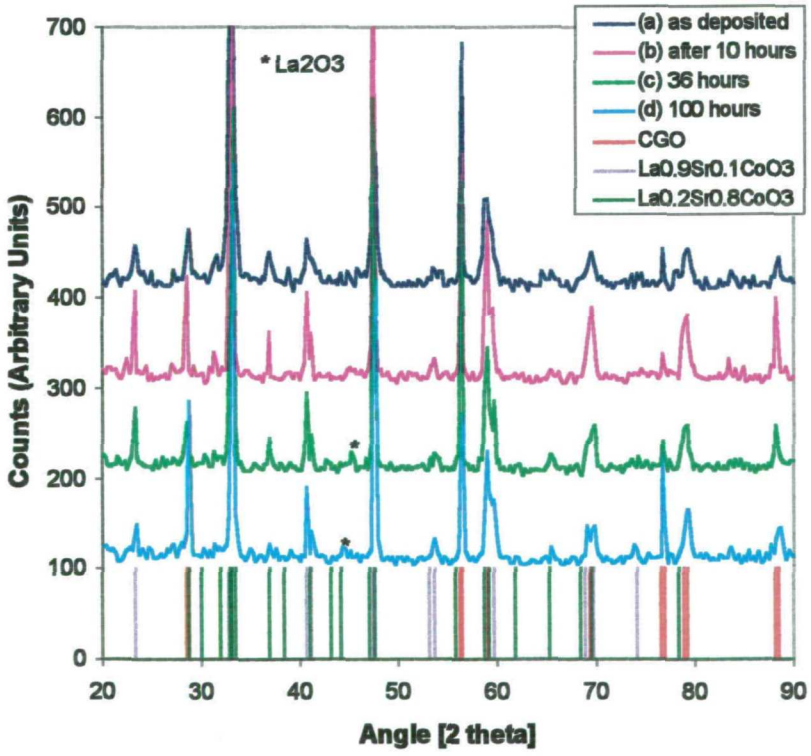


Fig A11 : XRD patterns of sample LSC12 (a) as deposited, after annealing for (b) 10 hours, (c) 36 hours, and (d) 100 hours.

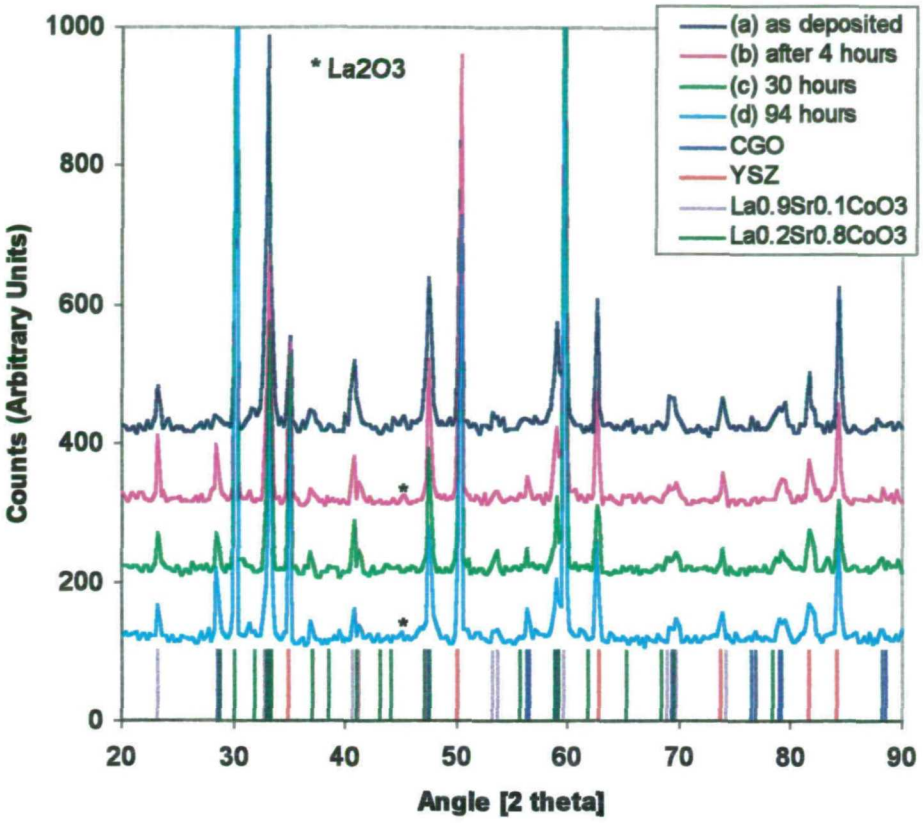


Fig A12 : XRD patterns of sample CG/LC10 (a) as deposited, after annealing for (b) 4 hours, (c) 30 hours, and (d) 94 hours.

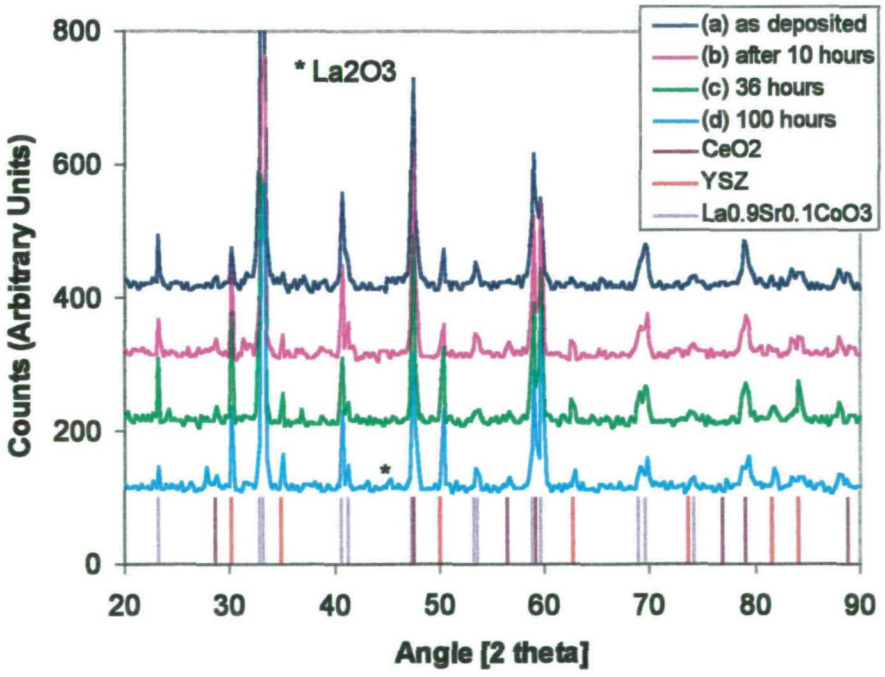


Fig A13 : XRD patterns of sample YC/LC (a) as deposited, after annealing for (b) 10 hours, (c) 36 hours, and (d) 100 hours.

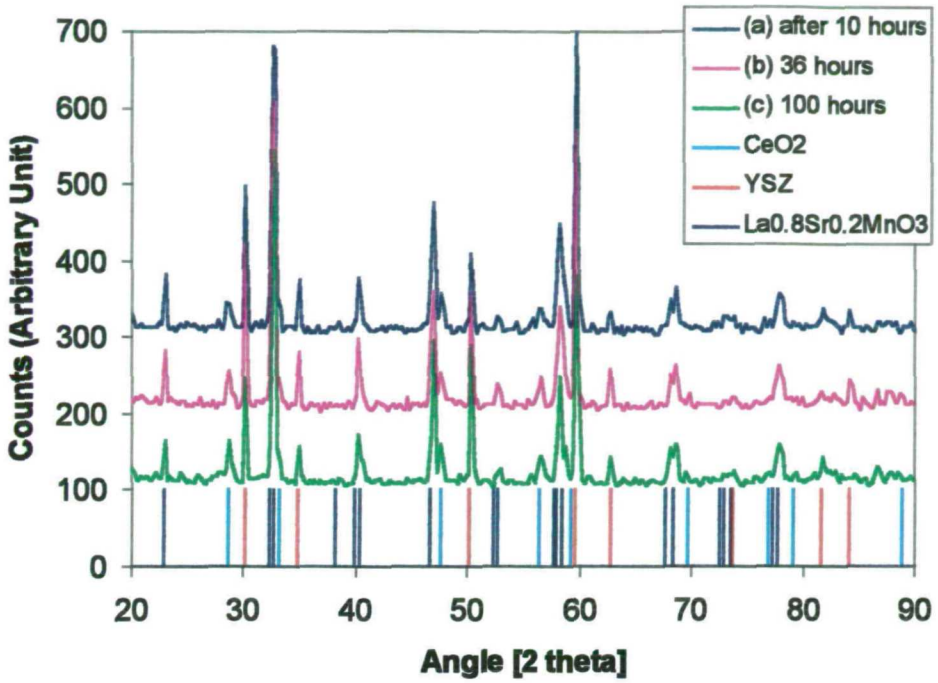


Fig A14 : XRD patterns of sample YC/LM (a) as deposited, after annealing for (b) 10 hours, (c) 20 hours, (d) 36 hours, and (e) 100 hours.

A5 MODELLING

A5.1 THEORY

(i) The Standard Wall Function

In a turbulent flow, the default Launder and Spalding's law-of-the-wall in computing the standard wall function is applied [225]:

$$\frac{uC_{\mu}^{\frac{1}{4}}k^{\frac{1}{2}}}{\frac{\tau_{\omega}}{\rho}} = \frac{1}{\kappa}\ln(Ey^{+}) \qquad \text{-----} \quad \text{(A1)}$$

which under equilibrium conditions reverts to the standard log-law:

$$\frac{u}{u^{*}} = \frac{1}{\kappa}\ln(Ey^{+}) \qquad \text{-----} \quad \text{(A2)}$$

where $u^{*} = \sqrt{\tau_{\omega}/\rho}$,

u is the fluid velocity at the point in the layer,

κ is von-Karman's constant (= 0.42),

k is the turbulent kinetic energy at the point,

μ is the dynamic viscosity of the fluid,

E is an empirical constant set by default to 9.8 (smooth wall), and

y^{+} is the dimensionless distance from the wall:

$$y^{+} = \frac{C_{\mu}^{\frac{1}{4}}\rho k_{p}^{\frac{1}{2}}y}{\mu} \qquad \text{-----} \quad \text{(A3)}$$

By assuming local equilibrium conditions and constant shear stress in the turbulent boundary layer, equation A3 becomes:

$$y^{+} = \rho u^{*} y/\mu \qquad \text{-----} \quad \text{(A4)}$$

Equation A1 is applied in turbulent flow when $y^{+} > 11.225$, and the near-wall cell centre lies in the viscous sub-layer of the turbulent boundary layer when y^{+} falls below this value. Equation A1 is then not valid in the sub-layer and the calculation of the wall shear stress has to be calculated using an equation for walls in laminar flow instead:

$$\tau_w = \mu \left.\frac{\partial u}{\partial n}\right|_{wall} \approx \mu \frac{\Delta u}{\Delta n} \qquad \text{-----} \quad \text{(A5)}$$

When this standard wall function is used, an equilibrium assumption is made to derive the boundary conditions for k and ε. The production and dissipation of turbulence are assumed equal in the boundary layer, implying that the dissipation rate at the wall follows the boundary conditions:

$$\varepsilon_p = \frac{C_\mu^{\frac{1}{4}} k_p^{\frac{3}{2}}}{\kappa y_p} \qquad \text{-----} \quad \text{(A6)}$$

The near-wall value for k_p is computed by solving the complete transport equations for k in the near-wall control volume, with the wall shear stress included in the production term and a zero normal gradient assumed for k at the wall.

(ii) Heat Transfer at Walls in Turbulent Flow

An effective fluid side heat transfer coefficient is obtained from the law-of-the-wall [225]:

$$\frac{k(\Delta T/\Delta n)}{q''} = \frac{1}{\kappa y^+}\frac{\mathrm{Pr}_t}{\mathrm{Pr}}\ln(Ey^+) + \frac{1}{y^+}\left(\frac{\mathrm{Pr}_t}{\mathrm{Pr}}\right)^{\frac{5}{4}} \frac{\frac{\pi}{4}}{\sin\frac{\pi}{4}}\left(\frac{A}{\kappa}\right)^{\frac{1}{2}}\left(\frac{\mathrm{Pr}}{\mathrm{Pr}_t} - 1\right) \qquad \text{(A7)}$$

where k = thermal conductivity of fluid

ΔT = T_w-T_f

Δn = distance from wall to near-wall node point P

q″ = wall heat flux

Pr = molecular Prandtl number

$\mathrm{Pr_t}$ = turbulent Prandtl number (1.2 at the wall)

A = van Driest constant (26)

κ = von Karman's constant (0.42)

E = empirical constant (9.81)

(iii) Species Diffusion at Walls in Turbulent Flow

An effective turbulent transport of species is computed via a simple Reynolds analogy between mass and momentum transfer, that is:

$$J_{i'} = \rho k_c \Delta m_{i'} \qquad \text{-----} \quad \text{(A8)}$$

where $$k_c = \frac{1}{Sc_t} \frac{u^*}{\frac{1}{\kappa}\ln(Ey^+)} \qquad \text{-----} \quad \text{(A9)}$$

and Sc_t is the effective 'turbulent' Schmidt number (momentum diffusivity/mass diffusivity)

A5.2 TEMPERATURE DISTRIBUTION CONTOURS

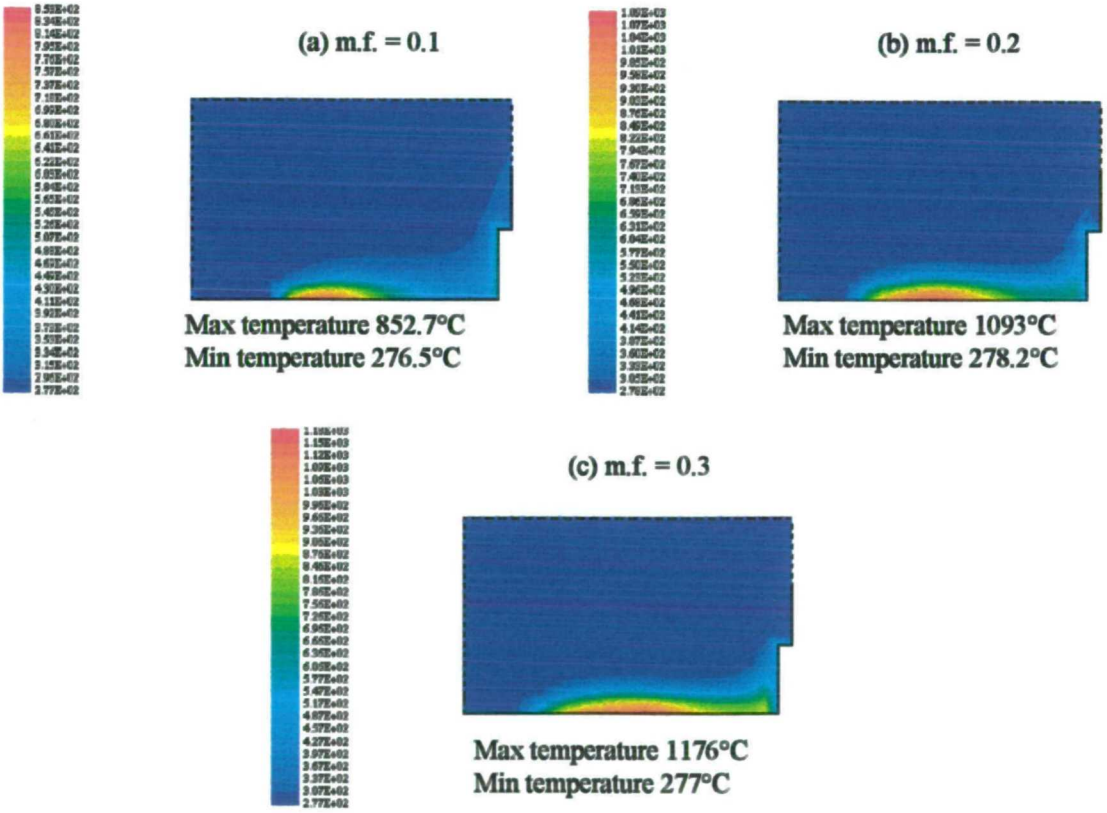


Fig. A15 : Temperature distribution contours of at different mixture fractions for 50% alcohol solution.

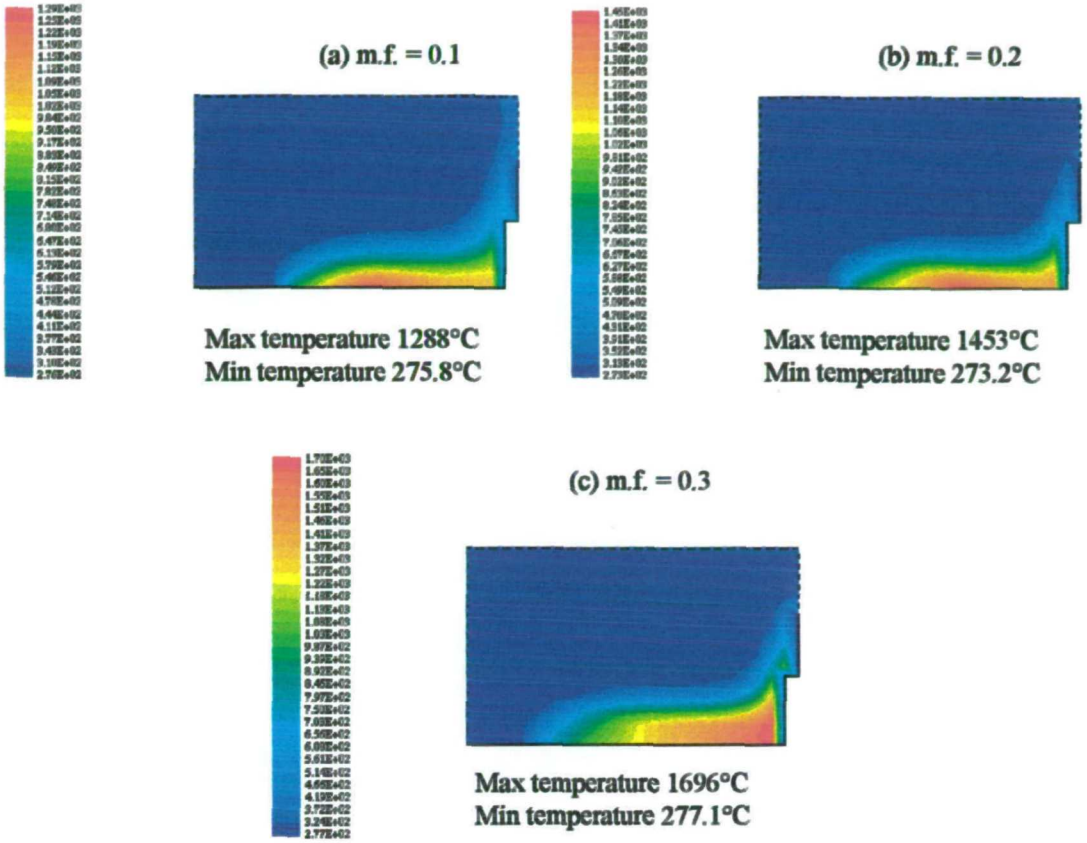


Fig. A16 : Temperature distribution contours of at different mixture fractions for 80% alcohol solutions.

A5.3 MASS FRACTION OF CHEMICAL SPECIES CONTOURS

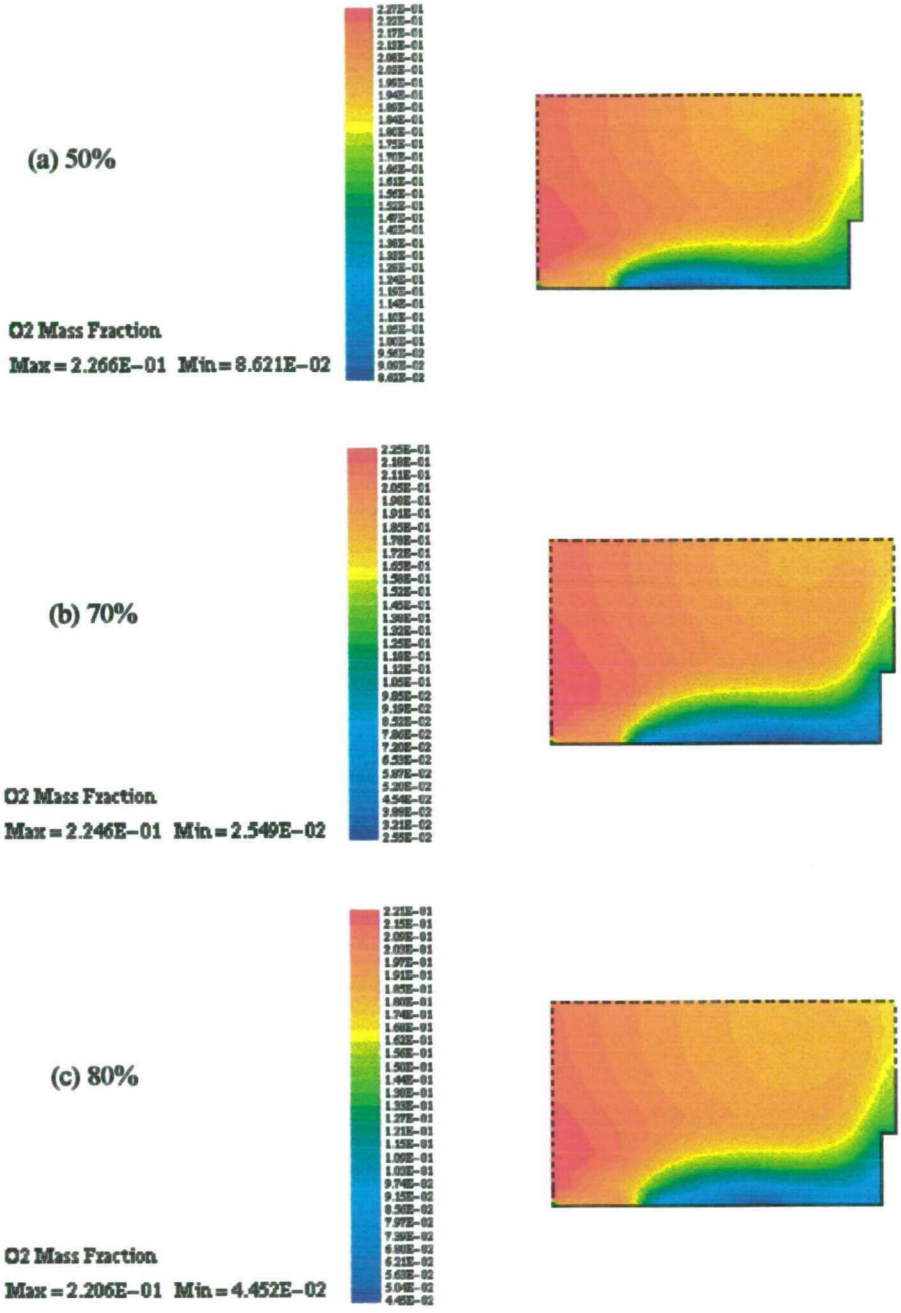


Fig. A17 : Mass fraction of oxygen gas present for (a) 50%, (b) 70%, and (c) 80% alcohol solutions.

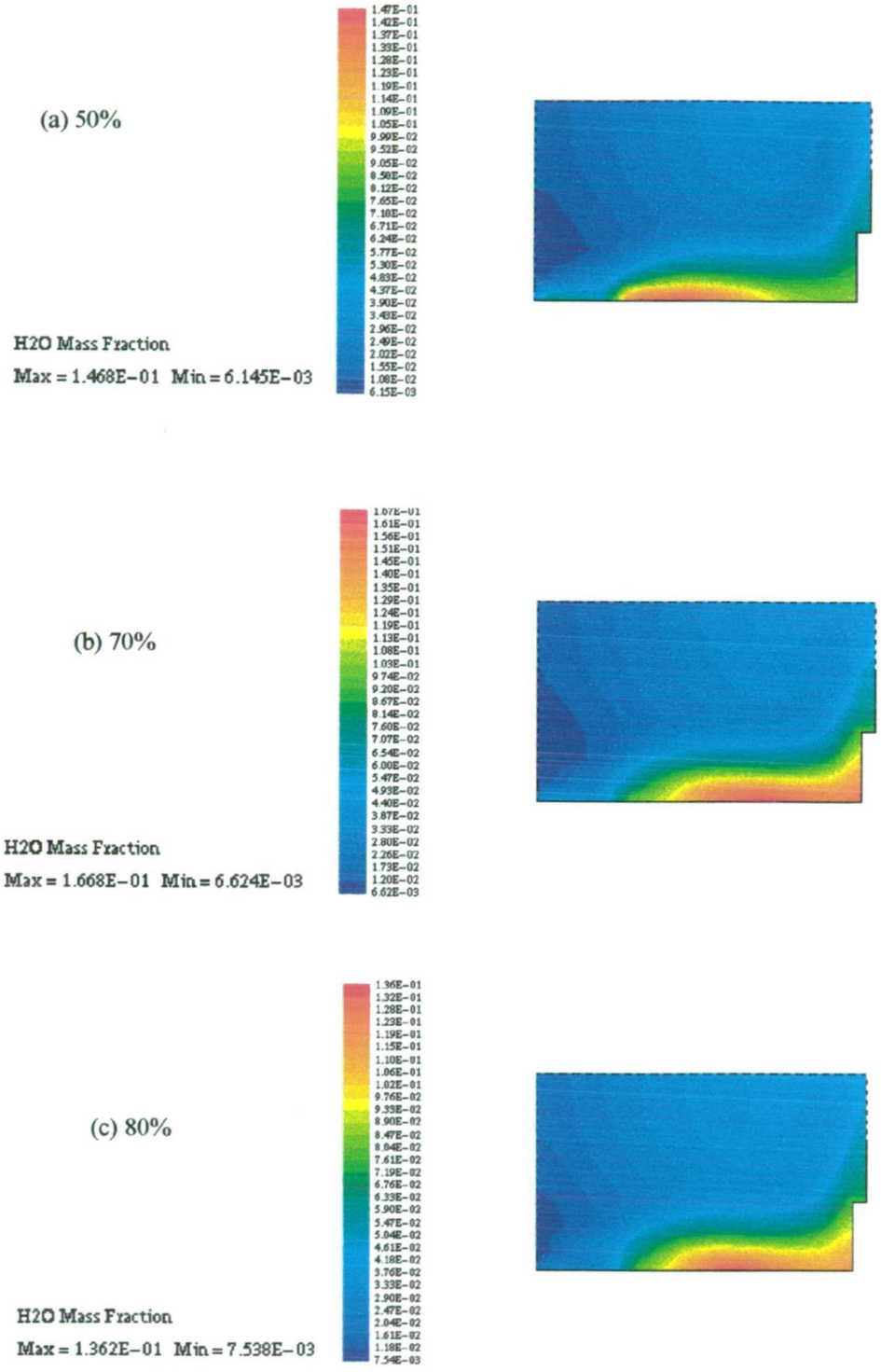


Fig. A18 : Mass fraction of water present for (a) 50%, (b) 70%, and (c) 80% alcohol solutions.

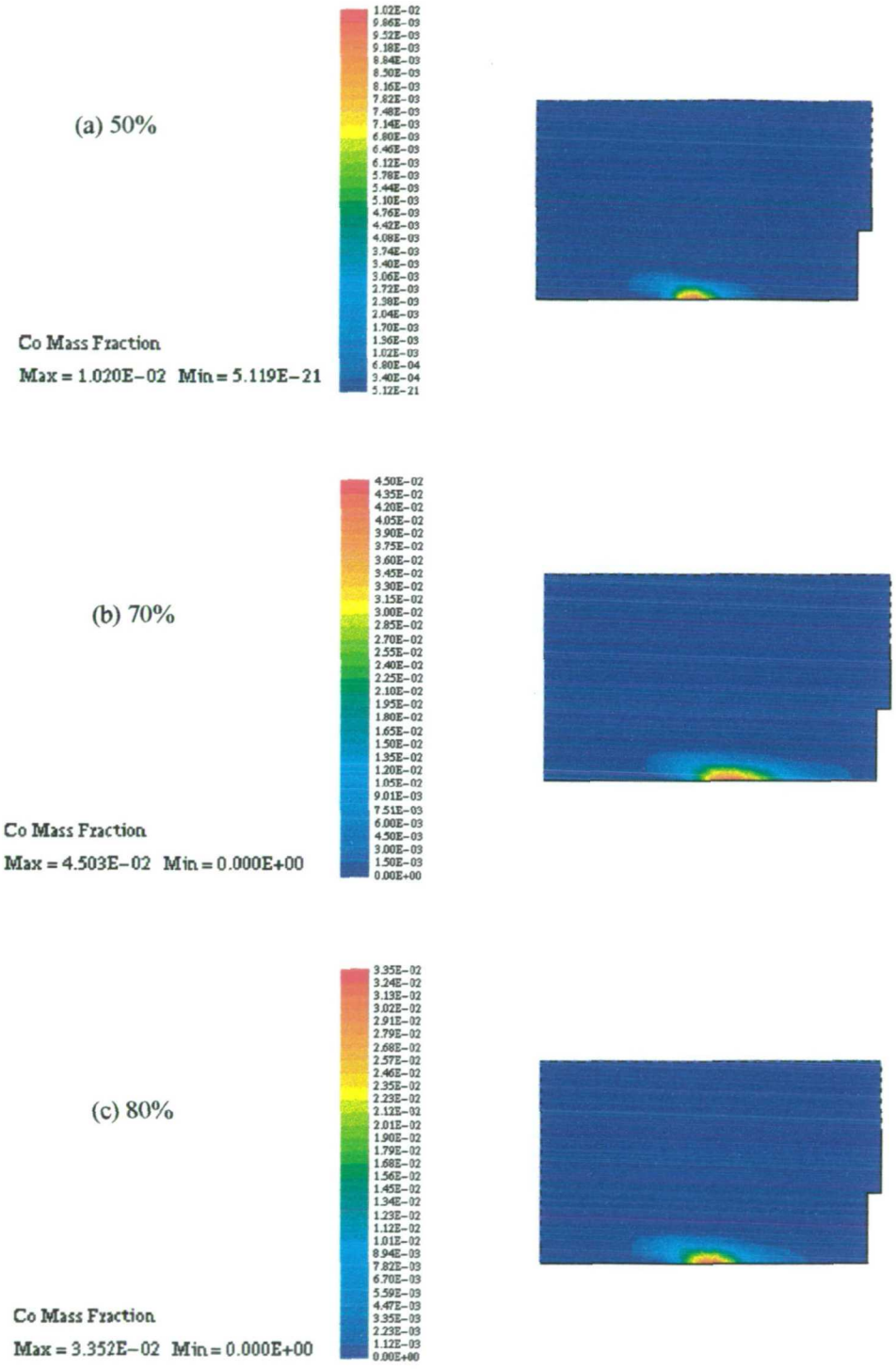


Fig. A19 : Mass fraction of carbon monoxide present for (a) 50%, (b) 70%, and (c) 80% alcohol solutions.

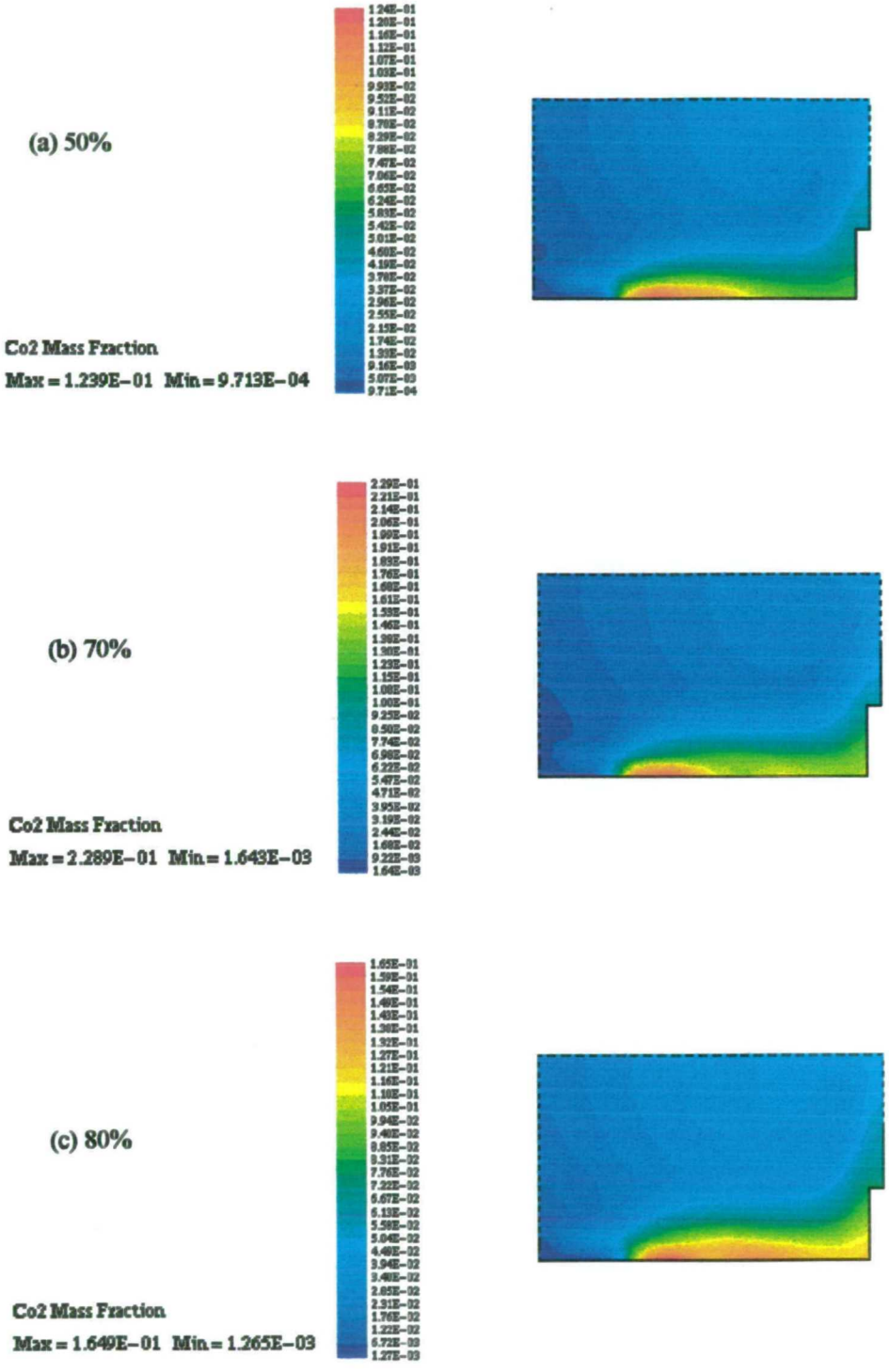


Fig. A20 : Mass fraction of carbon dioxide for (a) 50%, (b) 70%, and (c) 80% alcohol solutions.

BIBL LONDON UNIV.